



INVESTIGATION OF DRIZZLE ONSET IN LIQUID CLOUDS USING
GROUND BASED ACTIVE AND PASSIVE REMOTE SENSING
INSTRUMENTS

INAUGURAL – DISSERTATION
ZUR
ERLANGUNG DES DOKTORGRADES
DER MATHEMATISCH-NATURWISSENSCHAFTLICHEN FAKULTÄT
DER UNIVERSITÄT ZU KÖLN

VORGELEGT VON
CLAUDIA ACQUISTAPACE

AUS PISA, ITALIEN

KÖLN, 14. NOVEMBER 2016

BERICHTERSTATTER:
PD Dr. Ulrich Löhnert
Prof. Dr. Roel Neggers
Prof. Dr. Pavlos Kollias

TAG DER MÜNDLICHEN PRÜFUNG:
23.01.2017

*Considerate la vostra semenza:
fatti non foste a viver come bruti
ma per seguir virtute e canoscenza*

— Dante Alighieri —

Firenze, 1 June 1265 – Ravenna, 14 September 1321

Dedicated to my family

ABSTRACT

One of the major challenges of climate prediction is a correct representation of the interactions among aerosols, clouds and precipitation. Aerosols have a strong impact on the life cycle of boundary layer clouds, which are known to significantly influence the energy available to the Earth-Atmosphere system. Specifically, drizzle formation in low-level clouds, which has been shown to depend on aerosol concentration (second indirect aerosol effect), determines cloud life time. In models, the transition from liquid cloud to precipitation must be parameterized by the so-called autoconversion process. Different parameterizations of autoconversion have been developed, whereby the corresponding transition rates differ of up to one order of magnitude.

Even observations of this microphysical process are very challenging. Satellite observations have been exploited in the past to evaluate different autoconversion schemes but one of the main reasons for the encountered differences between models and observations was the poor representation of the vertical cloud structure in the satellite observations. In this context, ground-based cloud observations present a unique tool to provide observational constraints for model parameterization development by exploiting their highly temporally and spatially resolved profiling capability. In recent years, new ground-based techniques exploiting higher moments of the cloud radar Doppler spectrum (the skewness, in particular) have been successfully applied for the detection of drizzle onset in maritime clouds.

In this thesis, a new, extended ground-based dataset for continental liquid clouds is exploited in order to assess the potential for early drizzle detection. For this purpose, ground-based observations of liquid water path and of the cloud radar Doppler moments reflectivity, mean Doppler velocity, spectral width and skewness have been synergistically exploited. It has been found that skewness detects drizzle formation at an earlier stage than the other radar moments.

The different observational variables have been used for the development of a drizzle probability index (DI) to improve currently available drizzle classification schemes, i.e. Cloudnet. The DI represents the probability of each cloud radar bin to contain drizzle. In comparison to the Cloudnet classification, case studies show that the DI detects earlier stages of drizzle formation and eliminates falsely detected, inconsistent time-height drizzle structures. However, due to the presence of turbulence, the DI sometimes falsely attribute drizzle to a pixel.

In order to understand how turbulence can impact radar Doppler measurements and also in order to optimize the radar measurement

settings for the purpose of drizzle detection, sensitivity studies on integration time, spectral resolution and radar antenna beam width have been conducted using raw radar data and a forward radar simulator. It has been found that integration times no longer than 2 seconds should be used for drizzle detection and that the spectral resolution obtained with the fast Fourier transform (FFT) using 256 FFT points resolves the characteristics of the Doppler spectrum with sufficient accuracy. Also, simulations showed that smaller beam widths are beneficial for drizzle detection and that turbulence is responsible for an increase of spectral width and a reduction of observed skewness values.

Finally, a microphysical interpretation of the skewness signal is provided by comparing the simulations of drizzle formation from a 1D steady-state binned microphysical model to observations. The forward simulated vertical profiles of skewness based on the modeled cloud drop and drizzle size distributions strongly depend on the applied autoconversion parameterization. A validation of the different schemes indicates that the scheme from [Seifert et al. \(2010\)](#) best matches the observations of reflectivity and skewness. The comparison also suggests that the modeled autoconversion rates tend to produce large drizzle too fast and too early for continental liquid clouds. This first model comparison thus demonstrates that ground-based cloud radar observations, particularly skewness, can be used for testing autoconversion parameterizations.

The dataset and the results of this work constitute a unique basis for evaluating model outputs, e.g. in a next step the results of large eddy simulations, and for carrying out additional process studies to refine for example the drizzle detection criterion. Also, this data set could be exploited for future validations of satellite products, e.g. of EarthCARE. This thesis hence shows how ground-based cloud radar observations can be optimally exploited to better understand the autoconversion process and also represents an important step forward in bringing observations of drizzle and modeling together.

ZUSAMMENFASSUNG

Eine der größten Herausforderungen in der Klimavorhersage ist die korrekte Darstellung der Wechselwirkungen zwischen Aerosolen, Wolken und Niederschlag. Aerosole wirken sich stark auf den Lebenszyklus von Grenzschichtwolken aus, welche wiederum signifikant die verfügbare Energie im System Erde/Atmosphäre beeinflussen. Insbesondere bestimmt die Bildung von Niesel, welche von der Aerosolkonzentration abhängt (zweiter indirekter Aerosoleffekt), die Lebenszeit niedriger Wolken. In Modellen muss der Übergang von Wolkentropfen zu Niederschlag durch den sogenannten Autokonversionsprozess parametrisiert werden. Verschiedene Parametrisierungen der Autokonversion wurden entwickelt, wobei sich die entsprechenden Übergangsraten bis zu einer Größenordnung unterscheiden. Auch Beobachtungen dieses mikrophysikalischen Prozesses stellen eine große Herausforderung dar. In der Vergangenheit wurden von Satelliten aus durchgeführte Messungen verwendet, um verschiedene Autokonversionsschemata zu evaluieren. Einer der Hauptgründe für die Unterschiede zwischen den Modellen und Satellitenbeobachtungen war jedoch die schlechte vertikale Auflösung der Wolkenstruktur in den Beobachtungen. In diesem Zusammenhang bieten bodengebundene Wolkenbeobachtungen aufgrund ihrer hohen zeitlichen und räumlichen Auflösung eine einzigartige Beobachtungsgrundlage, um Parametrisierungen für Modelle zu entwickeln. In den letzten Jahren wurden bodengebundene Messverfahren, die höhere Momente des Wolkenradarspektrums (insbesondere die Schiefe) ausnutzen, erfolgreich angewendet, um das Einsetzen von Niesel in maritimen Wolken zu detektieren. In dieser Arbeit wird ein neuer, umfassender Datensatz bodengebundener Beobachtungen von kontinentalen Wasserwolken verwendet, um das Potential zur frühzeitigen Detektion von Niesel abzuschätzen. Zu diesem Zweck wurden bodengebundene Beobachtungen des Flüssigwasserpfad und der Dopplermomente eines Wolkenradars (Reflektivität, mittlere Dopplergeschwindigkeit, spektrale Breite und Schiefe) synergetisch ausgewertet. Es hat sich dabei gezeigt, dass die Schiefe im Vergleich zu den anderen Radarmomenten Nieselbildung in einem früheren Stadium detektiert. Die verschiedenen Beobachtungsgrößen wurden zur Entwicklung eines Nieselindizes (DI) herangezogen, um die zurzeit bestehenden Niesel-Klassifikationsschemata, z. B. Cloudnet, zu verbessern. Der DI beschreibt die Wahrscheinlichkeit, dass in dem jeweiligen betrachteten Wolkenradarvolumen Niesel vorkommt. Fallstudien zeigen, dass im Vergleich zu der Cloudnetklassifikation der DI früheren Stadien der Nieselbildung detektiert. Der DI entfernt zudem durch Cloudnet fälschlicherweise detektierte, d.h. in Zeit und Höhe inkonsistente, Nie-

selstrukturen. Das Auftreten von Turbulenz kann jedoch manchmal dazu führen, dass der DI irrtümlich Niesel detektiert. Um zu verstehen, welchen Einfluss Turbulenz auf die Radar-Dopplermomente hat und um die Messeinstellungen des Radars für die Detektion von Niesel zu optimieren, wurden Sensitivitätsstudien hinsichtlich Integrationszeit, spektraler Auflösung und Antennenöffnungswinkel durchgeführt. Dazu wurden die unbearbeiteten, ursprünglichen Radardaten und ein Radar-Vorwärtssimulator verwendet. Es hat sich gezeigt, dass die Eigenschaften des Dopplerspektrums mit einer ausreichenden Genauigkeit wiedergegeben werden, wenn die Integrationszeiten nicht länger als 2 Sekunden sind. Zudem reicht es, eine spektrale Auflösung zu wählen, die mit einer Fast-Fourier-Transformation (FFT) mit 256 FFT-Punkten erzeugt wird. Darüber hinaus haben die Simulationen gezeigt, dass kleinere Antennen-öffnungswinkel vorteilhaft für die Detektion von Niesel sind und dass Turbulenz die spektrale Breite vergrößert und die Schiefe des Dopplerspektrums verkleinert. Abschließend, wird eine mikrophysikalische Interpretation des Signals in der Schiefe gegeben, indem Simulationen von Nieselbildung basierend auf einem sogenannten "1D steady-state binned microphysical"-Modell mit Beobachtungen verglichen werden. Die Vertikalprofile der Schiefe, die auf Vorwärtssimulationen der modellierten Wolkentropfen- und Nieselgrößenverteilungen basieren, hängen stark von der jeweils verwendeten Autokonversionsparametrisierung ab. Eine Validierung der verschiedenen Schemata hat gezeigt, dass das Schema von [Seifert et al. \(2010\)](#) am besten die Beobachtungen der Reflektivität und Schiefe wiedergibt. Der Vergleich legte außerdem nahe, dass die modellierten Autokonversionsraten dazu neigen, große Nieseltropfen in kontinentalen Flüssigwasserwolken zu schnell und zu früh zu erzeugen. Dieser erste Modellvergleich zeigt daher, dass bodengebundene Wolkenradarbeobachtungen, insbesondere die Schiefe, genutzt werden können, um Autokonversionsparametrisierungen zu testen. Der Datensatz und die Ergebnisse dieser Arbeit bilden eine einzigartige Grundlage für die Evaluierung von Modellergebnissen, z.B. in einem nächsten Schritt die Ergebnisse von Large-Eddy-Simulationen, und für das Durchführen weiterer Prozessstudien um z.B. das Kriterium zur Nieseldetektion zu verfeinern. Außerdem kann dieser Datensatz zukünftig genutzt werden um Satellitenprodukte, z.B. von EarthCARE, zu validieren. Diese Arbeit zeigt, wie bodengebundene Wolkenradarbeobachtungen optimal genutzt werden können, um den Prozess der Autokonversion besser zu verstehen und macht zudem einen weiteren wichtigen Schritt hinsichtlich des Zusammenführens von Nieselbeobachtungen und Modellen.

CONTENTS

i	INTRODUCTION	1
1	MOTIVATION	3
2	SCIENTIFIC BACKGROUND	11
2.1	Warm rain processes: theoretical perspective	11
2.1.1	The theory of warm rain formation	11
2.1.2	The problem of the initiation of coalescence	16
2.2	Microphysical processes in models	17
2.3	Measuring liquid clouds and light precipitation	25
2.3.1	Microwave radiometer	25
2.3.2	Cloud radar	26
2.4	Observations of drizzle onset	35
ii	TOOLS AND DATA	41
3	INSTRUMENTS AND METHODS	43
3.1	HATPRO Microwave radiometer	43
3.2	35 GHz Cloud radar JOYRAD-35	46
3.3	Ceilometer	51
3.4	Cloudnet target categorization	51
3.5	Passive and Active Microwave Transfer (Pamtra) forward model	54
4	DATABASE FOR IDENTIFYING PRECIPITATION	59
4.1	Liquid clouds at JOYCE	59
4.2	Assessment of drizzle detection by Cloudnet	66
4.3	Extended analysis of drizzling/non-drizzling cloud properties	68
4.3.1	Statistical properties	68
4.3.2	Dataset characterization in terms of radar Doppler moments and LWP	70
iii	DETECTING DRIZZLE WITH SKEWNESS	75
5	MICROPHYSICAL INTERPRETATION OF SKEWNESS	77
5.1	The concept: interpreting the skewness signal	77
5.2	Observations from two case studies	78
5.3	Description of the model	80
5.4	Confronting model and observations	85
5.5	Interpretation of skewness in terms of drizzle droplet size	95
5.6	Conclusions and summary of the results	97
6	OPTIMIZING OBSERVATIONS OF DRIZZLE ONSET WITH MM-WAVELENGTH RADARS	99
6.1	Motivation and concept of the study	99

6.2	Methodology for the processing of the IQ raw radar data	101
6.3	IQ raw radar dataset	102
6.4	Impact of integration time and spectral resolution on the observations	104
6.4.1	Moments time series	105
6.4.2	Impact of spectral resolution	107
6.4.3	Probability density functions for each combination of settings	110
6.5	Simulation framework: statistics and impact of hardware parameters	113
6.5.1	Simulation statistics for early stage and mature drizzle cases	116
6.5.2	Effects of turbulence and varied antenna beamwidth	119
6.6	Conclusion and summary of main results	120
iv EXPLOITMENT OF SKEWNESS FOR OPERATIONAL APPLICATIONS 123		
7	REFINEMENT OF DRIZZLE DETECTION	125
7.1	Distributions of observed variables for drizzling/ non-drizzling clouds	125
7.2	The algorithm for calculating the drizzle index	132
7.3	Performance on case studies at high resolution	134
7.3.1	Drizzling case study of the 5 Jan 2013	134
7.3.2	Drizzling case study of the 9 October 2013	137
7.3.3	Transition case study of the 31 July 2013	139
7.3.4	Non-drizzling case study of the 1 October 2013	142
7.4	Comparison with Cloudnet	147
7.5	Conclusions and summary of main results	148
8	CONCLUSIONS AND OUTLOOK	151
ABBREVIATIONS		157
SYMBOLS		161
BIBLIOGRAPHY		163

LIST OF FIGURES

Figure 1.1	Increase of CO ₂ concentration in the period 1958-2016. 3
Figure 1.2	Change of the equilibrium temperature as predicted by 12 GCMs in the scenario of doubling the CO ₂ concentration (from Dufresne and Bony (2008)). 4
Figure 2.1	Example of cloud drop size distribution (from Wallace and Hobbs (2006)). 12
Figure 2.2	Collision efficiency for pairs of drops. 14
Figure 2.3	Microphysical growth rates for condensation and collision-coalescence. 16
Figure 2.4	Effect of GCCN on precipitation rates in ECHAM5 (from Posselt and Lohmann (2008)). 17
Figure 2.5	Characteristics times and scales of models. 18
Figure 2.6	Collision processes in bulk schemes (from Khain et al. (2015)). 20
Figure 2.7	Comparison of autoconversion rates (from Wood (2005b)) 24
Figure 2.8	Absorption coefficient for atmospheric gases as a function of frequency. 26
Figure 2.9	Dielectric constant for water in the range of frequencies 1 – 50 GHz. 30
Figure 2.10	Illustration of the standard procedure for deriving radar Doppler spectra from raw I/Q time series. 33
Figure 2.11	Example of an observed cloud radar Doppler spectrum. 34
Figure 2.12	Explanation of skewness as tracer for drizzle onset. 36
Figure 2.13	Skewness as a function of reflectivity for a marine stratus cloud (from Luke and Kollias (2013)). 39
Figure 2.14	Schematic representation of the dynamical induced skewness signal (from Luke and Kollias (2013)) 40
Figure 3.1	EM extinction in microwave region 45
Figure 3.2	Example of fit to the power law $\frac{-5}{3}$ for the energy spectrum $E(f)$. 49
Figure 3.3	Case study for calculation of ϵ . 50
Figure 3.4	Distribution of ϵ . 50
Figure 3.5	Drizzling, non-drizzling and transition vertical columns based on Cloudnet. 53
Figure 4.1	Precipitation amount at JOYCE between March 2012 and August 2013. 60

Figure 4.2	LWP statistics of JOYCE observation and COSMO-DE for the period mar 2012-mar 2013. 61
Figure 4.3	Geometrical thickness statistics of JOYCE observation and COSMO-DE for the period March 2012-March 2013. 62
Figure 4.4	2D probability of precipitation for JOYCE data for the period March 2012 - March 2013. 63
Figure 4.5	2D probability of precipitation for COSMO-DE data for the period March 2012-March 2013. 63
Figure 4.6	Example of boundary layer non-drizzling cloud. 64
Figure 4.7	Example of stratocumulus non-drizzling cloud. 64
Figure 4.8	Example of boundary layer drizzling cloud. 65
Figure 4.9	Example of stratocumulus drizzling cloud. 66
Figure 4.10	Example of physical inconsistency in Cloudnet target categorization. 67
Figure 4.11	Analysis of the inconsistency in Cloudnet target categorization. 68
Figure 4.12	Z_e mean values distributed as a function of distance from clout top and LWP. 71
Figure 4.13	V_d mean values distributed as a function of distance from clout top and LWP. 71
Figure 4.14	S_w mean values distributed as a function of distance from cloud top and LWP. 73
Figure 4.15	S_k mean values distributed as a function of distance from cloud top and LWP. 73
Figure 5.1	Z_e for the case of the the 31 July 2013, from 9.2 UTC to 10.0 UTC. 79
Figure 5.2	S_k field selected by the skewness mask for the case of the the 31 July 2013, from 9.2 UTC to 10.0 UTC. 80
Figure 5.3	V_d for the case of the the 31 July 2013, from 9.2 UTC to 10.0 UTC. 81
Figure 5.4	Scheme representing the working principle of the steady state bin microphysical model employed in this study. 82
Figure 5.5	LWC profiles of model and observations. 83
Figure 5.6	Cloud and drizzle drop size distributions. 84
Figure 5.7	Example of autoconversion rates profiles (left) and accretion rates profiles (right) for the different schemes. 85
Figure 5.8	Comparison of Z_e profiles derived using different N. 87
Figure 5.9	Comparison of Z_e profiles derived using different LWC profiles. 88
Figure 5.10	Comparison of Z_e profiles derived using different initial drizzle sizes. 89
Figure 5.11	Comparison of mean observed and simulated V_d profiles. 91

Figure 5.12	Comparison of mean observed and simulated S_w profiles. 92
Figure 5.13	Comparison of mean observed and simulated S_k profiles. 93
Figure 5.14	V_d as a function of S_k for the mature drizzle development case study. 96
Figure 5.15	Relation between skewness and equivalent drizzle size for observations. 97
Figure 5.16	Relation between skewness and equivalent drizzle size for model data. 98
Figure 6.1	Overview of the non drizzle case study of the 20 November 2014. 103
Figure 6.2	Overview of the drizzle case study of the 24 June 2015. 104
Figure 6.3	Time series of Doppler moments for different integration times for the drizzling case study. 105
Figure 6.4	Time series of Doppler moments for different integration times for the non-drizzle case study. 106
Figure 6.5	Impact of spectra resolution for non drizzling case. 108
Figure 6.6	Impact of spectra resolution for drizzle case. 109
Figure 6.7	PDFs of the moments for the non-drizzling case. 110
Figure 6.8	PDFs of radar moments for drizzling case. 112
Figure 6.9	DSDs used in the simulations of IQ experiment. 114
Figure 6.10	Comparison between simulated and observed spectra. 115
Figure 6.11	Distribution of simulated moments for drizzle DSD with $R_{\text{eff,d}} = 20\mu\text{m}$ and $r_{\text{LWC}} = 2.0\%$. 116
Figure 6.12	Distribution of simulated moments for drizzle DSD with $R_{\text{eff,d}} = 30\mu\text{m}$ and $r_{\text{LWC}} = 0.5\%$. 117
Figure 6.13	Distribution of a selected fingerprint of drizzle development. 118
Figure 6.14	Simulated skewness as a function of r_{LWC} . 119
Figure 7.1	Z_e distribution for the whole dataset. 127
Figure 7.2	V_d distribution for the whole dataset. 127
Figure 7.3	S_w distribution for the whole dataset. 128
Figure 7.4	S_k distribution for the whole dataset. 129
Figure 7.5	2D histogram for Z_e and S_k for non-drizzling pixels. 129
Figure 7.6	2D histogram for Z_e and S_k for drizzling pixels. 130
Figure 7.7	2D histogram for Z_e and S_k for transition pixels. 131
Figure 7.8	LWP distribution for the whole dataset. 131
Figure 7.9	Geometrical thickness distribution for the whole dataset. 132
Figure 7.10	DI index time height plot for the drizzle case of 5 January 2013. 135

Figure 7.11	Distribution of DI values obtained for the drizzling case of the 5 January 2013. 136
Figure 7.12	Overview of the variables in all pixels which have a $DI = 0.4$ for the drizzle case of the 5 January 2013. 137
Figure 7.13	DI index time height plot for the drizzle case of the 9 October 2013. 138
Figure 7.14	Distribution of DI values obtained for the drizzling case of the 9 October 2013. 138
Figure 7.15	Normalized distributions of Z_e , V_d , S_w , S_k and LWP for various DI values for the case study of the 09 October 2013, between 1.2 and 2.0 UTC. 140
Figure 7.16	DI index time height plot for the drizzle case of 31st July 2013. 141
Figure 7.17	Distribution of DI values obtained for the drizzling case of the 31 July 2013. 142
Figure 7.18	Normalized distributions of Z_e , V_d , S_w , S_k and LWP for various DI values for the case study of the 31 July 2013, between 9.2 and 10.0 UTC. 143
Figure 7.19	DI index time height plot for the non-drizzle case of the 1 October 2013. 144
Figure 7.20	Normalized DI distribution for the case of the 1 October 2013. 145
Figure 7.21	Normalized distributions of Z_e , V_d , S_w , S_k and LWP for various DI values for the case study of the 1 October 2013, between 5.2 and 6.0 UTC. 146
Figure 7.22	Comparison between Cloudnet and DI for the drizzle case of the 13 July 2013. 148

LIST OF TABLES

Table 3.1	Current radar settings for JOYRAD-35 system at JOYCE, Jülich (DE). 47
Table 3.2	Parameters provided to PAMTRA for simulating JOYRAD-35 observations 57
Table 4.1	COSMO model and observations characteristics for the statistical comparison. 62
Table 4.2	Statistical properties of the ensemble of case studies used. 69
Table 6.1	Radar settings for operating MIRA METEK systems. 100
Table 6.2	Number of averaged spectra for every integration time. 101

Table 6.3	Bias and standard deviation of moments derived with different spectral resolutions for the drizzle case. 107
Table 6.4	Bias and standard deviation of moments derived with different spectral resolutions for the non-drizzle case. 107
Table 6.5	Mean values of moments distributions: 20 November 2014. 111
Table 6.6	Mean values of moments distributions: 24 June 2015. 112
Table 7.1	Derivation of flag for every variable in the χ^2 test. 133
Table 7.2	Example of classification array for every pixel. 134

Part I

INTRODUCTION

*If I have seen further than others, it is by standing upon the
shoulders of giants.*

Isaac Newton

Woolsthorpe-by-Colsterworth, 25 December 1642 –
London, 20 March 1727

MOTIVATION

In the month of September 2016, the CO₂ concentration in the atmosphere for the first time exceeded the value of 400 ppm and it will remain above that value permanently (Fig. 1.1) (Betts et al., 2016). CO₂ is one of the substances that are called drivers of climate change, because it alters the Earth’s energy budget with its increasing concentration.

link to the physical science basis of the IPCC report of 2013: <http://www.climatechange2013.org/>

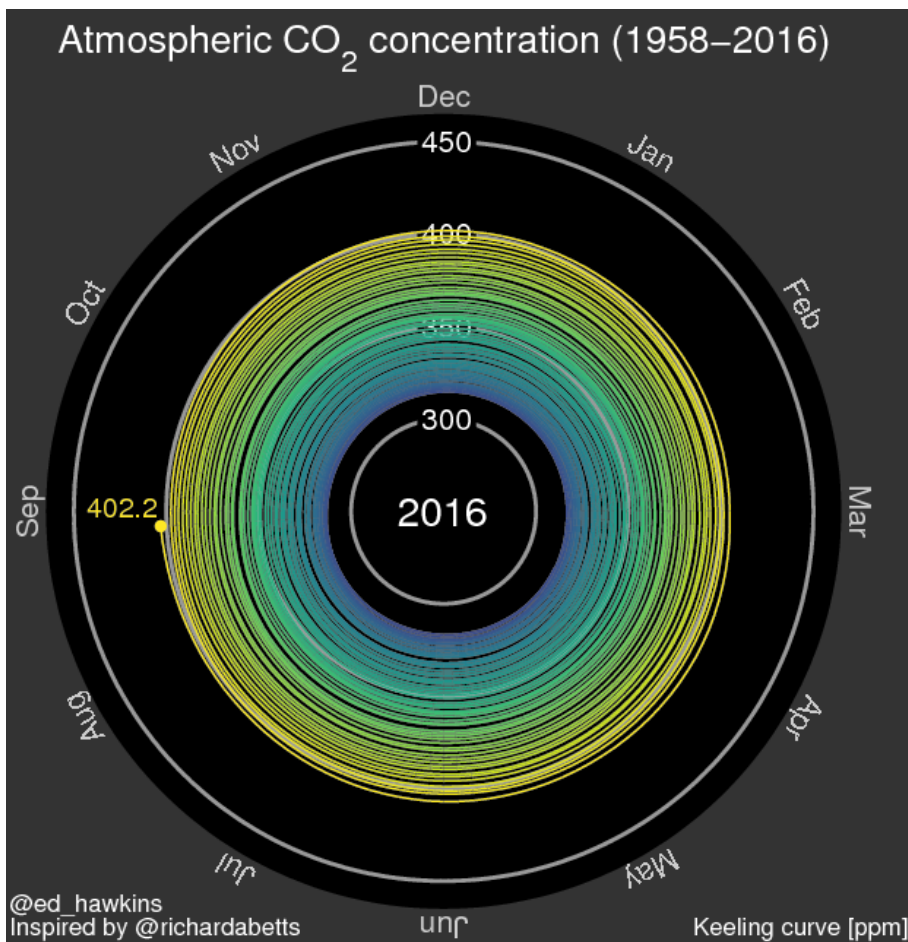


Figure 1.1: CO₂ concentrations measured at Mauna Loa station in the period 1958-2016 (produced by Ed Hawkins and available at <http://www.climate-lab-book.ac.uk/spirals/>), inspired by Betts et al. (2016). The spiral draws the evolution in time of the CO₂ concentration, starting from 320 ppm. Values measured in the preindustrial era (1800) were of 280 ppm (not shown here).

Radiative forcing quantifies the change in energy fluxes caused by the change of the drivers in the period of time from 1750 to present time. A positive forcing leads to surface warming (IPCC, 2014). The IPCC (2014) states that the total radiative forcing of the planet is pos-

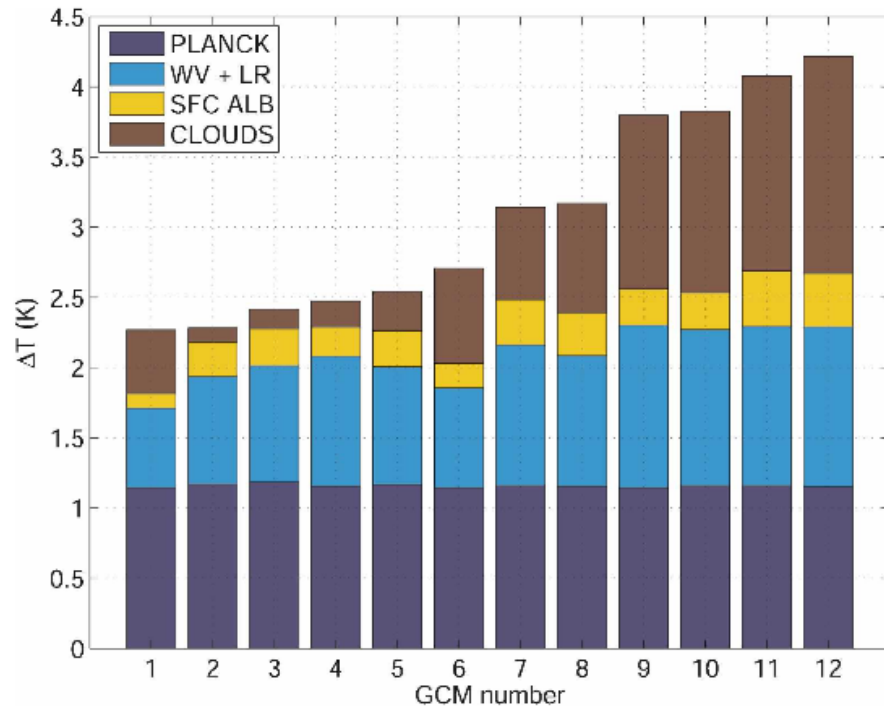


Figure 1.2: Change of average Earth temperature as predicted by 12 GCMs in the scenario of doubling the CO_2 concentration (from Dufresne and Bony (2008)). Impact of different feedbacks is shown in different colors: the Planck feedback gives the climate sensitivity in absence of variations of the climate system, the water vapour feedback accounts for the change in longwave radiation caused by water vapour, the surface albedo feedback accounts for change of the albedo at the surface and the cloud feedback considers the effects of clouds.

itive and the largest contribution to it comes from the increase of the concentration of atmospheric CO_2 . Plenty of observations show evidences that the climate is changing. General circulation models (GCMs) have been developed to forecast the average increase in temperature due to such forcings in future climate scenarios.

The overall response of a climate system to a change in radiative forcing, for example an increase of CO_2 , is defined as **climate sensitivity**. Processes that change the climate sensitivity are called **feedbacks** (Dal Gesso, 2015). Figure 1.2 shows the change of the surface temperature for a scenario of doubling CO_2 (Dufresne and Bony, 2008) for 12 different GCMs. The order of uncertainty among the predictions of different models is comparable to the variation of temperature itself. Moreover, from the decomposition of the feedbacks, the main contribution to this uncertainty comes from the cloud feedback, identified by Bony and Dufresne (2005) to be caused by **boundary layer clouds**. These are clouds that form at the top of the atmospheric layer (boundary layer) which is affected by the interactions with the surface.

In fact, low level liquid clouds (boundary layer clouds and stratocumuli) represent one of the main causes of the spread among different

model climate predictions (Bony et al., 2006). Mainly, this is because these clouds, so called warm because of the absence of ice, reduce the solar energy absorbed by the Earth system in the shortwave region and lead in general to a cooling effect with respect to cloud free conditions (Randall et al., 1984). The radiative properties of warm clouds are defined by their number concentration and by the horizontal and vertical distribution of cloud liquid water content (Weber and Quaas, 2012). Both these cloud properties are strictly connected with the aerosol presence. In fact, aerosols can have a strong impact on warm clouds properties in mainly two ways. An increase in the number of aerosol particles can produce a higher droplet total number concentration (N) and hence a higher cloud albedo, if the amount of liquid water in the cloud is considered constant (**first indirect effect**) (Twomey, 1977). The same increase in aerosol concentration can inhibit the coalescence between droplets and hence suppresses the precipitation (**second indirect effect**) (Albrecht, 1989). However, cloud systems exhibit a high variability caused by dynamics and it is hence very difficult to attribute changes in precipitation to aerosol perturbations (Sorooshian et al., 2009).

In warm clouds, the second aerosol indirect effect can inhibit drizzle production and change cloud properties, lifetime and extent, with consequences also on the cloud cover (Mann et al., 2014). Various modeling studies show that high concentrations of cloud condensation nuclei (CCNs) cause a reduction in drizzle formation in warm clouds (Wang et al., 2011b,a). The same effect was also present in field campaigns conducted to study marine stratocumuli (Wood, 2005a; Lu et al., 2007, 2009). Regarding the first aerosol indirect effect, satellite datasets have been used to quantify the impact of higher CCN concentrations on cloud droplet size (Lebsock et al., 2008) and also to estimate the cloud albedo effect (Forster et al., 2007; L'Ecuyer et al., 2009). Modelling cloud albedo is also linked to the representation of drizzle because more drizzle is generally associated with open cells, while overcasted areas of stratocumuli often show light drizzle. Therefore a proper description of vertical and horizontal distributions of cloud liquid water connected with drizzle formation is needed also for properly simulating other characteristics, i.e. cloud albedo, cloud fraction and radiative forcing of boundary layer clouds (Stevens et al., 2005; Ahlgrimm and Forbes, 2014).

In GCMs, the rate at which precipitation is produced is controlled by the autoconversion process, i.e. the process of collision-coalescence that forms new small drizzle droplets, converting liquid water into rain. Therefore, the impact of the aerosol effects is typically parametrized through the autoconversion (Hsieh et al., 2009). Different parametrizations for the autoconversion have been developed in the last 40 years (e.g. Kessler, 1969; Khairoutdinov and Kogan, 2000; Seifert and Beheng, 2001; Liu and Daum, 2004; Franklin, 2008; Tripoli and

Cotton, 1980; Seifert et al., 2010). Wood (2005b) and Hsieh et al. (2009) compare the autoconversion rates present in literature and find differences up to three orders of magnitude. Rotstayn and Liu (2005) show that changing the autoconversion parametrizations in a GCM can decrease the indirect aerosol effect by 60%. Sun et al. (2006) show that the occurrence of light precipitation is typically overestimated by GCMs. The dependence of the autoconversion rate on the total number concentration and the amount of cloud liquid water is hence involved in the uncertainty of the estimation of the magnitude of the radiative forcing due to aerosol-cloud-precipitation interactions (Michibata and Takemura, 2015).

Prigent (2010) compares the latitudinal distribution of zonally averaged annual precipitation for satellite observations and nine global circulation models, finding that model simulations differ significantly from satellite observations. These large differences in the rates for drizzle formation have a huge impact on simulations of hydrological cycle and also on the description of the precipitation patterns. Quaas et al. (2009) compare 10 different GCMs to satellite datasets, investigating the relation between aerosol optical depth and LWP. They find that all models overestimate this relation by more than a factor of 2 over land and partially attribute this overestimation to the dependency of autoconversion parametrizations on N. Also, Franklin (2008) demonstrates that the frequency of non precipitation/drizzle/-precipitation clouds is sensitive to the autoconversion rate. Suzuki et al. (2013) show that the global cloud-resolving model (GCRM) simulated reduction of rain production for a given aerosol increase is much smaller than that observed, due to the model deficiency of representing the water conversion process. In the frame of future climate change, one of the largest impacts on society will most likely come from changes in precipitation patterns, intensity and duration. Also in the context of operational applications, Fritsch and Carbone (2004) show that a detailed description of cloud microphysics is needed to produce accurate quantitative precipitation forecasts also in the short time range.

Lohmann and Feichter (2005) pointed out that better estimates of the aerosol indirect effect cannot be achieved if no better understanding of the microphysical formation of drizzle droplets is gained. The large variability in the autoconversion parametrizations provided by different authors comes from different factors. Hsieh et al. (2009) show that different autoconversion schemes start the conversion of liquid water to rain only when the cloud liquid water content exceed a fixed threshold, which can be different from one scheme to the other (Khairoutdinov and Kogan, 2000; Wood and Blossey, 2005). Moreover, also different physical processes are taken into account to describe the collision of droplets, for example with or without including the effects that turbulence can have on the dynamics of the collisions (Seifert and

Beheng, 2001; Ayala et al., 2008; Seifert et al., 2010). Also, different drop size distributions (DSDs) for the cloud droplets (gamma or log-normal) are assumed (Clark, 1974, 1976).

Finally, observations of this early stage of rain formation are challenging. In recent years, observations from in situ, satellite and ground based platforms have been exploited to develop specific comparisons with models aimed at evaluating and improving model performances. Providing observational constraints is nevertheless a challenging task, because of the limitations of each instrument platform. The RACORO field campaign (Vogelmann et al., 2012) was an aircraft campaign conducted over the Southern Great Plains (SGP) to obtain an in situ statistical characterization of continental boundary layer clouds. In situ observations from RACORO cases are employed for evaluating and quantifying model performances. The causes of observed biases between model simulations and observations are investigated (Vogelmann et al., 2015; Endo et al., 2015; Lin et al., 2015). Using Cloudsat observations, Stephens et al. (2010) provide an evaluation of the character of oceanic precipitation from three different types of global prediction models. They find that the differences between observed and modeled precipitation are larger than typical differences due to observational retrieval errors or due to the different sampling techniques adopted for observations and models. Exploiting the ground based observations from Graciosa Island (Azores), Ahlgrimm and Forbes (2014) evaluate the European Center for Medium Range Forecasts (ECMWF) model's performance in describing marine boundary layer clouds and provide guidance for parameterization changes.

The aim of this thesis is to provide observational insights towards drizzle onset to be exploited for constraining model parametrizations. Ground based observations offer significant advantages with respect to other platforms. In situ measurements provide interesting case studies but cannot provide a statistical characterization of clouds. Satellite observations like Cloudsat provide a global coverage of cloud measurements but suffer from ground clutter contaminations in the lower three radar bins (Lebsock and L'Ecuyer, 2011) which often correspond to the heights where liquid clouds occur. Moreover, they do not provide highly temporally resolved observations and the vertical resolution of CloudSat is coarser than the one provided by ground-based radars. This aspect is crucial since sometimes the thin liquid clouds do not even entirely fill a single range bin.

Michibata and Takemura (2015) show that the poor representation of the cloud vertical structure in satellite observations is one of the main reasons for the biases in the cloud radiative properties in the evaluation of the autoconversion schemes of GCMs. When using ground-based observations, highly temporally and spatially resolved atmospheric profiles are collected and well suited for comparison with model data.

Moreover, the thesis focuses on continental boundary layer clouds, since up to now only a limited number of studies is devoted to study of continental clouds and the drizzle development in them. (Del Genio and Wolf, 2000; Dong et al., 2000; Kollias et al., 2007c).

In recent years advances in the ground based methodologies to detect drizzle presence in the cloud have been developed. Drizzle retrievals have been developed based on Doppler radars and lidars (O'Connor et al., 2005; Westbrook et al., 2010). However, often lidar retrievals are limited by the fact that they cannot provide information of the internal structure of the cloud, as radars can do. In addition to the standard radar Doppler moments, i.e. reflectivity, mean Doppler velocity and spectral width, so called "higher Doppler moments", namely skewness and kurtosis of the cloud radar Doppler spectra, have been calculated for the marine stratocumulus cloud datasets (Kollias et al., 2011a,b; Luke and Kollias, 2013). In particular, Luke and Kollias (2013) show the potential of the skewness for an earlier identification of drizzle formation with respect the standard Doppler moments. However, the requirements for high quality radar Doppler spectra moments estimations represent an open question of big importance, considering the increasing amount of cloud radars that are being deployed worldwide. Moreover, the Cloudnet tool for classification of vertical cloudy columns (Illingworth et al., 2007) is extensively used for different purposes, for example the validation of GCMs (Ahlgren and Forbes, 2014) and identification of non-drizzling cloudy columns where retrievals of cloud properties, i.e. cloud droplet effective radius, based on non-drizzle conditions, can be applied. However, the Cloudnet algorithm regarding drizzle detection (Hogan and O'Connor, 1996) is based on simple thresholds in radar reflectivity, that may be improved by the usage of additional variables. Finally, ground based extended datasets of warm clouds may become a valuable tool for validating measurements from the future satellite mission Earth Clouds, Aerosol and Radiation Explorer (EarthCARE): scheduled for launch in 2018, the EarthCARE satellite mission will provide global profiles of cloud, aerosol, and precipitation with unprecedented accuracy (Illingworth et al., 2015), employing for the first time a Doppler radar in space.

In this thesis, a new extended ground based dataset for continental clouds is exploited to assess the new techniques for drizzle detection developed for maritime clouds. Chapter 2 provides the theoretical description of warm rain formation together with a summary of how drizzle is described in models and detected from the ground. In Chapter 3 the ground based instrumentation used and the methodologies applied to derive variables of use in the work are presented. Also, a description of the radar forward simulator adopted to reproduce observations from a model is provided. The dataset is extensively described in Chapter 4. Then, in Chapter 5, a microphysical interpretation of the skewness is provided by means of a comparison

with model data. Also, the drizzling/non drizzling observations are compared to a steady state 1D model implementing different auto-conversion rates. The goal is to validate the schemes by means of observations on a statistical basis. Chapter 6 shows the results of sensitivity studies aimed at optimizing radar settings for the purpose of drizzle detection. Finally, in Chapter 7, an operative implementation of an advanced criterion to detect drizzle presence in a cloudy vertical profile is presented. The aim of the criterion is to be adopted operationally and to be exploited for validation of GCMs and other datasets. Conclusions and an outlook for future research on this topic is given in Chapter 8.

SCIENTIFIC BACKGROUND

In this chapter, the theoretical description of the process of formation of drizzle droplets in a liquid cloud with a specific focus on the coalescence is outlined (section 2.1). Then, the different approaches with which this process is described in models are presented and an overview of the commonly used autoconversion parametrizations used in literature is given (section 2.2). The basic theory of radiative transfer and radars is presented in section 2.3, including a detailed description of the radar variables of interest for this work. Finally, in section 2.4 an overview of the observations of liquid clouds and drizzle from different platforms is given with specific focus on the exploitation of cloud radar Doppler moments for drizzle detection.

2.1 WARM RAIN PROCESSES: THEORETICAL PERSPECTIVE

Rain formation in warm clouds is the result of a complicated sequence of physical processes: the activation of cloud droplets on a cloud condensation nucleus (CCN), also known as nucleation, and the subsequent growth first by condensation of water vapor on the droplets and then by coagulation, i.e. droplets collide and grow to a larger size. Here, a brief overview of all these processes is presented.

2.1.1 *The theory of warm rain formation*

Rain formation not involving ice processes, commonly referred to as warm rain, is responsible for a significant amount of the global precipitation on Earth (Seifert et al., 2010). In particular, in the region of the tropics, approximately 70% of the total precipitation is due to warm rain (Lau and Wu, 2003). Typically, these clouds are constituted by cloud droplets on the order of $10\ \mu\text{m}$ which form on CCNs on the order of $0.1\ \mu\text{m}$. When the cloud starts to rain, drizzle droplets and raindrops measuring diameters of $10^2\ \mu\text{m}$ and $10^3\ \mu\text{m}$, respectively, are observed. In terms of droplet number concentrations, measurements for marine stratocumulus clouds show typical values on the order of $10^2\ \text{cm}^{-3}$ for cloud droplets (Kubar et al., 2009). For drizzle and raindrops, values on the order of $10^{-1}\ \text{cm}^{-3}$ to $10^{-4}\ \text{cm}^{-3}$ are observed (Wood et al., 2009). Therefore, the size of a cloud droplet has to increase 1000 times to form drizzle and one million cloud droplets are needed to generate one raindrop of 1 mm. Also, in the tropics, raindrops can be even larger.

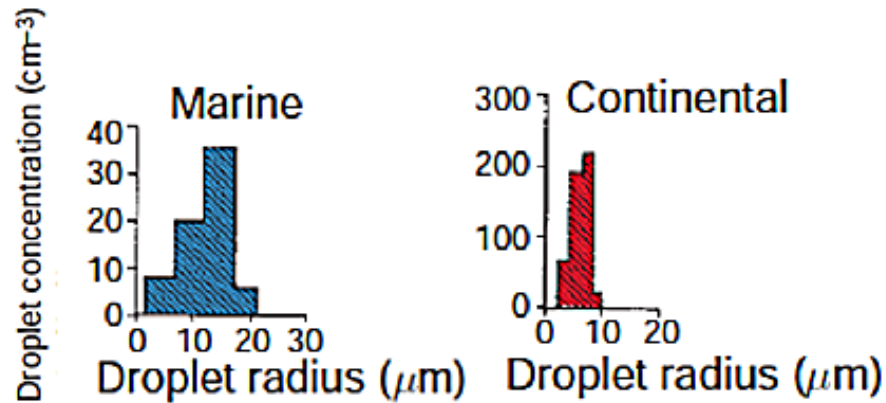


Figure 2.1: Example of cloud drop size distributions (Wallace and Hobbs, 2006): marine clouds have large droplet radii and small concentrations, while continental clouds have small droplet radii and large concentrations.

Observations show that the whole process of warm rain formation can happen in nature in time spans of 20 – 30 minutes (Stephens and Haynes, 2007). Simple dimensional considerations thus already show that warm rain formation is an extremely efficient process, which is able to increase the size of the hydrometeors of many orders of magnitude in a relatively short time.

Generally, rain formation is the result of a combination of micro-physical processes happening in the cloud (Beard and Ochs, 1993): **activation of droplets**, that is the formation of a cloud droplet on a CCN, **diffusional growth** which is the process of growth due to condensation of water vapor on the droplet, and **coalescence growth**, that describes the growth of a droplet by collisions with smaller ones. Initially, activation of droplets occurs in presence of CCN when the supersaturation (S) exceeds a critical value S^* (Rogers and Yau, 1996). Droplets are activated at the cloud base, where S is at maximum. The DSD, which is the frequency distribution of cloud drops over a given range of sizes, describes the activated droplets in terms of their size. An example of typically observed DSDs for marine and continental clouds is given in Fig. 2.1. Observations show that maritime stratiform clouds are characterized by low values of N and big droplets. In contrast, continental stratiform clouds have larger concentrations and smaller drop sizes (Miles et al., 2000). These differences arise from the different types of CCN. In the next stages, the DSD continues to evolve because of the diffusion of water vapor. Diffusion depends on different factors like temperature, pressure, supersaturation and dimension and distribution of CCNs. The diffusional growth of the cloud droplets as a function of time is described by the droplet growth equation, which is a combination of the diffusion equation for heat and water (Lamb and Verlinde, 2011). Initial DSDs highly depend on

the distributions of CCNs on which they are activated and on the supersaturation conditions.

The **coalescence growth** is controlled mainly by droplet size. In fact, collisions start when the droplets undergo gravitational effects caused by their size. Galileo Galilei was the first who formulated the expression of the terminal velocity of a falling object. The sedimentation or terminal velocity of a droplet is reached when the gravitational force of the droplet is balanced by the drag force, that is the aerodynamical resistance exerted on the droplet by the air F_g (Lohmann et al., 2016). The expression for the gravitational force is given by:

$$F_g = \frac{4}{3}\pi r^3 g \rho_l \quad (2.1)$$

where g is the gravitational acceleration, r is the droplet radius and ρ_l is the water density. The drag force F_D is given by:

$$F_D = \frac{\pi}{2} r^2 v^2 \rho C_D = 6\pi\mu r v \left(\frac{C_D R_e}{24} \right) \quad (2.2)$$

where μ is the dynamical viscosity of the air, C_D is the drag coefficient and $R_e = \frac{2\rho v r}{\mu}$ is the Reynolds number. If these two forces balance each other, the terminal velocity of the droplet can be derived as:

$$V_T = \frac{2}{9} \frac{r^2 g \rho_l}{\mu C_D R_e / 24}. \quad (2.3)$$

Depending on the size of the droplet, this relation can be approximated in different ways: for $r < 30 \mu\text{m}$, $R_e \ll 1$ (Rogers and Yau, 1996) and $V_T = \frac{2}{9} \frac{r^2 g \rho_l}{\mu} = k_1 r^2$ with $k_1 = 1.2 * 10^6 \text{cm}^{-1} \text{s}^{-1}$. For $30 \mu\text{m} < r < 0.6 \text{mm}$, V_T is given by the empirical formulation $V_T = k_2 r$, where $k_2 = 8000 \text{s}^{-1}$ (from Rogers and Yau (1996)). Finally, for large drops ($r > 0.6 \text{mm}$), for which $R_e > 100$, equation 2.3 reduces to $V_T = k_3 \sqrt{r}$, with $k_3 = 2010 \text{cm}^{\frac{1}{2}} \text{s}^{-1}$.

When droplets are falling at different velocities due to their different sizes, they start to collide. The interaction between two droplets is described by assuming the droplets to be solid spheres, and by defining an impact parameter, which describes the separation between the droplet centers (Rogers and Yau, 1996). The probability of two droplets to collide and form a new bigger droplet is described in terms of collision efficiency $E_{\text{collision}}$, which has been calculated by Schlamp et al. (1979) for collector drops having a radius R between 11 and 74 μm and collected drops having a smaller radii. Collision efficiencies are small when the ratio of the radii of collected drop r and collector drop R , i.e. $\frac{r}{R}$, is small. In fact, in this situation the collected droplets are small and they can be easily deflected by the flow around the collector drop (Fig. 2.2). For values of the ratio of up to 0.6, collisions are more probable, causing an increase in $E_{\text{collision}}$. The collected droplets are larger and hence have a larger inertia. For values of the ratio larger



Who was Galileo Galilei? more info here <http://galileo.rice.edu/index.html>

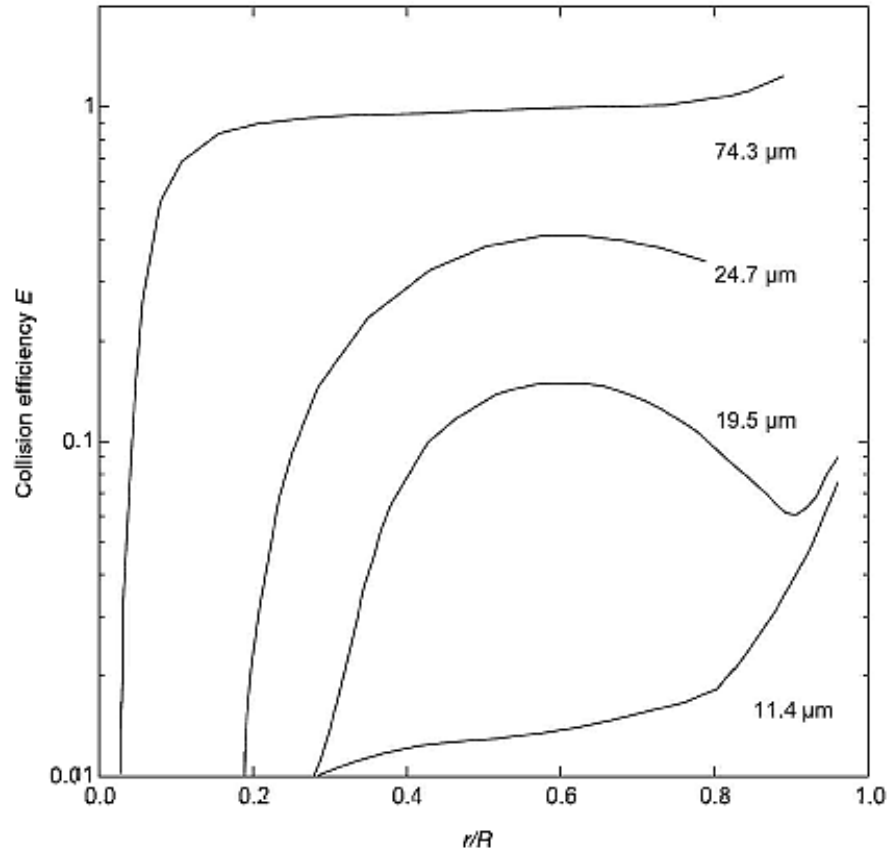


Figure 2.2: Collision efficiency as a function of the ratio ($\frac{r}{R}$) of the radius of the collector drop R and the radius of the collected drop r . Curves are labeled based on the radius R (from [Lohmann et al. \(2016\)](#)).

than 0.6, two counteracting effects influence $E_{\text{collision}}$: the inertia, proportional to the mass of the droplets, still increases and facilitates the collisions, but the deflection forces for these sizes have more time to act because the relative difference in the falling velocity is smaller. Finally, droplets can also be captured in the wake of a collector drop falling at almost the same speed, which is not taken into account by the definition of $E_{\text{collision}}$ given above.

After the collision, droplets can coalesce and stick together permanently, they can coalesce and then split again in their original size or they can then split in a big number of smaller droplets, i.e. called breakup. The coalescence efficiency $E_{\text{coalescence}}$, defined as the number of coalescence events divided by the total number of collisions, describes the probability that two drops remain stick together ([Lohmann et al., 2016](#)). Typically, for droplets with radius smaller than $100 \mu\text{m}$, coalescence efficiencies are almost 1. Drops larger than $100 \mu\text{m}$ with sizes close to raindrops tend to remain together only for a small amount of time and then they split in many smaller droplets. Breakup occurs because of the collisions with other droplets or because the aerodynamical effects overcome the surface tension of the

drop (Lohmann et al., 2016). A detailed description of collision and coalescence of small droplets is reported in (Klett and Davis, 1973). The collection efficiency is defined as $E_{\text{collection}} = E_{\text{collision}} \cdot E_{\text{coalescence}}$ and describes the growth of droplets by collision-coalescence. For $r < 100 \mu\text{m}$, a good approximation is that $E_{\text{collection}} = E_{\text{collision}}$.

The growth by collision and coalescence occurs because of random collisions. These collisions are individual events distributed in time and space. Typically, at the beginning these collisions are rare because of the small collection efficiency. As soon as the drops grows the collision becomes more probable. The stochastic coalescence equation (SCE) describes the stochastic growth of cloud droplets in terms of the probability of each drop to collect another smaller droplet. It calculates the evolution in time of the drop size distribution of the cloud by considering the probability for every possible combination of drops to coalesce and the evolution in time of these probabilities after every coalescence event (Berry, 1967). The SCE can be applied to the drop size distribution of the cloud to describe its evolution in time due to collisions between droplets. If $f(m, t)$ is the cloud DSD so that the quantity $f(m)dm$ is the number of hydrometeors having masses in the interval $[m, m + dm]$ per unit volume, the evolution of $f(m, t)$ in time t due to the collisions of liquid droplets without considering breakup (Pruppacher et al., 1998; Khain et al., 2015) is given by:

$$\begin{aligned} \frac{df(m, t)}{dt} &= \int_0^{\frac{m}{2}} f(m', t)f(m - m', t)K(m - m', m')dm' \\ &- \int_0^{\infty} f(m', t)f(m, t)K(m, m')dm'. \end{aligned} \quad (2.4)$$

where m and m' are the masses of the droplets in grams and $K(m, m')$ is the collision kernel. $K(m, m')$ describes the collision between a droplet of mass m and a droplet of mass m' occurring because of gravitational effects (Beheng, 2013) and has the dimensions of a volume per unit of time. The first integral on the right hand side describes the rates at which drops with mass m are generated by coalescence with droplets having masses m' and $m - m'$. The second integral is the loss integral describing the decrease in the concentration of drops with mass m .

Since the collisions considered by the collision kernel are solely due to gravitational force, the expression for the collision kernel depends linearly on the relative difference of the terminal velocities of the two droplets multiplied by the collection cross section $\sigma_{\text{collection}}$:

$$K_{\text{collision}} = \sigma_{\text{collection}} \cdot |v_T(m) - v_T(m')|. \quad (2.5)$$

The expression of $\sigma_{\text{collection}}$ can be written, for droplets smaller than $100 \mu\text{m}$, in terms of the collection efficiency $E_{\text{collection}}$ and the geometrical cross section $\pi(r' + r'')^2$ as $\sigma_{\text{collection}} = E_{\text{collection}} \cdot \pi(r' + r'')^2$, where r' and r'' are the radii of the colliding droplets. Thus:

$$K_{\text{collision}} = \pi(r' + r'')^2 E_{\text{collection}} \cdot |v_T(m) - v_T(m')|. \quad (2.6)$$

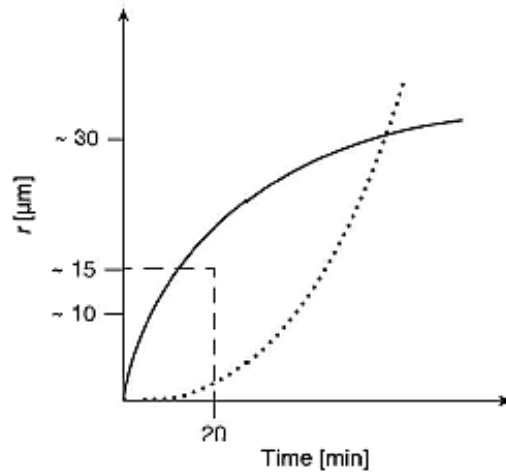


Figure 2.3: Increase of radius as a function of time for condensation (solid line) and collision-coalescence (dashed line) processes (from [Lohmann et al. \(2016\)](#)).

2.1.2 The problem of the initiation of coalescence

In section 2.1.1, the physical processes that explain the growth of cloud droplets to drizzle and rain has been described. It has been shown that initially, droplets grow by diffusion. The general solution of the diffusion equation ([Rogers and Yau, 1996](#)) for the radius r is proportional to $t^{1/2}$, where t is the time. Therefore, drops grow slower as they increase with size and the DSD distribution becomes narrower due to this physical process. However, considering $30\ \mu\text{m}$ as a threshold diameter for coalescence to become dominant, the time necessary to reach this size via diffusional growth is too long to explain rain formation (Fig. 2.3): in 20 minutes, radii not larger than $20\ \mu\text{m}$ can be produced by diffusion. Coalescence, on the other hand, is very fast and efficient in producing big droplets, but needs the presence of droplets larger than $30\ \mu\text{m}$ to be initiated.

A key problem is then to understand which other mechanisms come into play to initiate the collision and coalescence process earlier. In marine clouds, typically low CCN concentrations are observed, and hence the presence of large droplets effectively trigger the collision and coalescence. However, in continental clouds, where the number of CCN is larger than for maritime clouds and very small droplets are present, fast rain production is still observed.

In literature, different processes that broaden the droplet spectrum and start collisions are investigated. In particular, a lot of research has been focused on understanding the way in which turbulence can affect collisions ([Beheng, 2013](#)). While some works focus on improving the theoretical description ([Ghosh et al., 2005](#)), recent numerical simulations to quantify the effects of turbulence on collision efficiency (e.g. [Franklin et al., 2005](#); [Pinsky et al., 2006](#); [Ayala et al., 2008](#); [Grabowski and Wang, 2009](#)) have been carried out. Moreover, observational stud-

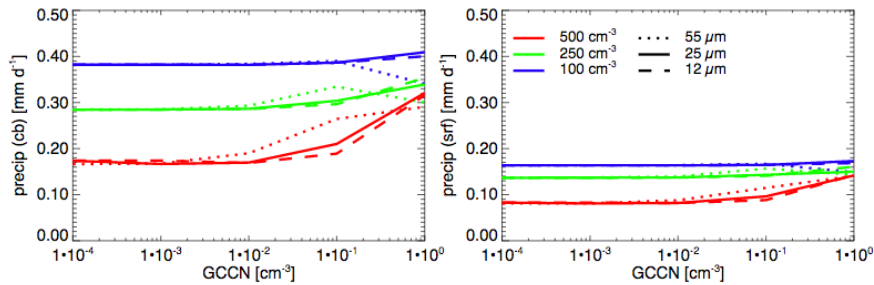


Figure 2.4: Precipitation rates at cloud base (left) and at the surface (right), for different activation radii (solid, dashed, dotted lines) and CCN concentrations (red, green and blue) as a function of GCCN concentration (from [Posselt and Lohmann \(2008\)](#)).

ies try to demonstrate the prevailing role of turbulence in collisions of small droplets ([Lehmann et al., 2007](#); [Siebert et al., 2010](#)). A new expression for the turbulent collision kernel is derived, based on kinematic pair statistics ([Grabowski and Wang, 2009](#)).

At the same time, intense research is conducted to understand the role of giant cloud condensation nuclei (GCCN), i.e CCN with radius larger than $5 \mu\text{m}$ ([Feingold et al., 1999](#)), and their potential in broadening the droplet spectrum and facilitating the occurrence of collisions among drops. [Feingold et al. \(1999\)](#) show simulations demonstrating that small concentrations of GCCNs observed in maritime clouds do actually induce the development of precipitation (in a non-precipitating cloud). Additionally, the authors show that in clouds with high drop number concentrations (like continental clouds), collision-coalescence would not be initiated in absence of GCCNs. Also, [Posselt and Lohmann \(2008\)](#) analyze how the presence of GCCN impacts the formation of warm clouds and precipitation in global models. They use the ECHAM5 General Circulation Model and find that adding GCCN induces faster precipitation and accelerates the hydrological cycle. This effect, negligible for marine clouds, matters for continental ones. Both at the cloud base and at the surface, the precipitation rate is almost doubled for continental clouds by increasing the GCCN concentration, while for maritime clouds it hardly varies as a function of GCCNs (Fig. 2.4).

2.2 MICROPHYSICAL PROCESSES IN MODELS

Atmospheric models solve the equations describing the dynamics and the thermodynamics of the atmosphere numerically by discretizing them on a grid and in time. Atmospheric phenomena occur on a wide range of scales at the same time. Models do not resolve processes smaller than the scale given by their grid, and therefore parametrizations are used to describe the unresolved subgrid-scale phenomena. General circulation models (GCMs) as well as numerical weather prediction models (NWP) do not resolve most clouds, but the global

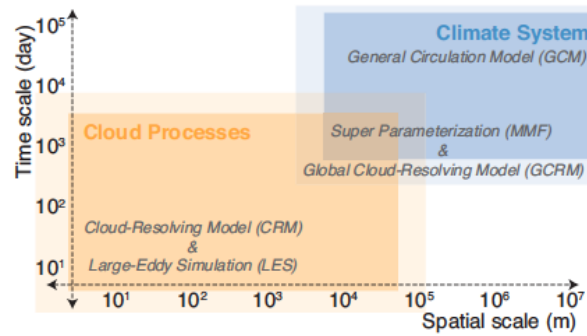


Figure 2.5: Characteristics times and scales of different models (from IPCC (2014)).

circulation and the synoptic systems (see Fig. 2.5). In both, clouds are part of several parametrizations. The thermodynamical conditions of the atmosphere are determined with the boundary layer parametrization and the convection parametrization. The boundary layer scheme provides the turbulent transport of heat, momentum and moisture. The convection parametrization describes the transport organized in thermals and removes instabilities. Once the thermodynamical profiles are determined, the cloud cover parametrization determines the macroscopical properties of the cloud. The cloud physics parametrization then, calculates the rates of condensation/evaporation, precipitation, latent heat fluxes and the microphysics, i.e. for a liquid cloud the cloud and rain liquid water contents.

Cloud resolving models, like for example LES, are able to resolve clouds, but they need to parametrize the cloud microphysical processes. Only direct numerical simulation (DNS) models can resolve the cloud droplets scale, but they are extremely expensive in terms of computation time and hence cannot be used on regional/global scales. Therefore, microphysical schemes are included in cloud parametrizations suitable for LES as well as in those adopted for GCMs/NWPs to simulate the changes of cloud and rain drop size distributions. Two types of microphysical schemes are currently being used in different cloud resolving models: spectral bin microphysical schemes and bulk microphysical schemes (Khain et al., 2015).

In **spectral bin microphysical (SBM) schemes** or explicit microphysical schemes, DSDs are defined as a function of mass of droplets on a finite difference mass grid that counts hundreds of mass bins. In this way, no a priori assumption on the shape of the distribution is needed. This approach is applicable to all cloud types. However, it is based on average on 200 – 300 prognostic variables (Khain et al., 2015). In SBM schemes, the distribution of nucleated droplets is calculated on the basis of the CCN drop size distribution and of the supersaturation S . The evolution of the DSD due to diffusional growth is calculated on the basis of the equation for diffusional growth (Rogers and Yau, 1996). For the description of droplet collisions, the SCE equa-

A prognostic variable is a variable which is directly provided by the model (computationally demanding). A diagnostic variable is calculated from the prognostic ones only at the time of forecast. No memory of them is available (Reitter, 2013).

tion (Eq. (2.4)) is solved explicitly for the entire DSD spectrum. There are several methods to do so, but due to the large computational costs, only a few LES models have implemented SBM schemes so far (Feingold et al., 1994).

In **bulk microphysical schemes**, the DSD (given by the function $f(m, t)$) is not explicitly resolved but it is approximated typically by gamma, exponential or lognormal functions, which are dependent on one or two parameters. All the equations describing the droplet formation and growth are given in terms of the moments of the DSD. The k^{th} -moment of a drop size distribution $f(m, t)$ is defined as

$$M^k = \int_0^{\infty} m^k f(m) dm \quad (2.7)$$

where k is an integer value. For $k = 0$, Eq. (2.7) results in the droplet number concentration N ($M^0 = N$) and for $k = 1$ in the total mass of liquid ($M^1 = \mathcal{M}$). Depending on the scheme typically one or two variables are forecasted, which are N and/or the total mass of the liquid \mathcal{M} . Three moments scheme also forecast the sixth moment of the DSD.

In bulk microphysics schemes, the DSD is separated in two categories: cloud water which does not precipitate and precipitable rain/-drizzle water (Kessler, 1969). This separation is based on the fact that condensation causes the growth of droplets smaller than $20 \mu\text{m}$ while bigger droplets grow because of collisions with smaller droplets. In this scheme, N is calculated at the cloud base from the CCN activation spectrum. After nucleation, the growth of the liquid water mixing ratio of the distribution due to diffusion is calculated by using saturation adjustments. Figure 2.6 gives an overview of how the different collision processes are separately treated. In fact, the different types of collision introduced for the model description are an artifact due to the separation of DSD in two categories (Khairoutdinov and Kogan, 2000). Namely, **self collection** is defined as the generation of cloud droplets/raindrops through collision among cloud droplets/raindrops, **autoconversion** is the generation of raindrops through collision among cloud droplets, while **accretion** is the generation of raindrops through collisions between a cloud droplet and a raindrop. The rates for different types of collisions are obtained from the SCE equation (Eq. (2.4)) (Beheng, 2013). They are given by:

$$\left(\frac{\partial M^{(k)}}{\partial t} \right)_{\text{autoconversion}} = - \int_{m'=0}^{m^*} \int_{m''=m^*-m'}^{m^*} f(m') f(m'') K(m', m'') (m')^k \cdot dm' dm'', \quad (2.8)$$

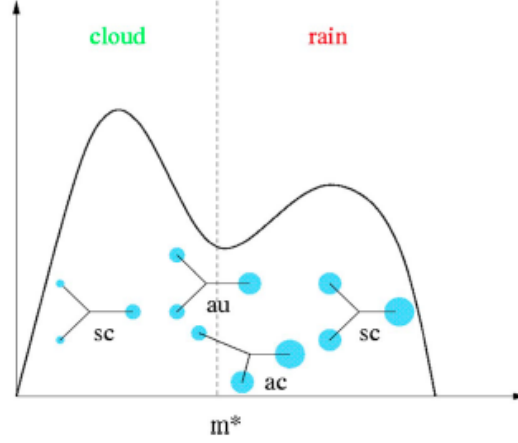


Figure 2.6: Schematic representation of DSD. The vertical dashed line separates the DSD into cloud and rain part. The collision processes are graphically represented: sc—self collection, au—autoconversion, ac—accretion. The mass m^* is the mass separating cloud droplets and raindrops (from (Khain et al., 2015)).

$$\left(\frac{\partial M^{(k)}}{\partial t}\right)_{\text{accretion}} = - \int_{m'=0}^{m^*} \int_{m''=m^*}^{\infty} f(m')f(m'')K(m', m'')(m')^k \cdot dm' dm'' \quad (2.9)$$

$$\left(\frac{\partial M^{(k)}}{\partial t}\right)_{\text{self-collection}} = -\frac{1}{2} \int_{m'=0}^{m^*} \int_{m''=0}^{m^*-m'} f(m')f(m'')K(m', m'')[(m' + m'')^k - 2(m')^k] dm' dm''. \quad (2.10)$$

where m' , m'' are the interacting masses of the droplets, $K(m', m'')$ is the collision kernel and k is the index of the moment, i.e. number concentration ($k = 0$) or mass ($k = 1$).

Bulk schemes are generally computationally much more efficient with typically 6 – 18 prognostic variables (Khain et al., 2015) and for this reason they are extensively used in many different cloud resolving models.

Autoconversion parametrizations: an overview

As previously discussed in section 2.1.2, several studies have focused on a better understanding of the initiation of the collision-coalescence cascade. Hereafter, an overview of the parametrizations of this stage of precipitation formation is presented. A wide variety of different

parametrizations for autoconversion has been introduced in literature. In the following, only the parametrizations of interest for this work are described in more detail.

The first parametrization of the autoconversion process was formulated by [Kessler \(1969\)](#) and it was based on semi-empirical considerations. According to Kessler, the rain rate production for the mass ($k = 1$) caused by droplet collision is linearly proportional to the cloud water content q_c :

$$\left(\frac{\partial M^{(1)}}{\partial t}\right)_{\text{autoconversion}} = \alpha \cdot (q_c - q_{c0})H(q_c - q_{c0}) \quad (2.11)$$

where α is a scaling parameter, q_{c0} is a threshold in liquid water mixing ratio of the cloud (in gkg^{-1}) for the activation of the parametrization, q_c is the liquid water mixing ratio of the cloud DSD (in gkg^{-1}) and H is the Heaviside function. This formula is widely used in bulk parametrization schemes, despite the fact that it makes the incorrect assumption that the collection efficiency is fixed and independent of droplet size (compare [Fig. 2.2](#)). Many schemes have been subsequently developed in order to improve the original parametrization. The dependency on N has been introduced to allow a dependency of the autoconversion rate on the cloud types.

The [Tripoli and Cotton \(1980\)](#) scheme originated from the [Kessler \(1969\)](#) scheme by assuming that the rain is distributed following the Marshall-Palmer distribution as assumed in a previous scheme by [Manton et al. \(1977\)](#). In addition to the dependency on N and q_c , the [Tripoli and Cotton \(1980\)](#) scheme depends on the mean collection efficiency E_c and on the mean terminal velocity V_c , estimated by using Stokes' law. The parametrization has the form:

$$\left(\frac{\partial M^{(1)}}{\partial t}\right)_{\text{TC}_{\text{aut}}} = f_c q_c H(\bar{q}_c - q_{c,m}) \quad (2.12)$$

where $f_c = \pi r_c^2 E_c V_c N_c$ is the mean collision frequency for cloud droplets which become raindrops after colliding, r_c is the cloud droplet radius corresponding to the mean droplet mass while N_c is the mean cloud droplet concentration and \bar{q}_c is the mean cloud water mixing ratio and $q_{c,m}$ is the minimum cloud water mixing ration below which no autoconversion is happening.

[Khairoutdinov and Kogan \(2000\)](#) formulated a microphysical parametrization for LES of stratocumulus topped boundary layer clouds. The goal is to account for the CCN-cloud drop concentration feedback, and for the non-linear dependency of the autoconversion rate on the number concentration and the water content. The parametrization has been derived by using a big ensemble of DSDs from four different LES having an explicit description of the microphysics of stratocumu-

lus topped boundary layer. The corresponding autoconversion rate obtained depends on N and q_c in the following way:

$$\left(\frac{\partial M^{(1)}}{\partial t}\right)_{\text{KK}_{\text{aut}}} = 1350 \cdot q_c^{2.47} N^{-1.79}. \quad (2.13)$$

Also, a three moment scheme has been developed by [Xie and Liu \(2009\)](#) based on the assumption that the cloud droplet size distribution can be described by a generalized gamma distribution function of the form:

$$n(r) = \frac{N\nu\lambda^{\frac{\mu+1}{\nu}}}{\Gamma(\frac{\mu+1}{\nu})} r^\mu \exp(\lambda r^\nu) \quad (2.14)$$

where r is the radius of the droplet, $n(r)$ is the number concentration per unit volume of droplet radius r , N is the total droplet number concentration and λ , μ and ν are the slope, the shape and the tail parameters, respectively. The [Xie and Liu \(2009\)](#) scheme hence depends on number concentration, mass content and reflectivity. The expression for the [Xie and Liu \(2009\)](#) autoconversion rate for the mass is given by:

$$\left(\frac{\partial M^{(1)}}{\partial t}\right)_{\text{XL}_{\text{aut}}} = \left(\frac{3}{4\pi\rho_w}\right)^2 K_2 \frac{\Gamma(\frac{\mu+1}{\nu})\Gamma(\frac{\mu+4}{\nu}, x_{cq})\Gamma(\frac{\mu+7}{\nu}, x_{cq})}{\Gamma^3(\frac{\mu+4}{\nu})} \cdot N^{-1} q_c^3. \quad (2.15)$$

where ρ_w is the water density, $K_2 = 1.9 \cdot 10^{17} \text{ m}^{-3} \text{ s}^{-1}$ and the term x_{cq} is given by

$$x_{cq} = \left[\frac{\Gamma(\frac{\mu+4}{\nu})}{\Gamma(\frac{\mu+1}{\nu})} \right]^{\nu/3} \cdot \left(9.7 \cdot 10^{-20} N^{\frac{3}{2}} q_c^{-2} \right)^{\nu/3}.$$

In recent years, general agreement has been achieved that turbulence fosters the frequency of the collisions among droplets having sizes between 10 and 50 μm ([Seifert et al., 2010](#)). In general, this happens because turbulence can modify the relative velocity between droplets, generates spatial inhomogeneities in the droplet concentration and also because it can modify the collision efficiency by alterations of the flow field ([Seifert et al., 2010](#)). More recent schemes have thus tried to introduce a turbulent collision kernel in the autoconversion parametrization, in order to take all these effects into account.

[Franklin \(2008\)](#) develops a parametrization by solving the SCE equation and implementing a turbulent collision kernel for drop sizes between 10 and 30 μm based on DNS simulations, for different values of eddy dissipation rate. The form of the autoconversion parametrization has been extrapolated from the derivation of [Khairoutdinov and Kogan \(2000\)](#) by analyzing the dependency of q_c and N on the eddy

dissipation rate. By fitting all the turbulent cases from the DNS simulations, the parametrization by Franklin (2008) results in:

$$\left(\frac{\partial M^{(1)}}{\partial t}\right)_{\text{Faut}} = (6.5 \cdot 10^{13} \text{Re}_\lambda^{-6.3} + 1.9) q_c^{3.4} \text{Re}_\lambda^{-0.23} N^{-5.3} \text{Re}_\lambda^{-0.38} \quad (2.16)$$

where Re_λ is the flow Taylor based Reynolds number. Overall, turbulence accelerates the transfer of mass to drops of sizes larger than 40 μm , causing an evident acceleration of the process of rain formation.

Finally, Seifert et al. (2010) derived a parametrization for autoconversion by implementing the turbulent kernel from Ayala et al. (2008). The parametrization is obtained by assuming that the turbulence effects can be parametrized by a dependency of the kernel parameter K_{cc} on the eddy dissipation rate and the Taylor-microscale Reynolds number Re_λ . K_{cc} is calculated by numerically solving the SCE equation with the turbulent kernel and adopting different initial conditions for the mean cloud droplet radius \bar{r}_c , the shape parameter of the cloud droplet size distribution ν , the liquid water mixing ratio q_c , and an ensemble of values for the eddy dissipation rate (ϵ) and the Re_λ . The expression for the autoconversion parametrization from Seifert et al. (2010) is given by:

$$\left(\frac{\partial M^{(1)}}{\partial t}\right)_{\text{Saut}} = \frac{K_{cc}}{20x^*} \cdot \frac{(\nu+2)(\nu+4)}{(\nu+1)^2} \cdot q_c^2 \cdot \bar{x}_c^2 \left[1 + \frac{\Phi_{\text{aut}}(\tau)}{(1-\tau)^2}\right] \quad (2.17)$$

where \bar{x}_c is the mean mass of the cloud droplets and $x^* = 1.2 \cdot 10^{-10}$ is the separating mass between clouds droplets and drizzle, corresponding to a radius of 45 μm . The function $\Phi_{\text{aut}}(\tau)$ (Seifert and Beheng, 2001) is the universal function describing the evolution of the autoconversion process during the development of rain and it depends on the parameter $\tau = \frac{q_r}{q_r+q_c}$, with q_r rain water content. The expression for the kernel K_{cc} is

$$k_{cc}(\bar{r}_c, \nu, \epsilon, \text{Re}_\lambda) = k_{cc,0} \left[1 + \epsilon \cdot \text{Re}_\lambda^{1/4} \left[\alpha_{cc}(\nu) \exp \left[- \left(\frac{\bar{r}_c - r_{cc}(\nu)}{\sigma_{cc}(\nu)} \right)^2 \right] + \beta_{cc} \right] \right] \quad (2.18)$$

where $\alpha_{cc}(\nu)$, $\sigma_{cc}(\nu)$ and $r_{cc}(\nu)$ are functions of ν depending on assigned coefficients as well as β_{cc} . The larger turbulent collision rates resulting from this parametrization already in conditions of moderate turbulence $\epsilon = 400 \text{ cm}^2 \text{ s}^{-3}$ can increase the autoconversion rate of a factor between 4 and 6. Moreover, the scheme from Seifert et al. (2010), as well as their previous version (Seifert and Beheng (2001)), is able to describe the evolution of the autoconversion rate during the process of rain formation, which is not represented in the other schemes.

Wood (2005b) and Hsieh et al. (2009) show the variability of some of the above mentioned autoconversion rates as a function of N and

The microscale Reynolds number Re_λ is the ratio between the time scale characteristic of the large eddies ($1/\omega$), and the time scale typical of the strain rate fluctuations λ/ν , where λ is the Taylor microscale, that is the scale where the viscosity of the fluid impacts on the dynamics of the turbulent eddies in the flow (Tennekes and Lumley, 1972).

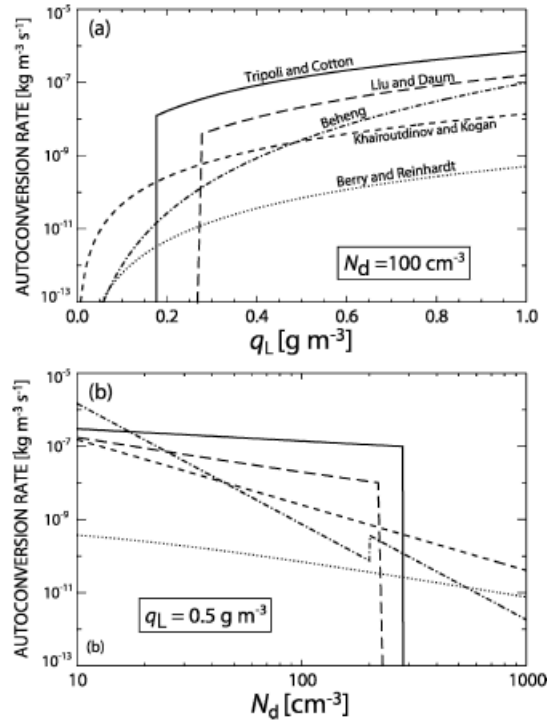


Figure 2.7: Comparison of autoconversion rates derived from different parametrizations. Top: dependency on liquid water content. Bottom: dependency on number concentration (from Wood (2005b)).

q_c . Figure 2.7 shows that differences among autoconversion schemes from different authors can be up to three orders of magnitude. Many reasons exist for such large differences: first, parametrizations not always use the same definition for autoconversion. For example, the threshold size used to separate drizzle and cloud droplets varies between $20 \mu\text{m}$ and $25 \mu\text{m}$. Then, often different DSDs types are used to develop the formulation. Finally, the form of the collection kernel used strongly impacts the autoconversion rate. For example, considering turbulence in the kernel description or not may lead to large differences between the obtained rates (Hsieh et al., 2009).

2.3 MEASURING LIQUID CLOUDS AND LIGHT PRECIPITATION

In this thesis, microwave remote sensing observations are exploited to obtain insight into the drizzle formation in clouds. The used microwave remote sensing instruments can be divided in two groups: active, known as radars, and passive, known as radiometers (Ulaby et al., 2014). Both radars and radiometers include an antenna and a receiver, but the radar has additionally a transmitter. A microwave radiometer is a receiver with a very high sensitivity that is able to detect very low levels of microwave radiation emitted by the atmosphere. Radars (Radio Detection And Ranging) are radio devices that send EM waves and receive the signal backscattered by the atmospheric targets in the direction of the radar. This section focuses on radiative transfer in the microwave region, because it is the spectral region mostly used in this work (some details on the ceilometer, working in the visible regime, are given in Chapter 3). The following theory is extensively described in Liou (2002), CIMINI et al. (2010a), and Ulaby et al. (2014). When EM radiation propagates in the air, it can be attenuated by absorption from the medium or by scattering. It can also be enhanced by thermal emission of the medium itself. When the radiant energy is absorbed by a molecule, it increases its internal energy. In the following, the theory regarding the interpretation of the signals for passive and active sensors is presented.

2.3.1 Microwave radiometer

Passive sensors like the microwave radiometer observe the thermal emission of the atmosphere at selected frequency channels. This emission is related to the dielectrical properties and the physical temperature of the observed volume and it is modulated by absorption and emission of the intervening atmospheric layers. The main contribution to the absorption/emission by the atmospheric gases in the mm-wavelength range is from the oxygen (O₂) and the water vapor (H₂O) lines. O₂ has an absorption band consisting of 37 lines between 50 and 69 GHz and also an additional absorption line at 118.75 GHz. Water vapor has one absorption rotational line at 22.235 GHz and another at 183.31 GHz. Moreover, there are several other water vapor lines at higher frequencies, i.e. at 325.15 GHz (Fig. 2.8).

The radiance $I(z = 0)$ reaching a zenith-pointing passive microwave sensor at the ground ($z = 0$) derived from the radiative transfer equation in a non-scattering atmosphere is given by

$$I(z = 0) = B_{\nu}(T_c) \exp(-\tau) + \int_0^{\infty} B_{\nu}[T(z)] k_a(z) \exp\left[-\int_0^z k_a(z') dz'\right] dz \quad (2.19)$$

A detailed description of the theory summarized here is present in Ulaby et al. (2014). In order to keep the same notation of Ulaby et al. (2014), only in this section the symbol ϵ is used to indicate the dielectric constant of a medium instead of the eddy dissipation rate, as in the previous section 2.2 and in the next chapters.

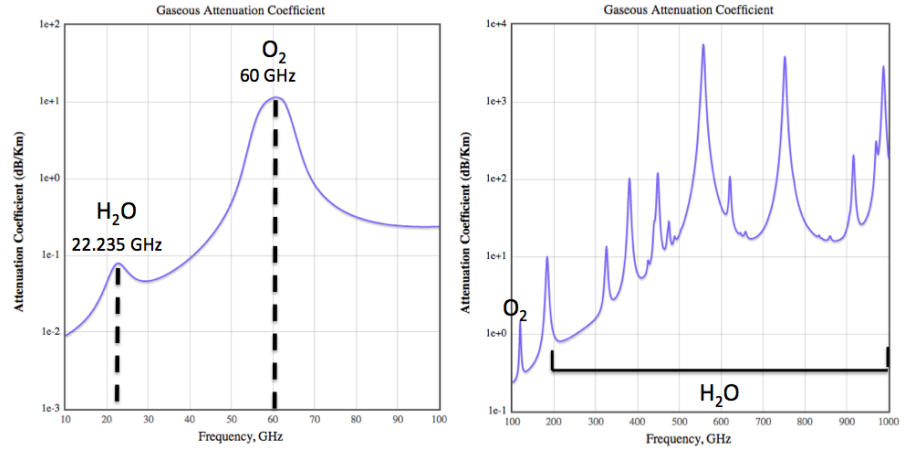


Figure 2.8: Left: Absorption coefficient due to O₂ and H₂O in the frequency range 1 – 100 GHz, at sea level. Right: Absorption coefficient due to O₂ and H₂O in the frequency range 100 – 300 GHz, at sea level (From http://mrs.eecs.umich.edu/microwave_remote_sensing_computer_codes.html).

where k_a is the total absorption coefficient of the atmospheric layer, including atmospheric gases and hydrometeors, $T(z)$ is the temperature in K, T_c is the cosmic background brightness temperature at 2.75°K and $\tau = \int_0^\infty k_a(z) dz$ is the total zenith optical depth. $B_\nu(T)$ is the Planck function at frequency ν and temperature T , given by

$$B_\nu(T) = \frac{2h\nu^3}{c^2} \frac{1}{\exp\left[\frac{h\nu}{\mathcal{K}T}\right] - 1} \quad (2.20)$$

with h Planck's constant and \mathcal{K} Boltzmann's constant. In Eq. (2.19), the radiation reaching the ground is the sum of the contribution due to the cosmic background attenuated by the absorption in the atmosphere (mainly due to oxygen, water vapour and cloud liquid water content), plus the emission from all the atmospheric layers between the ground and the top of the atmosphere. This emission is described as the emission from a grey body having emissivity equal to k_a and attenuated by the atmospheric layers along the path.

2.3.2 Cloud radar

Radars are active remote sensing instruments because they transmit a pulse of electromagnetic energy and receive the backscattered signal in the direction of the radar. The main used radar variable to quantify the amount of backscattered signal is the equivalent radar reflectivity factor (from here on called reflectivity Z_e). The expression for Z_e in Rayleigh scattering approximation for the targets is

$$Z_e = \frac{\eta\lambda^4}{|\mathcal{K}|^2 \cdot \pi^5} \quad (2.21)$$

where λ is the wavelength of the radar, η the radar reflectivity that measures how efficient a radar target is in intercepting and returning

energy and K is the dielectric factor, that is a function of the dielectric constant of the medium and is equal to 0.93 for liquid water. Z_e is usually measured in logarithmic units (dBz). The radar reflectivity η produced by such target in Rayleigh approximation is

$$\eta = \sum_i \frac{N_i \pi^5 |K|^2 D_i^6}{\lambda^4}. \quad (2.22)$$

In Rayleigh approximation, the equivalent radar reflectivity factor is the radar reflectivity factor Z of a target made of water droplets that are small compared to the wavelength used by the radar:

$$Z_e = Z = \sum_i N_i D_i^6, \quad (2.23)$$

where N_i is the number of hydrometeors per unit volume, D_i is their diameter.

Typically, the ability of a radar to detect targets depends on its wavelength, on the emitted power and also on the sensitivity of the receiver. When shorter wavelengths are used, radars detect signals from smaller targets because their sensitivity, i.e. their ability to detect small signals above noise level, increases. This is the main reason why mm-wavelength radars with higher sensitivities are exploited to detect small cloud droplets (like those which are object of this study) producing reflectivities between -60 dBz to -40 dBz. In contrast, for example, cm-wavelength radars cannot detect signals smaller than -20 dBz.

In order to minimize the impact of the attenuation due to atmospheric gases on the signal, cloud radars uses frequencies typically located in the window regions, i.e. 35 GHz or 94 GHz (see Fig. 2.8). However, the contribution in terms of attenuation to the signal caused by the water vapor continuum absorption at 35 and 94 GHz has to be accounted for. For observations of liquid droplets and drizzle, also attenuation due to liquid water present in the targets has to be taken into account. Despite the losses of signal due to absorption, cloud radars are well suited for measuring low liquid clouds developing drizzle.

Scattering and absorption of liquid hydrometeors

The characteristics in terms of scattering and absorption properties of a droplet assumed spherical in the air typically depend on the wavelength of the electromagnetic radiation incident on the particle, on the dielectrical properties of the particle, and on the particle radius r .

The dielectric constant $\epsilon = \epsilon' - i\epsilon''$ is a complex number, where ϵ' is the relative permittivity of the material and ϵ'' is the dielectric

loss factor. The dielectric constant can be expressed in terms of the complex index of refraction of the medium $n = n' - in''$ as

$$n^2 = \epsilon. \quad (2.24)$$

The expression of the imaginary (n'') and real (n') parts of the index of refraction n , which represent the absorption α and the phase β properties of the medium, respectively, can be written as a function of the wavenumber in free space $k_0 = \frac{2\pi}{\lambda_0}$ and ϵ as:

$$\alpha = k_0 \cdot n'' = -k_0 \cdot \text{Im}(\sqrt{\epsilon}), \quad (2.25)$$

$$\beta = k_0 \cdot n' = k_0 \cdot \text{Re}(\sqrt{\epsilon}), \quad (2.26)$$

In order to describe scattering and absorption in the microwave portion of the electromagnetic spectrum, the scattering and absorption cross sections are introduced. The absorption cross section Q_a of a particle suspended in air with geometrical area A is defined as the ratio between the fraction of incident power that is absorbed by the drop (P_a), and the power density S_i of the incident electromagnetic wave:

$$Q_a = \frac{P_a}{S_i}. \quad (2.27)$$

The ratio of Q_a to the geometrical area A is defined as the absorption efficiency factor ξ_a , which for spherical particles is

$$\xi_a = \frac{Q_a}{\pi r^2}.$$

The scattering cross section Q_s and the scattering efficiency factor ξ_s are analogously defined introducing P_s , which is the total power scattered by the particle on the entire solid angle 4π :

$$Q_s = \frac{P_s}{S_i} \quad (2.28)$$

and

$$\xi_s = \frac{Q_s}{\pi r^2}. \quad (2.29)$$

The extinction efficiency is defined as the sum of the scattering and absorption efficiencies:

$$\xi_e = \xi_a + \xi_s.$$

Given a dielectric sphere of arbitrary radius r , the exact solutions for scattering and absorption of an electromagnetic wave interacting with the sphere are provided by the Mie theory (Mie, 1908). A comprehensive description of the way in which the Mie solutions are obtained

can be found in Liou (2002). The general expressions of the solutions for scattering and extinction efficiencies are given by the Mie theory as functions of the refraction index n and the size parameter χ . The size parameter for a spherical hydrometeor in the air is

$$\chi = \frac{2\pi r}{\lambda_0}, \quad (2.30)$$

and the Mie expressions for the scattering and extinction efficiencies are:

$$\xi_s(n, \chi) = \frac{2}{\chi^2} \sum_{l=1}^{\infty} (2l+1)(|a_l|^2 + |b_l|^2), \quad (2.31)$$

$$\xi_e(n, \chi) = \frac{2}{\chi^2} \sum_{l=1}^{\infty} (2l+1) \text{Re}(a_l + b_l) \quad (2.32)$$

where a_l and b_l are known as Mie coefficients and are functions of n and χ . When the condition $|n|\chi \ll 1$ is valid, Eq. (2.31) and Eq. (2.32) reduce to the simpler expressions known as Rayleigh approximations. This is generally valid when $\chi \ll 1$, unless $\text{Im}(K) \ll |K|^2$, where

$$K = \frac{n^2 - 1}{n^2 + 2} = \frac{\epsilon - 1}{\epsilon + 2}, \quad (2.33)$$

the dielectric factor. This condition means that the particle is made of a very weakly absorbing material (not the case for water between 1 and 50 GHz). Then, the scattering and absorption cross sections can be re-written as

$$Q_s = \frac{2\lambda^2}{3\pi} \chi^6 |K|^2, \quad (2.34)$$

$$Q_a = \frac{\lambda^2}{\pi} \chi^3 \text{Im}(-K). \quad (2.35)$$

Since in the Rayleigh region $\chi \ll 1$ and Q_s is proportional to χ^6 while Q_a is proportional to χ^3 , Q_e can be approximated with Q_a . The real and imaginary parts of ϵ for water (ϵ_w) (Eq. (2.25) and Eq. (2.26)) are shown in Fig 2.9. Note that ϵ'_w and ϵ''_w also depend on the temperature.

By applying Eq. 2.24, n can be derived for the values of the dielectric constant shown in Fig. 2.9. In the range of frequencies up to 50 GHz for water it is found that, for typical sizes smaller than 0.1 mm, as it is the case for the hydrometeors that are object of this study, the Rayleigh approximation is valid.

When multiple scatterers are present and distributed over a volume, as in the case of a cloud, the total scattering, absorption and extinction

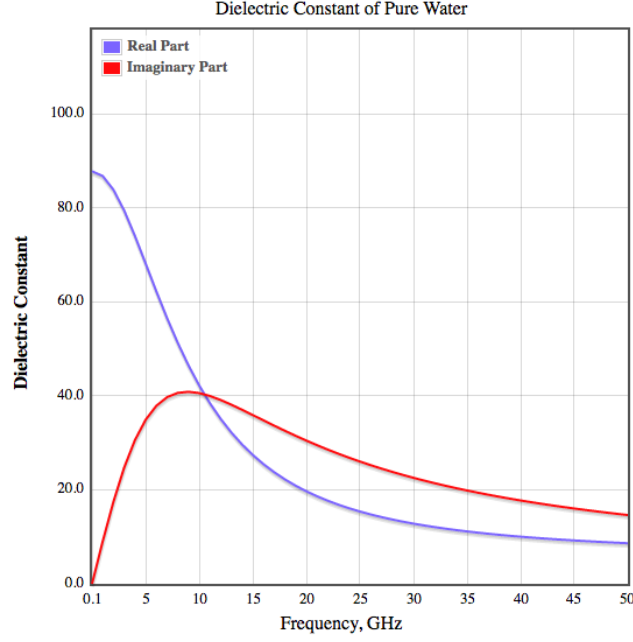


Figure 2.9: Real (ϵ') and imaginary (ϵ'') parts of the dielectric constant for pure water in the range of frequencies between 1 and 50 GHz, derived from measurements at a temperature of 0°C (Figure from [Ulaby et al. \(2014\)](#)).

volume coefficients k_s , k_a and $k_e = k_s + k_a$ (in m^{-1}) can be calculated by using the drop size distribution $n(r)$ of the cloud, as:

$$k_j = \frac{\lambda_0^3}{8\pi^2} \int_0^\infty \chi^2 n(\chi) \xi_j(\chi) d\chi \quad (2.36)$$

where the index j represents scattering, absorption and extinction. In Rayleigh approximation, simpler expressions of Eq. (2.36) can be obtained by using Eq. (2.34) and Eq. (2.35). Moreover, in the Rayleigh approximation, the cloud volume extinction coefficient k_e is approximated by the volume absorption cross section of all the particles contained in the volume. Given N_v , the number of particles contained in the unit volume:

$$k_e = \sum_{i=1}^{N_v} Q_a(r_i) = \sum_{i=1}^{N_v} \frac{\lambda^2}{\pi} \chi^3 \text{Im}(-K).$$

This expression can be re-written in terms of the cloud LWC = $\rho_w \sum_{i=1}^{N_v} \frac{4\pi}{3} r^3$ as

$$k_e = \frac{6\pi}{\lambda} \text{Im}(-K) \frac{\text{LWC}}{\rho_w} \quad (2.37)$$

where K is given by Eq. 2.33. Eq. 2.37 indicates that the extinction coefficient due to an ensemble of liquid hydrometeors depends linearly on the LWC, and is also a function of the dielectric constant ϵ , and thus of the frequency and the temperature. Typically, the volume extinction coefficient increases fast as a function of the frequency between 1 and 50 GHz, and more slowly when the temperature decreases ([Ulaby et al., 2014](#)).

Derivation of a radar spectrum

Radars like the one operating at the Jülich Observatory for Cloud Evolution (JOYCE) (Löhnert et al., 2015), transmit pulses of EM radiation of prescribed pulse length τ (also called width), and then switch to the receiver mode to listen to echos coming back. $T_0 = \frac{1}{\text{PRF}}$ is the time between two pulses, where PRF is the pulse repetition frequency of the radar. The EM wave is emitted by an antenna, which directs the radiation in a complex beam pattern with side lobes. The energy of the wave is higher towards the center of the beam and then decreases towards the edges of the beam. The beam width, defined as the angular width at which the power is half of the maximum power, defines the volume ΔV illuminated by the pulse along the beam (Cimini et al., 2010a). The expression of the volume is given by:

More information on JOYCE is provided in chapter 4

$$\Delta V = \frac{cT_0\Phi_{\text{horiz}}\Phi_{\text{vert}}}{8}\pi r^2 \quad (2.38)$$

where r is the radial distance from the radar, c is the speed of light, Φ_{horiz} and Φ_{vert} are the beam width along the horizontal direction and vertical direction respectively. The illuminated volume becomes larger with the square of the radial distance from the radar. A large radar beam width increases the influence on the spectrum shape of dynamical broadening effects like turbulence or spectral artifacts caused by partial beam filling. Typical partial beam filling situations are cases in which the cloud is not entirely filling the radar volume. Also, partial beam filling can occur when the volume is affected by wind shear. Problems of partial beam filling will also occur when the observed cloud is thin with respect to the pulse length (Uttal and Kropfli, 2001).

After transmitting the EM wave, the radar collects returned echoes. Since it is impossible to resolve backscattered echoes from each target of the radar volume individually, echoes are sampled in discrete time delays τ_s . The distance of the targets from the radar is derived comparing the instant of transmission of pulses with the instants when the backscattered sampled signal is received. The number of samples N_G that are collected between two consecutive radar pulses defines the number of different range gates from which the radar is collecting a signal. For each of such range gate, considering N_s scatterers per unit volume contained in the resolution volume, the electric field at the receiver antenna is (Clothiaux et al., 1996):

$$E(t) = \sum_{j=0}^{N_s} A_{r,j} e^{i(2k_c r_j - (\omega - \omega_{d,j})t + \phi_{s,j} + \phi_t)} \quad (2.39)$$

where ω is the frequency of the wave, $A_{r,j}$ is the amplitude of the wave scattered by the j -th scatterer, $\omega_{d,j}t$ is the shift in phase of the scattered wave in the radial direction due to the relative radial velocity of the target j with respect to the radar, $\phi_{s,j}$ is the phase shift due to scattering from target j and ϕ_t is the initial phase of the wave. The

real and imaginary parts of the received voltage are the so-called I and Q voltages, respectively, which can be obtained after some manipulations from (2.39):

$$I(t) = \operatorname{Re} \left[\sum_{j=0}^{N_s} V_{0,i} e^{i(2k_c r_j - \omega_{d,j} t + \phi_{s,j})} \right], \quad (2.40)$$

$$Q(t) = \operatorname{Im} \left[\sum_{j=0}^{N_s} V_{0,i} e^{i(2k_c r_j - \omega_{d,j} t + \phi_{s,j})} \right]. \quad (2.41)$$

where $V_{0,i}$ are the voltage amplitudes, that are functions of the backscattered power, the receiver antenna aperture, the impedance and the antenna loss and gain.

A power spectrum is derived from the I/Q time series by applying a standard method described in [Doviak and Zrnic \(2014\)](#). First, the raw I/Q time series are converted into a complex spectrum S_{compl} by applying a FFT transform with N_{fft} points to the time series of N_{fft} I/Q pairs. A power spectrum is then derived by:

$$S(f) = S_{\text{compl}} \cdot S_{\text{compl}}^* \quad (2.42)$$

where $S^*(f)$ is the complex conjugate of $S(f)$. Generally, an ensemble of spectra obtained in this way is averaged together to improve the quality of the signal (more details on this phase of the processing are given in Chapter 3 and Chapter 6). This procedure is exemplarily illustrated in Figure 2.10 only for the I signal.

The Doppler spectrum is the composition of all the backscattered signals from the targets within the volume. It represents the distribution of radial velocities of the targets in the radar volume weighted with the power of the signal ([Görsdorf et al., 2015](#)). It is defined between the maximum and minimum detectable Doppler velocities, given by $\pm V_{\text{Nyq}}$ (Nyquist velocity). They are defined as

$$v_{\text{Nyq}} = \frac{\text{PRF} \cdot \lambda}{4} \quad (2.43)$$

where PRF is the pulse repetition frequency of the radar and λ is the wavelength used. An example of measured Doppler spectrum, from a vertically pointing cloud radar is given in Fig. 2.11, where mean noise level and peak noise level, that is the maximum of the detected noise, are represented by the two horizontal lines. This spectrum is obtained by applying FFT transform and also all the calibration constants of the radar. The position of the main peak represents the average velocity with which the targets in the radar volume are moving in the radial direction.

Doppler radar moments

Usually, the definition of moments given in Eq. (2.7) for DSDs can be applied also to a radar Doppler spectrum $S(v)$ in $\text{mm}^6 \text{m}^{-4} \text{s}$. Certain

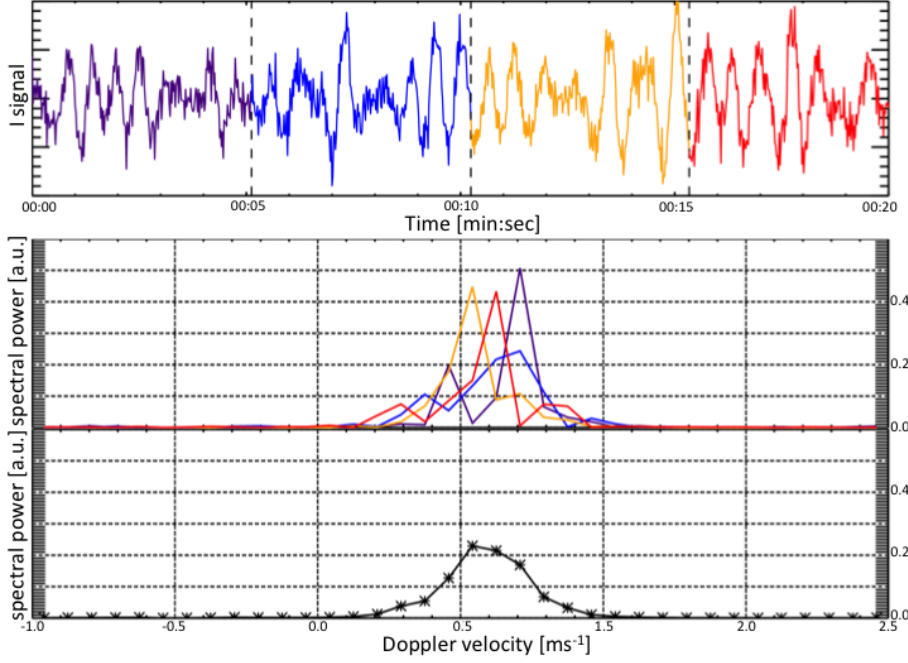


Figure 2.10: Example of measured I samples used to show the standard procedure for deriving radar Doppler spectra from raw I/Q time series by applying the FFT transform (see also detailed description of the method in [Doviak and Zrníc \(2014\)](#)). The upper panel shows a time series of 1024 in-phase (I) samples (Q time series not shown); the different colors denote four 256 point long subsamples which are used in combination with the corresponding Q samples to perform a 256 FFT resulting in the raw Doppler spectra shown in the panel below. The lowest panel shows the average of the four raw spectra.

moments of the Doppler spectrum can be related to specific processes. For simplicity, these radar variables are called moments of the Doppler spectrum, even if they are not exactly the moments but quantities proportional to the moments. They are reflectivity, mean Doppler velocity, spectral width and skewness. Traditionally only the first three moments reflectivity, mean Doppler velocity, spectral width have been used to investigate microphysical properties of clouds, while only in recent years also skewness has been introduced to investigate drizzle onset ([Luke and Kollias, 2013](#); [Kollias et al., 2011a,b](#)). Moments of the Doppler spectrum are calculated from $S(v)$, which is obtained from the Doppler spectrum \hat{S} in SI-units by converting from $\text{mm}^6 \text{m}^{-8} \text{s}$ to $\text{mm}^6 \text{m}^{-4} \text{s}$. This conversion is necessary to provide Z_e in the correct units:

$$S(v) = 10^{18} \frac{\lambda^4}{|K_w|^2 \pi^5} \hat{S}(v) \quad (2.44)$$

where $|K_w|$ is the dielectric factor for water, v is the Doppler velocity and λ is the radar wavelength. Commonly $|K_w|^2$ is fixed to 0.93 for the K_a -band radars, i.e. radars operating with wavelength in the range 7.5 – 11 mm. Radar moments are then calculated by subtracting the mean noise level from the spectrum $\hat{S}(v)$ of the Doppler velocity v (in

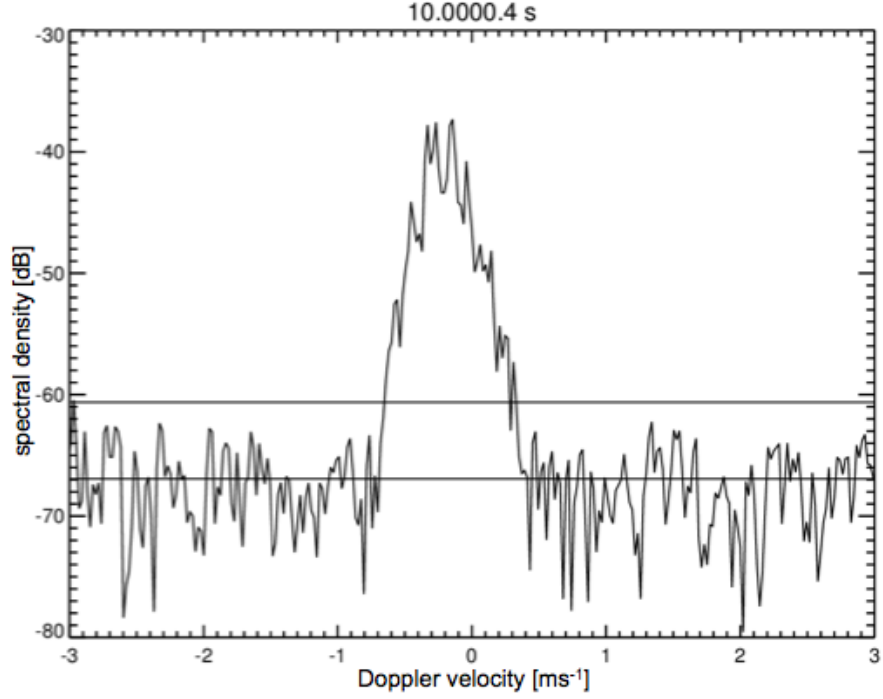


Figure 2.11: Example of an observed cloud radar Doppler spectrum obtained with the standard spectrum processing of the manufacturer of the radar: the horizontal upper line represents the peak noise level, while the lower one represents the mean noise level of the signal.

m s^{-1}) (Fig. 2.11) using the following expressions (e.g. [Kollias et al., 2011a](#)).

The reflectivity Z_e in $\text{mm}^6 \text{m}^{-3}$ can be obtained with

$$Z_e = \int_{-v_{\text{Nyq}}}^{v_{\text{Nyq}}} S(v) dv. \quad (2.45)$$

Z_e represents the integral of the spectrum over the Nyquist velocity range. For Rayleigh scatterers Z_e is equal to the reflectivity factor Z which is defined as the sixth moment of the DSD (Eq. 2.23) ([Doviak and Zrnic, 2014](#)).

The mean Doppler velocity V_d is related to the first moment of the Doppler spectrum and defined as

$$V_d = \frac{1}{Z_e} \cdot \int_{-v_{\text{Nyq}}}^{v_{\text{Nyq}}} S(v) \cdot v dv. \quad (2.46)$$

V_d is the reflectivity weighted mean velocity of the scattering particles relative to the radar. In this study, the adopted convention for the sign of Doppler velocities is that velocities are positive when moving

towards the radar (downwards). The radar spectral width is related to the second moment of $S(v)$ and defined as

$$S_w = \sqrt{\frac{1}{Z_e} \cdot \int_{-v_{Nyq}}^{v_{Nyq}} S(v) \cdot (v - V_d)^2 dv.} \quad (2.47)$$

The spectral width represents the variance of the hydrometeors' motions. In absence of vertical air motion and turbulence, the spectral width only depends on the variability of terminal fall velocities caused by the different particle sizes within the radar volume and hence reflects the width of the DSD. Air motion can additionally broaden the spectrum and enhance S_w ; a comprehensive description of broadening effects can be found in [Doviak and Zrnic \(2014\)](#).

The skewness S_k of the Doppler spectrum is related to the third moment and describes the asymmetry of a given spectrum with respect to an ideal Gaussian shape:

$$S_k = \frac{1}{Z_e \cdot S_w^3} \cdot \int_{-v_{Nyq}}^{v_{Nyq}} S(v) \cdot (v - V_d)^3 dv. \quad (2.48)$$

The sign of S_k depends on the sign convention adopted for the Doppler velocity. With the convention adopted in this work, S_k has positive values when the spectrum shows an asymmetry to the right of the main peak (see Fig. 2.12(right)). S_k and S_w are of particular interest for studying drizzle growth as revealed by former studies ([Luke and Kollias, 2013](#); [Kollias et al., 2011a,b](#)). Figure 2.12(right) shows forward simulated spectra obtained from lognormal distributions for cloud droplets and drizzle where the ratio between drizzle liquid water content (LWC) and cloud LWC is 0.1%. The assumed effective radius for cloud droplets is $5.4 \mu\text{m}$ while for drizzle it is $40 \mu\text{m}$. The presence of drizzle here induces an asymmetry to the right of the cloud peak, causing the skewness to turn positive. Skewness in general, can assume positive or negative values, depending on the drop size distribution of the drops in the radar volume (see Fig. 2.12(left)).

2.4 OBSERVATIONS OF DRIZZLE ONSET

Remote sensing consists of indirect measurements, that means measurements in which the quantity actually measured is a function of the parameter which is intended to be observed ([Rodgers, 2000](#)). The estimation of the atmospheric state from the indirect atmospheric observations is called inverse problem. Many different techniques are available to solve this kind of problem: statistical regression ([Löhnert and Crewell, 2003](#)), inversions using neural networks ([Solheim et al., 1998](#)), Kalman filtering ([Han et al., 1997](#)), variational methods

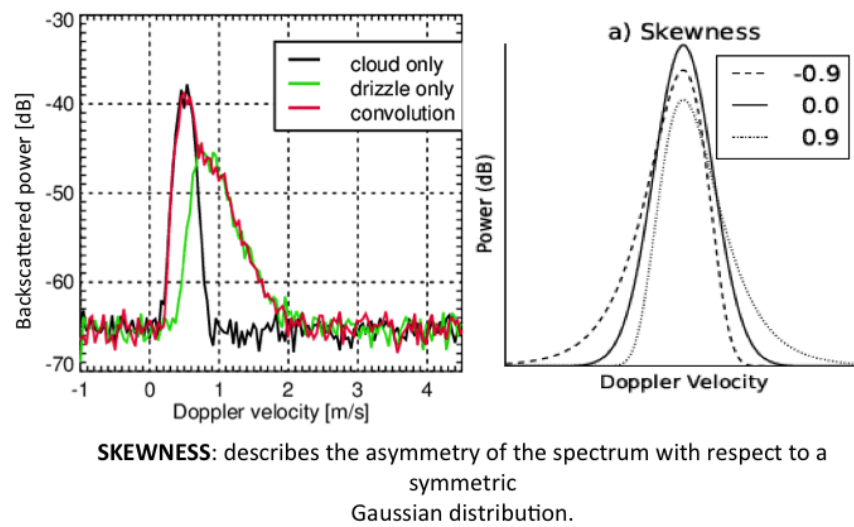


Figure 2.12: Left: Simulated spectra of lognormal distributions for cloud droplets and drizzle having effective radius $5.4 \mu\text{m}$ and $40 \mu\text{m}$ respectively. Positive Doppler velocities correspond to targets falling towards the radar. Black line: spectrum generated by the presence of cloud droplets with no drizzle. Green line: the spectrum generated by drizzle only. Red line: the spectrum due to the presence of both distributions. Right: schematic representation of spectra with positive and negative skewness compared to a gaussian shape, from [Maahn \(2015\)](#).

and combination of measurements with numerical forecast models (Cimini et al., 2010b).

Warm clouds and light precipitation formation have been observed mainly from satellite, in situ and ground based instrumentation and retrievals have been applied from every platform to derive cloud and drizzle properties.

In situ and satellite observations

In situ observations have been carried out since 40-50 years (Pruppacher et al., 1998). Recently, the RICO and the RACORO campaigns (Rauber et al., 2007; Vogelmann et al., 2012) investigate the properties of liquid clouds providing a test bed for validating and evaluating numerical simulations. Often in situ measurements are combined with remote sensing observations (Mech et al., 2014). One example is the Next-generation Aircraft Remote sensing for Validation Studies (NARVAL) campaign (Klepp et al., 2014), where in situ dropsondes have been launched and the aircraft was equipped with radiometers, radar, lidar, and optical spectrometers.

Based on the global coverage that they can provide, satellites observations of precipitation are suitable for global monitoring of precipitation which cannot be achieved from other platforms (Prigent, 2010). Precipitation is estimated from satellites exploiting the visible/infrared (VIS/IR) and the microwave spectral region. Retrievals based on VIS/IR channels typically assume that bright cold cloud tops are more likely to produce rain. Since the signal at these frequencies only detects properties of the top of the cloud, precipitation estimations are indirect measurements. Since warm clouds are often characterized by warm and spatially homogeneous cloud top brightness temperatures, warm rain processes are difficult to detect with these techniques (Ebert et al., 2007). In order to detect light precipitation from warm liquid clouds, multispectral information at high spatial (3 km) and temporal (15 minutes) resolution from the Spinning Enhanced Visible and Infrared instrument (SEVIRI) on board on the Meteosat Second Generation (MSG) is used to retrieve drizzle and microphysical cloud properties (Thies et al., 2008).

In the microwave region, the measured signal is affected by emission, absorption and scattering. Different retrievals have been developed exploiting scattering properties of ice and emission properties of liquid at different frequencies. The more recent ones are based on probabilistic techniques (Kummerow et al., 2001) based on well documented datasets obtained by coupling cloud resolving models and radiative transfer calculations (Prigent, 2010).

The first space borne precipitation radar (PR) on board the TRMM satellite, operating at 13.8 GHz launched in 1997 (Kummerow et al., 2000), had a minimum detectable signal of 17.8 dBz, which limits the

ability to observe light rain (Lebsock and L'Ecuyer, 2011). The Cloudsat cloud profiling radar (CPR), launched in August 2006 (Stephens et al., 2002, 2008), provides profiling observations of light rain and liquid clouds. CPR operates at a frequency of 94 GHz and has 500 m vertical resolution and 1.4 km spatial resolution. Its minimum sensitivity of -30 dBz makes it suitable for observing cloud non-precipitating properties. Retrieval of rain profiles are complicated by multiple scattering effects which occur at this frequency as well as attenuation and surface clutter contamination (Lebsock and L'Ecuyer, 2011). Moreover, the first two radar bins over ocean and the first three radar bins over land are affected by ground clutter, thus making the detection of liquid clouds over land particularly challenging.

Ground based

Millimeter wavelength (cloud) radars are a key component of ground based remote sensing because of their ability to detect and penetrate most cloud types, thus providing vertically-resolved cloud structure. The majority of worldwide installed cloud radars are Doppler radars with the ability to record the full Doppler spectrum. In warm clouds, the formation of drizzle in stratocumulus clouds and the characterization of its signatures in radar observations has been of particular interest during the last decades. Cloud radar observations have been exploited alone or combined with other remote sensors like microwave radiometers (e.g Frisch et al., 1995) and lidars (e.g O'Connor et al., 2005). First retrievals of precipitation are based on the fact that when recorded in zenith-mode, V_d is related to the vertical velocity of the hydrometeors (Atlas et al., 1973). Microphysical studies increasingly make use of higher moments such as spectral width (S_w). Gossard (1994); Frisch et al. (1995); Babb et al. (1999); Deng and Mace (2006) for example, exploit procedures using Doppler spectra moments or matching the forward modeled spectra of an assumed DSD with the observed ones. However, these techniques do not consider the impact that turbulence has on the spectrum shape and the determination of the moments. Other techniques (Shupe et al., 2004) exploit the separation occurring between cloud droplet peak and drizzle/ice crystals peak, where the cloud droplet is used as a tracer for air motion. However also in this case, turbulence can make the separation between the peaks a challenging task. Also, decomposition of the spectrum in cloud droplet peak and drizzle peak was attempted in (Gossard, 1994; Babb et al., 1999; Luke et al., 2010). Finally, Kollias et al. (2011a) show the added value of higher radar moments like skewness and the fifth radar Doppler moment, called kurtosis, for drizzle studies using forward simulations of radar Doppler spectra. They find that particularly the combined signatures of reflectivity and skewness are very sensitive to early drizzle formation (Fig. 2.13). The theoretical

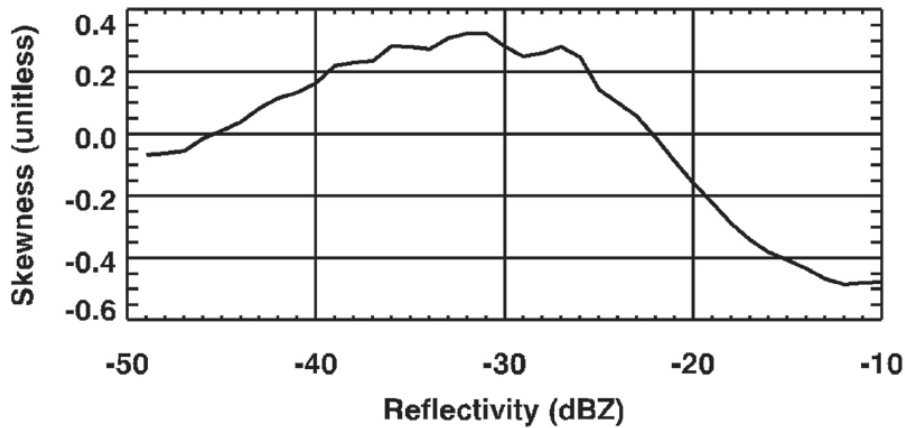


Figure 2.13: Skewness as a function of reflectivity for a marine stratus cloud, from Luke and Kollias (2013).

findings have been confirmed by a detailed observational study (Kollias et al., 2011b) where the authors also compare the observed vertical evolution of the signatures with drizzle simulations using a 1D bin microphysical model.

Exploitation of the higher moments of cloud radar Doppler spectra

In a follow-up study with respect to the previous work of Kollias et al. (2011a,b), Luke and Kollias (2013) developed a retrieval of drizzle particle size distribution based on the deconvolution of cloud and drizzle peak in regions where drizzle presence is identified by positive skewness. Figure 2.13 shows how skewness and reflectivity values are distributed for a 1 day of observations of a marine stratus cloud over a measurement site located on the Azores. The theoretical behavior of skewness is confirmed by observations: positive skewness values occur at low reflectivities indicating the presence of embryonic drizzle droplets. For increasing size and amount of droplets the skewness reverses sign and turns negative when the drizzle finally dominates the spectrum. In addition, a discussion on the factors generating scatter in the skewness observations is presented. The authors find that the skewness estimation is sensitive to signal to noise ratio and spectral width.

Finally, another factor having potential to cause skewed spectra is the sharp change (horizontal or vertical) of the vertical air motion. Since such dynamical perturbations develop on a scale which is comparable to the sampling volume of the radar, high frequency dynamic fluctuations are often observed in skewness time series. Figure 2.14 shows the detail of the mechanisms described.

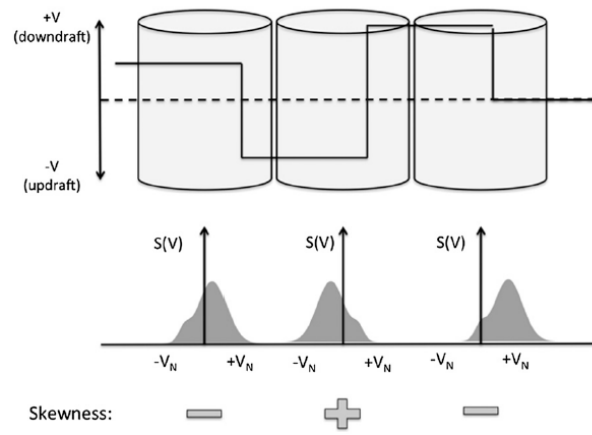


Figure 2.14: Schematic representation of the dynamical mechanism inducing a skewness signal in presence of horizontal variability of the vertical air motion: the figure shows three consecutive radar volumes, where the black line shows the variability of the vertical air motion within each of them. In the lower part, the corresponding spectrum skewed (Luke and Kollias, 2013).

Part II

TOOLS AND DATA

*A scientist in his laboratory is not a mere technician: he is also
a child confronting natural phenomena that impress him as
though they were fairy tales.*

Marie Skłodowska Curie

Warsaw, 7th November 1867 – Passy, 4th July 1934

In this chapter all the instruments and tools used in the thesis are described in detail. The instrumentation is operational at the Jülich Observatory for Cloud Evolution (JOYCE) (Löhnert et al., 2015). More information on JOYCE is provided in chapter 4. Section 3.1 provides a brief history of microwave radiometry (MW), the physical basis of a microwave radiometer and the liquid water path (LWP) retrieval. Section 3.2 is dedicated to the 35 GHz cloud radar: a historical overview of cloud radars, a basic description of the instrument and the retrieval used for estimating the eddy dissipation rate ϵ are briefly described. Then, section 3.3 briefly presents the ceilometer, while section 3.4 is devoted to describe the cloudnet target categorization, used to identify cloud base, cloud top and to provide a first classification of vertical cloud profiles as drizzling/non-drizzling. Finally, section 3.5 describes the passive and active microwave transfer forward simulator which was extensively used in this study for many applications.

LWP definition
from American Meteorological society glossary:
"measure of the weight of the liquid water droplets in the atmosphere above a unit surface area on the earth". It is measured in g m^{-2} .

3.1 HATPRO MICROWAVE RADIOMETER

Historical overview of ground based microwave radiometers

Microwave radiometers (MWR) are passive instruments measuring the radiant intensity in a finite number of frequency bands between 10 cm and 0.5 mm (Cimini et al., 2010a). Surface based microwave radiometry has a long history of application in many different fields: microwave (MW) measurements have been used in meteorology as well as in communication, climate, satellite validation, geodesy and fundamental molecular physics (Westwater et al., 2004, 2005). One of the main reasons for this extensive use in many different applications is the ability of passive MWRs to be operated without continuous surveillance for long periods of time. Therefore, MWRs are very well suited for developing an operational network being able to provide standardized and high time resolution observations. In recent years, new low cost microwave radiometers were conceived, suitable for automatic high quality observations of LWP (Rose et al., 2005). Based on the EU COST action EG-CLIMET (European Ground-Based Observations of Essential Variables for Climate and Operational Meteorology) (Illingworth et al., 2015), the MWRnet network was initiated to develop common procedures for calibration, data processing and determination of uncertainties in the same way as other networks (like EARLINET for aerosol lidar community).

link to the network of MWR radiometers
MWRnet: <http://cetemps.aquila.infn.it/mwrnet/>

HATPRO specifications

The Humidity And Temperature PROfiler (HATPRO) (Rose et al., 2005) microwave radiometer operating at JOYCE belongs to this new generation of instrumentation and is manufactured by RPG Radiometer Physics GmbH. It measures brightness temperatures at 14 frequencies in 2 bands: 7 of the frequencies are along the right slope of the water vapour absorption line at 22 GHz, while the other 7 are along the continuous band of oxygen, made up of 37 absorption lines forming collectively the 60 GHz oxygen complex. The radiometer operates continuously following different scanning strategies but most of the time HATPRO points zenith. The measurements at the two bands allow for the retrieval of integrated water vapour (IWV) and liquid water path (LWP) as well as tropospheric temperature and absolute humidity profiles. Attached to one side of the instrument, two broad band infrared (IR) pyrometers operate, which are sensitive to water vapour and clouds.

In this thesis, LWP values will be extensively used to characterize drizzling and non-drizzling clouds. Details on how LWP is retrieved from the measured brightness temperatures (T_B s) and a discussion on the accuracy of these LWP estimates are given in the following.

Statistical multiple frequency LWP retrieval

The most accurate method to derive LWP estimates are retrievals from MWR observations (Löhnert and Crewell, 2003). Two-channel retrievals typically exploit one frequency on the wing of the water vapour absorption line at 22.235 GHz so to measure the contribution due to the emission of water vapour, while the other frequency is chosen around 30 GHz, in the window region so that the sensitivity to the emission of liquid water is maximized (see Fig. 3.1).

Additional measurements, e.g. at other frequencies or from co-located infrared radiometer or ceilometer, may improve the quality of the LWP estimation (Crewell and Löhnert, 2003). First two-channel retrievals for LWP were developed by Westwater (1978) exploiting a direct proportionality with optical thicknesses at different frequencies. In the present study, the LWP retrieval is based on a multi-variate linear regression between LWP and brightness temperatures (T_B) (Löhnert and Crewell, 2003):

$$\text{LWP} = c_0 + c_1 \cdot T_{B_1} + c_2 \cdot T_{B_2} + c_3 \cdot T_{B_1}^2 + c_4 \cdot T_{B_2}^2 \quad (3.1)$$

where T_{B_1} and T_{B_2} are the brightness temperatures at the two selected frequencies. In order to retrieve c_i , LWP/ T_B pairs have been simulated. LWP is calculated from the radiosonde measurements under the following assumptions. Height, relative humidity, pressure and temperature (i.e. from radiosonde observations) are used to determine

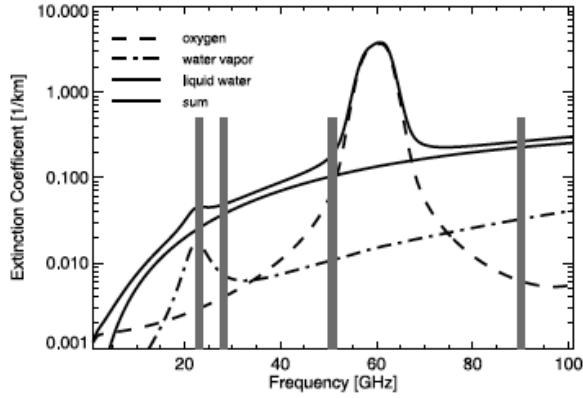


Figure 3.1: Extinction in the microwave range due to the continuous absorption bands of oxygen centered at 60 GHz, to the water vapor absorption line at 22.235 GHz and also to a typical cloud liquid water content of 0.2 g m^{-3} at 895 hPa. Grey vertical lines indicate frequencies typically used in MWR retrievals (Figure from [Löhnert and Crewell \(2003\)](#)).

the cloud liquid water profile between cloud base and cloud top. Corresponding brightness temperatures are simulated with a radiative transfer model, given atmospheric profiles of temperature, humidity, pressure and hydrometeors as input. For a given number k of LWP/simulated brightness temperatures pairs, a least squares regression is performed to minimize

$$\chi^2 = \sum_k (\text{LWP}_k - (c_0 + c_1 \cdot T_{B_1} + c_2 \cdot T_{B_2} + c_3 \cdot T_{B_1}^2 + c_4 \cdot T_{B_2}^2))^2. \quad (3.2)$$

In this way, the coefficients c_i are determined and LWP can be estimated from the measured brightness temperatures by Eq. (3.1). Currently, the retrieval adopted operationally is based of all 7 K-band channels.

In this study, non-drizzling clouds are often observed with LWP values below 50 g m^{-2} and drizzle presence is detected already for LWP values around 200 g m^{-2} . It is thus important to characterize the uncertainty on the LWP values that are used to discriminate between drizzling and non-drizzling populations. The accuracy of LWP estimation obtained from Eq. (3.1) depends on many different factors: uncertainties can be due to inaccuracies in the T_B measurements or to the forward model and the retrieval ([Crewell and Löhnert, 2003](#)). Main uncertainties in the measured T_B are related to instrument calibration and drifts in the receiver properties of the instrument ([Maschwitz et al., 2013](#); [Küchler et al., 2016](#)), which can induce biases in T_B . A bias in T_B can induce a bias in LWP. In order to correct for this, an offset correction can be applied based on clear sky situations where the LWP is assumed to be zero. The impact and the proper estimation of the errors are described in [Löhnert and Crewell \(2003\)](#); [Crewell and Löhnert \(2003\)](#). Typical LWP uncertainties of a 2-channel retrieval are $25 - 30 \text{ g m}^{-2}$. [Löhnert and Crewell \(2003\)](#) also show that

a small presence of drizzle does not affect the LWP estimation, while only for $LWP_{\text{cloud+drizzle}} > 700 \text{ g m}^{-2}$ LWP errors are of the order of 15% – 20%.

3.2 35 GHZ CLOUD RADAR JOYRAD-35

Historical overview of cloud radars

Millimeter wavelength (cloud) radars are a key component of ground based remote sensing because of their ability to detect and penetrate most cloud types, thus providing vertically-resolved cloud structure. The number of cloud radars around the world and the range of their application in weather and climate research have experienced significant growth in the last 20 years (Löhnert et al., 2004; Tridon et al., 2013; Kneifel et al., 2011; Oue et al., 2015). Cloud radars were introduced in atmospheric research in the 1960s (Petrocchi and Paulsen, 1966). During the 1980s, additional technological developments like dual-polarization, scanning and Doppler capabilities in combination with more efficient data processing and better hardware components (Hobbs et al., 1985) fostered the development of a variety of new applications (Lhermitte, 1987, 1990): from ground based as well as from satellites i.e. Cloudsat (Stephens et al., 2002), millimeter radars have provided simultaneous observations of updrafts and entrainment of droplets in ice and water clouds and insights of precipitation growth.

JOYRAD-35 specifications

JOYRAD-35 is a Ka-band Doppler cloud radar operated at JOYCE and has been manufactured by METEK GmbH, Germany (Görsdorf et al., 2015). It transmits linear polarized wave at 35.5 GHz (corresponding to a wavelength of approximately 8 mm) and simultaneously receives the co- and cross-polarized backscattered signal. The antenna beamwidth is 0.6° and the range resolution 30 m. The radar detects signals coming from heights between 150 m and 15 km above ground. The Nyquist velocity is 10.625 ms^{-1} . The technical specifications of JOYRAD-35 are summarized in Table 3.1.

Some of the relevant radar parameters necessary to capture signatures of drizzle development are hardware dependent, for example the radar beam width. Other parameters, like the **integration time** and **spectral resolution** can be adjusted by the user to improve drizzle observations. The integration time specifies how many initially derived Doppler spectra are temporally averaged by the radar processing software to a single spectrum which is then stored and from which all further radar moments are derived. A longer integration time reduces data storage space and helps to improve the signal to noise ratio (Doviak and Zrnica, 2014). However, also broadening effects

Table 3.1: Current radar settings for JOYRAD-35 system at JOYCE, Jülich (DE).

Parameter	Specification	Comments
Frequency	35.5 GHz	corresponding to wavelength of 8.5 mm
Peak power (max)	25 kW	
Average power	24 W	
Pulse width	200 ns	adjustable (100, 200, or 400 ns)
Pulse repetition frequency	5 kHz	adjustable (5-10 kHz)
Minimum height	150 m	full sensitivity above 400 m
Measuring range	15 km	adjustable (7.5-30 km)
Range resolution	30 m	adjustable (15, 30, or 60 m)
3 dB one way antenna beam width in the E and H planes	0.6 deg	
Doppler velocity resolution	0.025 m/s	depends on FFT length
Nyquist velocity	± 10.625 m/s	
Maximum sensitivity at 5 km (integration 0.1 s)	-45 dBZ	
Calibration system accuracy	± 0.5 dB	
Number of gates (with simultaneous stored raw data)	500	
Number of averaging spectra	200	adjustable (1-32768)
Manufacturer	Metek	

by turbulence and air motion increase with longer integration times and lead to increasingly Gaussian shapes of spectra and smearing out of microphysical signatures. The second critical parameter is the spectral resolution. The spectral resolution is defined by

$$\Delta v = \frac{2 \cdot v_{\text{Nyq}}}{N_{\text{fft}}} \quad (3.3)$$

where v_{Nyq} is the Nyquist velocity and n_{fft} is the length of the discrete Fast Fourier Transform (FFT) used to produce the Doppler spectrum. A too coarse spectral resolution might introduce biases in the Doppler spectrum moment estimation caused by uncertainties in discrete integration. This can also result in completely missing some microphysical signatures (e.g. the very narrow peak of super-cooled liquid water in mixed-phase clouds).

For this study, observations in zenith mode are used: they are usually obtained at JOYCE with an integration time of 1 s, and a 256 point FFT for generating the Doppler spectrum. JOYRAD-35 allows to change the number of FFT points from 256, 512, up to 1024. This feature has been exploited in chapter 6 where zenith measurements with various integration times and FFT points have been performed to investigate the sensitivity of radar observables to these parameters.

Eddy dissipation rate retrieval

Turbulent eddy dissipation rate (ϵ , in $\text{m}^2 \text{s}^{-3}$) represents the rate at which turbulence kinetic energy is converted into thermal internal energy. Turbulence plays a fundamental role in cloud lifecycle from entrainment to precipitation formation (Pruppacher et al., 1998) and estimations of ϵ are necessary for modeling studies (Kolmogorov, 1991) as well as for a description of cloud lifecycle (Khain et al., 2015). Here, ϵ is used to quantify turbulence affecting the radar Doppler spectrum skewness observations.

Different retrieval techniques are currently adopted by the scientific community to estimate this quantity. They generally use time series of Doppler velocity measurements in the subcloud layer from wind lidar (Tonttila et al., 2015; Röhner and Träumner, 2013), time series of Doppler velocity measurements from vertically pointing radar (Bryant and Browning, 1975; Kollias and Albrecht, 2000; Shupe et al., 2012) or Doppler spectrum width measurements in precipitation free regions (Fang et al., 2014). In this study, a retrieval based on time series of Doppler velocity measurements observed by the vertically pointing 35 GHz cloud radar has been developed.

Turbulent atmospheric signals are typically analyzed by applying the Fourier decomposition to the signal. This gives the statistical representation of the turbulent energy spectrum as a function of frequencies f . In the turbulent energy spectrum, the inertial subrange is the region in which energy is transferred at a constant rate from the larger scales to the dissipative ones. The intermediate range of scales between the scale of the turbulent eddies and the viscous scale (inertial subrange) is indicated by L . In theory, for homogeneous and isotropic turbulence, the Kolmogorov hypothesis states that within the inertial subrange the energy spectrum of a turbulent atmospheric signal is:

$$E(k) = \alpha \epsilon^{2/3} k^{-5/3} \quad (3.4)$$

where k is the wave number associated to a frequency f by the relation $k = \frac{2\pi f}{u}$, ϵ is the eddy dissipation rate, u is the characteristic velocity scale, and α is the Kolmogorov constant equal approximately to 0.5. Assuming the frozen turbulence hypothesis, meaning that turbulence does not modify significantly the mean flow, the length scale L can be expressed as $L = u * \Delta T$ where ΔT is the time interval over which the frozen turbulence hypothesis is considered to be valid. In this study 30 min is considered as realistic time interval where this condition holds.

By using the relation $E(f)df = E(k)dk$, the energy spectrum in the inertial subrange can be re-written as:

$$E(f) = \alpha \epsilon^{-2/3} \left(\frac{u}{2\pi} \right)^{2/3} f^{-5/3}. \quad (3.5)$$

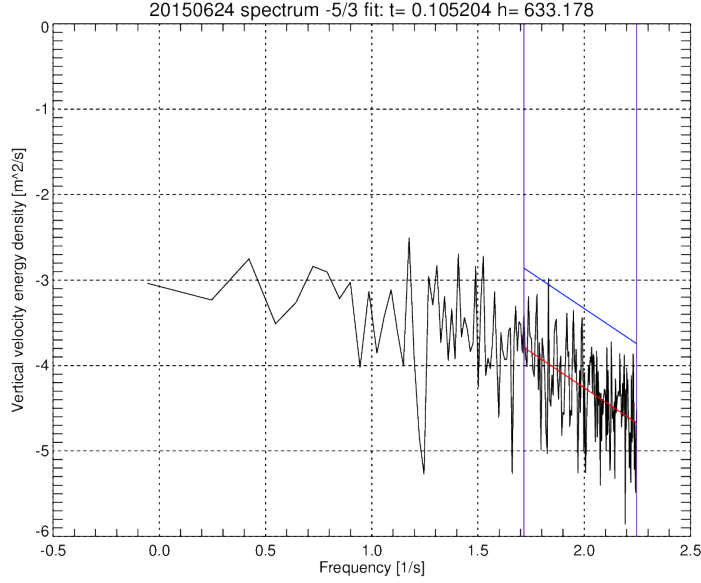


Figure 3.2: Spectrum of energy density derived at 633 m height from FFT for 30 minutes observations of mean Doppler velocity time series from cloud radar. To calculate $E(f)$ also values of u from closest in time wind lidar observations at cloud base are used.

By integrating Eq. (3.5) for $E(f)$ in the inertial subrange from a frequency f_s to a frequency f_e , we obtain:

$$\int_{f_s}^{f_e} E(f) df = \int_{f_s}^{f_e} \alpha \epsilon^{-2/3} \left(\frac{u}{2\pi} \right)^{2/3} f^{-5/3} df. \quad (3.6)$$

The left hand side of Eq. (3.6) can be defined as INT_S , i.e. $\text{INT}_S := \int_{f_s}^{f_e} E(f) df$, and can be calculated analytically (as shown later). After INT_S has been determined, the quantity ϵ , which is independent of the frequency f , can be obtained by manipulating Eq. (3.6):

$$\epsilon = \left(\frac{2\pi}{u} \right) \text{INT}_S^{3/2} \left(\frac{2}{3\alpha} \right)^{3/2} (f_s^{-2/3} - f_e^{-2/3})^{-3/2}. \quad (3.7)$$

Equation (3.7) is used to calculate ϵ : all the necessary quantities appearing in the formula are provided by measurements. Specifically:

- the characteristic velocity scale u is taken as the horizontal wind within the cloud, which is assumed to be constant for the whole cloud and equal to the value measured at cloud base by the wind lidar observations available at JOYCE.
- f_s and f_e are the starting and ending frequencies of the inertial subrange, necessary in order to evaluate the quantity $(f_s^{-2/3} - f_e^{-2/3})^{-3/2}$. They are determined by the identification of the interval where the fit of the energy spectrum $E(f)$ has the slope closest to the theoretical expected one $-\frac{5}{3}$ (see Fig. 3.2).

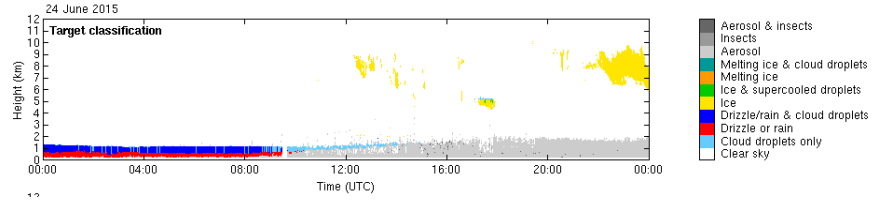


Figure 3.3: Case study for ϵ retrieval test: 24 June 2015 from 00:00:00 UTC to 09:00:00 UTC.

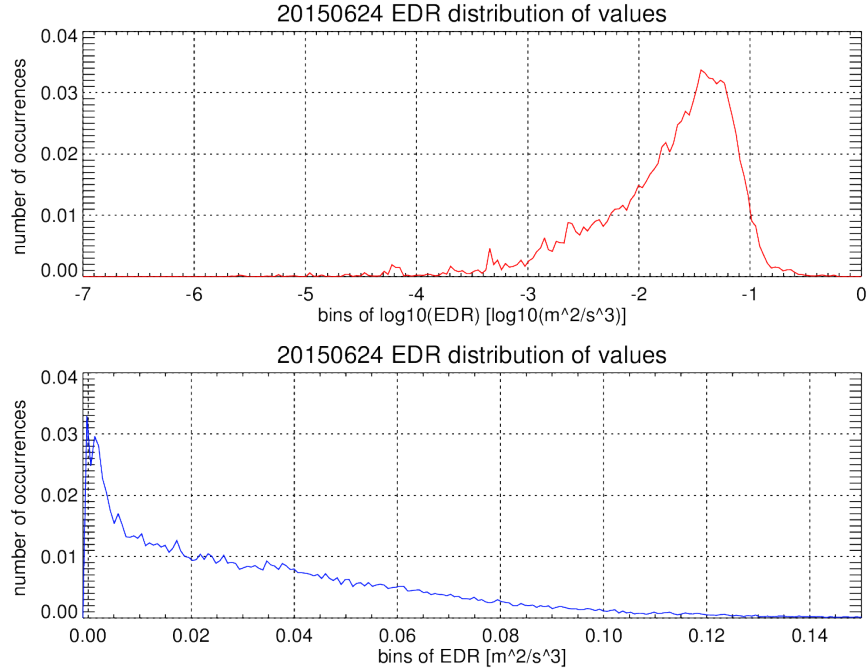


Figure 3.4: Distribution of ϵ values retrieved in the first 9 hours of the day.

- $\text{INT}_S = \int_{f_s}^{f_e} E(f) df$ is the integral of the energy spectrum in the inertial subrange. Once f_s and f_e are determined, it is calculated numerically from the power spectrum energy density $E(f)$ calculated at each time.

The retrieval has been tested in a case study for the 24 June 2015 shown in Fig. 3.3, using the measurements between 00:00 UTC and 09:00 UTC. A 30 min-running mean was applied to the time series of vertical velocity, in order to have an estimation of ϵ for each time. The distribution of ϵ values obtained over the period is shown in Fig. 3.4. Values obtained are in agreement with the values found in literature (see Table 4 in [Gultepe and Starr \(1995\)](#) and [Borque et al. \(2016\)](#)). The ϵ estimation derived with this methodology can be affected by multiple sources of uncertainties, for example the estimation of the frequency interval. They are discussed in detail in ([Borque et al., 2016](#)).

3.3 CEILOMETER

The ceilometer used in this study is a Vaisala CT25K lidar (Light Detection And Ranging) single lens system (Münkel et al., 2007). It operates at a wavelength of 905 nm in the near infrared wavelength region and can detect signals between 0 and 7500 m with a height resolution of 15 m. It measures the backscattered signal from each range of height. The instrument provides uncalibrated backscatter coefficient profiles and can identify up to three different cloud base heights. Ceilometers are widely used to derive cloud base height (see also section 3.4). Ceilometers like the one described have been exploited in the Cloud Detection System (CDS) network (Feijt and van Lammeren, 1996), where a combination of ground based and satellite observations allowed to gain a better description of the cloud geometry.

3.4 CLOUDNET TARGET CATEGORIZATION

The Cloudnet target categorization scheme is part of the Cloudnet algorithm suite and provides information on the macroscopical properties of clouds using ground based measurements from observational sites (Hogan and O’connor, 1996; Illingworth et al., 2007). The Cloudnet program package is operational at JOYCE and, in addition to the target categorization, it also provides retrievals of liquid and ice water content (Hogan et al., 2006) and drizzle microphysical properties (O’Connor et al., 2005). Here, the categorization is used to determine cloud base and cloud top and to discriminate columns of drizzling/non-drizzling clouds.

The Cloudnet project was started in 2001 and created a network of stations with the aim of evaluating the cloud and aerosol profiles in operational NWP models using observations. Providing accurate and useful measurements to improve forecast model performance has always been a major challenge: various attempts in detecting global cloud properties from space (Webb et al., 2001; Jakob, 2003) or from combined measurements from aircrafts and ground based observations (Willén et al., 2005) have been carried out in recent years.

Cloudnet provides continuous high time resolution vertical profiles (30 s resolution) of cloud variables in quasi real time. Its data products are standardized, e.g. converted in standard units and interpolated on a common time height grid for all the sites of the network. Therefore, the Cloudnet datasets are very valuable for model improvements (Ahlgrimm and Forbes, 2014).

The baseline instruments to derive Cloudnet products are a Doppler cloud radar, a low power lidar ceilometer, and a dual-wavelength microwave radiometer operating continuously 24/7. Hourly model forecast data or regular radiosonde information must also be available

*More on Cloudnet
project:
www.cloud-net.org*

More information
on COSMO-DE:
www.cosmo-model.org

for the site. At JOYCE, whose observations are used in this thesis, the operational forecast data of the NWP model COSMO-DE of the German Weather Service is used.

The target categorization is a product that classifies each radar range bin, here called pixels, in terms of the occurrence of liquid droplets, ice, insects, aerosols, etc.. An example for the targets identified by Cloudnet are shown in Fig. 3.3. For this work, the classified bins "*cloud droplets only*", "*drizzle or rain*" and "*drizzle/rain and cloud droplets*" are considered. Since multiple target types can be simultaneously present in the same pixel, the information contained in the target categorization is provided in the form of a bit field. Each target is represented by a combination of bits and the categorization provides 5 different bits. The bits of interest for this study are only 3. They are defined as follows:

- Bit 0: (droplet bit) small cloud droplets are present,
- Bit 1: (falling bit) hydrometeors are falling,
- Bit 2: (cold/melting bit) wet bulb temperature lower than 0° C (normally associated with ice presence).

Each of the targets regarding liquid drizzling/non-drizzling clouds is obtained with the following combination of bits:

- *cloud droplets only*: Bit 0 = 1, Bit 1 = 0, Bit 2 = 0,
- *drizzle or rain*: Bit 0 = 0, Bit 1 = 1, Bit 2 = 0,
- *drizzle/rain and cloud droplets*: Bit 0 = 1, Bit 1 = 1, Bit 2 = 0.

In this thesis, non-drizzling and drizzling atmospheric columns are identified analyzing the target categorization in each height level. When the target categorization indicates only the presence of cloud droplets in the profile a **non-drizzling column** is assigned. Whenever the categorization indicates that drizzle is present between cloud base and cloud top in more than 90% of the pixels and at the same time rain is detected below cloud base, the column is flagged as **drizzling**. All other types of columns are classified as columns in transition. An example of drizzling, non-drizzling, and transition columns is shown in Fig. 3.5.

Determination of the categorization bits

Here the way in which each of the pixels are classified is explained in detail (Hogan and O'connor, 1996). Bits are listed in the order they are used by the Cloudnet algorithm.

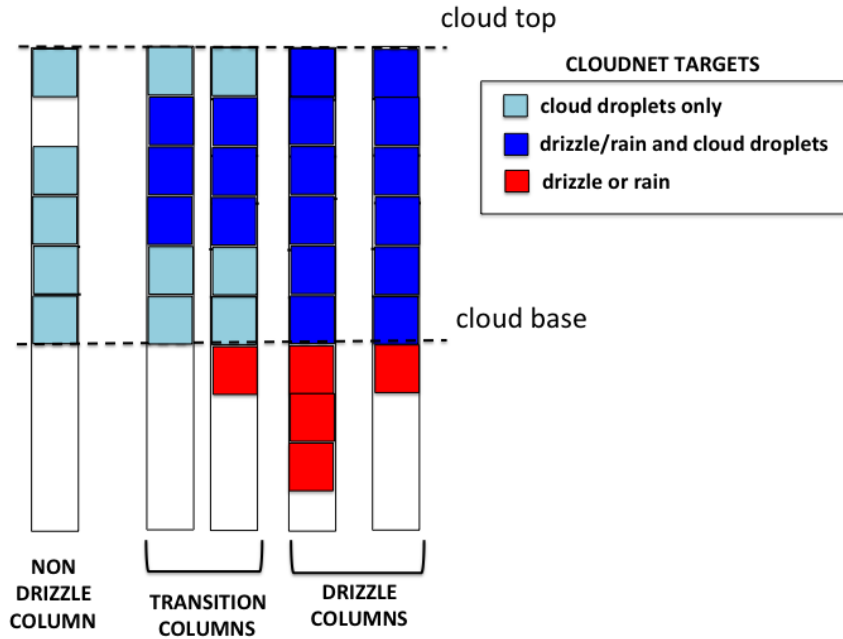


Figure 3.5: Schematic representation of target categorization vertical profiles classified as drizzling, non-drizzling and transition vertical atmospheric columns.

Bit 2: cold/melting bit

This bit assigns the phase of the species, which can be liquid or ice. This bit is determined using the model wet bulb temperature and the Doppler velocity V_d which has to be corrected for folding effects. Liquid precipitation has wet bulb temperature larger than 0°C . Moreover, a large and sharp increase in fall speed, and therefore in mean Doppler velocity, is expected at the point of melting. The algorithm exploits these two features to distinguish the liquid from the ice falling pixels. The mean Doppler velocity is also corrected for folding effects. The bit is set to 1 (ice and super-cooled phase) if the wet bulb temperature is less than 0°C .

Bit 0: droplet bit

This bit identifies the presence of cloud droplets in the pixel. The input for the droplet bit is the attenuated lidar backscattering coefficient β' , the radar reflectivity factor Z_e , the cold/melting bit and the temperature T . First, liquid cloud base and cloud top need to be identified. Cloud base height is defined as the height where liquid water is first detected. This height is assigned on the basis of a condition on the backscatter coefficient β' of the ceilometer. Then, the profile of β' is analyzed to determine the top height. When β' has been extinguished before and the radar still presents a signal, then the radar reflectivity is used. Finally, the droplet bit is set to 1 between the retrieved cloud base height and cloud top height.

Bit 1: falling bit

The falling bit indicates the presence of falling hydrometeors in a pixel, which are then identified as liquid or ice precipitation on the basis of the corresponding value of the cold/melting bit. The falling bit is determined using the profile of Z_e . In this thesis, only columns with liquid water droplets are analyzed. Therefore, in the following, only the determination of liquid precipitation (rain/drizzle) is presented.

For the region between cloud base and cloud top, the slope of the Z_e profile is investigated. For a cloud which contains only cloud droplets it is assumed that the liquid water increases adiabatically implying an increase of Z_e with height. However, when the cloud starts to generate drizzle, the profile of Z_e reverses sign. Therefore, the values of Z_e at a height 20% above cloud base is compared to the one measured at a height 20% below cloud top. If Z_e decreases with height all pixels between cloud base and the pixel below cloud top where $Z_e > -30$ dBz are assigned a bit $1 = 1$. Below cloud base, the falling bit is assigned wherever the radar echo is contiguous below cloud base.

3.5 PASSIVE AND ACTIVE MICROWAVE TRANSFER (PAMTRA) FORWARD MODEL

The Passive and Active Microwave Transfer (PAMTRA) model is a forward model that simulates passive and active instrument measurements: it provides upwelling and downwelling radiances at any elevation and azimuth angle. A detailed description of the model can be found in [Maahn \(2015\)](#). Here, only the main characteristics and settings which are relevant for this specific study are mentioned.

Forward simulators are widely used in cloud physics retrieval applications ([Maahn and Löhnert, 2017](#)), for the validation of numerical weather prediction (NWP) ([Caumont et al., 2006](#)) and global climate (GCM) models ([Reverdy et al., 2015](#)) and for sensitivity studies to optimally exploit the information of remote sensing instruments ([Maahn et al., 2015](#)). In this work, the forward model has been used to simulate cloud radar observations of liquid drizzling/non-drizzling clouds in two distinct applications. In the study on IQ raw radar observations (see chapter 6), simulations are used to confirm the main results from the observations, to generalize their validity and to test the impact of hardware dependent radar parameters on radar Doppler moments. In addition, PAMTRA allows for a comparison between observations and a 1D steady state model output of drizzle formation (see Chapter 5).

Overview of the model

Pamtra, developed in FORTRAN90 programming language, simulates radiances in the microwave wavelength region under the assumptions of a plane-parallel and horizontally homogeneous atmosphere. The model needs many different input parameters regarding the atmospheric state, including the hydrometeor properties and the specific settings of the instrument being simulated. For the present work, the hydrometeors considered are cloud droplets and drizzle: each hydrometeor type has to be specified with respect to phase, size distribution, fall velocity model and discrete bin sizes. This can be done either by providing a discrete binned DSD for cloud and drizzle or by providing the total number concentration N and the effective radius (R_{eff}) of specified DSD shapes for both hydrometeors' types. In PAMTRA (modified) gamma, exponential and lognormal distributions are implemented. In this study, for the IQ simulations, cloud droplet and drizzle drop size distributions are assumed to be lognormal.

Spectral radar simulator

For liquid hydrometeors, the radar Doppler spectra simulator is based on the work of [Kollias et al. \(2014, 2011a\)](#). In PAMTRA ϵ and vertical velocity can be provided by the user to properly simulate air motions. The methodology to obtain the attenuated Doppler spectrum $S(D)$ from the single scattering properties of each hydrometeor species is extensively described in [Maahn \(2015\)](#). To express then the spectrum as a function of Doppler velocity the following relation is applied:

$$S(v) = S(D) \cdot \frac{\partial D}{\partial v} \quad (3.8)$$

where the fall velocity v and the quantity $\frac{\partial D}{\partial v}$ are provided for liquid targets by [Khvorostyanov and Curry \(2002\)](#). The vertical air motion is in this work provided as a single value (see Table 3.2).

In order to mimic what a real cloud radar would measure, other radar parameters need to be specified to calculate the final shape of the spectrum: the number of FFT points (N_{fft}) to determine the velocity boundaries $\pm v_{N_{\text{fft}}}$, the radar receiver noise to be added to the simulated spectrum. In addition, the radar receiver noise power at 1000 m of range height is necessary to determine the factor $N_p(R)$ that accounts for the decrease of radar sensitivity due to range R . PAMTRA also calculates the broadening σ_k that the spectrum undergoes due to finite beam width, wind shear and turbulence ([Doviak and Zrnica, 2014](#); [Shupe et al., 2008](#)):

$$\sigma_k^2 = \sigma_w^2 + \sigma_s^2 + \sigma_t^2 \quad (3.9)$$

where σ_w^2 is the variance due to the finite beam width, σ_s^2 is the one due to the wind shear and σ_t^2 the one due to turbulence. The

following other radar quantities are needed to calculate each term of equation (3.9):

- the horizontal wind u ,
- the full width at half maximum one-way radar beam width θ ,
- eddy dissipation rate ϵ ,
- largest length scales observed by the radar $L_s = uT + R \sin \theta$,
- smallest length scale $L_\lambda = \frac{\lambda}{2}$,
- Distance between cloud base and radar R .

Finally, random perturbations to the noise can be added to the spectrum by the user by setting the parameter **randomseed** to a value between 0 and 1 (see Tab. 3.2). From the obtained simulated spectra, moments are then derived in the same way as described for observations in section 2.3.2. The values used for all these parameters are listed in table 3.2 together with the technical specifications of the radar mentioned before.

Table 3.2: Parameters provided to PAMTRA for simulating JOYRAD-35 observations

Parameter	Symbol	Value for IQ simulations (statistics)	Value for model validation
distance between cloud and radar	600 m	600 m	
eddy dissipation rate	ϵ	random value picked from the distribution derived in one hour of drizzling case study	$0.001327 \text{ m}^2 \text{ s}^{-3}$
half power half width one way radar beam width	θ	0.3°	0.3°
horizontal wind	u	5.5 m s^{-1}	5.5 m s^{-1} (mean observed value (from wind lidar) in one hour of drizzling case study)
number of spectral averages	—	variable	20 (corresponding to 2 s integration time for JOYRAD-35)
number of FFT points	N_{fft}	variable	512
Nyquist velocity	v_{Nyq}	$\pm 10.625 \text{ m s}^{-1}$	$\pm 10.625 \text{ m s}^{-1}$
radar clear air noise return at 1000 m	—	-38.095 dBz	-38.095 dBz
radar frequency	f	35 GHz	35 GHz
radar noise distance factor	-	1.5	1.5
randomseed		0	1
smallest length scale observed by the radar	L_λ	0.0042 m	0.0042 m
vertical air motion	v	random value picked from the distribution derived in one hour of drizzling case study	0.5 m s^{-1}

Here the clouds studied in the thesis are presented from a statistical perspective but also analyzed by looking at detailed case studies (section 4.1). Then, different examples of realistic but also physically inconsistent Cloudnet classifications are discussed and an objective separation between drizzling and non-drizzling column is introduced (section 4.2). Finally, the dataset used in the next chapter is described (section 4.3).

4.1 LIQUID CLOUDS AT JOYCE

JOYCE is located in Western Germany ($50^{\circ}54'31''\text{N}$, $6^{\circ}24'49''\text{E}$), 40 km west to Cologne. Besides the instruments mentioned in Chapter 3, it is equipped with other passive and active remote sensing instruments, e.g. a Micro Rain Radar (MRR) and a Doppler lidar. With its yearly precipitation ranging between 440 and 1040 mm (Löhnert et al., 2015), JOYCE represents a perfect location for monitoring the development of precipitation from continental clouds. Fig. 4.1 shows that only 3% of total precipitation observed is due to warm processes. Even though warm rain hence contributes sparsely to the total precipitation amount, continental warm clouds have a strong impact on boundary layer thermodynamics, cloud radiative properties and water cycle and little research has been done on them (Del Genio and Wolf, 2000; Kollias et al., 2007c). Moreover, the statistics presented in Fig. 4.1 do not account for all the rain which does not reach the ground. In fact, the 300 m height bin of MRR considered as proxy for liquid precipitation does not measure the rain evaporating before reaching that height. This is a common situation in drizzling liquid clouds.

Based on the continuous high resolution observations of the instruments available at JOYCE, a one-year (2012-2013) ensemble of liquid drizzling/non-drizzling cases has been compiled. This dataset is used to characterize macroscopical cloud properties of drizzling/non-drizzling clouds. Comparisons of the distributions of observed values of liquid water path and geometrical thickness with those derived from the instantaneous COSMO-DE output for the corresponding location have been carried out to evaluate the model performance in representing these clouds. Information about the two datasets is summarized in Table 4.1.

In addition, in order to exploit the information content on drizzle formation contained in the higher moments of the Doppler spectra, an ensemble of approximately 50 days of liquid drizzling and



link to the JOYCE
website:
www.joyce.cloud

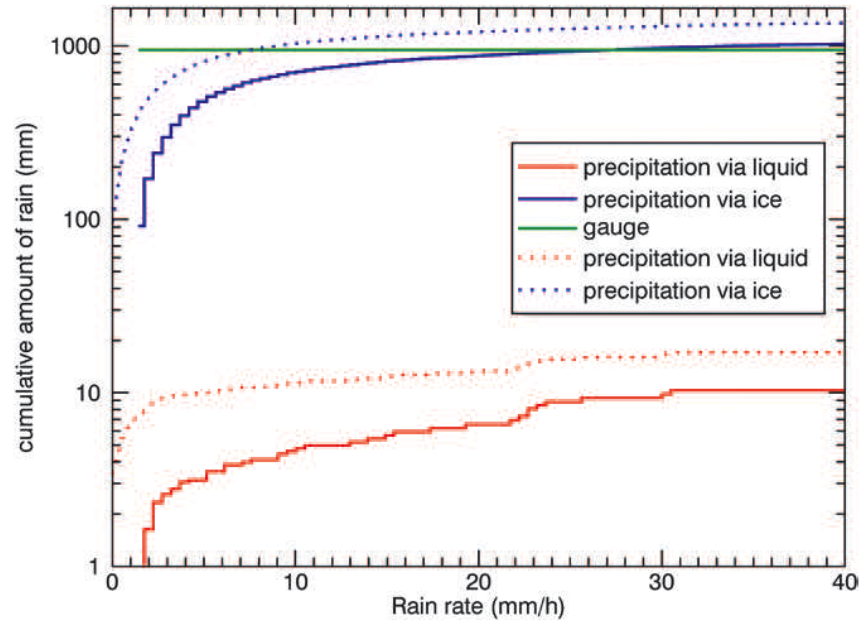


Figure 4.1: Cumulative histogram of precipitation amount [mm] as a function of rain rate for the period March 2012-Aug 2013 from MRR. Cloudnet categorization differentiates precipitation via ice (blue) and precipitation via liquid only (red). Dotted and solid lines denote histograms with different lower bounds for rain detection (0.02 and 1.5 mm h^{-1} , respectively). The total precipitation amount from gauge measurements is given as the green line (from Löhnert et al. (2015)).

non-drizzling clouds has been extracted from the period 2013-2015. For this dataset, the integration time (1 s) for the radar observations adopted during this period at JOYCE is exploited. Such short integration time is essential to capture microphysical signatures of drizzle formation (see Chapter 6).

One-year analysis of non-drizzling/drizzling liquid clouds

Two of the main variables which are correlated to drizzle presence are LWP and cloud geometrical thickness (Mann et al., 2014). In Figure 4.2 the frequency of occurrence of observed LWP values for the period March 2012-March 2013 and corresponding COSMO-DE model output for the same period are compared. COSMO-DE is a numerical weather prediction model developed by the Deutscher Wetterdienst (DWD) with the goal of performing short range weather forecasts of severe events. It has a horizontal resolution of 2.8 km and 50 vertical layers ranging 10 m and 22 km (Baldauf et al., 2011). The LWP distributions are divided into drizzle and non-drizzle columns identified on the basis of Cloudnet. A threshold on the mixing ratio is used to identify cloud presence in COSMO-DE model data. Typical values of LWP for non-drizzling clouds hardly exceed 50 gm^2 , while for the drizzling distribution the most frequent LWP observed is 190

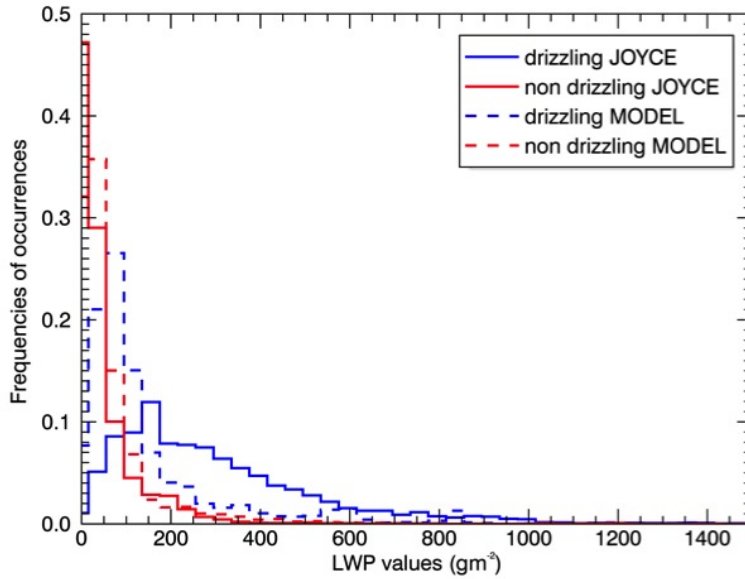


Figure 4.2: Histograms of LWP from MWR observations at JOYCE (solid lines) and corresponding model results from COSMO-DE (dashed lines). The period analyzed is March 2012-March 2013. In blue the drizzling population, in red the non-drizzling one. The dataset is formed by single layer liquid only clouds.

gm^2 . Histograms for the geometrical thickness are shown in Fig. 4.3. Also in terms of geometrical thickness, clouds with geometrical thickness larger than 600 m are typically identified as drizzling, while those which smaller geometrical thicknesses are non-drizzling. The model populations only partially match the observations: while the non-drizzling distribution from COSMO is similar to the observed one in terms of both LWP and geometrical thickness, drizzling clouds in the model appear to have a too small vertical extent. Moreover, observed drizzling clouds contain much more liquid water than the ones in the model. These discrepancies highlight the model difficulties in identifying when a cloud starts to form precipitation.

Figures 4.4 and 4.5 show the statistical frequency of occurrence of precipitation (which can be interpreted as a probability of rain) as a function of LWP and geometrical thickness for the observations and the COSMO model data respectively.

Figure 4.4 shows that practically no drizzle is observed in single layer liquid clouds when $\text{LWP} < 80 \text{ gm}^{-2}$ and the geometrical thickness is smaller than 400 m. At the same time, if $\text{LWP} > 250 \text{ gm}^{-2}$ and geometrical thickness is larger than 600 m, the probability of having some drizzle is almost 1. For model data (Fig. 4.5), these thresholds do not apply. In fact, between 200 gm^{-2} and 400 gm^{-2} LWP, and geometrical thicknesses between 700 m and 1500 m the model shows a rather low probability for drizzle occurrence.

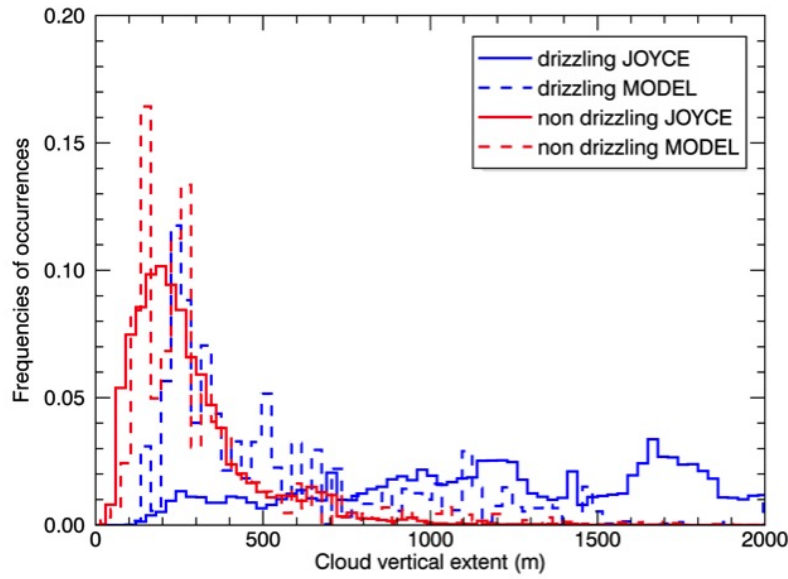


Figure 4.3: Histograms of cloud geometrical thickness from MWR observations at JOYCE (solid lines) and corresponding model results from COSMO-DE (dashed lines). The period analyzed is March 2012-March 2013. In blue the drizzling population, in red the non-drizzling one. The dataset is formed by single layer liquid only clouds.

Table 4.1: COSMO model and observations characteristics for the statistical comparison.

Settings	COSMO model	JOYCE observations
Cloud type	single layer liquid clouds	single layer liquid clouds
Period	March 2012 - March 2013	March 2012 - March 2013
Rainy columns	3590	18690
Non-rainy columns	11505	15708
Categorization used	categorization built on threshold of mixing ratio	Cloudnet target categorization
Dataset/Instruments	German operational NWP COSMO-DE 3 hour forecast (mean value over JOYCE, instantaneous measurement)	cloud radar, microwave radiometer (partially), ceilometer, measurements constrained by NWP models

Case studies of non-drizzling/drizzling liquid clouds

Between 2013 and 2015, 45 cases with liquid clouds at JOYCE are considered for the following analysis. They occur during different meteorological conditions over the site: often warm single layer liquid clouds are coupled to the boundary layer height development during the day. In other cases, conversely, typical stratiform clouds are observed which show a more homogeneous and persistent layered structure during the whole day. Both types of clouds are able to develop precipitation. Examples for non-drizzling situations are shown in Figs. 4.6 and 4.7. Figs. 4.8 and 4.9 instead show examples

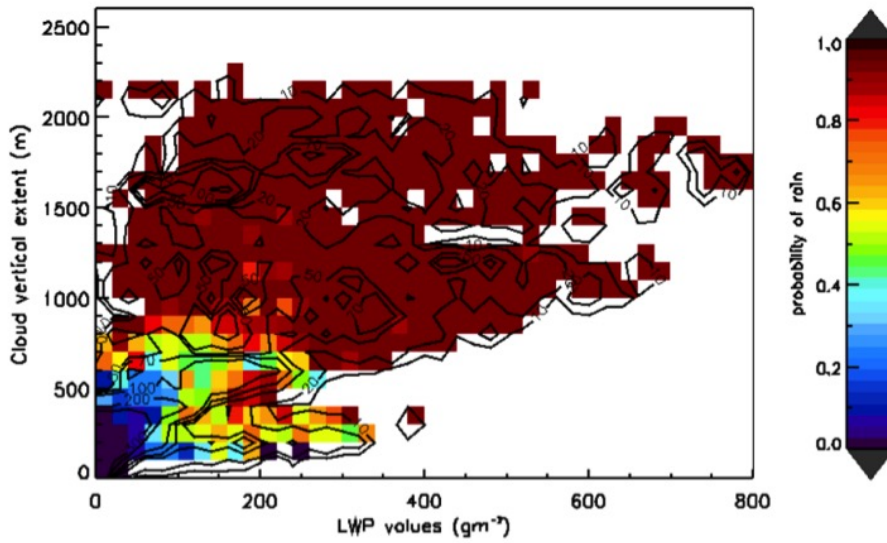


Figure 4.4: 2D Probability of precipitation (POP) derived statistically from the observations for the period March 2012 - March 2013 (from Löhnert et al. (2015)).

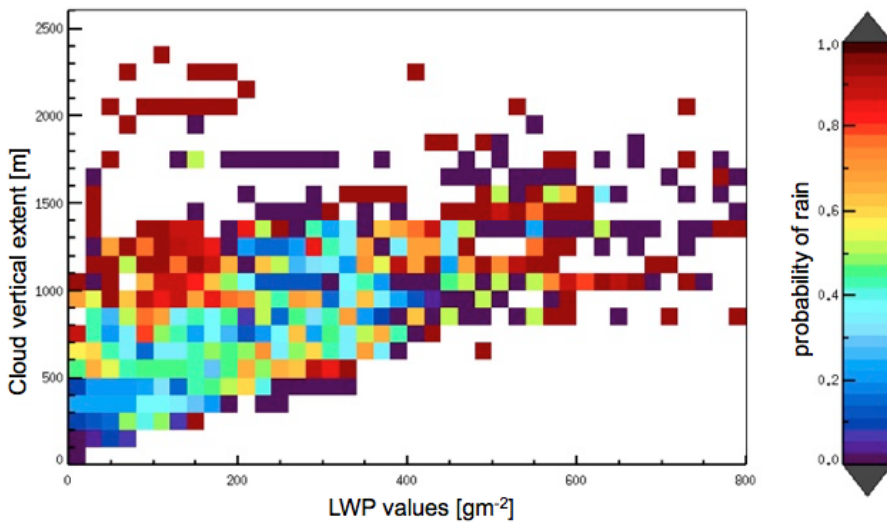


Figure 4.5: 2D probability of precipitation (POP) derived statistically from the COSMO output for the period March 2012-March 2013.

for drizzling cases. Sometimes, erroneous cloud base identification occurs due to the presence of insects in the lowest atmospheric layers close to the ground. This can be seen for example, in Fig. 4.6 between 10.5 and 10.7 UTC and also in the last 15 minutes of the hour in Fig. 4.7.

Typically, in absence of precipitation, reflectivity values observed are very low, i.e. below or equal to -30 dBZ and increase with height from cloud base and cloud top. In both cases the cloud layer is thin

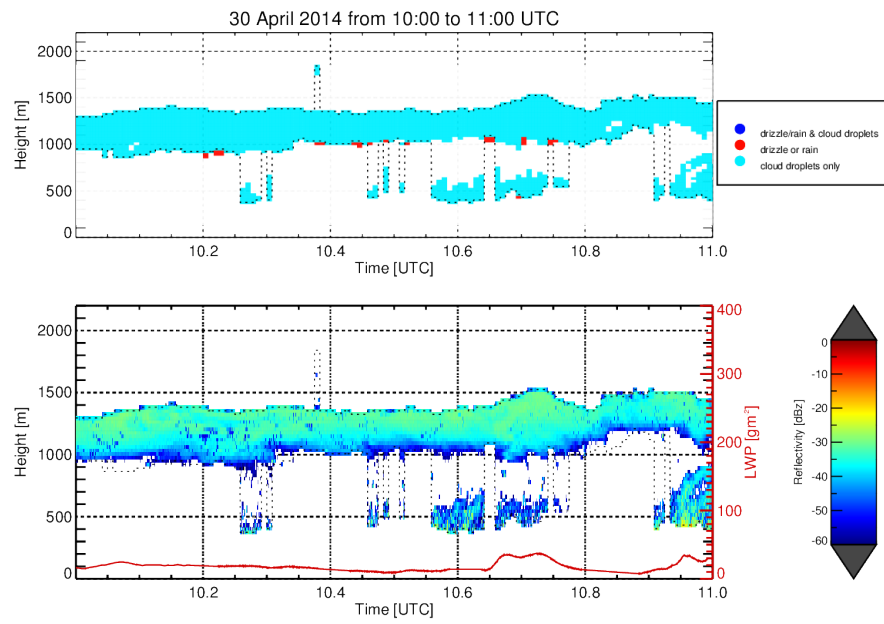


Figure 4.6: Example of boundary layer non-drizzling liquid cloud occurring at JOYCE from the 30th of April 2014 between 10:00 and 11:00 UTC. The upper panel shows the Cloudnet target classification, the lower panel the Z_e time-height plot and (in red) the observed time serie of LWP values from the MWR. Cloud base and cloud top are identified from Cloudnet (black dashed lines).

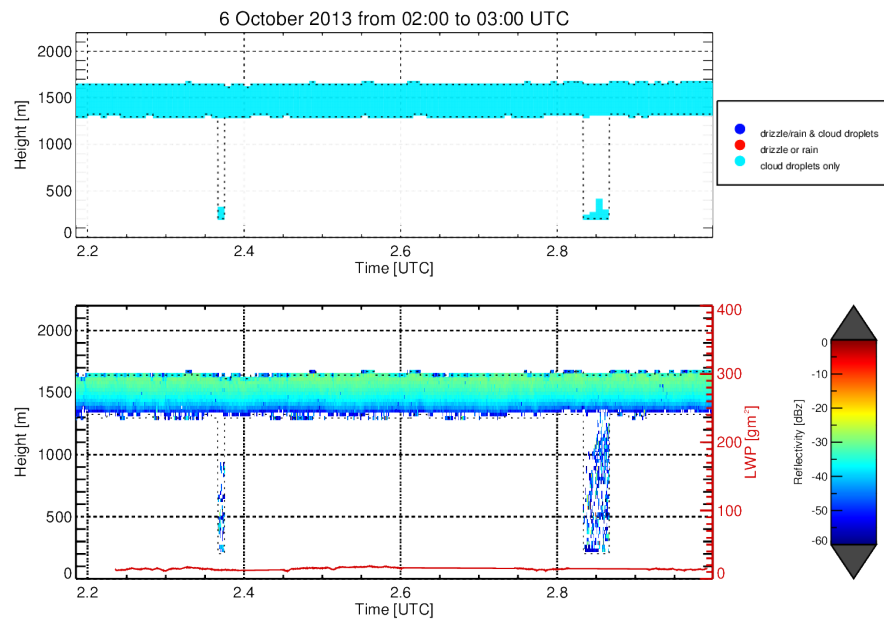


Figure 4.7: As in Fig. 4.6, only 6th October 2013.

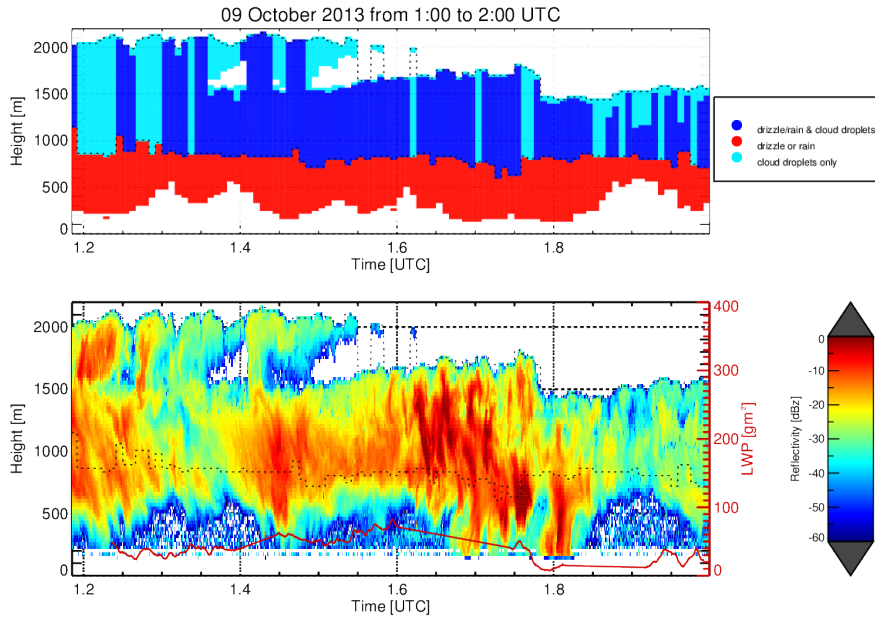


Figure 4.8: As in Fig. 4.6, only 9th October 2013.

and homogeneous. The observed values of LWP are very low, not exceeding 50 gm^{-2} . Cloudnet identifies these clouds as formed by cloud droplets with no presence of drizzle. Only in the case of Fig. 4.6 some bins are identified as drizzle or rain. This identification appears to be ambiguous and physically inconsistent on the basis of the correspondingly observed LWP and reflectivity values which are typical values of non-drizzling distributions (Fig. 4.2).

Drizzling cases are diverse. Fig. 4.8 shows an heterogeneous drizzling cloud with reflectivities up to 0 dBz and the cloud thickness of the cloudy layer is highly variable between 500 and 1000 m. Precipitating structures are evident below cloud base. In some situations, for example between 1.6 and 1.75 UTC, they presumably reach the ground (correspondingly no LWP measurements are available). Also the LWP shows a higher variability, as expected from Fig. 4.2, even if the mean value observed is still quite low (below 100 gm^{-2}). Cloudnet identifies rain below cloud base for the whole hour, while reflectivity values in some parts do not exceed -35 dBz . Thus, it is very unlikely that this signal is due to the presence of drizzle. Above cloud base, Cloudnet sporadically classifies columns not containing drizzle. This feature can be often seen in regions where Z_e values above -20 dBz occur, e.g. around 1.2 UTC or around 1.7 UTC, implying that drizzle droplets likely occur, according to typical drizzling Z_e values observed in literature (Kollias et al., 2011b).

In contrast to Figure 4.8, the drizzling case in Fig. 4.9 is much more homogeneous: here vertical structures of Z_e around -10 dBz extend continuously below cloud base and the hydrometeors evaporate be-

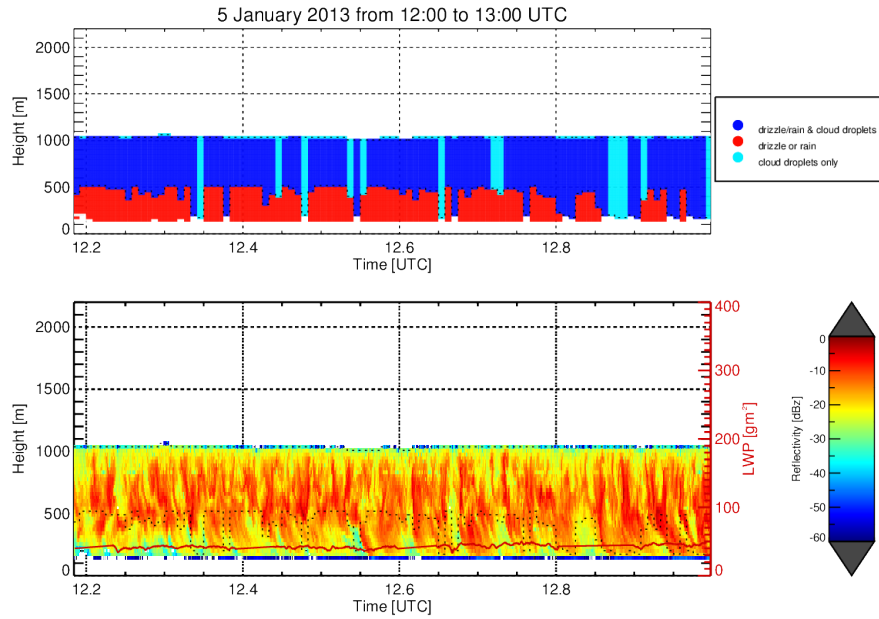


Figure 4.9: As in Fig. 4.6, only 5th January 2013.

fore reaching the ground. For the whole hour, the cloud top is almost at the same height. Also the LWP is approximately constant with a value around 50 gm^{-2} . Cloudnet identifies drizzle in the whole vertical profile, above and below cloud base, almost all time.

4.2 ASSESSMENT OF DRIZZLE DETECTION BY CLOUDNET

In the previous section some inconsistencies in the way Cloudnet classifies the cloud vertical profiles have been highlighted. Figures 4.10 and 4.11 focus on a specific example in which the Cloudnet target categorization provides a quite unrealistic classification of cloudy columns. In Fig. 4.10 two regions have been identified as physically inconsistent. In the first region between 0.0 and 4.0 UTC Cloudnet indicates a persistent presence of drizzle below cloud base without any drizzle between cloud base and cloud top. Every profile is a single snapshot of the vertical profile of the cloud above the site and thus no evolution of the cloud can be extrapolated from a series of ground based radar observations due to advection and shear above the site. However, it is unrealistic that drizzle is more or less continuously detected below cloud base, while not within the cloud. This sharp transition between cloud droplets only and rain below cloud base does not imply any drizzle development and thus seems physically inconsistent. Also, between 4.0 UTC and 8.0 UTC drizzle is identified below cloud base for a quite long time interval, but **intermittency** in drizzling and non-drizzling profiles is present between cloud base

*The term **intermittency** is referred to the fact that there is no observed continuity in time of a given type of vertical profile. Or, the profile occurs in an intermittent way during time.*

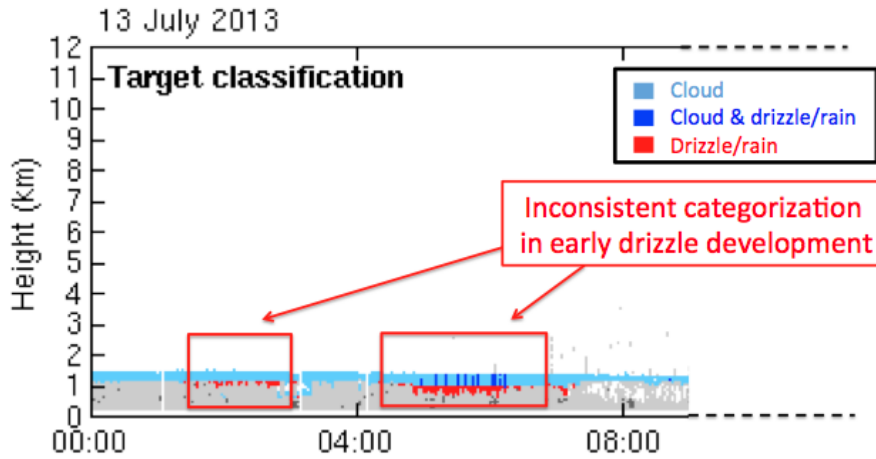


Figure 4.10: Target categorization from Cloudnet for the 13th July 2013: two areas are highlighted as situations of physically inconsistent categorization (red boxes).

and cloud top. Also in this case, it is difficult to provide a physical interpretation of the classification observed. Figure 4.11 gives an insight of the Z_e field associated with the intermittent cloudnet classification: between 4 and 8 UTC Z_e values range between -35 and -23 dBZ. The LWP is very low (around $20\text{-}30\text{ gm}^{-2}$) for the whole period. Reflectivity values not exceeding -25 dBZ below cloud base indicate that the size of the droplets producing the signal are very small, probably smaller than the typical size of $50\text{ }\mu\text{m}$ used to discriminate drizzle from cloud droplets. In this specific situation, higher moments of the Doppler spectra may provide additional useful information about the type of droplets contained in the cloud, as will be shown in the next chapters.

To reduce the uncertainty in identifying populations of drizzling and non-drizzling columns on the basis of Cloudnet, a more constrained criterion is developed. In the following, a vertical column will be classified as **drizzling** or **non-drizzling**, if corresponding drizzling (non-drizzling) Cloudnet columns are observed continuously within a 20 minutes time interval. In Fig. 4.11 such time interval is indicated by the two vertical dashed lines. If no continuity in time of the given type of the column is found, the column is flagged as a non-continuous or "**transition**" column. This is the case for the aforementioned example shown in Fig. 4.11: the non-drizzling column observed at 5.5 UTC is to be classified as transition because within the next 20 minutes interval, drizzling and non-drizzling vertical columns alternate. In the same way, cloud columns of the example given in Fig. 4.6 are entirely classified as non-drizzling cases. On the basis of this persistency criterion based on Cloudnet, a characterization of the populations in terms of higher moments of Doppler spectrum and other variables is developed (see chapter 5 and 7).

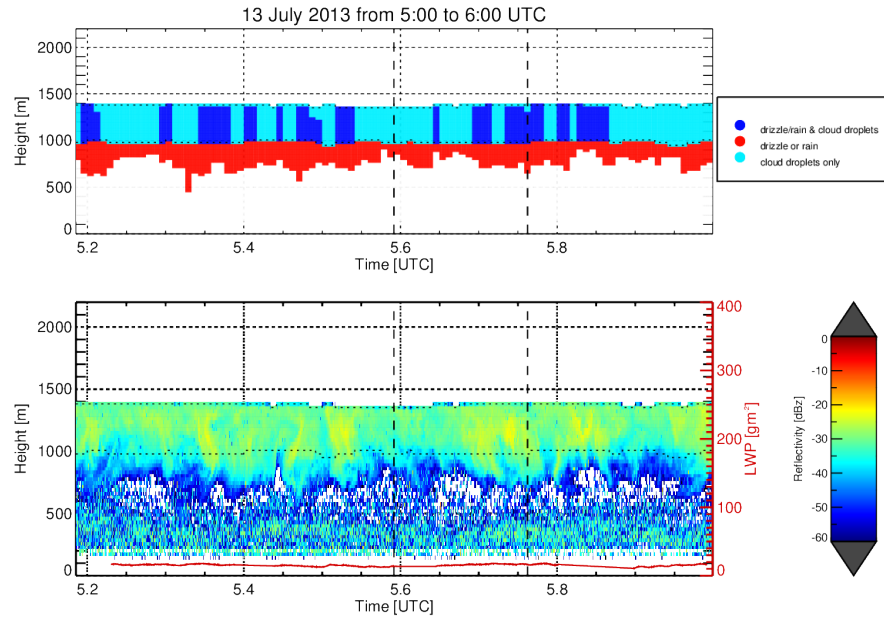


Figure 4.11: Zoom of the physical inconsistency identified in Cloudnet (Fig. 4.10) between 4:00 and 8:00 UTC. The upper panel shows the target categorization, while the lower panel exhibits the reflectivity fields and the time series of LWP (in red, y axis on the right).

4.3 EXTENDED ANALYSIS OF DRIZZLING / NON-DRIZZLING CLOUD PROPERTIES

As already mentioned, in this thesis two distinct datasets are used. The first one, extending from March 2012 to March 2013, is used to analyze macrophysical properties of clouds and to compare with COSMO-DE model. The second one (2013-2015) is a collection of case studies with high resolution cloud radar observations. This dataset is used to study radar Doppler moments of drizzling / non-drizzling continental clouds and develop a new drizzle detection criterion. After having shown some examples belonging to this ensemble in the previous section, here the statistical properties and the characterization of the dataset in terms of radar Doppler moments and LWP are presented. Table 4.2 in subsection 4.3.1 presents the statistical properties of the dataset. Subsection 4.3.2 shows a characterization of the dataset in terms of distance from cloud top, radar Doppler moments and LWP.

4.3.1 Statistical properties

Table 4.2 reports the total number of days, their distribution among different seasons, the total number of hours observed and the total amount of columns classified as drizzling, non-drizzling and transition compared to the standard Cloudnet classification.

Table 4.2: Statistical properties of the dataset used for analysis of higher moments of Doppler spectra.

quantity	Value
total number of days	45
total number of hours	500
days in summer	19
days in winter	8
days in spring	5
days in autumn	13
Cloudnet drizzle columns	12.4%
Cloudnet non-drizzle columns	60.2%
Cloudnet ambiguous columns	27.4%
total Cloudnet columns	1.095.725
drizzling persistent columns	14.5%
non-drizzling persistent columns	85.5%
transition columns	401563
total correlated in time classification	694162
Cloudnet drizzle radar bins	23.7%
Cloudnet non-drizzle radar bins	35.7%
Cloudnet ambiguous radar bins	40.6%
total Cloudnet radar bins	18018470
drizzling persistent radar bins	36.7%
non-drizzling persistent radar bins	63.3%
transition radar bins	9430990
total correlated in time radar bins	8587080

Transition columns are all the situations in which the new objective criterion to identify drizzle/non-drizzle continuously in time columns was not fulfilled. These are all the situations in which intermittency of the Cloudnet vertical profiles classification is observed (see previous section). Situations in which Cloudnet identifies drizzle below cloud base but not above are kept separated from the previously specified drizzling/non-drizzling columns because of the difficult physical interpretation of this type of classification and are referred to as Cloudnet' ambiguous columns.

4.3.2 Dataset characterization in terms of radar Doppler moments and LWP

The ensemble of case studies collected between 2013 and 2015 with high resolution cloud radar observations is displayed here. Each cloud pixel is characterized in terms of the distance d from cloud top, LWP and the Doppler spectrum moment. Different stages of drizzle development regimes for LWP and d are identified based on moments' values. The distribution of mean values of reflectivity calculated for each LWP/ d pair is shown in Fig. 4.12. The same for mean Doppler velocity, spectral width and skewness are shown in Fig. 4.13, 4.14 and 4.15, respectively.

Typically, the cloud top region of $-100 \text{ m} < d < 0 \text{ m}$ is characterized by homogeneous values of the moments for the whole range of LWPs. In fact, Z_e values are of approximately -30 dBz (Fig. 4.12) and skewness values are around 0 (Fig. 4.15). At the same time, spectral width shows a slight increase proportional to LWP (Fig. 4.14), while V_d is approximately 0 ms^{-1} (Fig. 4.13). Data do not show evidence of downdrafts caused by the radiative cooling happening at cloud top. However, the signature of such process may be masked by the averaging with updraft values ($V_d < 0 \text{ ms}^{-1}$). This thin layer seems to be detached from the dynamical and microphysical signatures detected in the lower part of the cloud as LWP is increasing.

An adiabatic regime is identified in the cloud for $d < -100 \text{ m}$ and $\text{LWP} < 100 \text{ gm}^{-2}$. Reflectivity gradually increases with height from cloud base to cloud top (Fig. 4.12) in agreement with an idealized adiabatic ascent of a cloud parcel. V_d (Fig. 4.13) is typically ranging between 0 and -0.5 ms^{-1} indicating predominant updrafts. Accordingly to the Z_e increase, also S_w increases with height (Fig. 4.14), while S_k is mostly around zero (Fig. 4.15).

For $d < -100 \text{ m}$ and $200 \text{ gm}^{-2} > \text{LWP} > 100 \text{ gm}^{-2}$ the cloudy region is characterized by homogeneous vertical profiles of Z_e and S_w (Fig. 4.12 and Fig. 4.14 respectively). This regions presents the first microphysical signatures of drizzle formation. The mean Doppler velocity shown in Fig. 4.13 shows now negative values (updrafts) around -0.5 ms^{-1} only in the region closer to cloud top while V_d is positive (downdrafts) at distances from cloud top $d < -500 \text{ m}$. In this region the adiabatic description of the ascent is not valid anymore. At cloud top, the skewness S_k shows positive values indicating the presence of drizzle. These larger droplets descend through the cloud and collect liquid water by autoconversion and collision coalescence with cloud droplets. This explains the reduction of the skewness signal from values of 0.2 at d around -200 m to values of 0.1 at d between -400 m and -500 m (Fig. 4.15). However, for lower heights, no negative values of skewness are observed, as would be expected for drizzle continuing growing and dominating the spectrum shape. Also, no larger Z_e or S_w

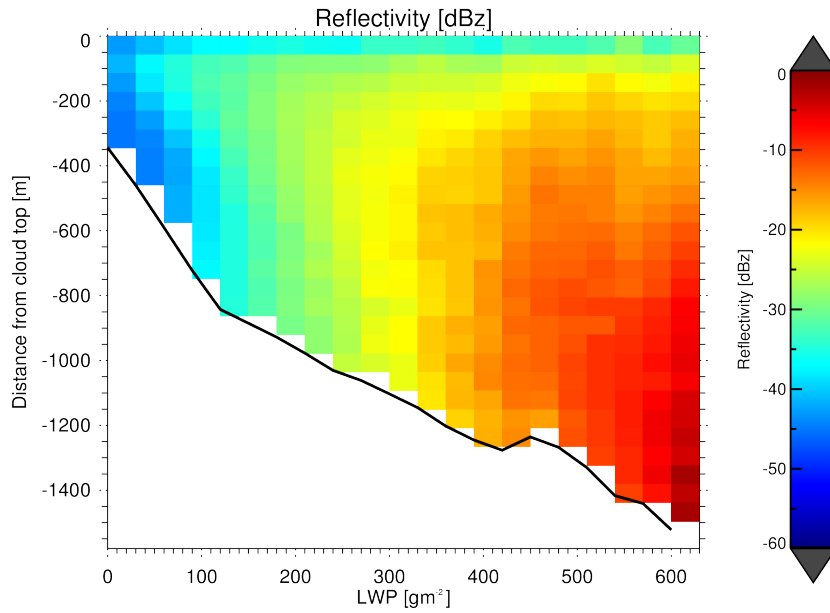


Figure 4.12: Distribution of mean Z_e as a function of distance from cloud top and LWP. Distance from cloud top is binned with a resolution of 50 m, while LWP is binned with a resolution of 30 gm². For each cloud top distance/LWP pair, the mean Z_e value over the ensemble of pixels is calculated. The dataset displayed is from the ensemble of 45 case studies collected between 2013 and 2015 at JOYCE.

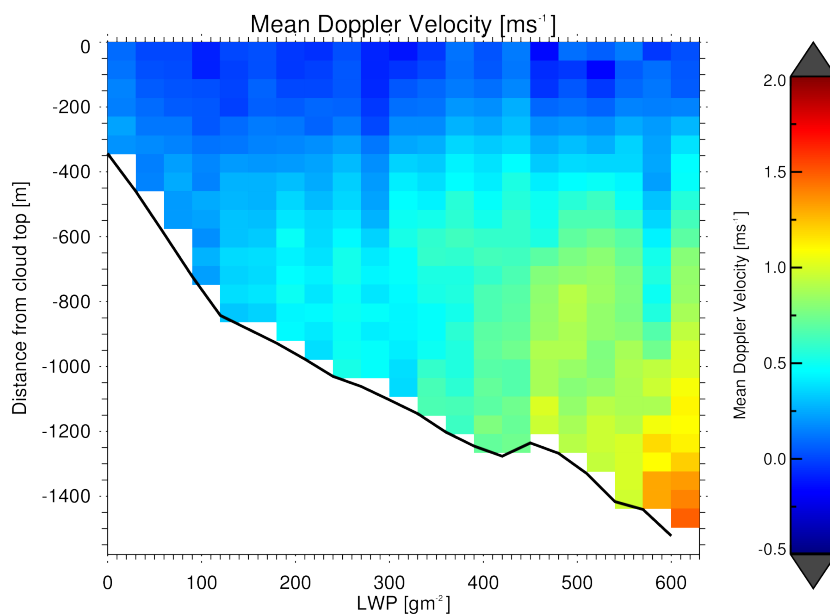


Figure 4.13: Same as Fig. 4.12, only for V_d .

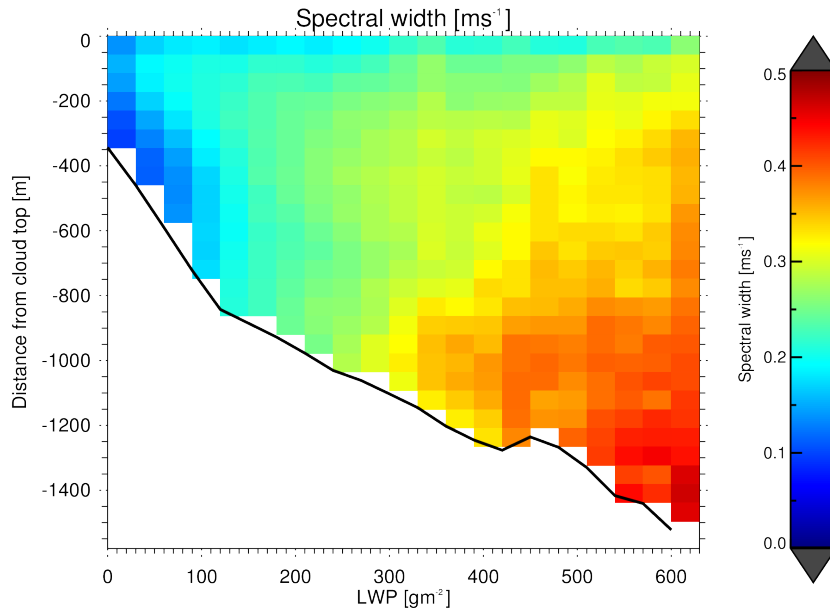
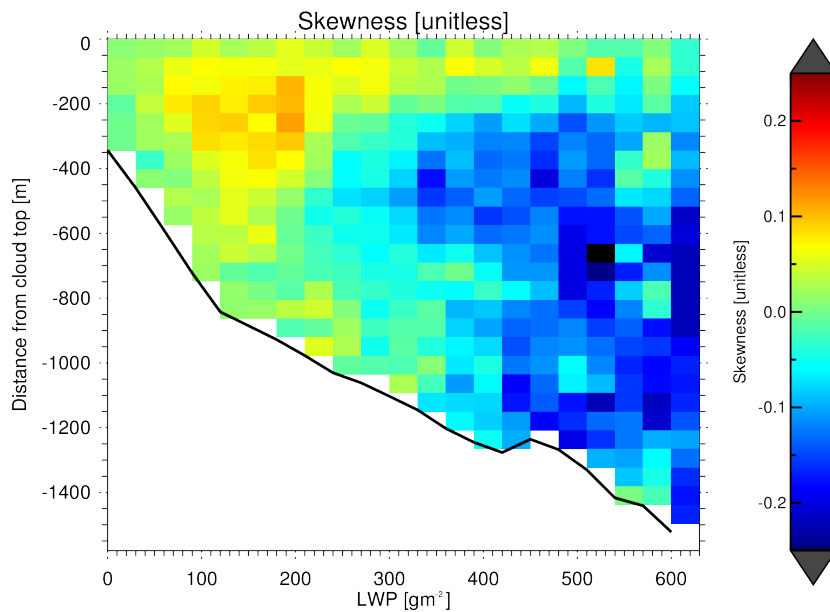
values are observed at d between -400 m and -500 m (Fig. 4.12 and Fig. 4.14 respectively). In this range of LWP values, the drizzle growth during the drops descent from cloud top to cloud base is interrupted.

A reason for this could be that there is not enough liquid water available or the cloud is not thick enough for the growth of drizzle to a size large enough to precipitate. In fact, continental clouds show higher droplet number concentrations (Miles et al., 2000), which generate typical cloud drop size distributions having more droplets of smaller sizes compared to maritime clouds. Due to their size, such droplets typically have smaller fall velocities that cause a less efficient drizzle production. Therefore, a drizzle drop would need more collisions to reach a size and a mass of liquid large enough to precipitate.

Two other regions are also identified: the one for $d < -100$ m and $400 \text{ gm}^{-2} > \text{LWP} > 600 \text{ gm}^{-2}$ represents a region of mature drizzle development, while the region for $d < -100$ m and $200 \text{ gm}^{-2} > \text{LWP} > 400 \text{ gm}^{-2}$ is identified as a transition between initiation and mature drizzle development. In the drizzle mature region Z_e is increasing from cloud top to cloud base (Fig. 4.12) and V_d shows strongly positive (downwards) values for $d < -300$ m (Fig. 4.13). Also S_w shows a strong increase in going from cloud top to cloud base (Fig. 4.14) and S_k is mainly negative except in the first 300 m from cloud top, where positive values occur (Fig. 4.15). All these variables correspond to a typical drizzle scenario. The transition from positive to negative values of S_k occurs within the first 400 m from cloud top, facilitated by the large mean LWC.

In the region between $200 \text{ gm}^{-2} > \text{LWP} > 400 \text{ gm}^{-2}$ a transition in the Z_e and S_w profiles from homogeneous with height to typical drizzling profiles with larger values close to cloud base is visible. Also the V_d shows larger values for increasing LWPs (Fig. 4.13) while the S_k shows a noisy pattern in this interval of LWP values (Fig. 4.15): small areas where $S_k = 0$ are found close to cloud base. These values closer to zero compared to the S_k values of the upper pixels in the cloud may be caused by turbulence, which generally smooths S_k . In fact, correspondingly, larger S_w values, often an indication of the presence of turbulence, are observed (Fig. 4.14). Another possible reason for the inhomogeneities in the S_k field may be caused by the different cloud regimes that are considered together in the dataset. Clouds having different geometrical thicknesses present the transition point for S_k turning from positive to negative values at different heights. This can affect the resulting statistics if different cloud regimes are averaged together.

Finally, in the region where LWPs values are larger than 300 g m^{-2} (Fig. 4.12, 4.13 and 4.14), Z_e , V_d , and S_w show strong vertical gradients from cloud top to cloud base. This interval of LWPs is clearly identified by the Cloudnet classification as drizzling (see Fig. 4.2). Only the S_k variable is able to detect modifications in the drop size distribution induced by early drizzle formation in a range of smaller LWP values (Fig. 4.15). In fact, S_k presents strong gradients between cloud top and cloud base already for $\text{LWP} < 200 \text{ g m}^{-2}$. This range of

Figure 4.14: Same as Fig. 4.12, only for S_w .Figure 4.15: Same as Fig. 4.12, only for S_k .

LWP is typically associated with non-drizzling clouds by Cloudnet algorithm for drizzle identification (Fig. 4.2). Therefore, the skewness is the only variable among the moments of the radar Doppler spectrum which has the potential to detect drizzle formation before the drops become large enough to fall.

Part III

DETECTING DRIZZLE WITH SKEWNESS

Misura cio' che e' misurabile e rendi misurabile cio' che non lo e'.

Galileo Galilei

Pisa, 15th February 1564 – Arcetri, 8 January 1642

In this chapter, a first microphysical interpretation of the skewness signal is given by comparing the output of a binned microphysical model with observations. Section 5.1 describes the methodology used to compare observations and model output. Section 5.2 contains a description of the selected case study and an overview of the two 3-minute time series of observations used for the comparison. The 1D steady-state spectrally resolved microphysical model used in this work is described in section 5.3. Section 5.4 presents the comparison between model and observations while section 5.5 provides an interpretation of the skewness in terms of drizzle properties.

5.1 THE CONCEPT: INTERPRETING THE SKEWNESS SIGNAL

At the end of chapter 4, it has been shown how skewness can point to first modifications in the drop size distribution caused by drizzle formation (Fig. 4.15). The skewness S_k detects an earlier stage of droplet growth compared to other radar moments, i.e. reflectivity, mean Doppler velocity and spectral width. However, it is difficult to attribute a range of typical sizes to the drizzle droplets generating the microphysical signature in S_k . Therefore, it is not also clear if the stage of drizzle formation detected is due to autoconversion or accretion processes. The goal of this chapter is to provide a microphysical interpretation of the skewness signatures by comparing the drizzle formation process simulated by the model with two selected observational case studies closely matching the conditions simulated by the model.

The approach of comparing profiles of measured moments with model simulated ones for a specific case study is similar to the one of Kalesse et al. (2015). In contrast to Kalesse et al. (2015), who focused on a riming event in a mixed phase cloud, in the following liquid clouds are analyzed. Two 3-minute long time series of radar measurements are selected: the first one corresponds to a case of early drizzle onset, while the second one represents a more advanced stage of drizzle development. The measurements of these case studies are then compared to model simulations. The 1D steady-state binned microphysical model used in this work provides simulated profiles of DSDs for different LWP, total droplet number concentration (N), and for 2 distinct LWC shape profiles, and two sizes of initial drizzle drops. The model simulated DSDs are provided in the output with a vertical discretization of 5 m. Every layer has hence to be regridded to

a resolution which is closer to the one of the radar range gate (28 m). Here, model data are thus averaged to 25 m. The modelled cloud and drizzle profiles are subsequently used as input for PAMTRA in order to simulate the radar observations, which can then be compared to the measured ones. When forward simulating the radar observations with PAMTRA, distance of cloud to radar, eddy dissipation rate ϵ , horizontal wind u and vertical air motion have to be provided. Observations of u are provided by wind lidar measurements at cloud base. In order to keep the microphysical features produced by the model separated from dynamical effects, no turbulence ($\epsilon = 0$) is added to the simulation. The study presented in Chapter 6 will show that the main effect of turbulence is to reduce the values of S_k and to increase the S_w , leaving Z_e and V_d unaltered. This generally means that S_k might be overestimated by the model, while the S_w might be underestimated. Also, no vertical air motion is included in the simulations. This choice may introduce differences between simulated and observed V_d profiles caused by updrafts or downdrafts in the observations. With these assumptions, the signatures in the modelled radar Doppler moments are thus solely due to microphysical changes in the cloud and drizzle DSDs.

Observed and simulated moment profiles are then compared and also information on drizzle effective radius is inferred from V_d . Positive (downward) values of mean Doppler velocity can be interpreted as the falling velocity of the droplets and thus drizzle size can be derived through the droplet radius- V_t relation, provided by the approximated expressions of Eq. 2.3. In the following, all the different parts of the methodology explained here are described in detail.

5.2 OBSERVATIONS FROM TWO CASE STUDIES

An observed boundary layer cloud developing drizzle on the 31 July 2013, (from 9.2 UTC to 10.0 UTC), has been selected to compare model output and observations. The evolution in time of the Z_e field between cloud base and cloud top is shown in Fig. 5.1 for the two case studies at 9.5 and 9.8 UTC (red boxes in the figure). In the time interval between 9.5 UTC and 9.8 UTC the cloud geometrical thickness and LWP increase. LWP values range from 100 gm^{-2} at 9.5 UTC to 215 gm^{-2} at 9.8 UTC, while geometrical thickness varies correspondingly from 410 m to 585 m. Also, in the time window between 9.55 UTC and 9.6 UTC Z_e increases with height from cloud base to cloud top, while between 9.75 to 9.8 UTC the highest values of Z_e occur at approximately 200 m below cloud top, in agreement with the typical behaviors shown by the statistics in section 4.3.2. The differences in LWP, geometrical thickness and Z_e between the two selected 3-minute time series suggest a change of the cloud DSD as a function of height. In order to understand if the observed features actually indicate some drizzle for-

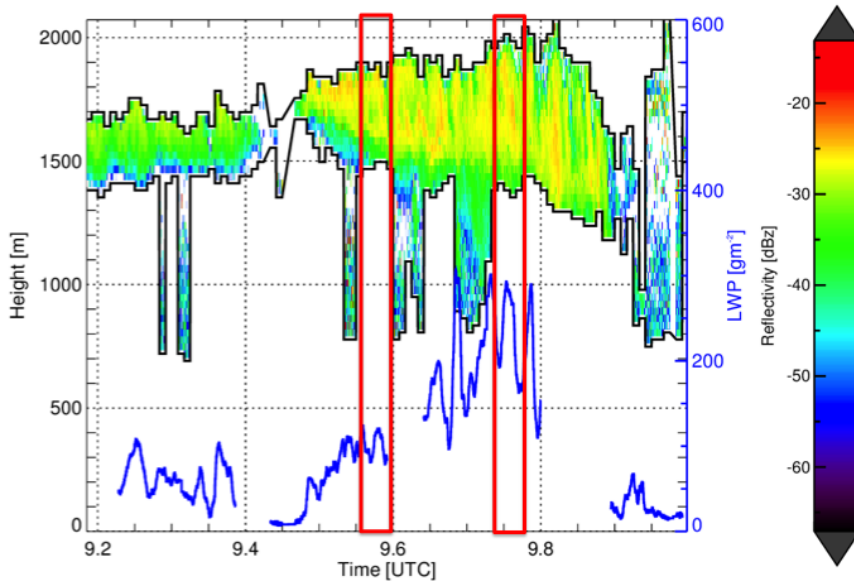


Figure 5.1: Time height plot of Z_e on the 31 July 2013, from 9.2 UTC to 10.0 UTC. Cloud base and cloud top height are indicated by the black lines. Also, the time series of LWP is shown in blue. The red boxes indicate the two selected case studies, at 9.5 and 9.8 UTC.

mation, a skewness mask has been applied to the S_k field. The mask selects all radar bins within the cloud having a skewness value larger than 0.3 and at least 3 contiguous radar bins with $S_k > 0.3$. The value of 0.3 is chosen as a threshold based on the estimation of the S_k uncertainty which has approximately the same values. The S_k uncertainty will be extensively discussed in Chapter 6.4.1. When positive skewness is caused by noise, such pixels are randomly distributed and the mask filters them out. When the mask is applied to the case study, coherent structures of contiguous pixels can be observed between 9.5 and 9.8 UTC (Fig. 5.2).

On the basis of these findings, the two 3-minute time series of measurements between 9.55 and 9.6 UTC and 9.75 and 9.8 UTC respectively (see red boxes in Fig. 5.2), have been chosen for the model comparison. These two cases represent two different stages of drizzle development. The interval between 9.55 and 9.6 UTC represents an early drizzle onset situation. It is characterized by a Z_e profile increasing with height and a moderate increase of S_k close to cloud base. Skewness only shows positive values up to 0.5. The interval between 9.75 and 9.8 UTC is a situation of mature drizzle development. It shows a nearly constant profile of Z_e and a stronger increase of S_k towards cloud base compared to the previous case. S_k also turns negative (-0.3) in the region close to cloud base. Also, the mean LWP value between 9.55 and 9.6 UTC (101 gm^{-2}) is almost half of the value between 9.75 and 9.8 UTC (215 gm^{-2}). The mean Doppler velocity

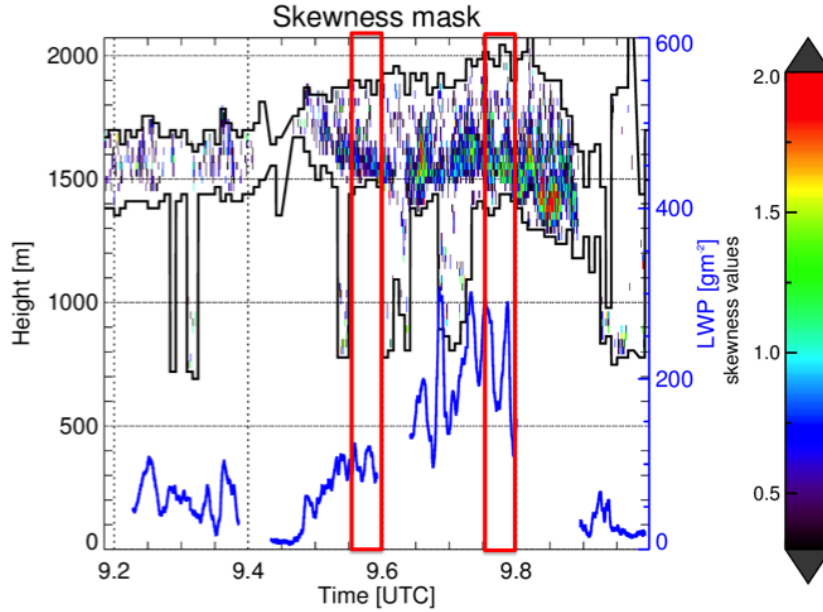


Figure 5.2: Same as in Fig. 5.1, only for the skewness mask.

field (Fig. 5.3) shows that updrafts are present in the upper part of the cloud for the drizzle mature case study.

A LWC profile from the observations has been calculated for the early drizzle onset case study, where the amount of drizzle present is assumed to be very low. The methodology applied is from Frisch et al. (1998), based on the radar reflectivity profile and the LWP measurement from the microwave radiometer. The observed LWC profile shape is used to select the modeled LWC profile shape that best matches the observations.

5.3 DESCRIPTION OF THE MODEL

The 1D steady-state spectrally resolved microphysical model describes the vertical evolution of the drizzle drop size distribution (DSD). The model simulates the equilibrium drizzle DSD profile which is consistent with the prescribed cloud environment. The model output used in this thesis has been provided by Dr. Wanda Szyrmer working at the McGill University of Montreal (Canada). The description of the model is based on personal communication with the author.

The model used in this study is based on a steady-state approach. In such an approach, partial time derivatives of every variable are set to zero. In general, in a 1D model, the total time derivative of a variable f which is dependent on the time and the spatial dimension h is:

$$\frac{df(h, t)}{dt} = \frac{\partial f(h, t)}{\partial t} + w \cdot \frac{\partial f(h, t)}{\partial h}. \quad (5.1)$$

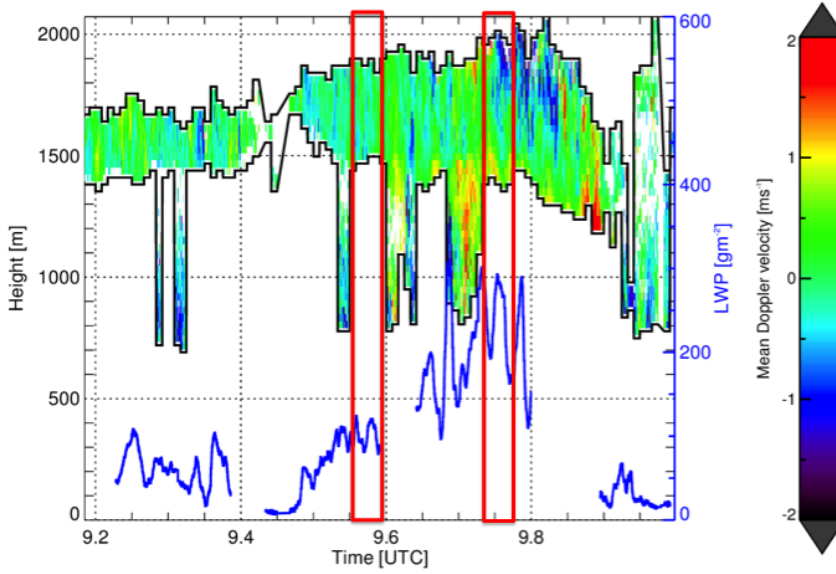


Figure 5.3: Same as in Fig. 5.1, only for the V_d .

Setting the partial time derivative equal to zero ($\frac{\partial f(h,t)}{\partial t} = 0$) in order to get steady-state solution gives:

$$\frac{df(h,t)}{dt} = w \cdot \frac{\partial f(h,t)}{\partial h}. \quad (5.2)$$

In this way, height instead of time becomes the independent variable in the model. Time steps are replaced by height steps, corresponding to the model vertical resolution and the resulting height dependent equations are solved by the model.

The choice of the vertical resolution for the model is connected with the way the autoconversion schemes work. Autoconversion schemes in this model treat the injected drizzle drops as monodispersed: they assume the formation of a given number of embryonic drizzle drops with the same size given by the threshold sizes. For the model runs considered in this study, such threshold is $60 \mu\text{m}$ and $80 \mu\text{m}$. When low vertical resolutions are adopted, i.e. 5 or 10 m, drizzle cannot be assumed to be monodispersed. Droplets have long resilience time in the layer because their fall speeds w are very small, and thus drizzle droplets grow via accretion to different sizes, generating a distribution which is not monodispersed. In this case, the simulation results would depend on the assumption about the assumed injected drizzle DSD when prescribed autoconversion parameterizations are used. With a high vertical resolution like the one adopted that is 50 cm, the assumption that drizzle drops injected have the same size is valid. They can therefore be treated as monodispersed by the autoconversion scheme. Since in this study the aim is to evaluate the impact of the

autoconversion schemes without taking into account the influence of the assumed DSD of the injected drizzle, high vertical resolution, and hence monodispersity for drizzle, is chosen. Figure 5.4 graphically shows the working principle of the model.

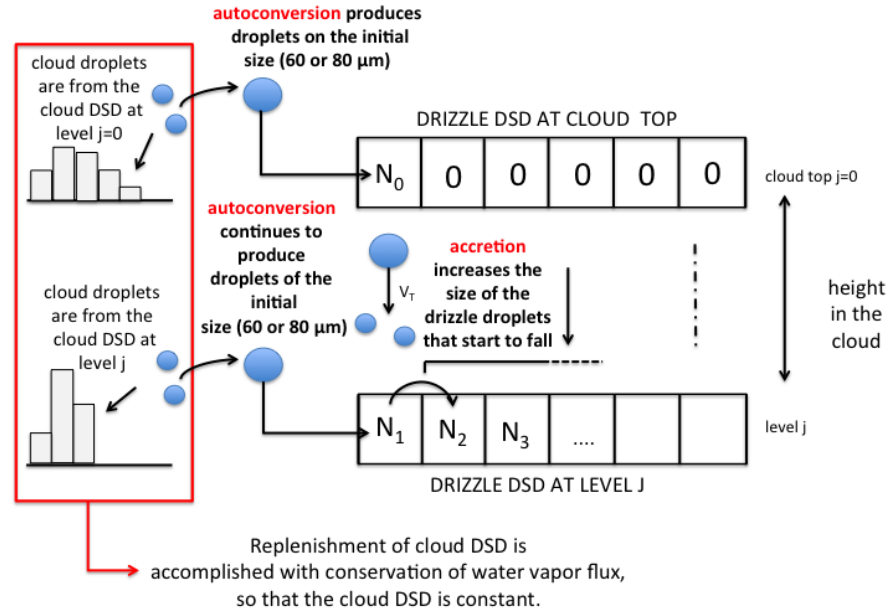


Figure 5.4: Scheme representing the working principle of the steady state bin microphysical model employed in this study. (Personal communication with Dr. W.Szyrmer)

The model is based on the assumption of horizontally uniform and steady-state conditions, which implies a balance between the removal of cloud droplets through embryonic drizzle formation and the rate of cloud droplets replenishment. In steady-state conditions, conservation is imposed to the water vapor flux. This assumption guarantees that droplet replenishment equals the removal of water by drizzle (due to autoconversion and accretion) and by condensation on drizzle.

As model input, vertical profiles of pressure, temperature (assumed to be pseudoadiabatic), relative humidity and vertical air motion are needed. Cloud top is coincident with the model top. For a given cloud thickness, the liquid water content (LWC) profile is calculated within the model as the product of an adiabatic LWC profile and a weighting function for the departure from the adiabatic configuration. Two LWC profiles are employed with LWC maxima at normalized height of -0.1 and -0.25 respectively. They are shown together with the profile derived from the observations, in Fig. 5.5(a).

For every layer, a cloud DSD is given by a lognormal function using a size bin representation. The parameters of the cloud DSD are derived from constraints on LWC, cloud number concentration (N) and relative dispersion parameter. Different configurations for N and LWC profiles are applied. Number concentrations (N) of 50, 100, 200, 400,

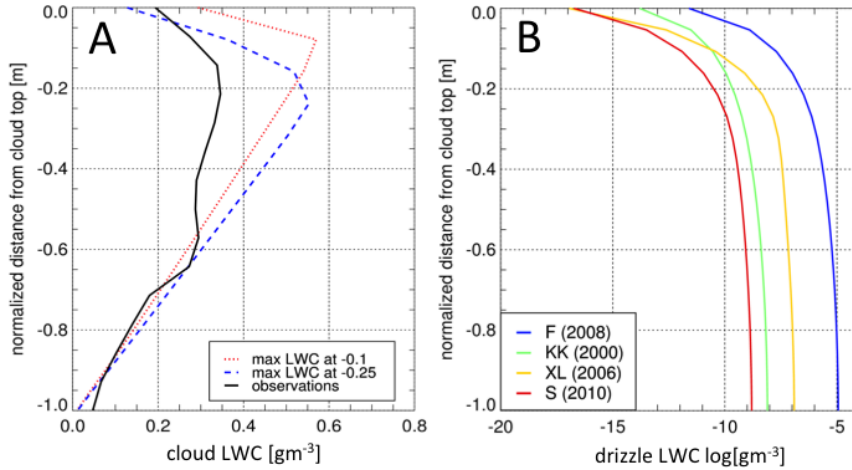


Figure 5.5: (a) LWC profiles as a function of the distance from cloud top for the observation of the early drizzle onset case study on the 31 July 2013 at 9.5 UTC with $\text{LWP}=101 \text{ gm}^{-2}$ (black). For the model, 2 different LWC profile shapes with $\text{LWP}= 100 \text{ gm}^2$, and maximum at -0.1 from cloud top (red) and at -0.25 from cloud top (blue) are assumed. For the observations, the LWC has been derived by applying the methodology of Frisch et al. (1998). (b) Drizzle LWC as a function of the normalized distance from cloud top for the mature drizzle case study on the 31 July 2013 at 9.8 UTC with $\text{LWP}= 200 \text{ gm}^2$. Different colors correspond to the different autoconversion schemes: Franklin et al. (2005) (blue), Khairoutdinov and Kogan (2000) (green), Xie and Liu (2009) (yellow), Seifert et al. (2010) (red).

750 and 1000 cm^{-3} are available in the model output. Three different cloud thicknesses of 330 m , 400 m and 480 m are simulated, with corresponding LWP values of 100 gm^{-2} , 150 gm^{-2} , and 200 gm^{-2} . The cloud DSD at each level is an input, and does not change. In the model, the only process of drizzle drops initiation is autoconversion: at each cloud layer (top layer or any in-cloud layer), the autoconversion rate is calculated. The 5 different autoconversion schemes available from the model are Franklin (2008), Khairoutdinov and Kogan (2000), Xie and Liu (2009), Tripoli and Cotton (1980) and Seifert et al. (2010). However, the scheme from Tripoli and Cotton (1980) is not shown in the following because it does not produce drizzle in the combination of parameters that results in best matching the observations. This depends on the threshold value for the activation of the parametrization ($r = 13 \mu\text{m}$ (see section 2.2)). In the majority of schemes, the autoconversion rate, that is a function of local cloud parameters like LWC, N or the cloud DSD width, represents the mass that has to be transferred from cloud to drizzle. Then, for the selected initial drizzle size, the number concentration of injected drizzle drops is computed, and a new drizzle bin is formed having the mean size of initial drizzle. Two initial sizes of 60 and $80 \mu\text{m}$ are used in this work. Drizzle droplets generated in this way then fall at their terminal velocity (V_t) calculated using the formulation from Beard (1976) and grow by accretion of cloud droplets.

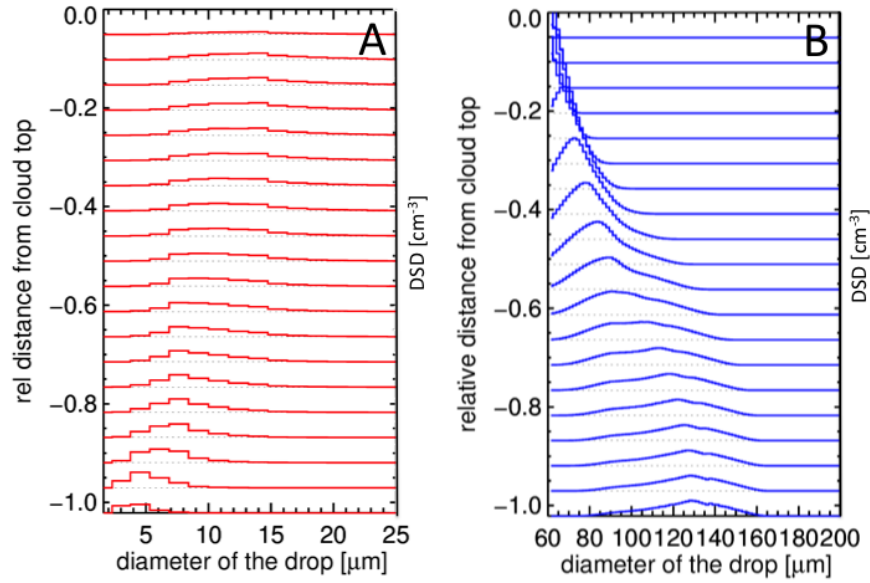


Figure 5.6: (a) Cloud drop size distribution for $N = 1000$, LWC profile with maximum at -0.25 relative distance from cloud base, and $LWP = 200 \text{ gm}^{-2}$. (b) Drizzle drop size distribution obtained with the Xie and Liu (2009) autoconversion parametrization as a function of relative distance from cloud top.

In the model, the growth by accretion is then accounted for by integrating the stochastic collection equation (SCE) that represents the probability of collection including the whole cloud DSD with the collection kernel. The collection kernel is the one derived by Long (1974) and used in many studies, e.g. Kollias et al. (2011a). The evolution of drizzle in each layer is computed by only taking into account the adjacent layers. In fact, the vertical evolution of each bin of drizzle in the layer is calculated separately taking into account its growth by accretion and condensation between two consecutive layers and fall velocity (eventually also air motion). The model computes the number concentration of each bin from the number concentration at the concentration of the layer above. For each drizzle bin (except the new generated) the continuity relation holds between two levels, taking into account the increase of mass and the fall velocity. The model does not simulate any dynamical effect, i.e. turbulence and horizontal advection. Furthermore, no feedbacks of the microphysical processes are included, i.e. drizzle self-collection. However, since the concentration of drizzle is rather low, the probability for self-collection is rather small. Two examples of cloud and drizzle DSD are shown in Fig. 5.6. While the cloud droplet DSD vertical profile is constant (Fig. 5.6(a)), the drizzle DSD (Fig. 5.6(b)) evolves from cloud top to cloud bottom. At cloud top, only the injected drizzle is visible, due to the autoconversion process, while going to cloud base the drizzle DSD evolves and becomes wider, because of the accretion process.

Figure 5.7 shows the autoconversion and accretion rates for one selected model output. The parametrization of the accretion rate is the same for all the autoconversion schemes used in the model. However, differences in the accretion rates for different autoconversion schemes are evident. They are due to the fact that the accretion rate depends not only on the cloud characteristics but also on the collector drizzle drops, which are different at each level for different autoconversion schemes.

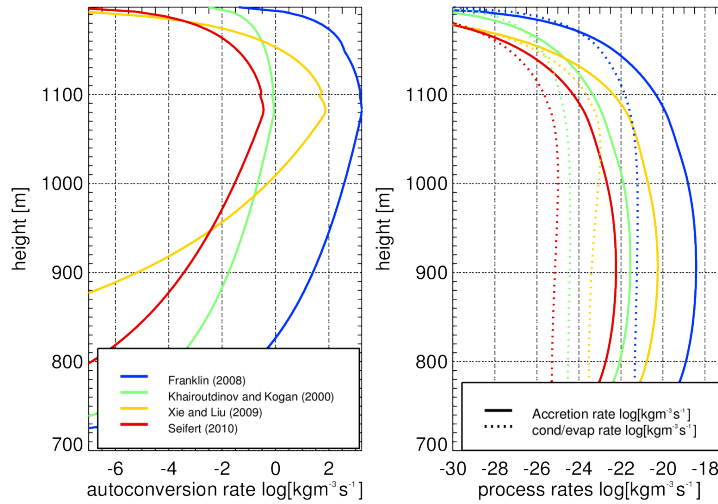


Figure 5.7: Example of autoconversion rates profiles (left) and accretion rates profiles (right) for the different schemes. The simulation shown here is for $N = 1000\text{cm}^{-3}$, LWC profile with maximum at normalized height of -0.1 and LWP of 200gm^{-2} .

5.4 CONFRONTING MODEL AND OBSERVATIONS

The goal of this chapter is to provide a microphysical interpretation of the observed radar moments profiles by means of a model. The comparison of simulated vs observed radar moments profiles can give indications on the microphysical characteristics, i.e drizzle mean size, of the drizzle droplets generating the observed signatures in Z_e , V_d , S_w and S_k . In order to perform a reasonable comparison, the most realistic cloud settings have to be selected. Even if some cloud properties can be selected to match the observed ones, i.e. the LWP, for variables like N , the LWC profile shape or the initial drizzle size, the true cloud properties are not known. In order to select the most suited model runs for the comparison of the radar Doppler moments profiles, Z_e profiles for different N , LWC profiles shapes and initial drizzle size are calculated. For the model simulations with large discrepancies in

Z_e , no valuable information can be extracted from V_d , S_w and S_k (see equations in Chapter 2.3.2).

Once the combination of N , LWP, LWC profiles shapes and initial drizzle diameter that best fit the observed Z_e profiles in the two cases of early and mature drizzle development are identified, observed and simulated profiles of Z_e , V_d , S_w and S_k are compared for the different autoconversion schemes.

Simulated Z_e profiles for different model parameters

Since Z_e is proportional to N , the impact of N is at first analyzed. The mean profile of Z_e collected during the early drizzle onset case is compared to the simulated Z_e profiles obtained from model outputs having an initial drizzle size of $60\ \mu\text{m}$, a LWC profile shape with maximum at -0.25 relative height from cloud top and a LWP of $100\ \text{gm}^{-2}$ (Fig. 5.8). Each simulated profile corresponds to a different autoconversion parametrization. By increasing N from $400\ \text{cm}^{-3}$ (Fig. 5.8(a)) to $750\ \text{cm}^{-3}$ (Fig. 5.8(b)) and $1000\ \text{cm}^{-3}$ (Fig. 5.8(c)), the simulated profiles get closer and closer to the observed profile, reaching an almost perfect matching for most of the schemes with N equal to $1000\ \text{cm}^{-3}$. The autoconversion schemes which result in a Z_e profile closest to the observations are Seifert et al. (2010), Xie and Liu (2009) and Khairoutdinov and Kogan (2000).

Once selected $N = 1000\ \text{cm}^{-3}$, the sensitivity with respect to the LWC profile is tested. Figure 5.9 shows the reflectivity profiles for model outputs based on two different LWC profiles having LWC maxima at -0.1 and -0.25 relative distance from cloud top, respectively. The model simulations are done for an initial drizzle diameter of $60\ \mu\text{m}$, LWP = $100\ \text{gm}^{-2}$ and $N = 1000\ \text{cm}^{-3}$. For both LWC profiles, the agreement between simulations and observations is good. However, Z_e profiles derived using the LWC profile having a maximum at -0.25 relative distance from cloud top (Fig. 5.9(b)) are closer to the observations (black line) compared to those obtained from the LWC profile having maximum at -0.1 relative distance from cloud top (Fig. 5.9(a)). This is particularly evident between cloud top and -0.2 relative distance from cloud top, and also for distances between -0.5 and -0.8 . For this reason, the LWC profile having a maximum at -0.25 is chosen for the subsequent analysis.

Finally, a test for the initial drizzle size has been performed. Drizzle development through accretion is affected by the size of the initial drizzle drop formed via autoconversion. Since the main impact is expected on the drizzle DSD, the simulated Z_e profiles are compared to the observed one for the case of mature drizzle development, where more drizzle presence is expected in the entire observed cloudy column. Figure 5.10 shows the Z_e profiles for initial drizzle diameter of $60\ \mu\text{m}$ (Fig. 5.10(a)) and $80\ \mu\text{m}$ (Fig. 5.10(b)). The other settings for the

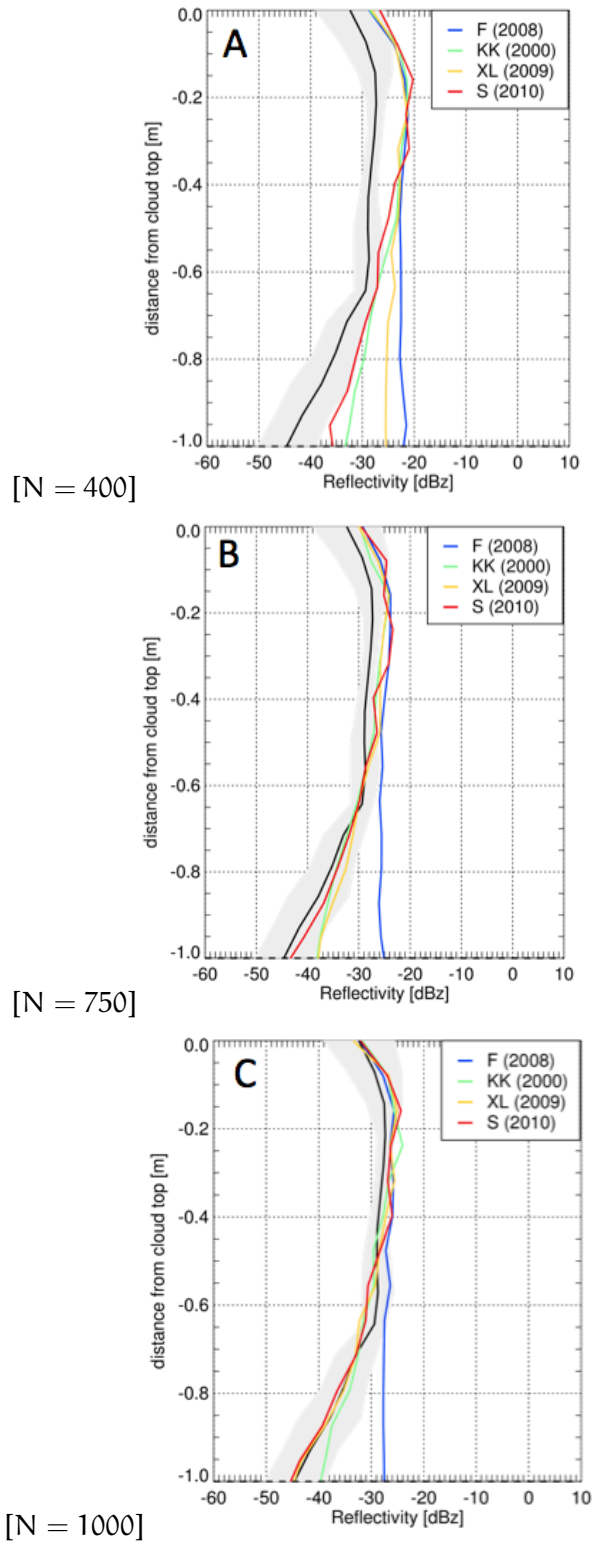


Figure 5.8: Comparison of observed (black) mean Z_e profile for the early drizzle onset case with Z_e simulated profiles based on model data using $N = 400$ (a), $N = 750$ (b) and $N = 1000$ (c) cm^{-3} total number concentrations. Grey area represents the uncertainty of the observations. Further model settings are: initial drizzle diameter of $60 \mu\text{m}$, LWC profile with maximum at -0.25 relative distance from cloud top and $\text{LWP} = 100 \text{ gm}^{-2}$. Different colors correspond to the different autoconversion schemes: Franklin et al. (2005) (blue), Khairoutdinov and Kogan (2000) (green), Xie and Liu (2009) (yellow), Seifert et al. (2010) (red).

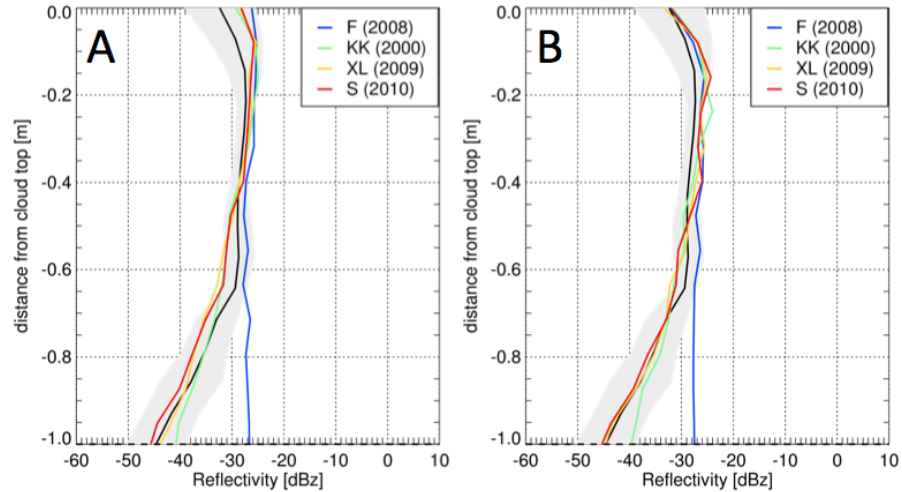


Figure 5.9: Comparison of observed (black) mean Z_e profile for the early drizzle onset case with Z_e simulated profiles derived using LWC profile having maximum at -0.1 relative distance from cloud top (a) and -0.25 relative distance from cloud top (b). Grey area represents the uncertainty on the observations. Other settings for the model output are the same for the three profiles: initial drizzle diameter of $60\mu\text{m}$, $\text{LWP} = 100\text{gm}^{-2}$ and $N = 1000\text{cm}^{-3}$.

model in this case are: $\text{LWP} = 200\text{gm}^{-2}$, LWC profile shape with maximum at -0.25 relative distance from cloud top and $N = 1000\text{cm}^{-3}$. In this case the behavior of the simulated Z_e profiles depends on the chosen autoconversion scheme. The Z_e simulated profile obtained using the autoconversion parametrization from Seifert et al. (2010) in both cases is very close to the observed one in the lower part of the cloud (Fig. 5.10(a) and 5.10(b)). The autoconversion schemes from Xie and Liu (2009) and Franklin (2008) are far away from the observations close to cloud bottom. The scheme from Khairoutdinov and Kogan (2000) performs better for initial drizzle diameter of $60\mu\text{m}$. When using initial drizzle diameter of $60\mu\text{m}$, at least two parametrizations (Khairoutdinov and Kogan, 2000; Seifert et al., 2010) appear to follow the observed profile better than in the case of drizzle initial diameter of $80\mu\text{m}$, thus $60\mu\text{m}$ is chosen as drizzle diameter for the following analysis.

To summarize, the most appropriate model settings for the two early onset and drizzle mature case studies are $N = 1000\text{cm}^{-3}$, LWC profile with maximum at -0.25 relative distance from cloud top, drizzle initialing diameter of $60\mu\text{m}$ and $\text{LWP} = 100$ and 200gm^{-2} , respectively.

Comparison of radar moments profiles

In this section, observed mean profiles or radar moments are compared with the simulated ones based on the model simulations as described in the previous section. Figures 5.11, 5.12, and 5.13 show profiles of V_d , S_w and S_k for both datasets and case studies. The Z_e

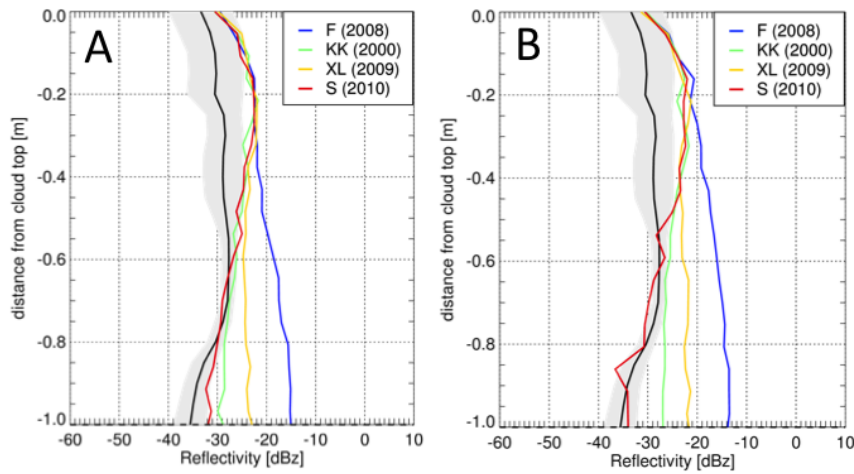


Figure 5.10: Comparison of observed (black) mean Z_e profile for the mature drizzle development case with Z_e simulated profiles derived initial drizzle size of $60 \mu\text{m}$ (a) and $80 \mu\text{m}$ (b). Grey area represents the uncertainty on the observations. Other settings for the model output are the same for the three profiles: LWC profile with maximum at -0.25 relative distance from cloud top, $\text{LWP} = 200 \text{gm}^{-2}$ and $N = 1000 \text{cm}^{-3}$.

profile for the early drizzle onset case study are given in Fig. 5.9(b), while those for the mature drizzle case study are given in Fig. 5.10(a).

As seen already in Fig. 5.9, in the early drizzle onset case all parametrizations except Franklin (2008) describe the increase of Z_e with height in agreement with the observations (Fig. 5.9(b)). The profiles lie within the uncertainty given by the standard deviation of the observed Z_e profiles. All parametrizations are also able to describe correctly the small decrease in Z_e occurring at cloud top. Probably, the good matching obtained in this case is due to the fact that the limited amount of liquid water available ($\text{LWP} = 100 \text{gm}^{-2}$) does not allow the growth of large drizzle drops.

Generally, the simulations for the early drizzle onset case with $\text{LWP} = 100 \text{gm}^{-2}$ (Fig. 5.9(b)) perform better than the mature case (Fig. 5.10(a)). In the mature drizzle development, the larger vertical extension of the cloud and the larger amount of cloud water induce a fast generation of drizzle close to cloud top in all schemes, which is not observed in the measurements. In fact, for heights between cloud top and -0.5 , all simulated profiles overestimate the reflectivity by up to a maximum of 10 dB. Since it is common to all the different parametrizations, this bias can be more probably related to uncertainties in the LWC profiles assumptions. Fig 5.5 shows the LWC profiles available in the model and the one derived from the cloudy column

at 9.6 UTC. A good agreement is visible only in the region of the cloud closer to cloud base, while in the upper part LWC is overestimated compared to the observations of approximately 50%. Since the overestimation is happening already in the early drizzle onset case and LWC can evolve rapidly, it is plausible that the LWC profile at 9.8 UTC is different from the assumed one. In the lower part of the cloud between -0.6 and cloud base, strong differences in the Z_e profiles indicate that the drizzle drops, which have been developed by all schemes around -0.2 relative distance from cloud top, evolve in completely different ways depending on the selected autoconversion scheme. An overestimation of Z_e occurs in the higher part of the cloud implying that the modeled drop size distributions are not correct. The overestimation of Z_e propagates from cloud top to cloud base and thus the comparison of the Z_e profiles in the lower part of the cloud can only be performed qualitatively.

In the schemes of Seifert et al. (2010) and Khairoutdinov and Kogan (2000), Z_e decreases from -0.2 relative height to cloud base. Both schemes are relatively close to the observed profile between -0.5 and -0.8 while between -0.8 relative height and cloud base, both tend to overestimate Z_e with respect to the observations.

The schemes of Xie and Liu (2009) and Franklin (2008) largely overestimate Z_e between the relative height of -0.2 and cloud base. In these schemes, too large autoconversion and accretion rates grow the drizzle generated at -0.2 relative height to larger sizes towards cloud base (see Fig 5.7). This is also evident in the drizzle LWC, which is the largest for these two schemes (see Fig. 5.5(b)).

Figure 5.11 compares the profiles of simulated and observed mean Doppler velocities for the two cases. In the early drizzle onset case, the observed profile is almost constant with height except in the region between -0.8 and cloud base, where it increases from 0 to 0.2 ms^{-1} . This slight increase is captured only by the parametrizations of Xie and Liu (2009), Seifert et al. (2010) and Khairoutdinov and Kogan (2000). Larger V_d values identify the presence of larger drops which start to fall towards the radar ($V_d > 0$). However, no increase of Z_e at that height is observed. This increase of V_d can partially be due to the reduction of the number of small droplets with zero mean velocity because of evaporation and collection. The V_d increase is partially correlated with the shape of the skewness profile, as will be discussed later.

In the mature drizzle case of Fig. 5.11(b), the observed profile is affected by an updraft, as can also be seen in Fig. 5.3 for the second time interval selected, and cannot thus be exploited for the comparison. The simulated V_d profiles increase from cloud top to cloud base. This increase in V_d can be related to the increase of the size of the drizzle drops which is described by the relation linking the terminal velocity of the drop to its size. Considering the increase of V_d as an in-

dication of where in the profile the drizzle drops with non-negligible fall speed are formed, different schemes produce such drops at different heights: Seifert et al. (2010) at cloud base, while Khairoutdinov and Kogan (2000), Xie and Liu (2009) and Franklin (2008) show values of V_d larger than 0.3 at higher levels in the cloud (see Fig. 5.11(b)). Between -0.8 and cloud base, the observed V_d is strongly increasing, indicating that drops are falling out of the cloud. The observed value at cloud base is 0.7 ms^{-1} , larger than the simulated ones around 0.5 ms^{-1} . Interpreting V_d as a proxy for the terminal velocity of the drops, observations seem thus to suggest that drizzle sizes produced at the base of the cloud are larger than the one obtained in the simulations. However, V_d can be biased by vertical air motions and beam filling issues, which are not considered in the simulations.

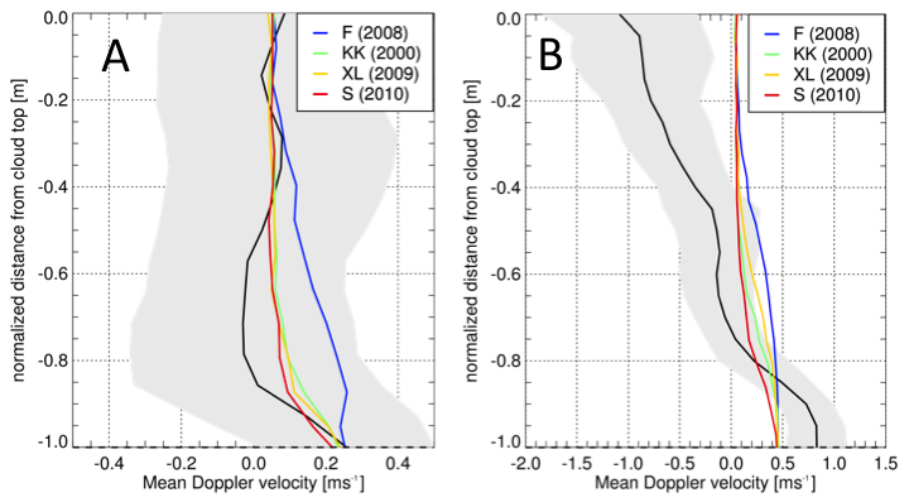


Figure 5.11: Comparison of mean observed and simulated V_d profiles. Simulations are run using $N = 1000 \text{ cm}^{-3}$, LWC profile with maximum at normalized height of -0.25 and initial drizzle size at cloud top of $60 \mu\text{m}$. LWP of 100 gm^{-2} and 200 gm^{-2} have been used to reproduce observed conditions for the first (panel A) and the second interval of time (panel B), respectively. Different colors for the simulated profiles correspond to different autoconversion schemes: Seifert et al. (2010) (red), Xie and Liu (2009) (yellow), Franklin (2008) (blue) and Khairoutdinov and Kogan (2000) (green).

Observed and simulated values of spectral width are shown in Fig. 5.12. For both cases, observed values are much larger than the simulated ones. This is expected because observed S_w profiles are affected by turbulence, which has been neglected in the simulations. However, the qualitative behavior of the simulated profiles can still be discussed. As for V_d , simulated S_w increases from cloud top to lower cloud layers for both case studies and all autoconversion parametrizations (Fig. 5.12(a) and (b)). This is due to the growth of larger drops inducing a bimodality in the spectrum shape. However, the maximum of the S_w values is located at different heights for different autoconversion schemes, depending on where the largest drizzle drop production occurs: for Seifert et al. (2010) it is generally close to cloud base, while

for Xie and Liu (2009), Khairoutdinov and Kogan (2000), and Franklin (2008) the height of the larger drizzle production is at higher levels in the cloud.

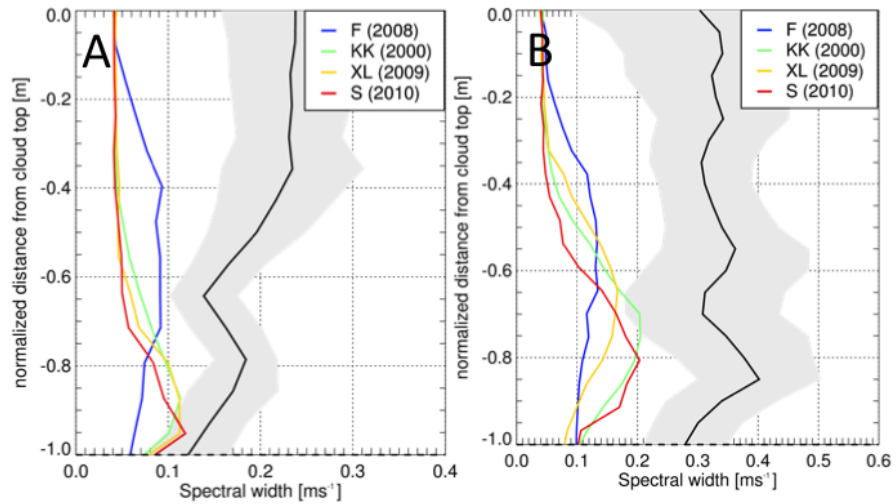


Figure 5.12: As in Fig. 5.11, only for S_w .

Finally, Fig. 5.13 shows the comparison between observed and simulated skewness profiles. Here, large differences are found in the absolute values of S_k compared to the observed ones, and also profiles of different schemes are very different among each other. For the early drizzle onset case (Fig. 5.13(a)), observations show a slight increase of skewness up to 0.5 between -0.6 relative distance from cloud top and cloud base, while $S_k = 0$ in the rest of the profile. In the mature drizzle case, the skewness observed profile reaches its maximum between -0.6 and -0.8 relative height and turns to negative values at cloud base. The simulated S_k values are generally larger than the observed ones for both case studies because the simulations are performed without turbulence, which generally reduces the S_k values, as will be shown extensively in Chapter 6. The qualitative shape of S_k profiles is highly dependent on the way each parametrization develops drizzle. In the simulations for the early drizzle onset case (Fig. 5.13(a)), only three schemes (Xie and Liu, 2009; Seifert et al., 2010; Khairoutdinov and Kogan, 2000) show a qualitative increase of S_k in the lower half of the cloud. The height at which the maximum S_k is found corresponds to where the observations show the maximum for the scheme of (Seifert et al., 2010), while Xie and Liu (2009) and Khairoutdinov and Kogan (2000) present the maximum at -0.7 relative distance from cloud top. The skewness profile of the autoconversion scheme from Franklin (2008) shows a transition of S_k values from positive (0.8) at -0.4 relative distance from cloud top to negative values (-0.8) at -0.8 relative distance from cloud base. This transition indicates that the scheme is producing drizzle in the upper part of the cloud, which then increases in size while falling to cloud base. In

agreement with what was previously shown for the other moments, the drizzle production in this scheme appears to be too fast and not sensitive to the amount of liquid water available.

For the drizzle mature simulation, the scheme of Franklin (2008) shows the same qualitative behavior as for the early drizzle onset case, implying a low sensitivity to the amount of liquid water present in the column. The schemes of Xie and Liu (2009); Seifert et al. (2010) and Khairoutdinov and Kogan (2000) instead show different profiles compared to the case of early drizzle onset. With more liquid water present in the cloudy column, these parametrizations show profiles of S_k with maxima closer to cloud top at -0.5 , -0.45 and -0.4 for Seifert et al. (2010), Khairoutdinov and Kogan (2000), and Xie and Liu (2009), respectively. The larger amount of liquid water available facilitates the generation of drizzle drops, which occurs at a higher level in the cloud compared to the simulated profiles of the early drizzle onset case (Fig. 5.9(b)). This is confirmed by the increase of simulated Z_e observed in Fig. 5.10(a). Drizzle drops then grow while falling through the cloud and in this case their size close to cloud base is large enough to turn the S_k to negative values of -1.0 for the scheme by Seifert et al. (2010), and -1.5 for the scheme by Khairoutdinov and Kogan (2000) and Xie and Liu (2009). The transition to negative skewness values is also in agreement with the observed profile, showing at cloud base $S_k = -0.2$. Even if observed S_k values are much smaller than the simulated ones, the qualitative behavior is similar. Compared to the early drizzle onset case, the growth of larger drizzle drops is also facilitated due to the larger cloud thickness (480 m compared to 400 m). Therefore, the drizzle droplets have more chances for collisions.

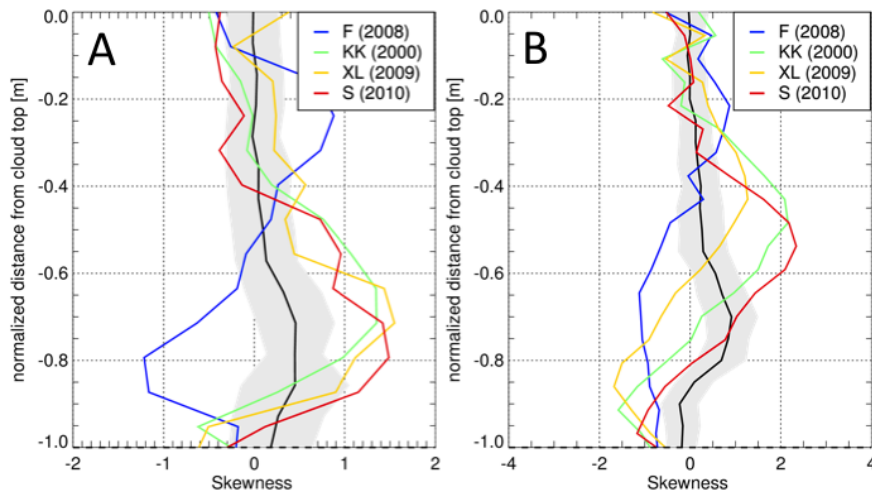


Figure 5.13: As in Fig. 5.11, only for S_k .

From the comparison of simulated and observed profiles of radar Doppler moments, some conclusions on the performances of different autoconversion schemes can be drawn. The scheme that best performs

in this comparison is the autoconversion scheme of [Seifert et al. \(2010\)](#), with a close agreement of Z_e profiles and a qualitatively correct reproduction of the S_k features. Moreover, the scheme is able to capture also some characteristics of the V_d profile. The schemes from [Khairoutdinov and Kogan \(2000\)](#) and [Xie and Liu \(2009\)](#) also catch the skewness observed features but show larger biases in Z_e close to cloud base, indicating that too big or too many drizzle droplets are produced. The scheme from [Franklin \(2008\)](#) appears to be independent of the LWP and the cloud thickness of the cloud and it produces drizzle too easily and too fast compared to the observations. However, all schemes show S_k maxima at too high cloud heights compared to the observations. This discrepancy is to be expected for continental clouds with large number concentrations: for larger N and thus smaller cloud effective radii compared to maritime case, drizzle drops need more collisions. Hence, they need to travel a longer distance in the cloud to grow to a size that is able to perturb the shape of the radar Doppler spectrum. This is why the peak of the S_k is at lower heights in the observations.

Also, in the simulations the Z_e maximum is located above the S_k maximum. This seems in contrast to what shown in the statistics presented in [Figs. 4.12 and 4.15](#) for the cloud columns identified by LWP around 200 gm^2 .

For both case studies, the agreement between model and observations is reasonable: the model is able to catch the features of the reflectivity within the uncertainty given by the observations for the LWP case of 100 gm^{-2} for most of the parametrization schemes. Also in the 200 gm^{-2} case, the agreement is good even if some biases are present, probably due to the assumptions on the LWC profile. Even if V_d and S_w cannot be compared to the observed profiles because of the impact of turbulence and vertical air motion, the skewness profiles can provide important information on the performances of the different autoconversion schemes. In fact, the biggest differences among different autoconversion schemes are found in the skewness profiles. This indicates that this parameter can be used as an indirect constraint to improve the schemes. In the present case study, it has been found that the [Seifert et al. \(2010\)](#) autoconversion scheme performs best. The comparison can be improved in future by running a statistical ensemble of simulations for realistic air motion and turbulent conditions, and compare then the mean profile of the moments with the observations. This should reduce the noise in the skewness estimation, especially evident (see [Fig. 5.13](#)) for skewness values close to zero. Also, more realistic V_d and S_w values are then expected.

5.5 INTERPRETATION OF SKEWNESS IN TERMS OF DRIZZLE DROPLET SIZE

This section focuses on deriving the size of the drizzle droplets generating the signature in the observed skewness. Figure 5.14 shows the observed mean Doppler velocity as a function of the observed skewness for the case study of mature drizzle development. Values smaller than 0 ms^{-1} for V_d , which occur within 400 m from cloud top, are associated with $S_k \geq 0$. In this region, droplets are so small that they can be considered as air tracers. The presence of slightly positive skewness values indicates that the updraft ($V_d < 0$) can foster the droplet growth. Also, the maximum of the skewness occurs for values of mean Doppler velocity equal to zero, at approximately 400 m below cloud top. In the lower part of the cloud, V_d increases while S_k decreases. Maximum values of V_d occur at cloud base where skewness is negative. These values indicate that drizzle is falling out of the cloud.

The relation between V_d and S_k can be exploited together with the relation between the terminal velocity of a drop and its size (see Eq. 2.3 in Chapter 2.1.1), to infer information on the drizzle size. If V_d is assumed to represent of the falling velocity of a drop, then the positive values of V_d (in the dashed box in Fig. 5.14) can be used to calculate the corresponding drizzle size. In Fig. 5.15 the upper panel shows the skewness as a function of V_d for the selected points of the observed profile where $V_d > 0$. Drizzle sizes are inferred by applying Eq. 2.3.

From the observations, positive values of skewness are associated with drizzle sizes up to $40 \mu\text{m}$, while skewness becomes zero for sizes of $60 \mu\text{m}$ and turns negative for sizes between $80 \mu\text{m}$ and $100 \mu\text{m}$.

Also for model data, the same approach can be applied. The parametrization from Seifert et al. (2010) has been selected to analyze the relation between skewness and the size of the drizzle for model data. In this case, the drizzle equivalent radius to be associated with the skewness measurements can be additionally derived directly as the effective radius of the modeled drizzle DSD at the corresponding level. Note that in contrast to the observations, all mean Doppler velocity values in the model output are larger than zero (Fig. 5.11(b)).

Drizzle sizes based on the drizzle effective radius calculation provides a narrow range of sizes (Fig. 5.16(bottom)): drizzle drops have a radius of $30 \mu\text{m}$ radius at cloud top, $40 \mu\text{m}$ in the middle of the cloud, and reaches $45 \mu\text{m}$ at cloud base. Applying the fall speed-size relation (Eq. 2.3) gives different results. In the upper half of the cloud, drizzle radii vary between $20 \mu\text{m}$ and $30 \mu\text{m}$. In the lower part of the cloud (between -0.7 relative distance from cloud top and cloud base), larger radii from $30 \mu\text{m}$ to $55 \mu\text{m}$ are found. Note that there is an intermediate region of points, corresponding to relative heights between

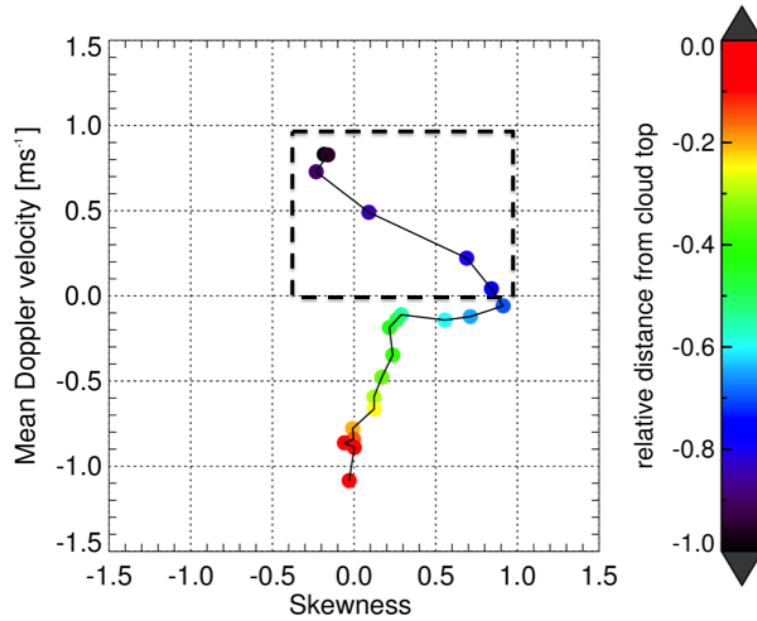


Figure 5.14: Observed mean Doppler velocity V_d as a function of skewness S_k for the mature drizzle development case study. Colors are associated with the distance of the radar bin from cloud top. The dashed box indicates the ensemble of points selected for the derivation of the drizzle equivalent size by means of the relation between V_t and radius of the droplet.

−0.6 and −0.75 which cannot be attributed to any drizzle size. This is because the size obtained using each of the two approximations exceeds the validity range for the radius for the applied equation.

Fig. 5.16 (middle and bottom) can be compared with the observed relation between skewness and drizzle equivalent radius (Fig. 5.15(top)). Since turbulence is reducing the S_k values in the observations, the comparison can only be done qualitatively. The largest values of S_k in the model simulation are associated with drizzle sizes of $40\ \mu\text{m}$ if they are estimated using the effective radius of the drizzle DSD, while they correspond to drizzle sizes of $25\ \mu\text{m}$ if they are estimated using the relation with V_t and the droplet radius. This is in partial agreement with the observations, where the largest S_k values occur for drizzle sizes between 20 and $40\ \mu\text{m}$. However, skewness turns to zero in the observations for drizzle sizes of $60\ \mu\text{m}$, while in the simulations this happens for drizzle sizes between 30 and $35\ \mu\text{m}$. Also, sizes associated to negative S_k values are larger in the observations compared to the model. This is due to the fact that the observed mean Doppler velocities are larger than the simulated ones by a factor of 2 and this induces a larger drizzle equivalent radius estimation in the observations.

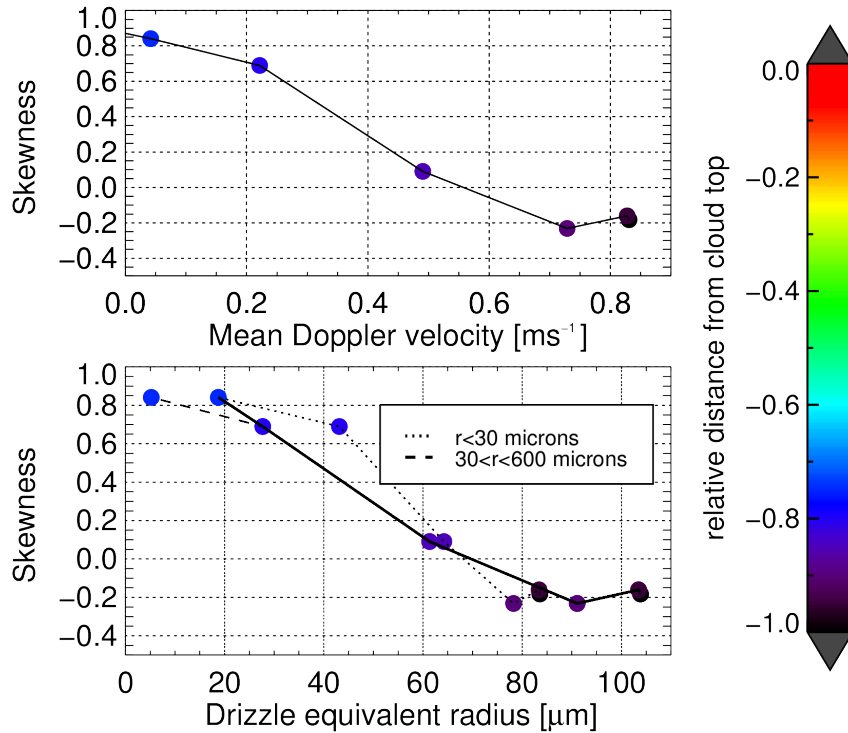


Figure 5.15: Relation between skewness and equivalent drizzle size. Top: skewness as a function of the drizzle equivalent radius calculated using the two equations for the different regimes. The solid line represents the interpolation of the two regimes based on their intervals of validity. Bottom: skewness as a function of mean Doppler velocity for the selected ensemble of observations.

5.6 CONCLUSIONS AND SUMMARY OF THE RESULTS

In this chapter a microphysical interpretation of the signatures of the radar moments, in particular of skewness, in presence of drizzle is provided. Forward simulated profiles of radar Doppler moments from a 1D steady-state binned microphysical model are compared with observed cloud radar profiles of early and mature drizzle development. Model settings are chosen to match the observed LWP during the two situations. Other model parameters are chosen in such a way that the reflectivity profile in observations and model agree best. For these optimum model settings, model simulations are performed for the 2 case studies using different autoconversion schemes. Profiles of radar moments are simulated and compared to observations. Performance of each scheme is evaluated and strengths and limitations of different parametrizations are pointed out. The parametrization from [Seifert et al. \(2010\)](#) seems to be the one that is performing best for the case studies analyzed. Differences between observed and simulated profiles are discussed. It has been hypothesized that the autoconversion rates tend to produce large drizzle too fast and too early for continental polluted clouds. Moreover, assuming that the mean Doppler velocity can be interpreted as the falling velocity of the drops, the

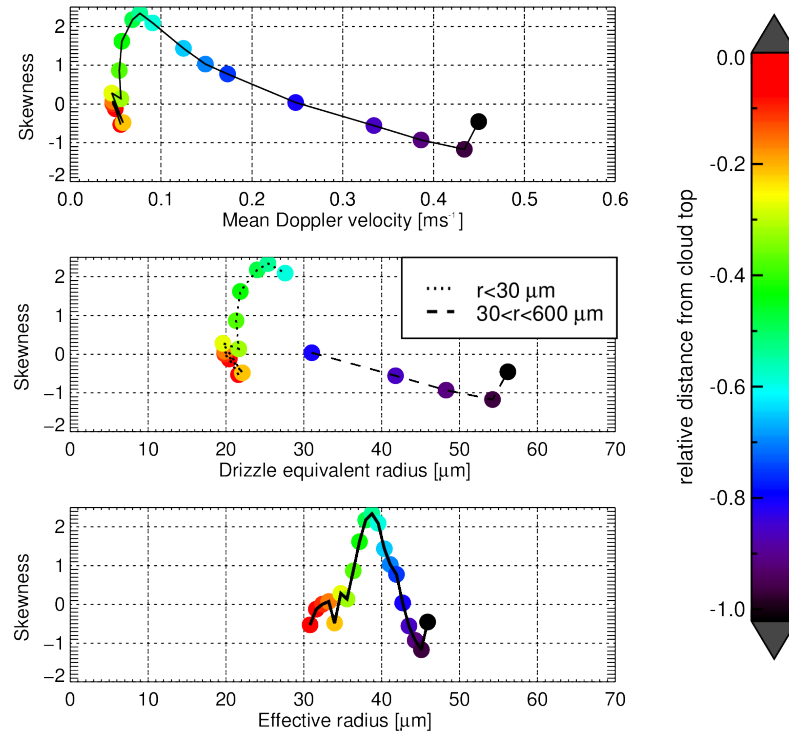


Figure 5.16: Top: skewness as a function of mean Doppler velocity for the simulated profile. Middle: skewness as a function of equivalent drizzle radius derived by using the relations between V_t and the droplet radius applied to V_d . The two different regimes of radii for the relation are indicated by different lines. Bottom: skewness as a function of drizzle equivalent radius determined as the effective radius of the drizzle DSD for every layer.

relation between falling velocity and drops size is applied to analyze the relation between S_k and the equivalent drizzle radius. Both in models and observations show that the size associated to the largest skewness values is between 20 and 40 μm .

OPTIMIZING OBSERVATIONS OF DRIZZLE ONSET WITH MM-WAVELENGTH RADARS

In this chapter the main results of the sensitivity studies conducted with IQ raw data observations to optimize radar settings for the purpose of drizzle detection are presented. This work is part of the publication "Optimizing observations of drizzle onset with millimeter-wavelength radars" which has been submitted to the journal *Atmospheric Measurements Techniques* (AMT).

Section 6.1 describes the motivation for this study. Section 6.2 presents the methodology to process the IQ raw radar data, while section 6.3 provides details on the case studies during which IQ raw data are stored. Then section 6.4 shows the results obtained by using different integration times and spectral averages for data processing. Moreover, section 6.5 shows the findings obtained by running an ensemble of simulations that is compared to the observed drizzle case study. Finally, the main results of the work are summarized in section 6.6.

6.1 MOTIVATION AND CONCEPT OF THE STUDY

Large effort has been undertaken e.g. within the US Department of Energy Atmospheric Radiation Measurement (ARM) program to ensure a high quality of radar Doppler spectra. The importance of high quality (artifact free) radar Doppler spectra collected with high spectral resolution (Kollias et al., 2007b) has often been highlighted in literature (e.g. Kollias et al., 2011a,b; Luke and Kollias, 2013). The current generation of the ARM program profiling W and Ka band cloud radars uses sampling strategies that enable the detection of microphysical signatures (Kollias et al., 2016). These strategies have been developed based on long-term experience and extensive data analysis for various cloud types. However, a systematic approach concerning the accuracy of higher moments estimates and their sensitivity to basic radar system settings such as spectral resolution, integration time, and beamwidth is still missing.

At the same time, the majority of cloud radars installed across Europe are Ka-band systems (Tab. 6.1) of the type MICrowave RADar (MIRA) manufactured by METEK GmbH (Görsdorf et al., 2015). Their number strongly increased during the last ten years almost reaching the number of Ka band radars deployed within the ARM program. Due to differences between radar systems (e.g. radar beamwidth) it is not clear whether the settings found within ARM are directly transferable to the MIRA systems. In this study, the requirements for

Location	Institution	Integration time ΔT [s]	n_{fft}	PRF [kHz]	V_N [ms^{-1}]	Comments
Chilbolton (UK)	University of Leeds	10	512	7.5	15	
Cleveland (Ohio, USA)	National Aeronautics and Space Administration (NASA)	10	256	5	10	
Galway (Ireland)	National University of Ireland (NUI)	10	256	5	10	
Hamburg (Germany)	Max Planck Institute (MPI)	10	256	5	10	
Iqaluit (Canada)	Environment Canada (EC)	1	256	5	10	
Jülich-JOYCE (Germany)	University of Cologne (IGMK)	1	256	5	10.6	
Karlsruhe (Germany)	Karlsruhe Institute of Technology (KIT)	—	256	5	10	mainly used for campaigns
Kuopio (Finland) (before Helsinki and Sudonkylä)	Finnish Meteorological Institute (FMI)	10	512	5	10	
Leipzig (Germany)	Leibniz Institute for Tropospheric Research (TROPOS)	10	256	5	10	1 s resolution stored for 5 days, for special events (defined by the radar users) moment-data is re-processed with 1 s resolution
Lindenberg (Germany)	Deutscher Wetterdienst (DWD)	10	256	5	10	
Munich (Germany)	Ludwig-Maximilian Universität München (LMU)	10	256	7.5	10	
Potenza (Italy)	Consiglio Nazionale delle Ricerche: Istituto di Metodologie per l'Analisi Ambientale (CNR-IMAA)	10	256	5	10	
Huancayo (Peru)	Laboratorio de Microfísica Atmosférica y Radiación (LAMAR), Instituto Geofísico del Perú (IGP)	10	128	5	10	
Zugspitze (Germany)	German Aerospace Center (DLR)	10	256	5	10	

Table 6.1: Current radar settings for operating MIRA METEK systems in the world.

high quality radar Doppler spectra are explored for this new class of operating radars. The developed strategies to obtain the optimal settings can also be applied to any other radar system.

The impact of integration time and spectral resolution, which are parameters adjusted by the user, is here assessed for the purpose of drizzle detection. Moreover, by means of forward simulations, also the impact of the beamwidth, which is a hardware parameter, is assessed in the context of drizzle detection. In chapter 3, the importance of the choice of integration time and spectral resolution has already been highlighted. As can be seen from Table 6.1, the most widely used

settings in the MIRA community for integration time and spectral resolution are 10 s and 0.08 ms^{-1} ($N_{\text{fft}} = 256$), respectively. In contrast, the majority of cloud radars operated within the Atmospheric Radiation Measurement (ARM) program use a much smaller integration time of 2 s and a finer spectral resolution of 0.03 ms^{-1} ($N_{\text{fft}} = 512$) (Kollias et al., 2007a). Moreover, different antenna beamwidths, i.e. 0.3° and 0.6° , are used in ARM and MIRA communities. Considering the number of researchers working with both systems, it is important to address the question whether such differences in radar hardware and sampling strategy affect the portability of retrievals algorithms from one cloud radar system to another.

6.2 METHODOLOGY FOR THE PROCESSING OF THE IQ RAW RADAR DATA

The MIRA system at JOYCE, i.e. named JOYRAD-35, has a raw radar data processing similar to the method described in Doviak and Zrnic (2014) and briefly summarized in chapter 2.3.2. The raw IQ time series are converted into Doppler spectra from which the final Doppler spectrum is generated by averaging the raw spectra over a given integration time. This procedure is illustrated in Figure 2.10 only for the I signal for the thin liquid cloud described in the following sections. Raw IQ data are usually not stored because of their immense data volume: a raw file containing 1 min of IQ observations results in a file of 1.2 GB size. For this study, the original IQ data are recorded in order to analyze the sensitivity of the spectra and their moments to different N_{fft} and integration times ΔT while using identical raw data. However, due to data storage limitations the maximum length of the recorded data is restricted to four minutes.

The raw IQ data are processed using $N_{\text{fft}} = 256, 512, 1024$ and three different integration times $\Delta T = 0.4 \text{ s}, 2 \text{ s}, 10 \text{ s}$. A different number of radar Doppler spectral averages is used for different N_{fft} in order to achieve the final Doppler spectrum for one of the selected ΔT (Table 6.2). Only spectra within the cloud boundaries as identified by the

Table 6.2: Number of averaged spectra N_{spectra} to obtain each integration time for different N_{fft} cases (256, 512, 1024).

Integration time ΔT [s]	N_{spectra}^{256}	N_{spectra}^{512}	$N_{\text{spectra}}^{1024}$
0.4	8	4	2
2	40	20	10
10	200	100	50

Cloudnet classification algorithm are analyzed. The same procedure as described in Hildebrand and Sekhon (1974) is applied to estimate the radar Doppler spectra noise floor (mean and peak value) (see

Chapter 2.3.2 for major details). Moments of the cloud radar Doppler spectra are calculated as described in chapter 2.3.2.

6.3 IQ RAW RADAR DATASET

Two four minutes long IQ time series from stratiform thin liquid clouds which have been classified by the Cloudnet algorithm to be non-drizzle and drizzle clouds, respectively, are analyzed. The non drizzle case is recorded at JOYCE on 20 November 2014 between 12:00 and 13:00 UTC. The thin cloud layer is located between 300 m and 500 m above ground (Fig. 6.1). The liquid water path (LWP) derived from the collocated microwave radiometer only reaches values up to 50 gm^{-2} . The time-height structure of spectral width S_w processed for the three different spectral resolutions (N_{fft}) and integration times (ΔT) is shown for 1 minute of IQ observations in the lower panels of Figure 6.1. Longer integration time smooths the microphysical and dynamical structures and results in an increase of S_w with longer ΔT . However, the spectral resolution has only a minor effect on the derived S_w . Also the effects of the different settings on the reflectivity and skewness S_k field (not shown) are small.

The time series of a drizzle event was recorded on 24 June 2015 between 09:00 and 10:00 UTC (Fig. 6.2). The drizzling cloud first appeared during nighttime. Its cloud boundaries ranged between 700 m and 1000 m. The Cloudnet classification identified this cloud as drizzling until approximately 09:00 UTC. When the IQ data were recorded, drizzle stopped over JOYCE and the cloud disappeared within the following hours. LWP decreased from the highest values observed in the morning (200 gm^{-2}) to values of 93 gm^{-2} during the IQ collection period.

Compared to the non-drizzle case (Fig. 6.1), the presence of drizzle is clearly indicated in the 10 dB larger reflectivities and enhanced positive S_k up to 1.5 (Fig. 6.2). Unlike the non-drizzling case, particularly the higher radar moments like S_k are now revealing larger sensitivity to the radar settings. The spectral resolution (as indicated by the different N_{fft} values) has a relatively small effect on the temporal-spatial structure of S_k . The variability of S_k appears to be best captured with 2 s integration time while extreme values and structure is lost when using 10 s integration time. A smaller value of 0.4 s seems not to provide more structure but rather to increase the noise. Both in the non drizzle and drizzle case, a much larger "smearing effect" is found when changing from 2 s to 10 s averaging time compared to moving from 0.4 to 2 s averaging time. While this effect is certainly connected to the scales of variability of the underlying cloud structures, it is noteworthy because the majority of cloud radars across Europe use 10 s integration time while the typical integration time for cloud radars at the ARM sites is 2 s. One question which this study

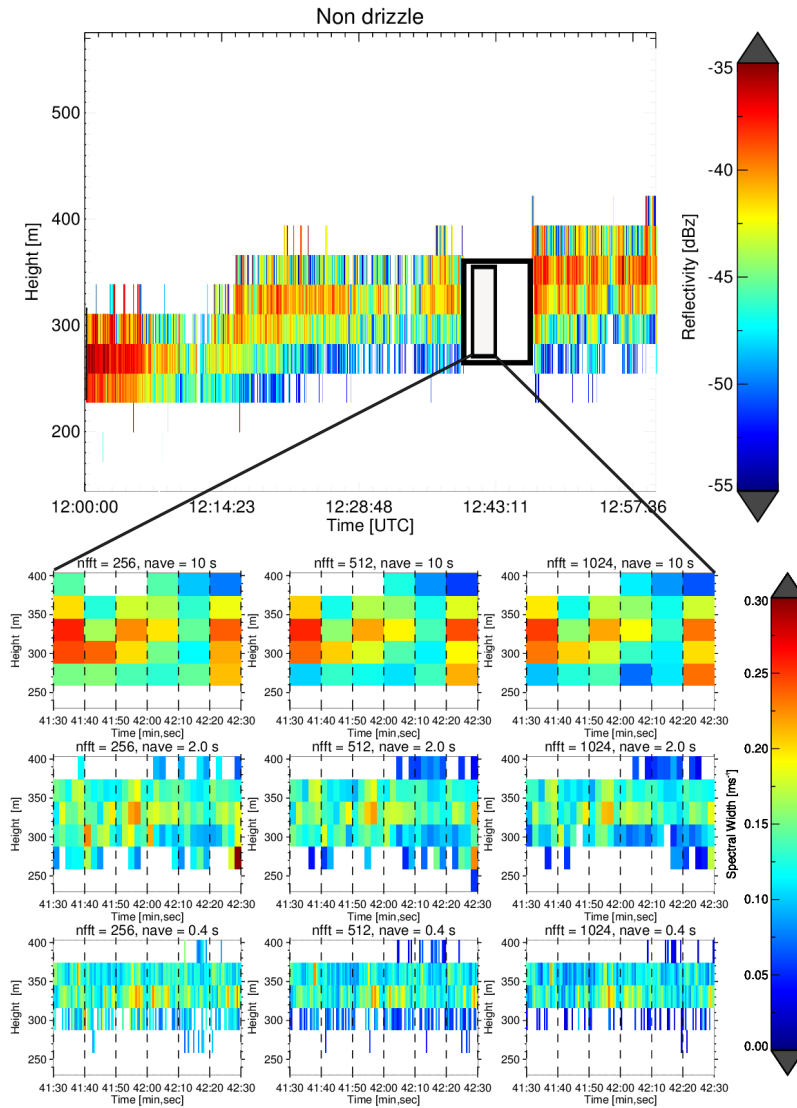


Figure 6.1: Time-height plot composite of reflectivity and spectral width for the non drizzle case on 20 November 2014. The larger upper panel shows the reflectivity for the entire one hour period obtained with standard radar settings of $n_{\text{fft}} = 256$ and $\Delta T = 1$ s; the larger black box denotes the four minute time period of IQ data recording. The lower subplots show time-height plots of a one minute time period (small black box) of spectral width for three different integration times (decreasing from top to bottom) and spectral resolutions (increasing from left to right).

addresses is whether the choice of integration time is relevant only for specific case studies or whether such discrepancies in radar settings might also have implications on the derived radar moment statistics, which may affect the quality of evaluating drizzle parametrizations in numerical models.

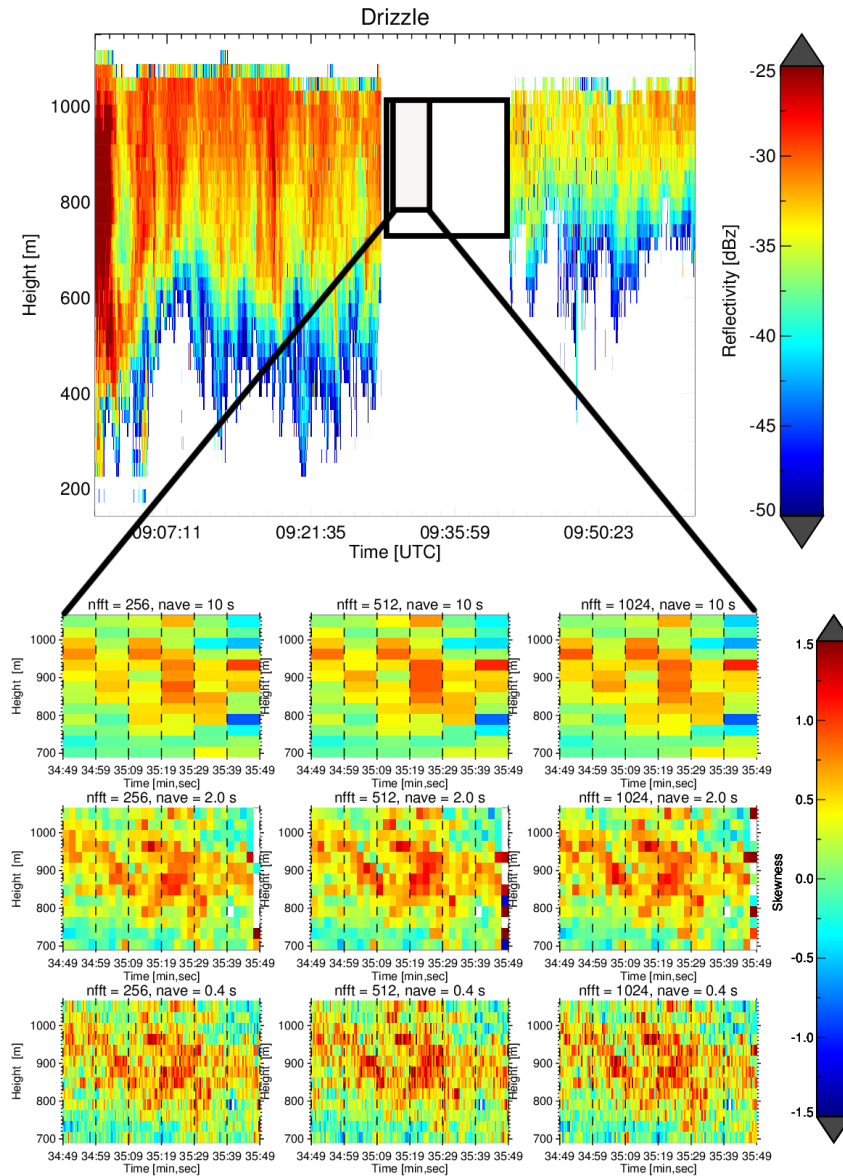


Figure 6.2: Similar to Figure 6.1 but for the drizzle case on 24 June 2015. For this case the subplots show skewness instead of spectrum width.

6.4 IMPACT OF INTEGRATION TIME AND SPECTRAL RESOLUTION ON THE OBSERVATIONS

In this section the results for different integration times and spectral widths are shown. First moments time series derived with different integration times are shown to visually highlight the different effects of this parameter (subsection 6.4.1). Then, the impact of the spectral resolution is assessed by comparing moments derived with fixed 2 s integration time and different n_{fft} (subsection 6.4.2). In subsection 6.4.2, probability density functions (PDFs) for every combination of integration time and spectral resolution are derived.

6.4.1 Moments time series

The impact of different integration times on the radar moments is illustrated in Fig. 6.3. Time series of the four radar moments are shown

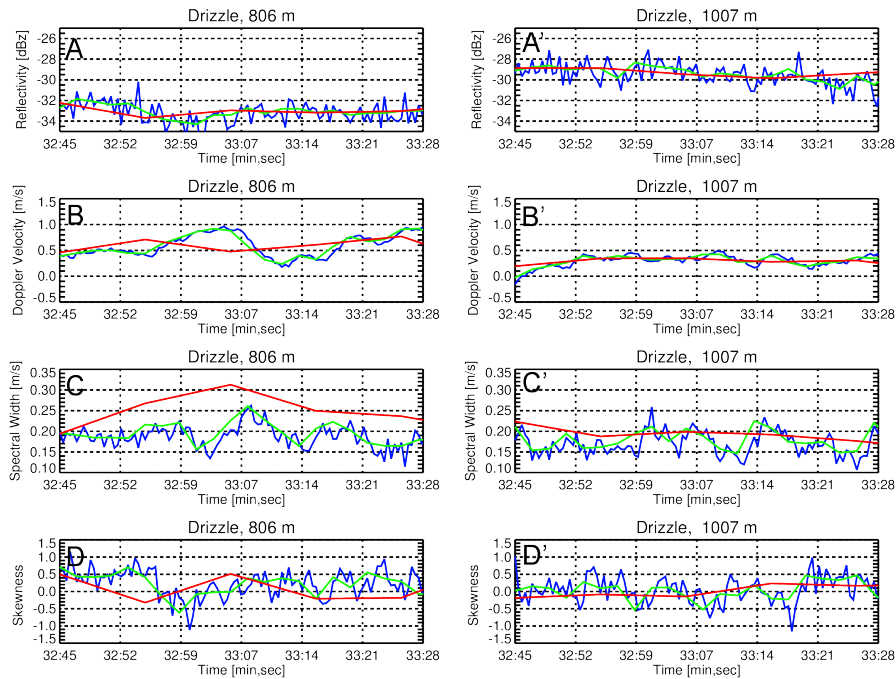


Figure 6.3: Example time series of the first four Doppler moments obtained from altitudes close to cloud bottom (left column) and close to cloud top (right column) for the drizzle case on 24 June 2015 (see Fig. 6.2). Different colors correspond to different integration times of 10s (red), 2s (green), and 0.4s (blue); N_{fft} for all time series is 512.

for the drizzle case (Fig. 6.2) close to cloud top at 1007 m and close to cloud base at 806 m. The selection of the radar integration time impacts the higher moments of the radar Doppler spectrum strongly (Fig. 6.3(c),(d) compared to (a),(b)). In addition, the impact close to cloud base is higher than at cloud top (Fig. 6.3 right column) which can be explained by the broader DSD at the lower regions of the cloud where the microphysical processes of autoconversion and accretion will result in larger drizzle particles and a broader drizzle DSD. The integration time has little effect on the recorded radar reflectivity values. The Z_e absolute differences between values derived with different integration times are smaller than 2 dB and as expected, longer integration times reduce the variability of Z_e : the standard deviation of the time series of Z_e at 0.4 s, 2 s and 10 s is reduced from 1.0 dBz to 0.6 dBz and 0.56 dBz respectively. The small dependency of Z_e on the integration time is consistent with the incoherent nature of the return power measurements.

Larger deviations are found for mean Doppler velocity V_d particularly between the 10 s and the two shorter integration times. While the differences at cloud top are relatively small, at cloud bottom V_d val-

ues obtained with 10 s integration time sometimes deviate up to 50% from the values derived with 2 s and 0.4 s integration time. This is due to the broader and more skewed spectra observed at cloud bottom in combination with more variable vertical motions. Furthermore, the spectrum width increases with longer integration times because narrow individual spectra which are shifted due to vertical air motions are averaged together; this also results in a more Gaussian shape of the average spectrum and hence skewness values are closer to zero (Luke and Kollias, 2013). It is noteworthy that for all radar Doppler spectra moments only small differences are found between the 2 s and 0.4 s integration time but much larger differences when using 10 s. At least for drizzle studies, integration times equal or shorter than 2 s should be preferred for capturing small-scale vertical motions of higher moments (S_w , S_k) of the Doppler spectrum. In fact, this integration time allows to keep microphysical signatures distinguished from noise, ensuring high quality of higher moments estimates.

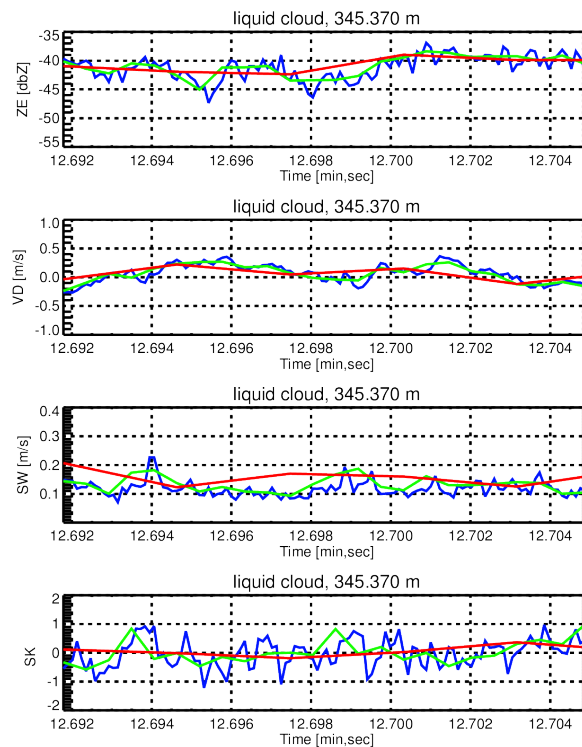


Figure 6.4: Example time series of the first four Doppler moments obtained from an altitude in the middle of the non-drizzle case on 20 November 2014 (see Fig. 6.1). Different colors correspond to different integration times of 10s (red), 2s (green), and 0.4s (blue); N_{fit} for all time series is 512.

Moreover, the non-drizzle case is used as a benchmark for the statistical variance of the radar measurements. In non-drizzling conditions, the radar Doppler spectrum is dominated by turbulence (Kollias et al., 2001). Therefore, the impact of microphysics on the shape of the radar Doppler spectrum can be neglected. For this reason, the uncertainty due to instrumental noise and air motions can be estimated in these

conditions. From the measurements, the uncertainty derived from the skewness time series collected in the non-drizzling cloud shown in Fig. 6.3 can be estimated. Using 2 s integration time and spectral resolutions of 256, 512 and 1024 it ranges between 0.389 and 0.369 with a mean value over the three cases of 0.379. For relatively narrow spectra, as they are found in clouds with no or little drizzle production, the spectral resolution might be of relevance for the quality of the derived moment estimates. The spectral resolution could affect the quality of integral values such as reflectivity if a narrow spectrum – e.g. due to cloud droplets – is only resolved with a few spectral bins. A larger impact is expected for higher moments where the spectral shape becomes important and hence spectral resolution potentially smoothes out spectral features.

6.4.2 Impact of spectral resolution

In order to investigate these potential effects of spectral resolution on the different moments, Doppler spectra for all heights are derived applying 256, 512, and 1024 N_{fft} respectively. The integration time for all N_{fft} is kept constant (2 s) to ensure that the spectra are based on identical time series of raw IQ data and hence they contain identical information about dynamics and cloud microphysics. Figures 6.5 and 6.6 show the scatter plots of $N_{\text{fft}} = 256$ versus 512 and 512 versus 1024 for the drizzle and the non-drizzle case. Table 6.3 and 6.4 exhibit the biases and standard deviations (STD) of the scatter plots.

Table 6.3: Bias and standard deviation of the difference of moments derived from corresponding spectra having different spectral resolutions for the drizzling case of the 24 June 2015.

Drizzle	BIAS		STD	
	256-512	512-1024	256-512	512-1024
Z_e	0.02	0.06	0.42	0.46
V_d	-0.0011	0.0009	0.05	0.04
S_w	0.007	0.003	0.02	0.02
$\times S_k$	-0.017	0.005	0.16	0.18

Table 6.4: Bias and standard deviation of the difference of moments derived from corresponding spectra having different spectral resolutions for the non-drizzling case of the 20 November 2014.

Non Drizzle	BIAS		STD	
	256-512	512-1024	256-512	512-1024
Z_e	0.28	0.32	0.89	1.16
V_d	0.001	-0.006	0.08	0.12
S_w	0.013	0.011	0.04	0.03
S_k	-0.004	-0.006	0.31	0.39

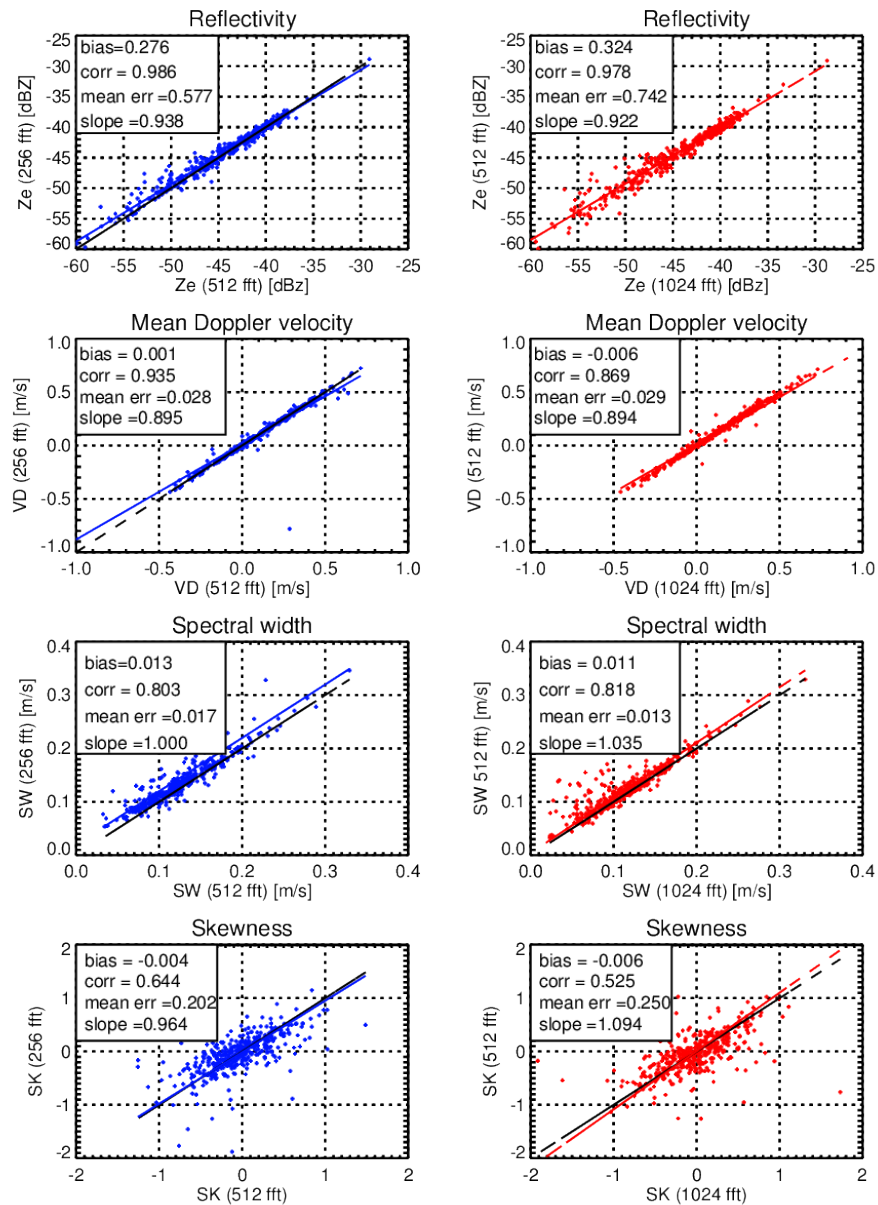


Figure 6.5: Scatter plots of moments derived with different fft lengths n_{fft} for the non-drizzle case: 512 vs 256 fft length (left column), 1024 vs 512 fft length (right column). Moments are reflectivity, mean Doppler velocity, spectral width and skewness (from top to bottom). All spectra are calculated with 2s integration time.

In summary, the impact of different spectral resolutions is surprisingly small compared to the natural variability of the various moments shown in Fig. 6.3. Biases and STD are slightly larger for the non-drizzle case while differences around 0.3 dB for reflectivity can still be considered negligible for most applications because uncertainties on Z_e are typically larger than this value. The larger deviations in the non-drizzle case are attributed to the insufficiently resolved narrow spectra which lead to uncertainties in the estimate of the integral and spectral shape. For example, narrow non-drizzling cloud spectra are often represented by only few spectral bins when using

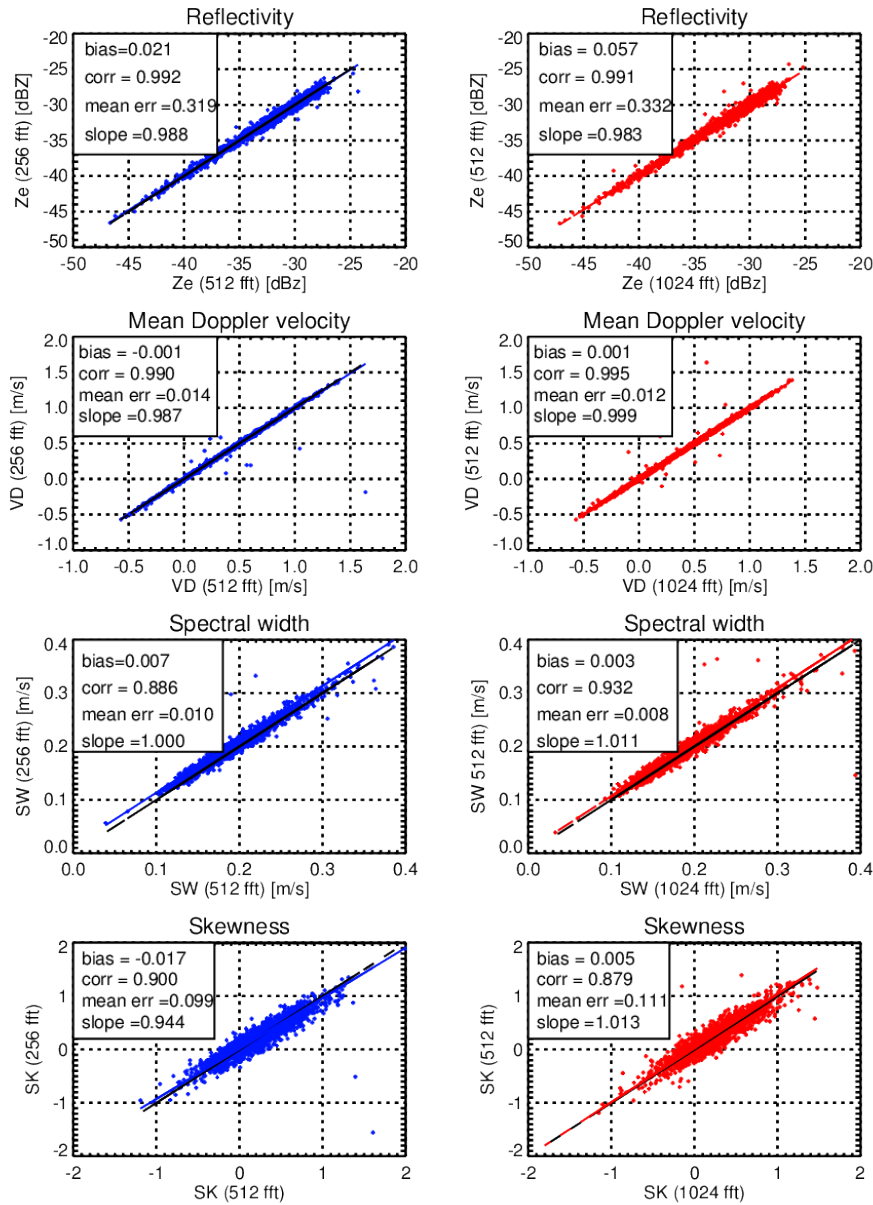


Figure 6.6: Scatter plots of moments derived with different n_{fft} for the drizzle case: 512 vs 256 ft length (left column), 1024 vs 512 ft length (right column). Moments are reflectivity, mean Doppler velocity, spectral width and skewness (from top to bottom). All spectra are calculated with 2s integration time.

a spectral resolution of 0.08 ms^{-1} ($N_{\text{fft}} = 256$) as it is widely used by MIRA systems (Tab. 6.1). Such a coarse resolution also affects higher moments like S_w and S_k . In the drizzle case, the spectra are broader and sufficiently resolved even with the coarsest spectral resolution.

6.4.3 Probability density functions for each combination of settings

The observed PDFs, normalized by the number of measurements of all radar Doppler spectra moments for the three different integration times, and three N_{fft} for the non-drizzling case (Fig. 6.7) and for the drizzling case (Fig. 6.8), are assessed in order to closer examine the reasons for the mismatches.

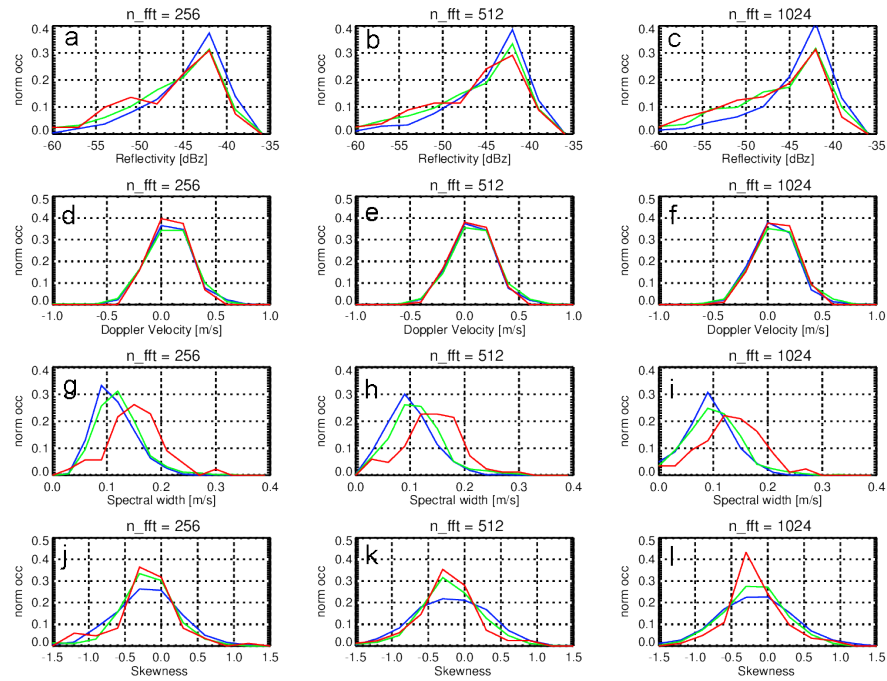


Figure 6.7: Distributions of moments for the non-drizzling case of the 20 November 2014. Each line of the figure shows the distribution for a given moment at the different fft lengths (from left to right 256, 512 and 1024): Z_e on the first line, V_D on the second line, S_W on the third line, S_K on the fourth line. Different colors correspond to different integration times: red (10s), green (2s) and blue (0.4s).

Since the impact of different spectral resolutions is rather limited as shown already in the previous section, discussion here mainly focuses on the impact of integration time. For the non-drizzle case, the distributions of moments mainly show an expected increase in radar sensitivity and a shift in spectral width S_W towards larger values with longer integration time. The low spectral width and the low signal-to-noise ratio of the non-drizzle spectra cause the spectra to be rather noisy. Higher moments like S_K are more affected by the low signal-to-noise conditions, which explains the relatively broad S_K distribution. The following analysis focuses mainly on the drizzle case and on the impact of the two radar settings on radar moments during drizzle formation. Moreover, higher signal-to-noise conditions during drizzling conditions are expected to limit the influence of noise on the derived distributions. The presence of drizzle is visible in the distributions of radar moments (Fig. 6.8): in comparison to the non-drizzle case (Fig. 6.7), Z_e values are increased by about 10 dB and

Table 6.5: Mean values of the distributions of radar Doppler moments for the non-drizzling case of the 20 November 2014.

Mean of distributions: 20 November 2014				
Moments	Integration time ΔT [s]	$n_{\text{fft}} = 256$	$n_{\text{fft}} = 512$	$n_{\text{fft}} = 1024$
reflectivity	0.4	-43.0	-43.3	-43.1
	2.0	-44.5	-45.0	-45.0
	10	-46.0	-46.0	-46.1
mean Doppler velocity	0.4	0.17	0.17	0.16
	2.0	0.16	0.16	0.14
	10	0.17	0.17	0.21
spectral width	0.4	0.13	0.11	0.11
	2.0	0.15	0.16	0.13
	10	0.17	0.16	0.15
skewness	0.4	-0.04	-0.01	-0.005
	2.0	-0.04	0.01	-0.1
	10	-0.08	-0.07	-0.06

also the mean Doppler velocity peaks at about 0.25 ms^{-1} compared to the value of 0.16 found for the non-drizzle case (Tables 6.5 and 6.6). Furthermore, the distribution of higher moments shows typical signatures of drizzle with S_w values larger by 0.6 ms^{-1} compared to the non drizzle observations (see Table 6.6).

The skewness values reveal the typical transition from almost zero S_k in the non-drizzle case to positive values with a mean value of 0.25 , indicating an asymmetry of the spectrum towards larger fall velocities due to larger drizzle particles; these signatures are in general agreement with former studies (e.g. [Kollias et al., 2011a](#)).

Integration time as well as spectral resolution seem to have a negligible influence on the distributions of Z_e (Fig. 6.8(a)-(c)) and V_d (Fig. 6.8(d)-(f)). The S_w values are considerably increased for the 10s integration time while the shift is small for the two smaller integration times (Fig. 6.8(g)-(i)). The mean of the S_k distributions slightly decreases due to longer integration times (Table 6.6) which can be again explained by the more Gaussian shape of the spectra obtained using a longer integration time. Particularly, the largest values found in the positive S_k region decrease for longer integration times. A similar but weaker effect can be found for the most positive V_d values which can be explained by relatively narrow regions within the cloud layer that already developed a larger amount of drizzle compared to the surrounding cloud layer. In the light of early detection of drizzle onset regions, a 10s integration time seems to be insufficient. The differences obtained in the skewness distributions can have impacts on the ability to detect positive skewness signals induced by drizzle. [Luke and Kollias \(2013\)](#) showed S_k time series where the highest observed values of skewness reach up to 1.5 . A reduced ability in detecting such extremes values due to longer integration times, for

Table 6.6: Mean values of the distributions of radar Doppler moments for the drizzling case of the 24 June 2015.

Mean of distributions: 24 June 2015				
Moments	Integration time ΔT [s]	$n_{\text{fft}} = 256$	$n_{\text{fft}} = 512$	$n_{\text{fft}} = 1024$
Reflectivity	0.4	-31.7	-31.8	-31.9
	2.0	-31.6	-31.6	-31.7
	10	-31.5	-31.5	-31.5
Mean Doppler Velocity	0.4	0.25	0.26	0.26
	2.0	0.26	0.26	0.26
	10	0.26	0.26	0.26
Spectral width	0.4 s	0.19	0.18	0.18
	2.0	0.21	0.20	0.20
	10s	0.22	0.21	0.21
Skewness	0.4 s	0.24	0.26	0.25
	2.0	0.25	0.24	0.27
	10	0.21	0.23	0.23

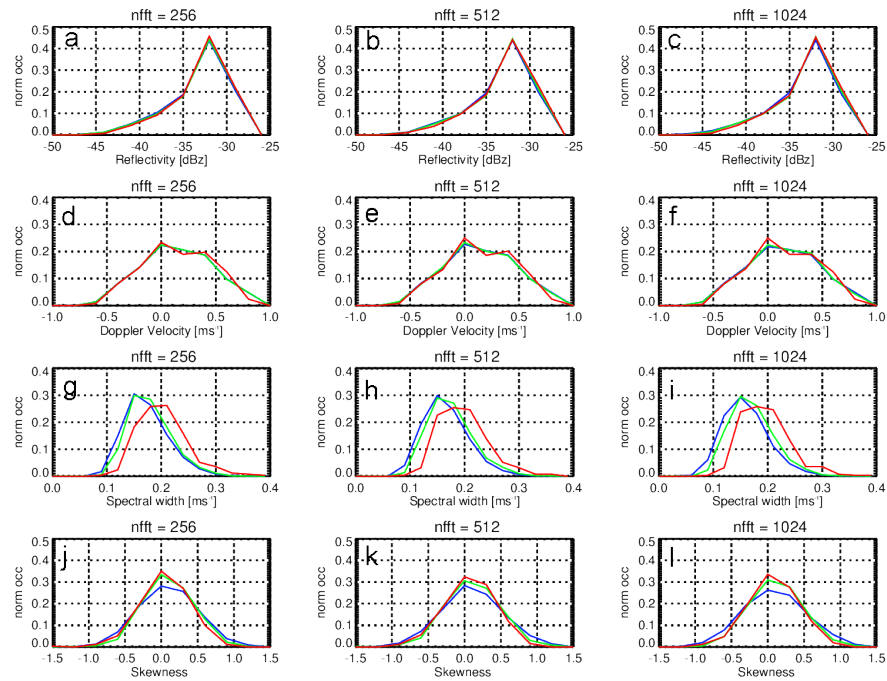


Figure 6.8: Distributions of radar moments for the drizzle case on 24 June 2015 (Fig. 6.2). The total number of values used for the different PDFs ranges between 252 for the 10s integration time and 6174 for the 0.4s integration time. Different colors in each plot correspond to different integration times of 10s (red), 2s (green), and 0.4s (blue). The spectral resolution (n_{fft}) increases from left to right; radar moments are from upper to lowest row: reflectivity (Z_e), mean Doppler velocity (V_d), spectral width (S_w), and skewness (S_k).

example with 10 s integration time, the maximum value observed is 1, can affect the potential to disentangle the low frequency variability induced by the microphysics and the high frequency variability due to noisiness and beam filling issues. Finally, the coarsest spectral res-

olution using $N_{\text{fft}} = 256$ is found to be sufficient to properly capture the typical signatures of drizzle onset.

6.5 SIMULATION FRAMEWORK: STATISTICS AND IMPACT OF HARDWARE PARAMETERS

The observed radar Doppler spectra are affected by the underlying microphysics but also by dynamical effects such as turbulence. In reality, a complete separation of both effects is often a challenging task (Tridon and Battaglia, 2015). The limitations for storing the large amounts of IQ raw data also limited the total observed time of drizzle clouds. The radar forward simulator included in the PAMTRA framework (Maahn, 2015) is used to produce forward simulations of radar Doppler spectra and their corresponding moments (for a description of PAMTRA see chapter 3). The aim of the simulations is to analyze the effects of dynamics and microphysics separately but also to investigate whether the observed drizzle signatures are consistent with commonly used assumptions about drizzle microphysics. The main goal of the simulations is to derive a range of possible microphysical and dynamical conditions which lie within the observed range of radar moments. This helps to prove that the observed differences due to radar settings are significant for identifying drizzle onset. In addition, it allows to overcome one main limitation of the observations, i.e. their short time series. The simulations can further be used to separately analyze the effects of turbulence and vertical air motion (provided as input to PAMTRA) from the microphysics when observed with different N_{fft} and ΔT . In the following, all the assumptions and settings assumed for the simulations are described.

For the cloud droplet and drizzle components a log-normal DSD of the form

$$N(D) = \frac{N_0}{\sqrt{2\pi}\sigma D} \exp\left[\frac{-\log\left(\frac{D}{D_0}\right)^2}{2\sigma^2}\right] \quad (6.1)$$

is assumed, where N_0 is the total number concentration (cm^{-3}), D_0 is the median diameter (in m) which is related to the effective diameter (D_{eff}) by $D_0 = D_{\text{eff}} \exp\left[-\frac{5}{2}\sigma^2\right]$ (Miles et al., 2000), and σ is the width of the DSD. The effective diameter is connected to the effective radius R_{eff} by the relation $D_{\text{eff}} = 2 \cdot R_{\text{eff}}$. Following (Miles et al., 2000) who provided typical values for continental stratus and stratocumulus clouds, for cloud droplets an effective radius $R_{\text{eff},c}$ of $5.4 \mu\text{m}$, a logarithmic spread σ_c of 0.35 and total number concentration N_0 of 300 cm^{-3} are assumed. With these assumptions, the obtained liquid water content (LWC) of the cloud droplets is $\text{LWC}_c = 0.137 \text{ gm}^{-3}$. This LWC value is very close to the LWC of 0.133 gm^{-3} which is obtained in the drizzle case when dividing the average LWP measured

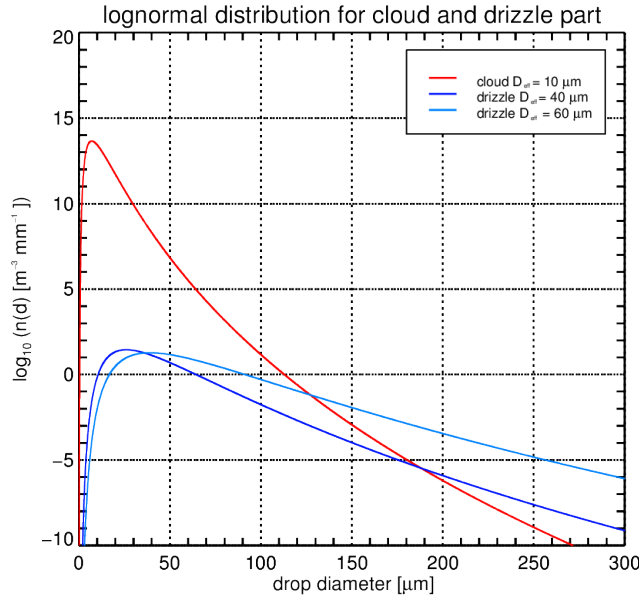


Figure 6.9: DSDs used for radar forward simulations of the drizzle case. A single log-normal size distribution (red) is used for cloud droplets; for drizzle log-normal distributions with fixed $r_{LWC} = 0.5\%$ and two different effective diameters are used: $40 \mu\text{m}$ (dark blue), $60 \mu\text{m}$ (blue). The total number concentration N_d of the drizzle distribution is determined based on the other parameters according to Eq. (6.1).

by the MWR by the average geometrical thickness of the cloud layer. The LWC due to drizzle (LWC_d) is assumed to be much smaller than LWC_c . This is a common assumption in simulations of drizzle onset. In Frisch et al. (1995), the LWC ratio derived from the standard parameters used to discriminate between cloud and drizzle is 5%, while in O'Connor et al. (2005) drizzle LWPs are often 2 orders of magnitude lower than cloud LWPs. For the simulations, the LWC ratio (r_{LWC}) defined as $r_{LWC} = \frac{LWC_d}{LWC_c}$ is varied between 0.1 and 5%. For the log-normal drizzle DSD the adopted σ_d is 0.35 (Frisch et al., 1995) and the drizzle effective radius $R_{\text{eff},d}$ varies from $10 \mu\text{m}$ to $60 \mu\text{m}$. The drizzle number concentration N_d is then calculated based on the selected LWC ratio r_{LWC} . The DSDs for cloud droplets and drizzle are shown in Figure 6.9.

The eddy dissipation rate ϵ and mean Doppler velocity V_d distributions have been derived for the one hour period before the IQ recording in order to obtain observational constraints for turbulence and vertical air motion needed as input to the radar forward simulations. Eddy dissipation rate values are derived with the methodology shown in Chapter 3. The ϵ distribution reveals a mean ϵ of $3 \times 10^{-4} \text{ m}^2\text{s}^{-3}$ and a standard deviation of $1.3 \times 10^{-4} \text{ m}^2\text{s}^{-3}$. The observed statistics of V_d are used as a first order approximation for the vertical air motion. A mean value of 0.43 ms^{-1} and a standard deviation of

0.39 ms^{-1} is observed. Due to the non-negligible terminal velocity of the drizzle component, the true air motion is likely to be smaller.

Simulated spectra respectively for $r_{\text{LWC}} = 2\%$ and $R_{\text{eff,d}} = 20 \mu\text{m}$ and $r_{\text{LWC}} = 0.5\%$, and $R_{\text{eff,d}} = 30 \mu\text{m}$ (to simulate different stages of drizzle onset), and ϵ representing the mean ($3 \times 10^{-4} \text{ m}^2\text{s}^{-3}$) and largest values ($5 \times 10^{-3} \text{ m}^2\text{s}^{-3}$) observed are shown exemplarily in Figure 6.10. The first scenario represents an early drizzle onset, while the second scenario represents a more developed stage of drizzle. For $R_{\text{eff,d}} = 20 \mu\text{m}$, the contribution of the cloud droplet peak dominates the radar spectrum even for low turbulence conditions. When the $R_{\text{eff,d}}$ is increased to $30 \mu\text{m}$, the drizzle contribution becomes stronger and causes the spectrum to become positively skewed. Increasing the eddy dissipation rate ϵ in general leads to a smoothing and symmetrical broadening of the spectrum but the overall asymmetry due to drizzle is still clearly visible (Fig. 6.10). A comparison of our simulations with observed spectra from regions where early and more mature drizzle cases (Fig. 6.10) shows an overall good agreement in terms of spectral shape, Z_e , and S_k when ϵ is small.

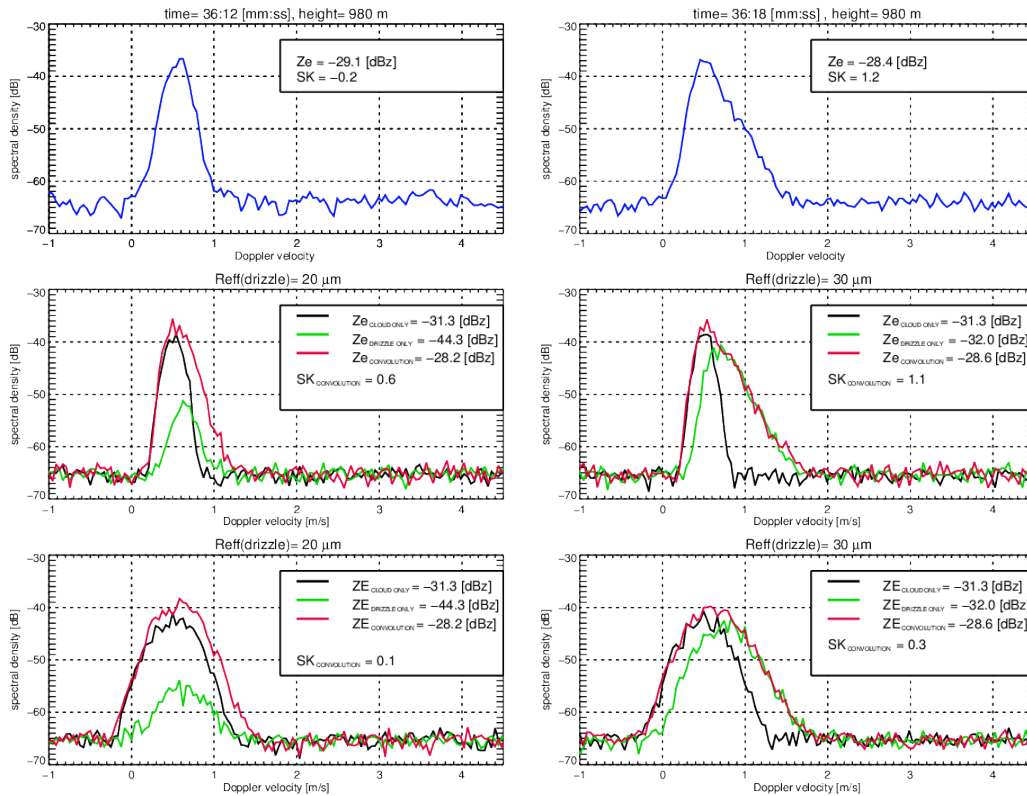


Figure 6.10: Comparison between simulated and observed spectra. Upper panels shows real Doppler spectra obtained during the drizzle-case for $n_{\text{fft}} = 512$ and $\Delta T = 2 \text{ s}$ in regions of early (left) and more mature drizzle development (right). The 4 lower panels show examples of simulated Doppler spectra for cloud droplets (black), drizzle (green) and cloud+drizzle drops (red) for a low ϵ of $3 \times 10^{-4} \text{ m}^2\text{s}^{-3}$ (middle panels) and high ϵ of $5 \times 10^{-3} \text{ m}^2\text{s}^{-3}$ (lower panels). The left column shows spectra for a log-normal drizzle DSD with effective radius of $20 \mu\text{m}$ while the right column is calculated with a drizzle effective radius of $30 \mu\text{m}$.

6.5.1 Simulation statistics for early stage and mature drizzle cases

In order to take the effects of turbulence and changes in vertical velocity on the distribution of the Doppler spectra moments into account, the same microphysical scenarios as described above are used. For each scenario, 1000 PAMTRA simulations are run choosing randomly the noise and a pair of values of ϵ and vertical air motion represented by the mean Doppler velocity (V_d) based on the one-hour period observed distributions. In this way, for each simulated spectrum, a wide range of air motion conditions are derived which are expected to represent the observed values. The simulations are repeated for the three N_{fft} and ΔT in order to derive distributions of radar moments similar to the observations shown in Fig. 6.8 for the "early stage" and the "more mature" drizzle cases, respectively.

Statistical distributions of simulated moments of the convoluted spectra from cloud and drizzle droplets are shown in Fig. 6.11 and Fig. 6.12.

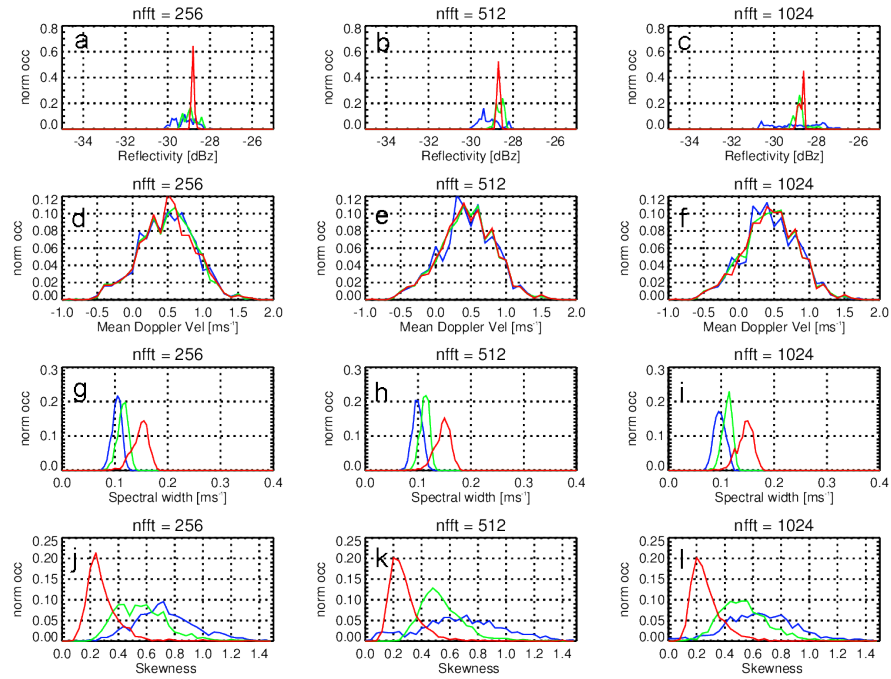


Figure 6.11: Distributions of simulated radar moments Z_e , V_d , S_w , S_k (from top to bottom) normalized by the total number of simulations ($N = 1000$) for cloud and drizzle droplets for the "early stage" drizzle case with $R_{\text{eff},d} = 20\mu\text{m}$ and $r_{\text{LWC}} = 2.0\%$. The moments are derived for averaging times of 10s (red), 2s (green), 0.4s (blue), and different N_{fft} (increasing from left to right).

Both simulation experiments produce reflectivities which are among the highest observed Z_e values (Fig. 6.8). The simulated Z_e values lie in a narrow interval because only a single DSD of cloud and drizzle drops respectively, is assumed and the only parameters which are allowed to vary are ϵ and vertical air motion. The increasing variability of the moments with smaller averaging time and larger N_{fft} is related

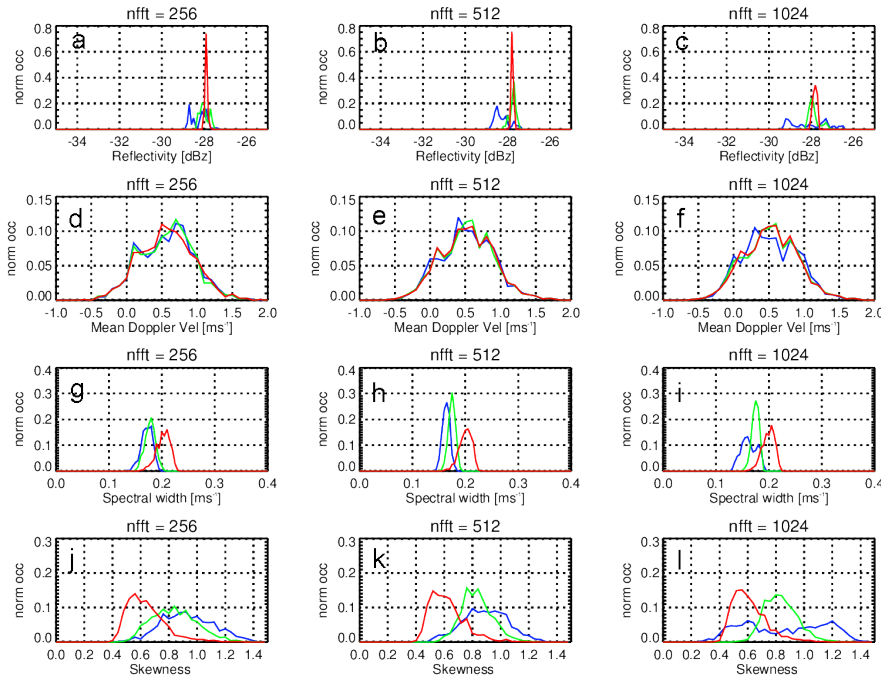


Figure 6.12: Similar to Figure 6.11 but using $R_{\text{eff,d}} = 30\mu\text{m}$ and $r_{\text{LWC}} = 0.5\%$.

to the increasing noisiness of the simulated spectra due to the small number of spectral averages. Very small effects of N_{fft} and ΔT are found for mean Doppler velocity. This behavior is similar compared to the observations (cf. Fig. 6.11(d), (e), (f) and Fig. 6.12(d), (e), (f) with Fig. 6.8(d), (e), (f)). The simulated V_d distributions appear to be biased to positive velocities. This is not surprising considering that the distribution of V_d previous to the IQ experiment is assumed as proxy for vertical air motion and that this distribution is biased towards larger positive velocities due to sedimentating drizzle drops. For spectral width S_w , the mean values of the distributions are found to increase with larger integration times in both observations and simulations. The magnitude of the increase in both simulated drizzle cases closely matches the observations (Fig. 6.8); S_w distributions from the simulations (Fig. 6.12(g),(h) and (i)) as well as from the observations (Fig. 6.8(g), (h) and (i)), are not affected by the n_{fft} . In contrast to the observations, the simulated S_k values are only positive and range up to 1.5. This effect is related to the choice of the specific drizzle DSDs. The large positive values of simulated skewness are a result of the long tail of the selected shape for the drizzle DSD. While this shape might be typical for mature drizzle distributions, the distribution is expected to be narrower during the early stages of drizzle production i.e. near cloud top. Three factors are responsible of the absence of negative skewness values in the distributions of simulated values (Fig. 6.12(j),(k),(l) and Fig. 6.11(j),(k) and (l)). During heavy drizzle conditions a reversal of the sign of the S_k is expected. However, for the selected simulated cases, the drizzle spectrum does not exceed the

cloud droplet spectrum. The second factor is the absence of non-linear horizontal shear of the vertical air motion in the PAMTRA simulator, which would induce negative values of S_k caused by wind fluctuations (see 2.14). This is discussed in detail in Luke and Kollias (2013). Finally, low signal-to-noise conditions can increase the uncertainty of the measured radar Doppler spectra skewness and thus give rise to negative radar Doppler spectra skewness values, i.e. as the ones observed by JOYRAD-35 and this is probably the most likely reason.

Despite the missing negative S_k values in the simulations, smaller values of skewness using 20 μm effective radius for drizzle (Fig. 6.11) compared to the simulation for $R_{\text{eff}} = 30 \mu\text{m}$ (Fig. 6.12) are observed and a shift of the S_k distributions to larger values for smaller ΔT is found in both simulations.

This simulated effect is confirmed by observations particularly if the analysis is focused to cloud regions with spatio-temporal coherent positive skewness structures as shown in Figure 6.13.

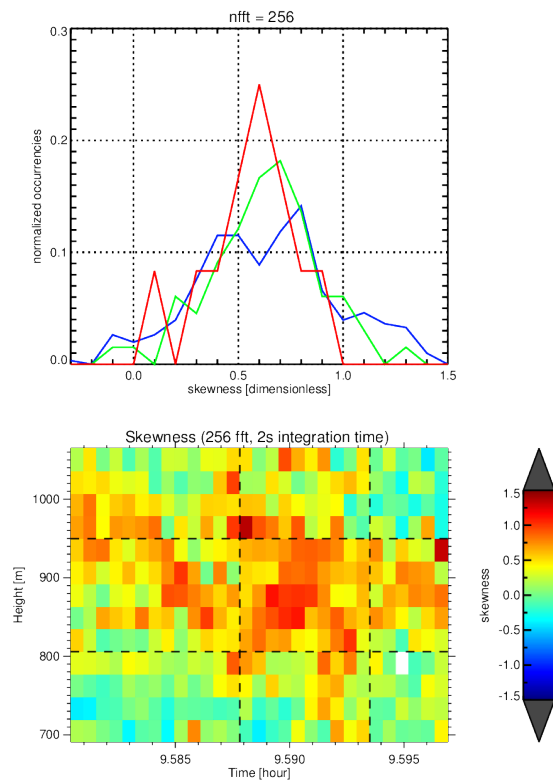


Figure 6.13: Selection of positive skewness values due to drizzle fingerprint in the observations from the case study of the 24 June 2015. Upper panel: distributions of skewness observed values derived using a spectral resolution of 256 and integration time of 10s (red), 2s (green) and 0.4s (blue). Lower panel: the central dashed box is the area of positive skewness values selected for the analysis.

The distributions of skewness values for the three different integration times and a spectral resolution of $n_{\text{fft}} = 256$ are shown in the upper panel of Fig. 6.13. A comparison with Fig. 6.12 reveals that the

range of observed skewness values as well as the shifting of the peak and change in positive S_k extremes resembles the simulations.

Overall, the simulated distributions reveal – in agreement with observations – an only minor effect of N_{fft} on the S_k distributions. The distributions of simulated moments reproduce the main effects induced by integration time and spectral resolution on the moments estimations, confirming the choice of 256 fft length and 2 s integration time as optimal settings for drizzle detection.

6.5.2 Effects of turbulence and varied antenna beamwidth

ARM radars typically use narrower beamwidths (0.3°) than radars of the MIRA community, which adopt 0.6° antenna beamwidths. It is thus important to assess the impact that this hardware parameter can have on moments estimations by exploiting the simulations. Here, the impact on skewness is shown for different microphysical situations and the two selected antenna beamwidths. Keeping the integration time fixed and also the cloud droplet DSD, various drizzle DSD are simulated varying the effective radius of drizzle and the LWC ratio. The skewness is analyzed as a function of assumed level of turbulence and the radar antenna beamwidth in Fig. 6.14. At low turbulence con-

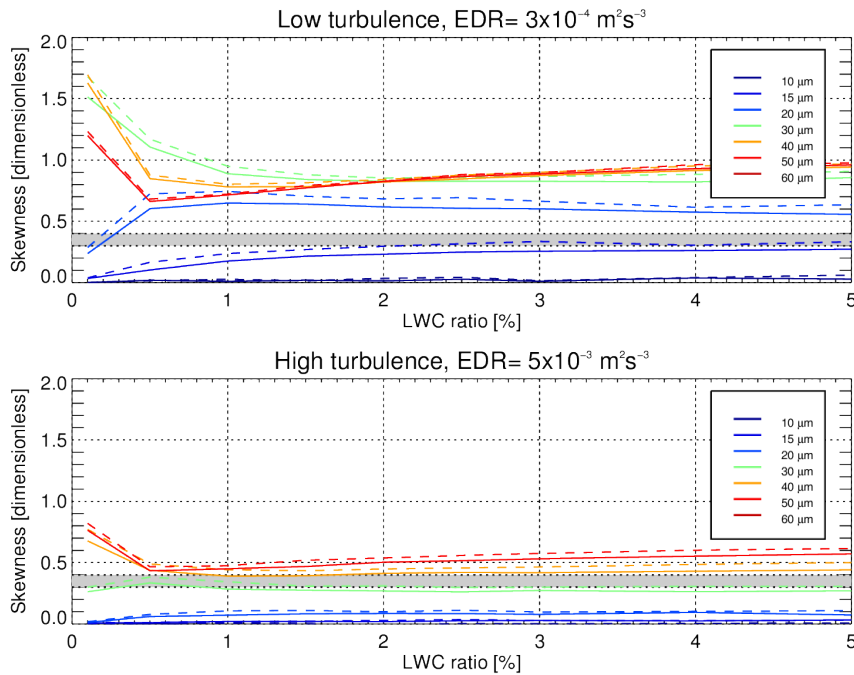


Figure 6.14: Skewness of the convoluted spectrum of cloud and drizzle drop size distributions as a function of r_{LWC} for different drizzle effective radii and low EDR (upper panel) and high EDR (lower panel). Simulations have been performed using 0.6° (solid line) and 0.3° (dashed line) radar beamwidths. The grey bar represents the uncertainty of the skewness observations, that depending on the radar settings varies between 0.36 and 0.39 (see 6.4).

ditions and very small liquid water content ratios r_{LWC} , the skewness

shows very high values. For larger r_{LWC} , the skewness is typically smaller. In fact, increasing the liquid amount for drizzle, i.e. increasing r_{LWC} , generates a more pronounced drizzle peak which results in a spectrum being more similar to a Gaussian shape and less asymmetric than in the case of low r_{LWC} . The value of the skewness observed depends on whether the drizzle effective radius is large enough to introduce a sufficient asymmetry on the right of the cloud peak (see Fig. 6.10). If the effective radius of the drizzle is too small, e.g. for the cases with $R_{eff} = 10 \mu\text{m}$, $15 \mu\text{m}$, and $20 \mu\text{m}$ (Fig. 6.14), the drizzle contribution is concealed by the cloud part and the skewness is just slightly positive for increasing r_{LWC} . Figure 6.14 also shows that under low turbulence conditions the skewness signal generated by the presence of drizzle characterized by an effective radius of at least $20 \mu\text{m}$ is always greater than 0.4, which is the detection limit that has been estimated for the observations (see Subsection 6.4). This indicates that there is potential for the detection of drizzle in the cloud already at drizzle drop sizes of $R_{eff} = 20 \mu\text{m}$ if the turbulence is low. In presence of high turbulence, all skewness values are damped compared to the ones in low turbulence conditions (lower panel of Fig 6.14). Here, most of the expected skewness values are below the estimated detection threshold. Only drizzle drops being larger than $40 \mu\text{m}$ can be detected. Smaller beamwidths allow the detection of slightly higher skewness values in both turbulence conditions. The gain due to the beamwidth appears more evident for effective radii around $20\text{-}30 \mu\text{m}$, but overall it shows the marginal influence of this parameter for the accuracy of skewness estimation.

6.6 CONCLUSION AND SUMMARY OF MAIN RESULTS

This chapter shows the importance of well-chosen radar settings in order to establish high-quality datasets of cloud radar observations in drizzle clouds. Indeed, the choice of radar settings is also crucial for enabling future comparisons of long-term datasets obtained from different radar systems at different sites. An optimal compromise between limiting the data amount on the one hand and conserving relevant microphysical information on the other hand needs to be found. In the specific context of liquid clouds and drizzle initiation, longer integration times mainly modify spectral width and skewness leaving the other moments hardly altered. For drizzle applications, the uncertainty of skewness measurements has been found to be about 0.4. Simulations performed with a radar forward simulator which allows to explicitly define the state of drizzle are in general agreement with observations. Spectral width is increased by longer integration times due to the broadening of the spectrum shape. In the observations, this effect is attributed to turbulence and is confirmed by simulations.

Skewness becomes smaller when longer integration times are used. Both the increase in S_w and reduction in S_k in case of the 10 s averages can lead to significantly different microphysical interpretations with respect to drizzle water content and effective radius (Fig 6.14) compared to shorter integration times.

For the specific application of drizzle detection the integration time of 2 s is the optimal compromise considering the turbulence-induced increase in S_w at longer integration times and the preservation of larger values of S_k . FFT lengths have a small impact on the moment estimations and thus on the microphysical interpretation of the drizzle signal: a FFT length of 256 seems to be appropriate for the calculation of moments since no significant differences compared to moments derived using 512 or 1024 FFT lengths have been found.

Finally, simulations provided additional insight into the microphysical interpretation of the observed skewness signatures: in low (high) turbulence condition, only drizzle drops bigger than 20 μm (40 μm) can generate skewness values above the detection level. Furthermore, slightly higher skewness values are obtained in simulations when smaller beamwidths, i.e. 0.3° instead of 0.6° , are assumed. Thus, small antenna beamwidths have small impact for drizzle detection.

Part IV

EXPLOITMENT OF SKEWNESS FOR
OPERATIONAL APPLICATIONS

It can't rain all the time.

The Crow

REFINEMENT OF DRIZZLE DETECTION

At JOYCE, radar Doppler spectra are collected using 256 fft points and 1 s integration time, which on the basis of the results of the previous chapter, almost correspond to the optimal settings for drizzle detection. Differences between 1 s and 2 s integration time (not shown in the previous chapter) are found to be almost negligible. Therefore, the dataset presented in this work is well suited for the development of a criterion to detect drizzle using an ensemble of ground based observations. Here, 5 observational variables have been selected as best performing in discriminating drizzling from non-drizzling pixels. Section 7.1 shows the statistical features of drizzling and non-drizzling cloudy pixels for the selected variables. They are used here to set up χ^2 statistical tests to assess the drizzle status of each pixel observed. The drizzle status is defined by a drizzle index (DI) which represents a probability for the pixel to be drizzling weighted with the amount of information available for every pixel. Section 7.2 describes the algorithm to calculate DI in detail. Then, the DI is tested on typical situations of drizzling and non-drizzling case studies and also for a case of cloud developing drizzle (section 7.3). Finally, in section 7.4 a comparison with the Cloudnet algorithm is presented and a quantitative evaluation of differences and analogies between the two classifications methods is performed.

7.1 DISTRIBUTIONS OF OBSERVED VARIABLES FOR DRIZZLING / NON-DRIZZLING CLOUDS

The basis for developing a statistical criterion for drizzle detection is an accurate a priori discrimination of the drizzling and non-drizzling populations. In Chapter 4, a method to unambiguously discriminate between drizzling and non-drizzling population is presented. This method is based only on continuous non-drizzling, respectively drizzling cases as classified by Cloudnet avoiding sudden, apparently random transitions between non-drizzle and drizzle (see. Table 4.2). Columns are identified as non-drizzling, drizzling and in transition according to what explained in Chapter 4.

Many different variables are observed from ground based instrumentation but only some of them have potential to efficiently discriminate between drizzling and non-drizzling pixels. In this thesis, 5 different variables are used to provide information about the drizzle status of a pixel. They are Z_e , V_d , S_w , S_k , and LWP. While the first four variables are defined per pixel, the last one is a columnar vari-

able. In addition to these 5 variables, one other additional columnar variable is also described here, which is the geometrical thickness. Despite its ability in discriminate drizzling from non-drizzling pixels, it has not been exploited in the algorithm for DI calculation. The main reason for its exclusion is that it relies on the correct identification of cloud boundaries (top and base) which is sometimes erroneous in Cloudnet (see Fig. 4.6). In the following, first the distributions of pixel variables Z_e , V_d , S_w , S_k , and then the distributions of columnar variables LWP and geometrical thickness are introduced, together with a corresponding physical interpretation.

Variables defined "per pixel"

Figs. 7.1, 7.2, 7.3 and 7.4 show the normalized distribution of Z_e , V_d , S_w and S_k values for the drizzling, non-drizzling and transition datasets respectively. Every distribution is normalized over the total number of occurrences.

As mentioned in chapter 2, the reflectivity Z_e is proportional to the sixth power of the droplet diameter D . Thus, it is highly sensitive to the presence of drizzle drops. Drizzling and non-drizzling Z_e distributions have a mean value of -16.1 dBz and -39.2 dBz respectively. As can be seen from Fig. 7.1, they are well separated: only 8.8% of the values of the non-drizzling distribution are larger than 30 dBz, while 90.3% of the drizzling distribution is larger than -30 dBz. Therefore, -30 dBz can be assumed as a separating threshold between the two. The distribution for pixels which have been identified to be in the transition region lies in between the previous two, and ranges over a wider interval of reflectivities from -60 dBz to 10 dBz compared to the drizzling, respectively non-drizzling distributions. Its main peak is at -30 dBz.

Mean Doppler velocity is used to provide information on the falling velocity of the droplets in absence of turbulence and vertical air motion. Cloud droplets, as air tracers, have V_d of zero. The non-drizzling distribution in fact has a mean V_d equal to 0.06 ms^{-1} (Fig. 7.2). For drizzle growing in size, larger fall velocities are expected and thus also an increase in V_d . The drizzling distribution shows a mean value at 0.58 ms^{-1} . When no turbulence is present, V_d can thus provide indirect information on the presence of drizzle. However, the separation between drizzling and non-drizzling V_d distributions is not as evident as for Z_e : the drizzling distribution is slightly skewed to the right, with a longer tail towards positive (downward) observed Doppler velocity values. Also the transition distribution is slightly shifted towards positive Doppler velocities.

Spectral width provides information on the width of the spectrum and it is thus sensitive to bimodality in the shape induced by drizzle presence. However, this parameter is the one being most sensitive

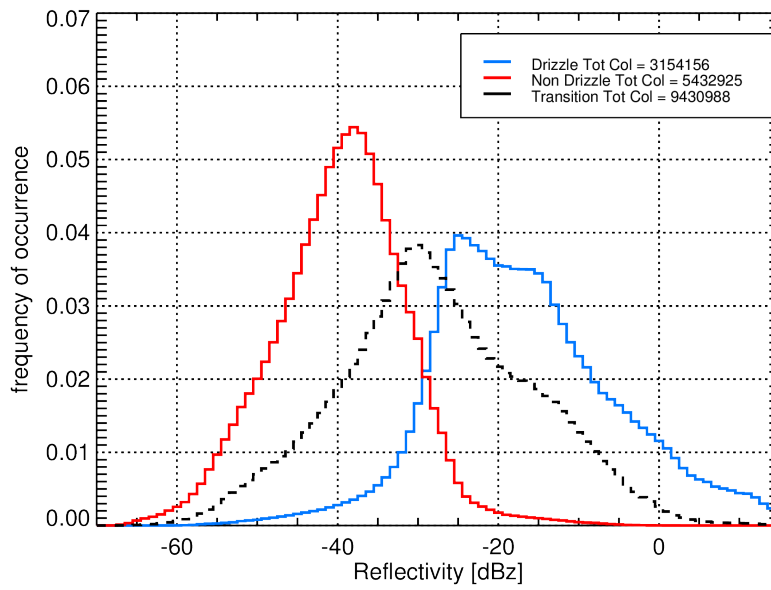


Figure 7.1: Distributions of Z_e values for the non-drizzling (red), drizzling (blue) and transition (black dashed) populations. Each distribution is normalized by its total number of pixels.

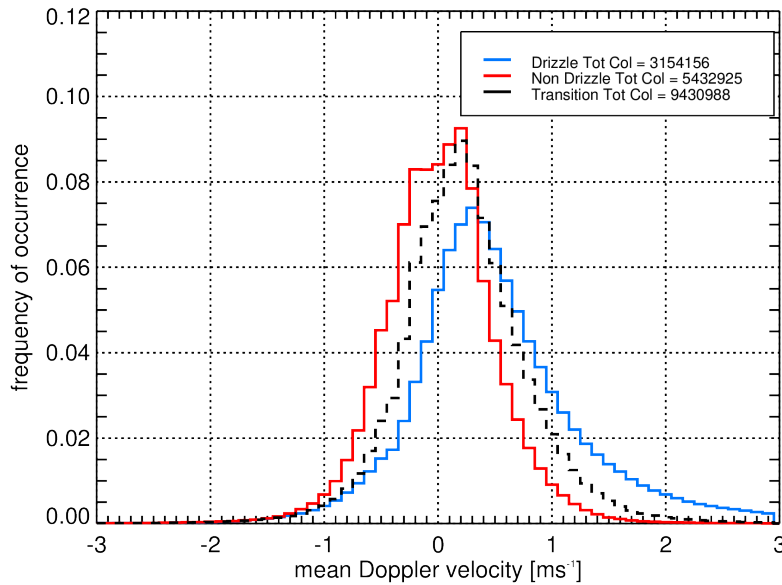


Figure 7.2: As Fig. 7.1, only for V_d .

to the presence of turbulence that typically broadens the shape of the spectrum. Figure 7.3 shows the distributions for spectral width. The mean value of S_w for non-drizzling pixels is 0.17 ms^{-1} while it reaches 0.32 ms^{-1} for the drizzling population. Moreover, 75% of the

drizzling distribution has values larger than 0.2 ms^{-1} , while 73.5% of the non-drizzling distribution has values smaller than 0.2 ms^{-1} .

Finally, the skewness distributions are shown in Fig. 7.4. Positive skewness values indicate the onset of drizzle in the cloud, while negative values represent situations in which the drizzle signature is dominating the signal. As expected, mean S_k for drizzle is -0.08 while for non-drizzle is 0.07 . For the skewness, the differences between different distributions are smaller with respect to the differences between drizzling and non-drizzling distributions found for example, for S_w . However, 63.5% of the drizzling distribution shows negative skewness values, while the non-drizzling one is almost symmetrical around zero (49% of non-drizzling skewness values are larger than zero). The transition distribution looks similar to the non-drizzling distribution showing a shape similar to a Gaussian curve.

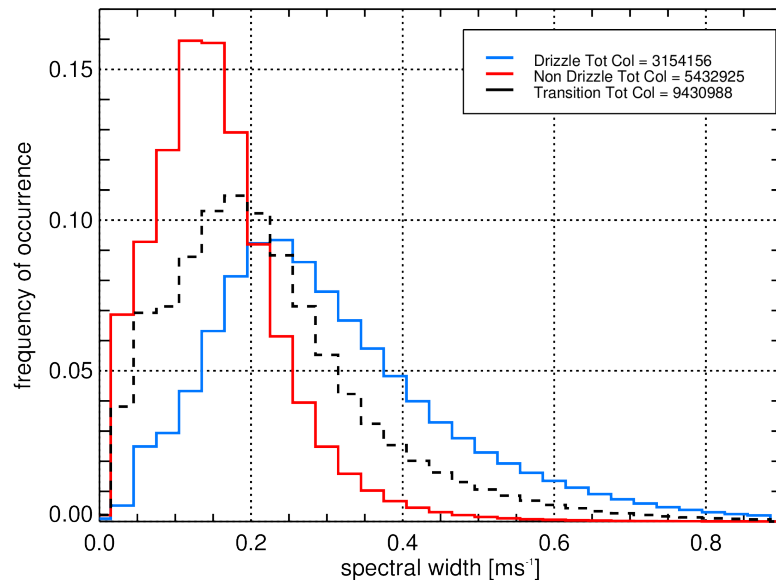


Figure 7.3: As Fig. 7.1, only for S_w .

In order to gain a better picture of the drizzling and non-drizzling features in the observed variables, two dimensional frequencies of occurrence for S_k and Z_e have been derived for the non-drizzling (Fig. 7.5), the drizzling (Fig. 7.6) and the transition (Fig. 7.7) ensembles of pixels, respectively.

Figure 7.5 shows that cloud droplets of very small size with $Z_e < -40 \text{ dBz}$ show S_k values which are symmetrically distributed around zero. For such sizes, fluctuations in the skewness are mainly due to turbulence and beam filling issues, and result therefore in equally distributed positive and negative values of S_k . In the range of -40 dBz to -30 dBz , where most of the observations occurrences are located, the sizes of the droplets are slightly larger and the skewness is slightly

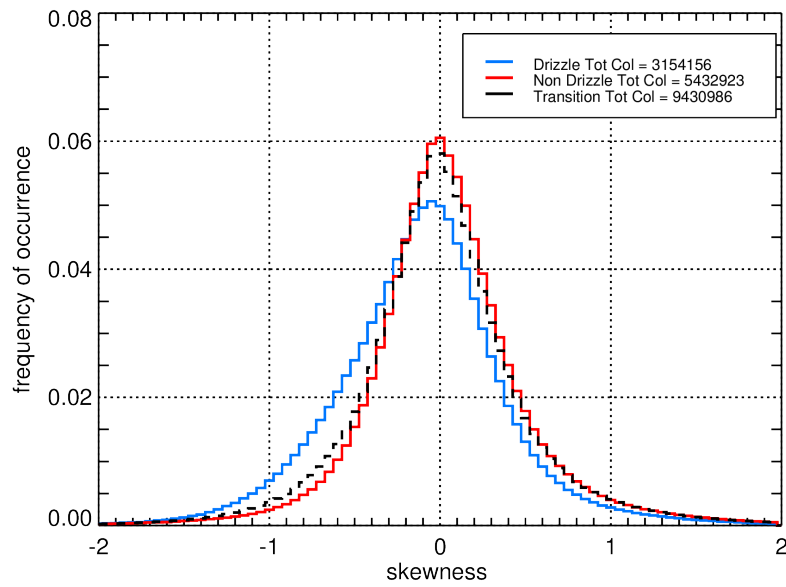


Figure 7.4: As Fig. 7.1, only for S_k .

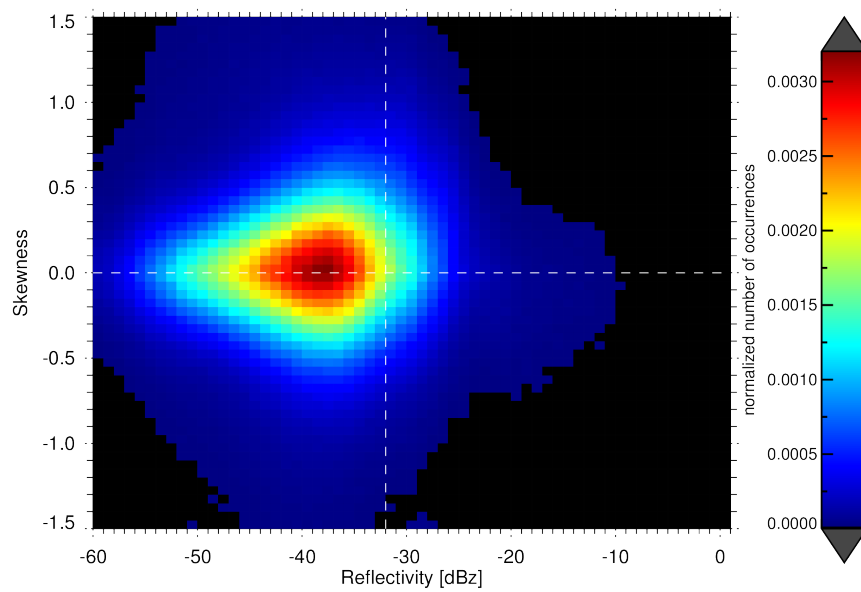


Figure 7.5: Normalized number of occurrences of pairs (Z_e, S_k) for the non-drizzling population. The distribution is normalized over the total number of non drizzling pixels.

positive. This signature is in agreement with the findings of [Luke and Kollias \(2013\)](#). Even though these pixels have been classified as cloud droplets, the skewness indicates the embryonic growth of some larger droplets, causing an asymmetry to the right of the main spectrum peak, and thus inducing a positive S_k (see also Fig 2.13).

Fig. 7.6 shows the skewness-reflectivity relation when these embryonic droplets continue to grow. For the drizzling classified pixels, the skewness turns from positive to negative values in the Z_e interval from -30 dBz to -10 dBz. The embryonic drops generate here a drizzle peak in the spectrum that dominates the cloud droplet peak, causing the skewness to change sign.

The intermediate state between these two situations is represented by the transition pixels, whose $S_k - Z_e$ distribution is represented in Fig. 7.7. Here skewness mainly shows positive values for reflectivities in the range of -40 dBz and -20 dBz.

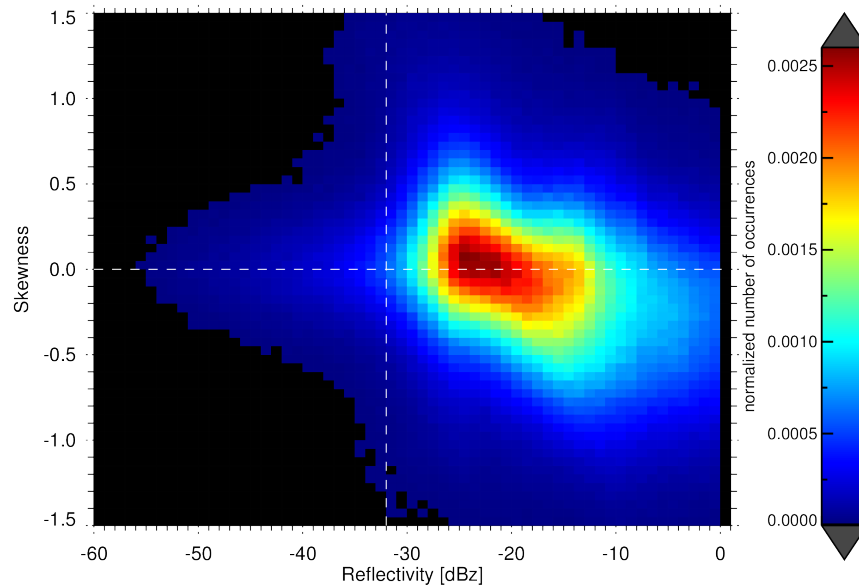


Figure 7.6: As in Fig. 7.5, only for the drizzling population.

Columnar variables LWP and geometrical thickness

Figure 7.8 shows the LWP distributions for drizzling, non-drizzling and transition columns. Typically, non-drizzling columns have LWP around 50 gm^{-2} and rarely exceed 100 gm^{-2} . In fact, only 8.9% is larger than 100 gm^{-2} . Drizzling clouds show a maximum occurrence of LWP values between 150 and 300 gm^{-2} . Only 10.5% of the values have LWP smaller than 100 gm^{-2} . Transition columns appear much more equally distributed over all the LWP bins between 0 and 400 gm^{-2} with 51.8% of the occurrences for $\text{LWP} > 100 \text{ gm}^{-2}$ and 48.2% of the occurrences for $\text{LWP} < 100 \text{ gm}^{-2}$.

The next Figure 7.9 shows the distributions for the geometrical thickness not used in the version of the drizzle detection criterion described in this thesis. Geometrical thickness is a variable which is

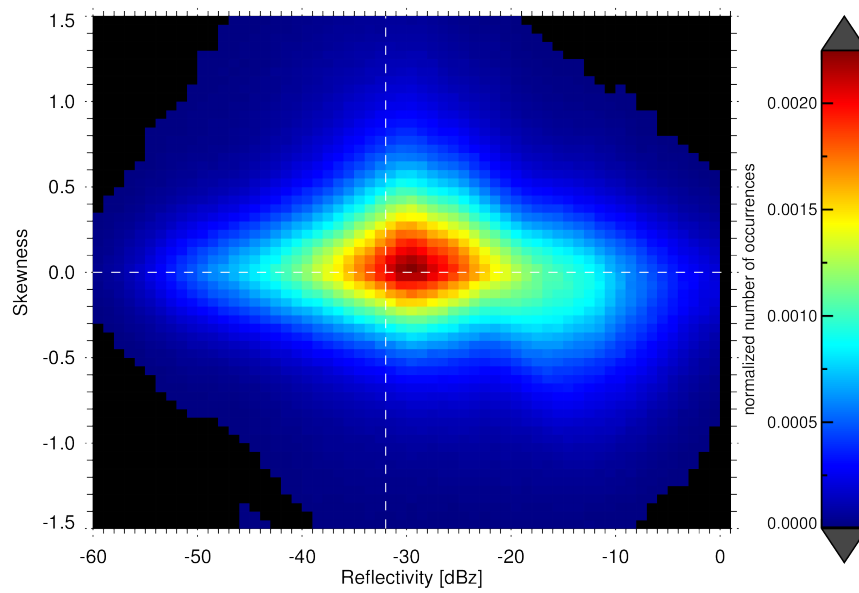


Figure 7.7: As in Fig. 7.5, only for the transition population.

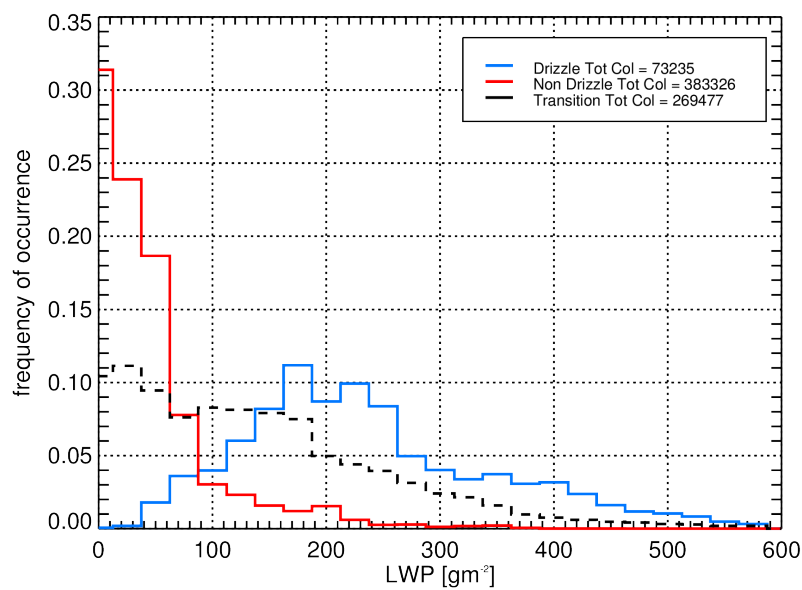


Figure 7.8: Normalized distributions of LWP values for the non drizzling (red), drizzling (blue) and transition (black dashed) populations. Each distribution is normalized over its total number of pixels. The total number of pixels given by the sum of the three populations is indicated in the legend

often used as a proxy for LWP. It can thus provide additional information for the determination of DI every time that LWP observations are not available, for example in presence of rain. Typical geometri-

cal thicknesses of non-drizzling clouds range between 100 and 450 m with a mean value of 335 m and only a few clouds (14.3%) exceeding 450 m (see Fig. 7.9). Drizzling clouds show thicknesses between 500 m and 1000 m and mean value of 888 m with 91.5% of the values larger than 450 m, while transition columns have a significative number of occurrences (54.5%) between 200 m and 700 m.

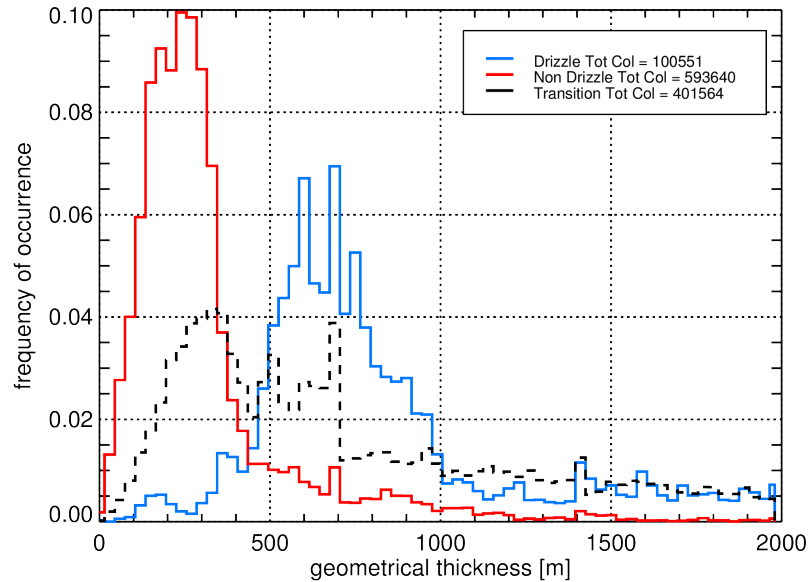


Figure 7.9: Normalized distributions of geometrical thickness values for the non drizzling (red), drizzling (blue) and transition (black dashed) populations. Each distribution is normalized over its total number of pixels. The total number of pixels given by the sum of the three populations is indicated in the legend.

7.2 THE ALGORITHM FOR CALCULATING THE DRIZZLE INDEX

In this section, the concept of the algorithm for calculating the drizzle index (DI) is explained. The goal of the criterion is to associate a drizzle status to each observed pixel. The drizzle status is defined by a drizzle index (DI) which represents a probability for the pixel to be drizzling. This probability is a coefficient derived on the basis of the values of the 5 variables in the pixel.

To determine the drizzle status of one pixel, the χ^2 test is applied. The χ^2 is a method to establish whether a particular vector or element belongs to a given Gaussian distribution (Rodgers, 2000). Here, a test for checking if a pixel belongs to the drizzling distribution and an independent test for checking if a pixel belongs to the non-drizzling distributions is developed. In the following, the methodology for belonging to the drizzling distribution is described, but the same concept is valid for the non-drizzling population. For this work, the null hy-

pothesis is formulated for each variable in the following way. For each of the variables f , the observed value \mathbf{z}_f is part of the drizzling ensemble $f_{\text{drizzle}} - \bar{f}_{\text{drizzle}}$ having mean equal to zero and covariance given by \mathbf{S}_z . Since each variable is treated independently, \mathbf{z} is the scalar value assumed by the selected variable and S_z is a coefficient given by the inverse of the variance of the corresponding drizzling/non-drizzling distribution for that variable.

The chosen significance level for the test is 75%. This means that if the test accepts the null hypothesis, the probability that the value \mathbf{z}_f belongs to the drizzling distribution is 75%. This significance has been chosen based on sensitivity tests. The χ^2 is calculated using the definition:

$$\chi^2 = \mathbf{z}^T \mathbf{S}_z^{-1} \mathbf{z}. \quad (7.1)$$

For this work, the χ^2 tests for drizzling and non-drizzling pixels are developed for Z_e , V_d , S_w and S_k , and LWP separately, and this statistical procedure is carried out for each of the 5 selected variables. Also a different definition of the χ^2 , based on treating all the 5 variables simultaneously, has been attempted. However, the resulting χ^2 was not able to determine a drizzle status for most of the cloudy pixels.

In the same way as described above for the drizzling population, a χ^2 test can be conducted also to check if the pixel belongs to the non-drizzling population. Therefore, the two tests provide two answers to the independent questions if the pixel belongs to the drizzling population and if the pixel belongs to the non-drizzling population with a probability of 75%.

To obtain a unique answer that exploits the information coming from the two independent tests, a flag is assigned to the pixel depending on the combination of answers as shown in Table 7.1. The flag

Table 7.1: Possible flags obtained by the combination of the χ^2 tests for belonging to drizzle and non drizzle distributions respectively.

belonging to drizzling distribution?	belonging to non-drizzling distribution?	flag	coefficient
yes	no	drizzle	+1
yes	yes	both	0
no	yes	non-drizzle	-1
no	no	non classified	0

can be **drizzle** if the pixel has been found to belong to the drizzle population and not to the non-drizzle one. It can be **non-drizzle** if the pixel has been found to belong to the non-drizzle population and not to the drizzle one; it can be **both** or **non classified** if it has been assigned to both populations or none of them, respectively. For every pixel, there will thus be 5 flags, indicating the drizzle status based on each variable (see Table 7.2).

In order to derive the DI, each flag is marked with a coefficient c_i that is used to weight the flag. DI is defined as

$$DI = \frac{1}{N_{\text{var}}} \sum_{i=0}^{N_{\text{var}}} c_i \quad (7.2)$$

where N_{var} is the number of variables used in the test and c_i are the coefficients assigned to the flag. As shown in Table 7.1, the coefficient for drizzle is +1, for non-drizzle -1, while for both and non classified it is 0.

Table 7.2: Example of classification array for every pixel formed by all the flags collected for each of the variables of the test.

variable	Z_e	V_d	S_w	S_k	LWP
flag	drizzle	non-drizzle	both	non classified	drizzle
coefficient	+1	-1	0	0	+1

radar range bins are here for brevity called pixels, as it has been introduced in section 3.4.

DI is calculated for every **radar pixel**. In this work, the assumption that all variables have the same influence on the DI determination is done. This choice, needed to initially evaluate the effectiveness of the general DI approach, can in the future be modified in order to give more importance to specific variables. The DI can be regarded as a probability of having drizzle weighted with the amount of information available. By definition, it ranges between -1 and +1. Values close to +1 point to the presence of drizzle, while values close to -1 indicate that the pixel is probably non-drizzling. Following from the definition, values close to zero are obtained when a few observations are available or when there is an equal number of drizzling and non-drizzling flags.

7.3 PERFORMANCE ON CASE STUDIES AT HIGH RESOLUTION

In this section, the DI is calculated for different case studies: 2 situations very likely identified as drizzling (continuity in time as identified by Cloudnet), another showing a transition from non-drizzling to drizzling conditions and further a non-drizzling one. Values of the Z_e , V_d , S_w , S_k and LWP are analyzed for different values of DI in order to obtain a physical understanding of the potential and the limitation of DI in detecting drizzle formation. The goal is to understand how the DI is performing and to provide consistency checks based on the detailed investigation of case studies as well as an evaluation with respect to Cloudnet target categorization.

7.3.1 Drizzling case study of the 5 Jan 2013

Figure 7.10 shows a time height plot of the Cloudnet classification between 12.2 and 13.0 UTC (top) and the corresponding time height plot

of the drizzle index DI. Looking at the general structure, the two classifications agree in identifying this hour of observation as drizzling with non-drizzling cloud pixels at cloud top. Based on its higher time resolution and its more detailed methodology for detecting drizzle, the DI index gets rid of the suspicious non-drizzling vertical columns identified at discrete instants of time by Cloudnet. Moreover, the DI shows the potential to describe the development of drizzle between cloud base and cloud top. In fact, close to cloud top DI shows values between -0.4 and -0.2 , and then increases to reach values close to 1 within the 200 m below cloud top. Still large values are observed within the cloud layers below 800 m. The variability of DI is larger in this layer, due to wind shear, falling velocity of the drops and air turbulence. The distribution of the retrieved DI values for this case is given in Fig. 7.11.

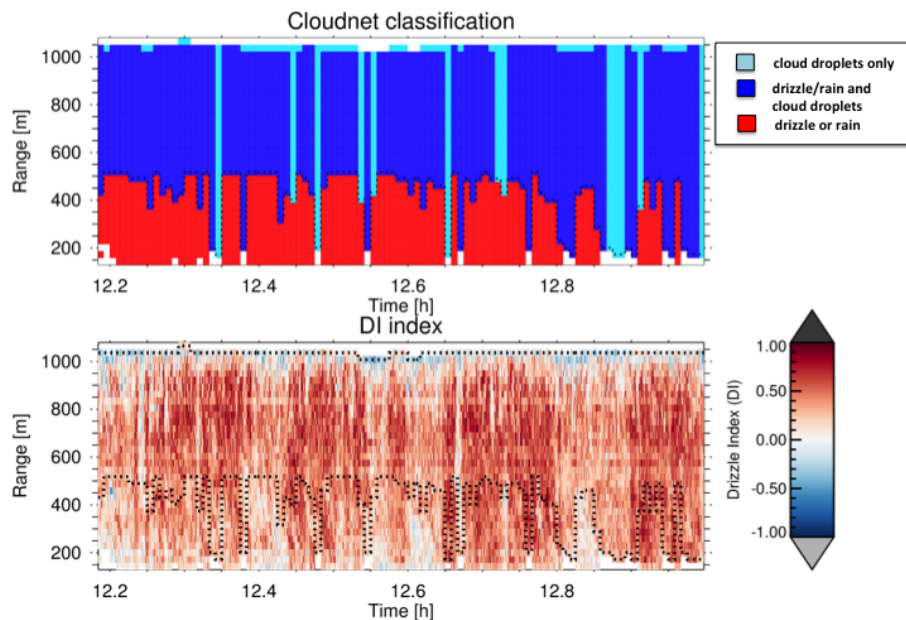


Figure 7.10: Top: time height plot of the Cloudnet categorization for the drizzle case study of the 5 January 2013, between 12.2 and 13.0 UTC. Bottom: time height plot of the corresponding DI index.

Fig. 7.11 shows the distribution of DI values obtained for this case study. The value of 0.4 has the highest number of occurrences during the hour. The measurements shown in Fig. 7.12 correspond to those pixels whose DI is equal to 0.4 and all 4 radar moments are available, which is the 30.4% of the total of 89919 pixels. Scatter plots of skewness, reflectivity, spectral width, and mean Doppler velocity for all these pixels are shown in Fig. 7.12.

Most of the pixels correspond to columns with LWP values larger than 220 gm^{-2} and Z_e values above -35 dBz (Fig. 7.12(b)). Also, for the sampled pixels, Z_e increases and S_k becomes negative when going

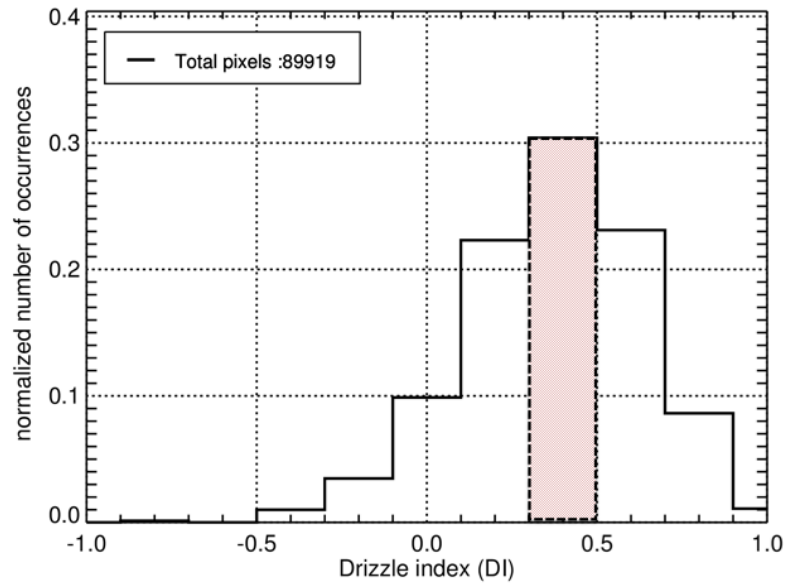


Figure 7.11: Normalized distribution of values of DI obtained for the drizzle case study of the 5 January 2013, between 12.2 and 13.0 UTC. The column shaded in red represents the most populated interval of DI values, whose physical characteristics are shown in Fig. 7.12.

from cloud top to cloud base (Fig. 7.12(a)): pixels located at heights above 900 m (red in Fig. 7.12(a)) show Z_e between -40 and -20 dBz and S_k values around 0 but with some dispersion towards positive values up to 2. For pixels located below 800 m (green and blue colors in Fig. 7.12(a)), Z_e values are between -30 dBz and 0 dBz. The corresponding S_k values become negative at a height variable between 500 and 400 m. Fig. 7.12(c) shows that, correspondingly, spectral width is increasing proportional to Z_e . Smaller values are found close to cloud top (red). Also, Z_e , S_w become larger towards cloud base: at 400 m height, typical values of S_w are between 0.2 and 0.4. Also V_d is increased towards cloud base (Fig. 7.12(d)). Moreover, some of the pixels located below cloud base (heights of 200-300 m, black points in Fig. 7.12(a),(c),(d)) show S_k values around zero and very small reflectivity values around -60 dBz (Fig. 7.12(a)). Also, they have spectral width values between 0.1 ms^{-1} and 0.35 ms^{-1} (Fig. 7.12(c)), slightly smaller than the rest of the pixels, and falling velocities between 0.5 ms^{-1} and 1.0 ms^{-1} (Fig. 7.12(d)). Since the pixels are located below cloud base, this signal can be interpreted as evaporating virga. DI identifies these observations as drizzling because LWP values are overall very large, typical of drizzling pixels (see Fig. 7.8). Globally, the distribution of pixels having $DI = 0.4$ exhibits mean Doppler velocity values that are typical for drizzling clouds (see Fig. 7.2) and reflectivities and skewness values that are in the typical range of drizzling distributions (see Fig. 7.6).

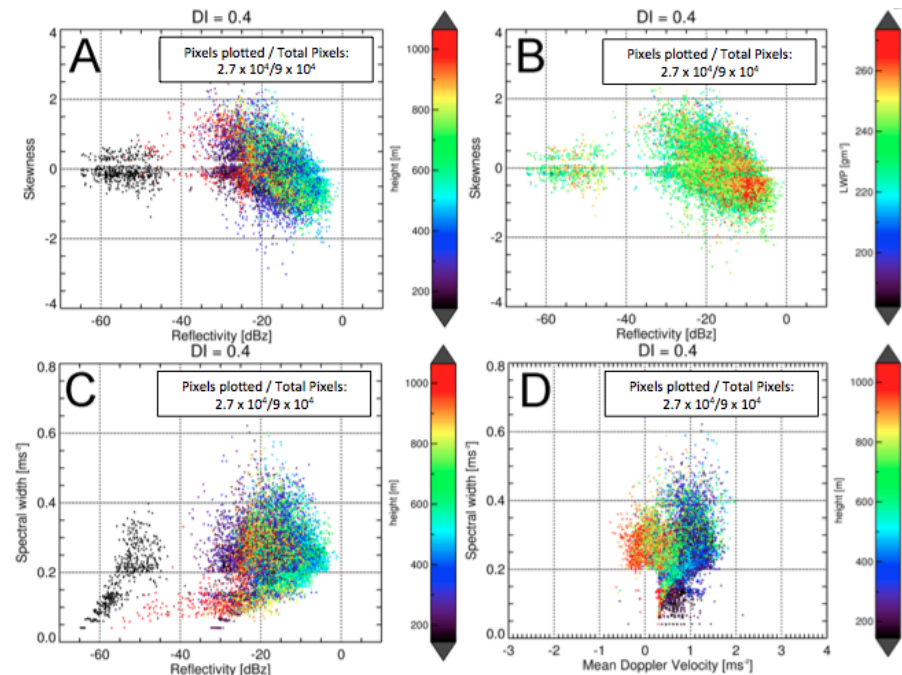


Figure 7.12: Overview of the variables in all pixels which have a $DI = 0.4$ for the drizzle case of the 5 January 2013. (a) Scatter plot of reflectivity and skewness, with colors indicating the height of the pixel. (b) Scatter plot of reflectivity and skewness with colors indicating the observed LWP in the vertical column from where the pixel is taken. (c) Scatter plot of reflectivity and spectral width with colors indicating the height of the pixel. (d) Scatter plot of mean Doppler velocity and spectral width with colors indicating the height of the pixel.

7.3.2 Drizzling case study of the 9 October 2013

The drizzle case study of the 9 October 2013 has a more complex cloud structure than that of the 5 January 2013 shown in the previous section, as can be seen from Fig. 7.13. Major differences between the Cloudnet and the DI classification are found in this case. At the beginning of the hour, around 1.2 UTC, DI indicates the presence of drizzle through the whole cloudy column, while Cloudnet classifies the same columns as non-drizzling. Also, between 1.8 and 2 UTC, at the end of the observing period, DI shows rare spots of drizzle in the cloud, while Cloudnet alternates drizzling to non-drizzling columns. Like in the previous case (Fig. 7.10), DI captures drizzling microphysical structures in the cloud and provides additional information with respect to the Cloudnet target categorization. For example, between 1.4 and 1.6 UTC a precipitating structure is highlighted by values of DI very close to 1. The drizzling structure develops between 1100 m and 900 m height, while the upper part of the cloudy column shows no or lighter drizzle. The same region is classified uniformly as drizzling by Cloudnet.

Figure 7.14 shows the distribution of DI values for the case study. The most populated classes of DI are $DI = 0.$, $DI = 0.2$, $DI = 0.4$ and $DI = 0.6$. Figure 7.15 shows the distributions of the observed values

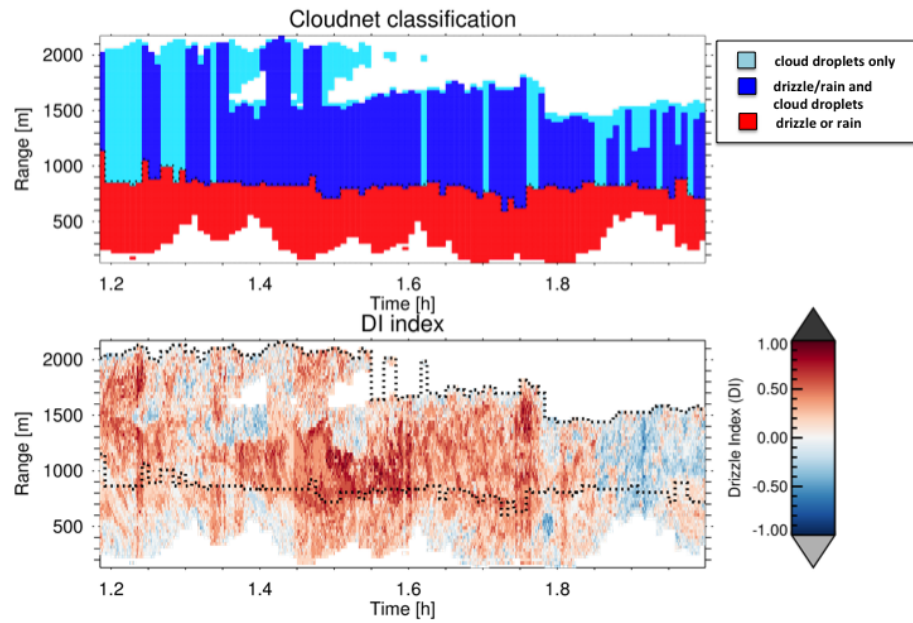


Figure 7.13: Top: Time height plot of Cloudnet categorization for the drizzle case study of the 1 October 2013, between 01:00 and 02:00 UTC. Bottom: Time height plot of the corresponding DI index.

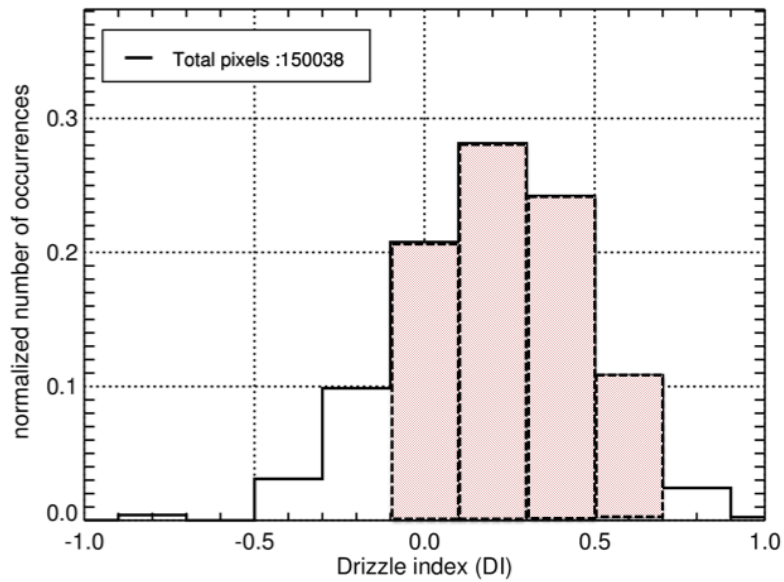


Figure 7.14: Normalized distribution of values of DI obtained for the drizzle case study of the 09 October 2013, between 1.2 and 2.0 UTC. The columns shaded in red represent the intervals of DI values, whose physical characteristics are shown in Fig 7.15.

of reflectivity, mean Doppler velocity, spectral width, skewness and LWP for different classes of pixels, identified by DI of 0, 0.2, 0.4, and 0.6. The histograms allow to investigate the differences in terms of the observed variables among pixels classified with different DI indexes.

Figure 7.15(b) shows that for increasing DI index, Z_e values become larger. For example, the distribution for $DI = 0$ has its maximum at -25 dBz, while the distributions for $DI = 0.4$ or $DI = 0.6$ peak between -22 and -12 dBz. In fact, drizzle increases the reflectivity due to the larger size of the droplets. A similar behaviour is visible for mean Doppler velocity (Fig. 7.15(c)), spectral width (Fig. 7.15(d)) and LWP (Fig. 7.15(a)). Going from a DI of 0 to a DI of 0.6, the number of occurrences of V_d between 0.3 and 1 increases. Larger values of V_d are expected because of the terminal velocity of the drizzle drops, which is not negligible as for cloud droplets. However, large values of V_d are also associated with small values of DI probably due to turbulence. The maximum of S_w shifts from 0.19 to 0.25 and then 0.3 for DI going from $DI = 0$ to $DI = 0.6$. In presence of drizzle, the bimodality in the spectrum shape induces a larger spectral width compared to the case when only cloud droplets are present. Also for LWP, the frequency of occurrence of values above 200 gm^{-2} increases for larger DI values (Fig. 7.15(a)). Finally, skewness distributions are shown in Fig. 7.15(e). Increasing DI leads to a reduction of occurrences of positive S_k values of 0.2 and an increase of the occurrences of negative values around -0.3 .

All the described trends in the observed variables associated to increasing values of DI are expected when drizzle starts to dominate the Doppler spectrum. Therefore, the DI seems to segregate distinct phases of drizzle development, exploiting the synergy of the different observational variables.

7.3.3 Transition case study of the 31 July 2013

Figure 7.16 shows the Cloudnet target categorization (top) and DI index (bottom) for the case study of a cloud developing drizzle on the 31 July 2013. Here, the ability of DI to detect the onset of drizzle is investigated. As can be seen from the Cloudnet classification time height series, this case is more ambiguous and the retrieved DI values occurring are generally smaller than in the previously discussed cases. The two classifications are almost in agreement except for the time window between 9.7 and 9.8 UTC. In this region positive DI at 9.7 UTC identifies drizzle presence where Cloudnet indicates the unrealistic situation of either "cloud droplets only", or "cloud droplets only" in the cloud and "drizzle/rain" below cloud base. Also, where Cloudnet identifies drizzle presence from cloud base to cloud top (at 9.8 UTC), DI shows some variability of drizzling and non-drizzling pixels between cloud base and cloud top. The distribution of DI values

Carl-von-Linne-Weg, 50829 Köln, Germany

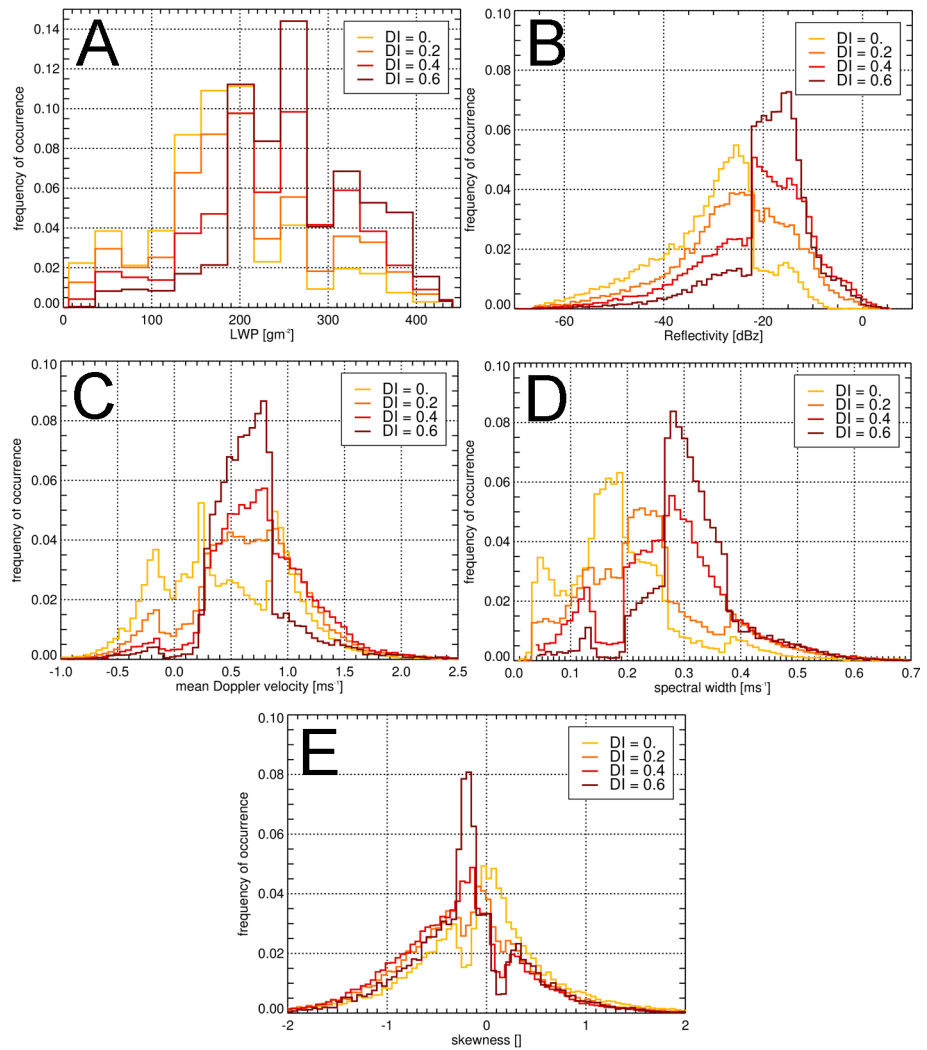


Figure 7.15: Normalized distributions of a) LWP, b) Z_e , c) V_d , d) S_w , e) S_k for the most populated DI values (highlighted in red shadow in Fig. 7.14) for the case study of the 09 October 2013, between 1.2 and 2.0 UTC.

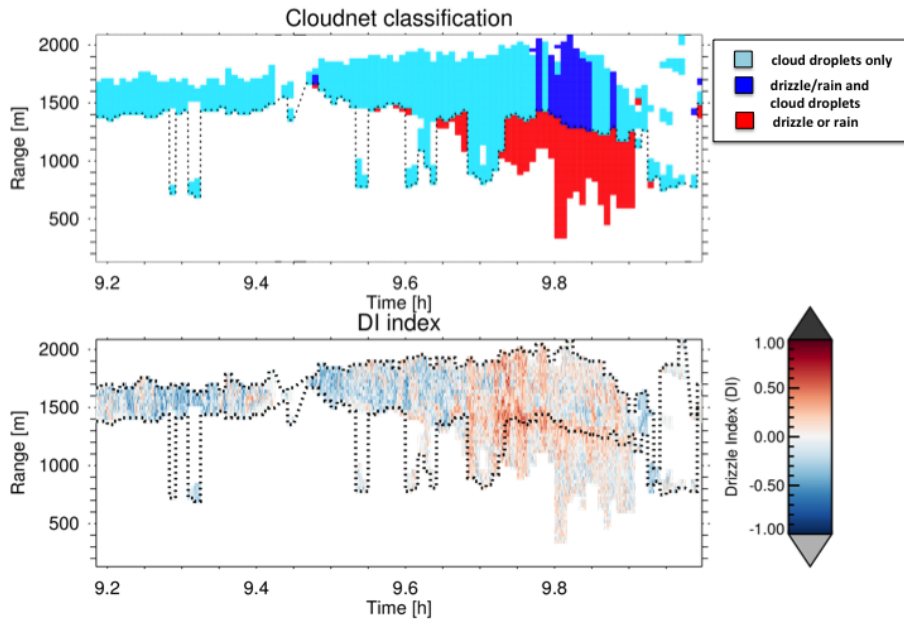


Figure 7.16: Top: time height plot of Cloudnet categorization for the drizzle case study of the 31st July 2013, between 09:00 and 10:00 UTC. Bottom: Time height plot of the corresponding DI index.

for the case study is shown in Fig. 7.17. In order to understand how well DI captures drizzle onset and how able the index is in detecting drizzling and non-drizzling pixels in ambiguous conditions, the two ensembles of pixels having $DI = -0.2$ and $DI = 0.2$ (shaded in red in Fig. 7.17) are here analyzed in detail. $DI = -0.2$ indicates pixels probably non-drizzling, while $DI = 0.2$ identifies probably drizzling pixels. The goal is to understand which are the main differences between these two ensembles and also to highlight which variables play a major role in changing DI from -0.2 to 0.2 for this case of complex drizzle formation.

Figure 7.18(b) shows that there are no differences between the two reflectivity distributions, hence Z_e is not providing information to distinguish the drizzle from the non-drizzle situations. The same is almost true also for S_w (Fig. 7.18(d)): only S_w values larger than 0.27 ms^{-1} are associated to probably drizzling situations, while a narrow interval of S_w between 0.13 and 0.2 ms^{-1} is attributed to probably non-drizzling pixels. Drizzling and non-drizzling LWP distributions (Fig. 7.18(a)) show some distinct features: the distribution for $DI = -0.2$ has a peak for $LWP < 50 \text{ gm}^{-2}$ and does not extend to $LWP > 200 \text{ gm}^{-2}$. Pixels belonging to the distribution of $DI = 0.2$ are equally distributed over the whole range of LWPs between 0 and 300 gm^{-2} . V_d values smaller than 0.3 are predominantly assigned to non-drizzling distribution, while values larger than 0.3 are mainly belonging to drizzling distributions (Fig. 7.18(c)). Finally, Fig. 7.18(e)

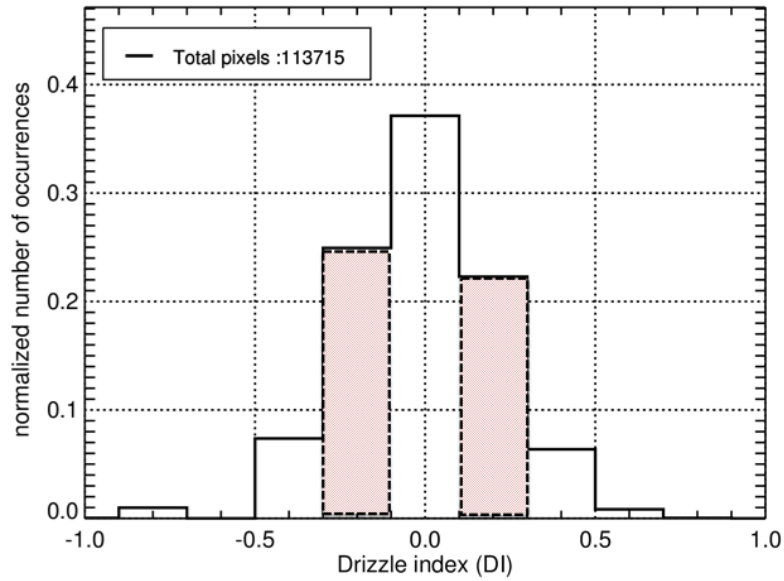


Figure 7.17: Normalized distribution of values of DI obtained for the drizzle case study of the 31 July 2013, between 9.2 and 10.0 UTC. The columns shaded in red represent the intervals of DI values, whose physical characteristics are shown in Fig 7.18.

shows the distributions for skewness. The two distributions are overlaid, except in the region of the maxima between ± 0.5 . There, negative values are predominantly assigned as probably drizzling, while positive S_k values are classified as non-drizzling.

From Fig. 7.18, the $DI = 0.2$ ensemble is discriminated on the basis of larger LWP values, positive V_d values (downwards) and also by negative S_k values. The performance of DI for this complex case study is very good. Exploiting the synergy of different observations, the algorithm is detecting drizzle with relatively high probabilities and is also identifying drizzling structures in the time height plot.

7.3.4 Non-drizzling case study of the 1 October 2013

Figure 7.19 shows the Cloudnet classification (top) and the DI classification (bottom) for the non-drizzle case study of the 1 October 2013. As Cloudnet is homogeneously identifying non-drizzle pixels during the full hour, the DI index shows values between -0.8 and $+0.6$ (see Fig. 7.20), with highest occurrences between -0.2 and 0.2 . Moreover, the drizzle index shows a strong vertical variability with predominantly negative values close to cloud top and larger values towards cloud base. In addition, DI identifies small regions showing some probability to contain drizzle.

The distributions of DI values is shown in Fig. 7.20. In order to take a closer look on why DI is mostly 0, Fig. 7.21 shows how Z_e ,

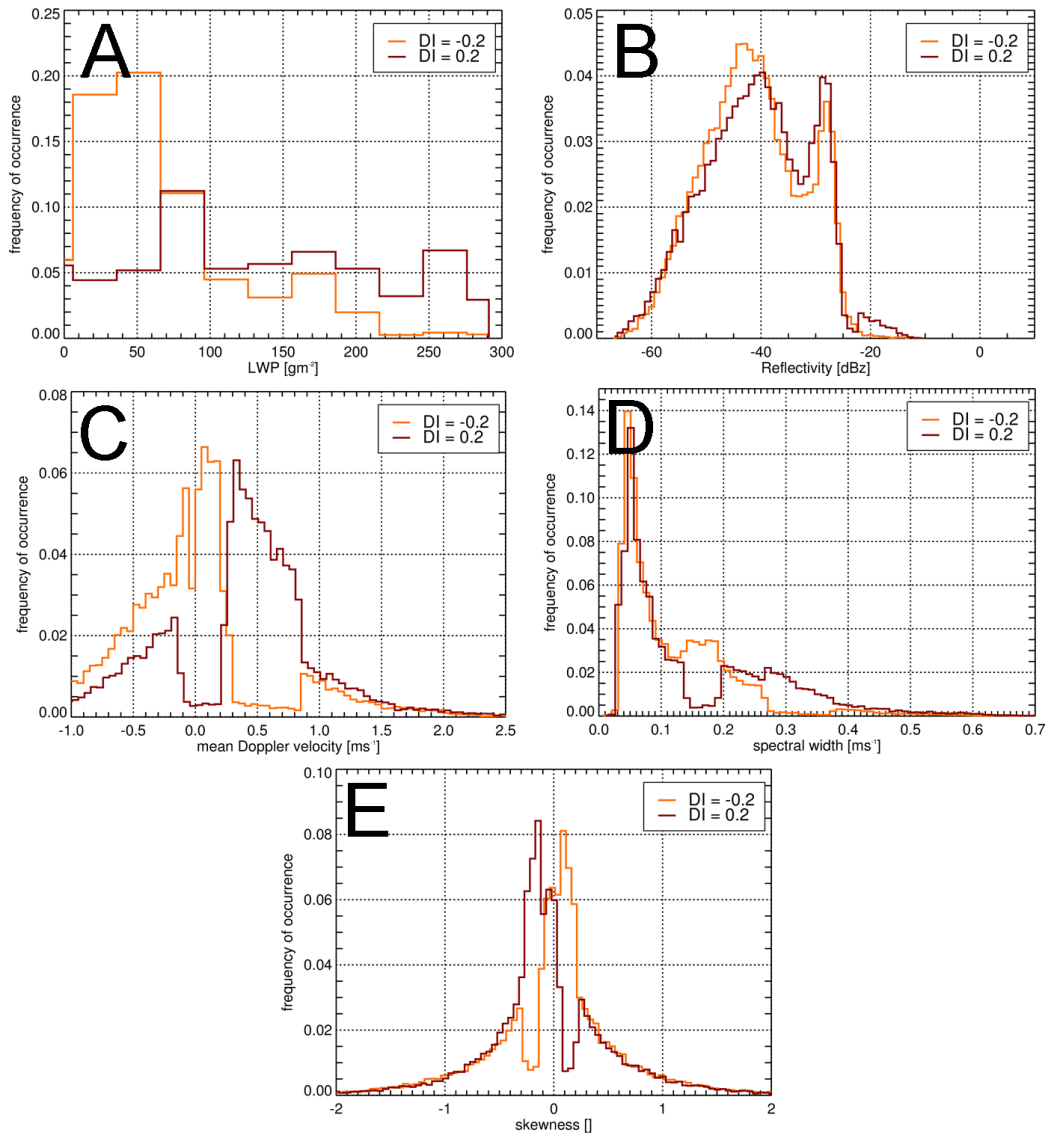


Figure 7.18: Normalized distributions of (a) LWP, (b) Z_e , (c) V_d , (d) S_w , (e) S_k for the most populated DI values (highlighted in red shadow in Fig. 7.17) for the case study of the 31 July 2013, between 9.2 and 10.0 UTC.

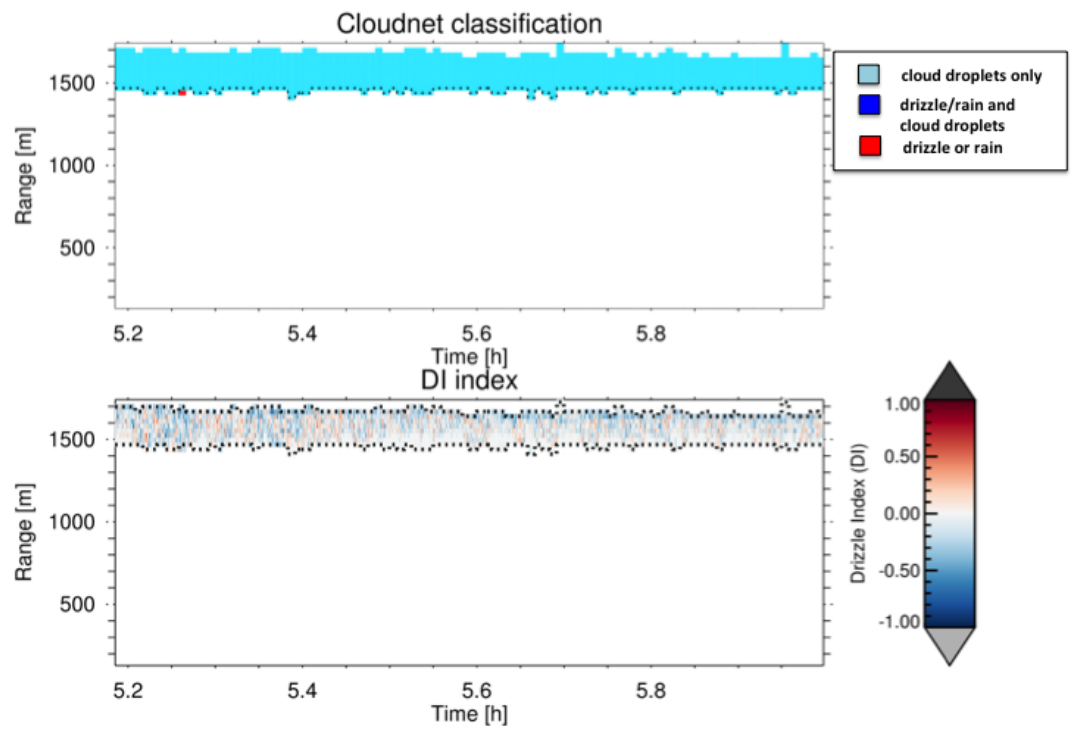


Figure 7.19: Top: time height plot of Cloudnet categorization for the non-drizzle case study of the 1 October 2013, between 5.2 and 6.0 UTC. Bottom: Time height plot of the corresponding DI index.

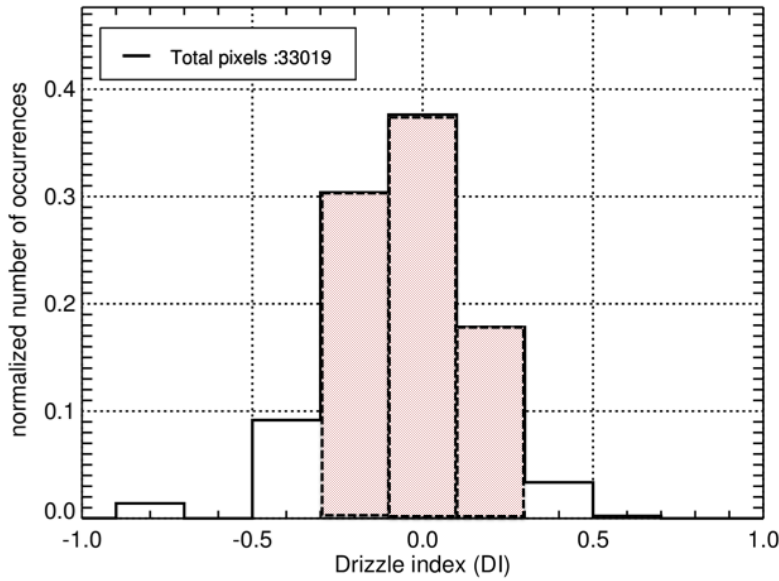


Figure 7.20: Normalized distribution of values of DI obtained for the case study of the 1 October 2013, between 5.2 and 6.0 UTC. The columns shaded in red are the ones whose physical characteristics are shown in Fig. 7.21.

V_d , S_w , and S_k are distributed for the most populated DI bin ($DI = 0, 0.2, -0.2$). Typically, pixels show S_k values around zero and reflectivities below -30 dBz with only a few values with $Z_e > -30$ dBz for all DI ensembles (Fig. 7.21(a)). All pixels have extremely low LWP values between 15 and 25 gm^{-2} . Pixels with $DI = 0.2$ show higher V_d values between 0.2 and 1 ms^{-1} , negative S_k and slightly larger than 0.3 ms^{-1} S_w values. For smaller DI, V_d becomes smaller (Fig. 7.21(b)), S_k grows to positive values (Fig. 7.21(c)) and higher occurrences of S_w values between 0.15 and 0.2 ms^{-1} are found (Fig. 7.21(d)). These observations can be associated to the presence of turbulence, which causes large values of S_w and big fluctuations of V_d while Z_e remains small. In this case study, pixels are segregated in different DI classes on the basis of the V_d and S_k . However, the fluctuations in these variables in this case seem to be induced more by turbulence than by the microphysics of drizzle formation: DI is probably falsely indicating drizzle where turbulence is present, because of features in the variables similar to those induced by drizzle. Still, DI values are rather small, indicating a small probability of having drizzle. Therefore, DI does nevertheless a good job also in this challenging situation.

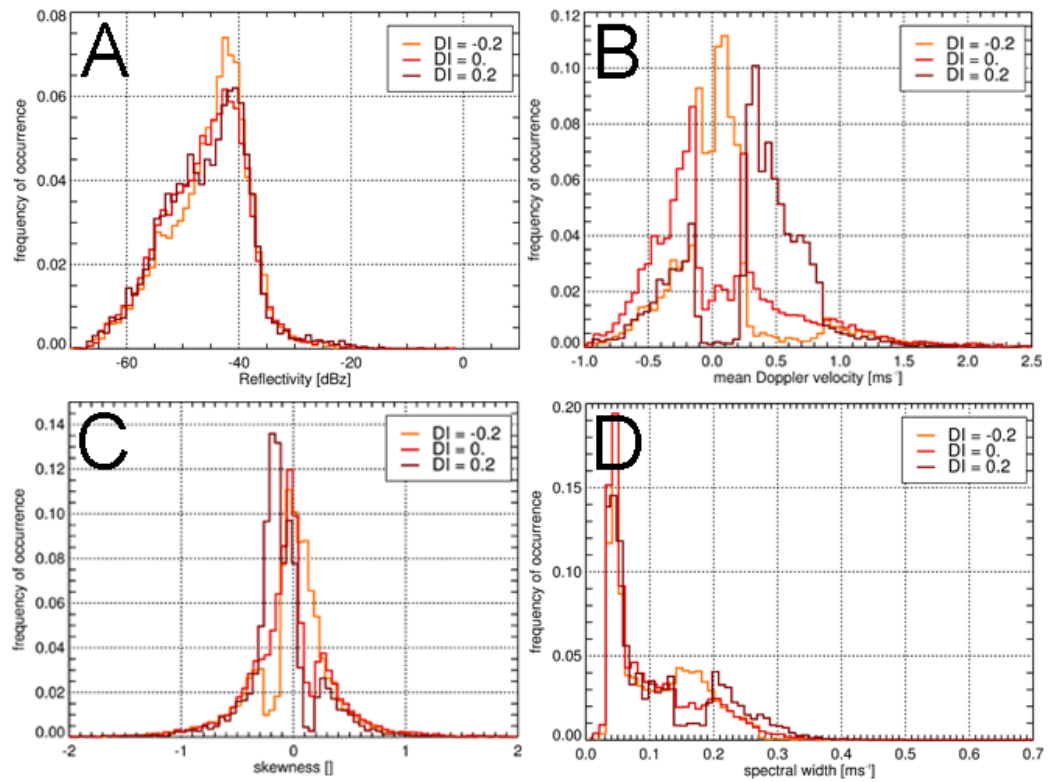


Figure 7.21: Normalized distributions of (a) LWP, (b) Z_e , (c) V_d , (d) S_w , (e) S_k for the most populated DI values (highlighted in red shadow in Fig. 7.20) for the case study of the 1 October 2013, between 5.2 and 6.0 UTC.

7.4 COMPARISON WITH CLOUDNET

In the previous section, the performance of the DI is compared to the Cloudnet categorization using different temporal resolutions. In order to enable a one-to-one comparison between the Cloudnet classification and the drizzle index, the DI has to be translated from a probabilistic approach to a deterministic one by losing some of the information it provides. In order to sample the original DI resolution of 1 s to the 30 s resolution of Cloudnet, a weighted mean of the DI associated to each Cloudnet time stamp has been calculated. Since by definition of DI, values closer to 0 are those more uncertain or those for which no measurements are available, if simply the mean of the DI values were calculated, the valuable information of the rare pixels having DI close to ± 1 would be smoothed by the mean. For this reason, the distribution of DI values obtained in the 30 s interval for a given radar pixel is derived. From the distribution, the DI value to be assigned to the pixel is obtained calculating a weighted mean over the bins of the distribution and the weight is chosen proportional to the distance from 0. Then, DI values are translated to the Cloudnet categories "cloud droplets only", "drizzle/rain and cloud droplets" and "rain" in the following way:

- Pixels located above cloud base and having $DI < 0$ are assigned to the category "cloud droplets only";
- Pixels located above cloud base and having $DI \geq 0$ are assigned to the category "drizzle/rain and cloud droplets";
- Pixels located below cloud base and having $DI \geq 0$ are assigned to the category "drizzle/rain";
- Pixels located below cloud base and having $DI < 0$ are not assigned to any of the previous categories.

Figure 7.22 presents the case study of the 13 July 2013. The DI degraded classification presents patterns of drizzle structures. Fig. 7.22 shows that in correspondence of the spots of non-drizzling DI areas at 5.57 and 5.82 UTC, there is no drizzle below cloud base. Also, wherever drizzle is found in the cloud at the cloud base height, then drizzle is also identified below cloud base. For the case study of the 13 July 2013 (Fig. 7.22), 41.6% of pixels identified as "cloud droplets only" by Cloudnet is identified as drizzling by the DI. The population of pixels classified by Cloudnet as "drizzle/rain and cloud droplets" is split in half by DI classification: 51% is also classified as drizzle above cloud base, while 48.9% is classified as non-drizzling. Also, DI recognizes as drizzling only the 41.3% of the pixels identified as "drizzle/rain" by Cloudnet.

In general, the deterministic drizzle classification based on DI detects more drizzle pixels in the cloud than Cloudnet: a statistic based

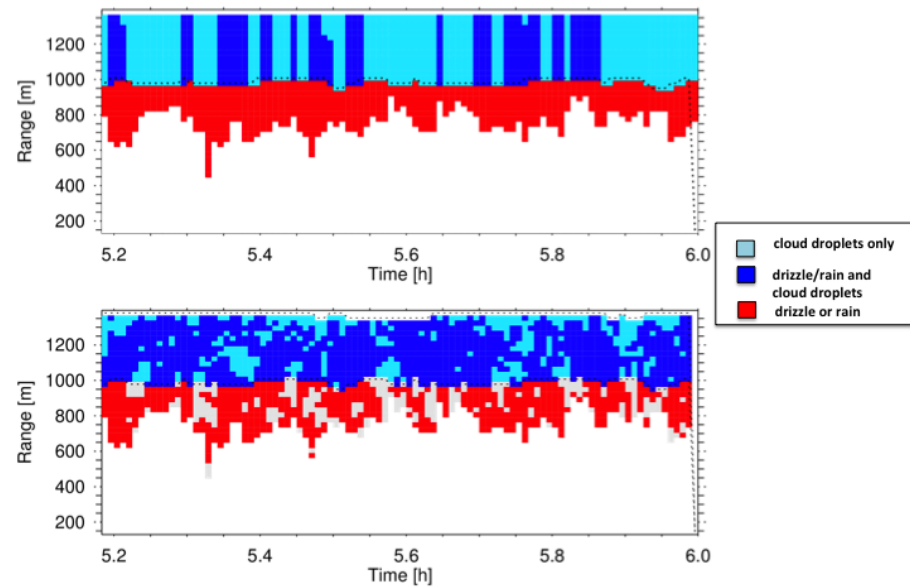


Figure 7.22: Comparison of Cloudnet categorization with DI index classification for the drizzle case of the 13 July 2013. Top: Cloudnet target categorization. Bottom: DI index interpreted in terms of Cloudnet categories as explained in the text.

on three case studies (drizzle, non-drizzle and the case study shown in Fig. 7.22) shows that in fact in only 40% of the cases DI and Cloudnet agree on the presence of cloud droplets only, while in the remaining 60% of the cases DI assigns drizzle. Furthermore, only 20% of the pixels classified as drizzle and cloud droplets by Cloudnet are recognized as non-drizzling by the DI. Regarding the presence of drizzle below cloud base, drizzle is found by DI only in the 74% of the situations in which Cloudnet identifies drizzle below cloud base. DI seems to identify regions where drizzle is evaporating and virga vanishes. Possible evaluations of the classification can be performed using in situ data.

7.5 CONCLUSIONS AND SUMMARY OF MAIN RESULTS

A new criterion to detect drizzle presence exploiting the synergy of ground based observations has been developed. The criterion is based on the derived distributions of drizzling and non-drizzling populations of radar bins. It exploits independent statistical χ^2 tests conducted for Z_e , V_d , S_w , S_k and LWP for drizzling and non-drizzling populations. The criterion provides a drizzle index representing for each radar pixel the probability of containing drizzle droplets weighted with the amount of information available for the pixel. The criterion has been tested on case studies.

As shown in section 7.3, the probabilistic (DI) drizzle classification provides a more complex description with respect to a deterministic approach (Cloudnet) based on a binary state drizzle/non-drizzle. In fact, DI is able to detect earlier stages of drizzle formation compared to Cloudnet. Drizzle droplets detected by DI are often not large enough to precipitate. The potential of DI is based on the synergy of variables, among them skewness. Skewness is independent on radar calibration and it is thus not affected by biases in Z_e . However, S_k is also prone to noise, beam filling problems and shear wind (Luke and Kollias, 2013) which can falsely attribute positive drizzling DI values. Moreover, the current methodology applied for the identification of drizzling pixels does not allow to obtain an a priori drizzling dataset exhibiting positive skewness values, which constitutes a real refinement in drizzle identification. In addition, the DI is not subjected to a selection of fixed thresholds in Z_e , whose effectiveness is highly dependent on the cloud type. For example, maritime vs continental clouds may show different ranges of Z_e in which drizzle is developed. Furthermore, the DI is not affected by the intermittency problem often seen in the Cloudnet classification (see Chapter 4).

However, DI seems to be prone to the effects induced by turbulence on radar Doppler moments which have a similar signature than drizzle microphysical processes. The non-drizzle case study (subsection 7.3.4) shows that turbulence can drive DI index falsely towards positive values, which indicate drizzling situations. In any case, turbulence plays an crucial role in triggering and driving the formation of drizzle drops (Grabowski and Wang, 2013). Therefore many of the positive DI regions induced by turbulence may actually be regions of formation of drizzle droplets. In order to quantify the turbulence, the eddy dissipation rate parameter ϵ can be added to the variables to be used, in order to flag pixels with high turbulence in the DI classification. Also, geometrical thickness can be added to the DI algorithm, once a better retrieval of cloud base height is developed.

A comparison with respect to Cloudnet shows a general tendency of DI to classify more drizzle in the cloud. Moreover, in the analyzed cases, there is only a sporadic occurrence of values smaller than -0.5 . Absolute values of DI close to 1 are obtained in situations where almost all the variables are providing information for the pixel and they agree on the classification assigned. Future work has thus to be focused on trying to understand if the low occurrence of values smaller than -0.5 is due to the specific selection of case studies presented, or if it is a structural feature of the DI definition.

Moreover, other improvements are possible. A refinement of weights of each variable can be implemented to give more importance to selected variables like S_k in the DI calculation. Neural networks in place of the statistical criterion could also be trained by using the drizzling

and non-drizzling distribution and they can be adopted to predict the drizzle status of radar pixels.

CONCLUSIONS AND OUTLOOK

This work exploits a synergy of ground based measurements to study the development of drizzle in liquid low level continental clouds. Recent studies (Kollias et al., 2011a; Luke and Kollias, 2013) show the potential of the skewness of radar Doppler spectrum for drizzle detection in maritime clouds. This work assesses the potential of the skewness, together with LWP, reflectivity, mean Doppler velocity, and spectral width, for the detection of drizzle onset.

The analysis performed within this study revealed that skewness can be used to detect drizzle formation at an earlier stage compared to the other radar moments, namely reflectivity, mean Doppler velocity and spectral width. Typically, positive values of skewness occur close to cloud top for a range of LWP values between 75 and 200 gm^{-2} (see Fig. 4.15). This corresponds to the range of LWP values where the most overlap between the drizzling and non-drizzling clouds identified on the basis of the current operational classification algorithm Cloudnet occurs (see Fig. 7.8). Therefore, skewness can provide additional information for drizzle detection. Moreover, it is independent of radar calibrations. However, skewness observations are subject to other sources of uncertainty: turbulence and beam filling issues can induce positive as well as negative skewness values which can lead to a false identification of drizzle presence.

In order to better understand how turbulence impacts skewness measurements and which radar settings minimize the uncertainty in the observations, sensitivity studies have been conducted using raw radar data and a forward radar simulator. In fact, an optimization of the skewness observations for the purpose of drizzle detection is essential for enabling future comparisons of long-term datasets from different sites. The experiment conducted presents a first step towards the optimal choice of radar parameter settings when retrieving drizzle parameters exploiting higher Doppler spectra moments. One clear limitation of the study is the restriction to two short case studies, due to the extremely large amount of data to be handled when working with IQ raw measurements. In this context, the agreement obtained between the simulations performed and the observations is even more striking, because the big amount of simulations performed (1000) underline and confirm what was observed during the short observation period. Moreover, the developed methodology, showing how such requirements can be derived in general, can be applied to other cloud types and microphysical processes to verify how radar settings can impact the identification of spectral features like bi-modalities found

in mixed-phase clouds due to the presence of super-cooled liquid water, ice, snow, and rimed particles (Shupe et al., 2004; Verlinde et al., 2013; Kalesse et al., 2015).

It has been found that for drizzle detection, using integration times longer than 2 seconds reduces skewness values and increases the observed spectral widths, but does not modify the other moments. Therefore, 2 seconds has been suggested as the optimal choice for conserving microphysical information and at the same time to limit the amount of data produced. Also, uncertainty in skewness measurements was found to be about 0.4. FFT length does not show significant impact on moments estimation and 256 fft seems therefore to be appropriate for the purpose of drizzle detection. Radar forward simulations allows to evaluate the impact of radar beam width, showing that smaller 0.3° compared to 0.6° antenna beam widths are beneficial for drizzle detection. Additionally, simulations confirm the observed dependencies in Doppler moments as a function of integration time and spectral resolution and show that turbulence is responsible for an increase of the spectral width and a reduction of the observed skewness values. In low (high) turbulence condition, only drizzle drops bigger than $20\ \mu\text{m}$ ($40\ \mu\text{m}$) of radius can produce skewness values above the detection level of 0.4 (see Fig. 6.14).

In order to exploit the skewness variable for operational applications aiming at the identification of drizzle presence in the cloud, a microphysical interpretation of the observed signal has been provided. Therefore, the drizzle formation process simulated by a 1D steady-state binned microphysical model has been compared with an ideally selected observational case study closely matching the conditions simulated by the model. The model implements different autoconversion schemes from different authors. Khairoutdinov and Kogan (2000) and Xie and Liu (2009) are two and three moments schemes, respectively. The more recent parametrizations of Franklin et al. (2005) and Seifert et al. (2010) implement a turbulent kernel. Seifert et al. (2010) also contains a description of the evolution of the autoconversion rate with time. Forward simulated profiles of radar Doppler moments are compared with observed cloud profiles of early and mature drizzle development from the observations.

It has been found that different autoconversion schemes result in completely different skewness profile in the cloud and only some of the tested schemes are able to at least qualitatively reproduce the features of the skewness observed vertical profile. Seifert et al. (2010) has been found to be the best performing scheme, while the others generally show a tendency to overestimate the drizzle production. The comparison between the observed and all the modeled skewness profiles suggests that the autoconversion rates tend to produce large drizzle too fast and too early for continental polluted clouds.

Moreover, the scheme from [Seifert et al. \(2010\)](#) has been used to assign a drizzle equivalent size to the skewness signatures and this estimation has been compared with the one obtained from the observations. It has been found that the largest observed positive skewness values in models and observations are associated to drop radii of the order of 20 to 40 μm .

Despite the uncertainty on the impact that turbulence can have, the skewness can add valuable information in a criterion for drizzle detection based on a synergy of ground based observations. The current operational criterion for classifying vertical columns (Cloudnet), which is often adopted as a basis for the set up of comparisons between GCMs and observations ([Ahlgrimm and Forbes, 2014](#)), is based solely on the vertical profile of radar reflectivity and ceilometer backscattering coefficient. Due to this simple approach adopted, Cloudnet sometimes shows inconsistent cloud column classifications, which can probably be improved by a refinement based on a multi-variable approach.

Statistics of radar bins in terms of LWP, radar reflectivity, mean Doppler velocity, spectral width and skewness have been compiled for drizzling and non-drizzling temporally continuous populations defined on the basis of the current Cloudnet classification for a dataset of 500 hours of observations. A drizzle probability index (DI) is calculated based on independent statistical χ^2 tests conducted for Z_e , V_d , S_w , S_k and LWP for drizzling and non-drizzling populations and represents the probability for each radar pixel of containing drizzle droplets. Tests on case studies show that DI is able to detect earlier stages of drizzle formation compared to Cloudnet, where drizzle droplets are often not large enough to precipitate. It also provided more realistic drizzling and non-drizzling patterns, solving the intermittency characteristic (see Chapter 4) of some Cloudnet profiles. The potential of DI is based on the synergy of variables and on the fact that it is not subjected to a selection of fixed thresholds in Z_e as for Cloudnet. However, in some cases, turbulence seems to drive DI towards false drizzling DI values. On the one hand turbulence fosters drizzle formation and thus turbulent regions can easily be regions of formation of drizzle droplets, on the other it can also lead to misclassified bins due to positive skewness values and large spectral widths.

Even if DI already shows good performances in the classification, many further improvements can be implemented. Different possibilities of calculation for DI, i.e. weights to different variables and χ^2 test applied to groups of variables instead of to single ones, can be tested. Also, neural networks can be employed in place of a statistical criterion and the eddy dissipation rate can be added as additional variable to the criterion.

In the current configuration, the statistical populations that are adopted in the DI algorithm are derived for continuous drizzling and non-drizzling regimes defined on the basis of Cloudnet. Cloudnet target categorization has been used to build populations of clearly drizzle and clearly non-drizzle radar bins because no other information is available on whether drizzle is present in the cloud. For such ensembles, the skewness signal is close to its "saturation": on average zero for non-drizzling, and mostly negative except a few positive pixels, for drizzling. The radar pixels classified as "transition" based on Cloudnet show the largest occurrence of positive skewness values. However, these most positive values, tracking the first drizzle formation and mainly occurring in the transition dataset, are not exploited in the DI calculation. The separation of drizzling and non-drizzling radar bins on the basis of the Cloudnet refined criterion is thus preventing the exploitation of the full information on drizzle contained in the skewness signature of the transition dataset. At the same time, the continuous drizzle and non-drizzle datasets on which the criterion is based may include pixels affected by turbulence or wind shear. For such pixels, the skewness signature is not driven by the microphysics but by the dynamics, and they can drive a false classification for DI.

The effectiveness of applying the correlation in time and space to the skewness field in order to get rid of skewness noise has been shown (see Fig. 5.2). Therefore, a possible different approach for the definition of the statistical populations at the basis of the drizzle criterion could be built on the basis of the skewness values, exploiting the correlation in time and height of the skewness field. By applying the skewness mask to regions of positive and negative skewness correlated in time-space areas, proper drizzling onset and drizzling mature populations could be defined, while areas of zero skewness and reflectivities smaller than 30 dBz, could be associated to non-drizzling populations. This approach may get rid of positive/negative skewness values due to noise. Moreover, it could find its theoretical basis in the model simulations, showing that in presence of growing drizzle, the skewness is expected to first show positive and then negative values. Then, multi-variate χ^2 tests, could better exploit the information contained in the data. Also, neural networks in place of the statistical χ^2 tests could be used to derive the drizzle status of each pixel.

The dataset compiled for this study is large and provides a unique basis for evaluating model outputs. Forward simulations of LES runs for JOYCE can be compared on a statistical and case study basis with the observations exploiting the PAMTRA forward simulator tool. This would add the turbulence and air motion contribution to the simulated moments, globally improving the comparison. Moreover, skewness profiles extracted from case studies suitable for process studies can be used as an indirect tool for sensitivity tests for the autoconversion parametrization, i.e. the [Seifert et al. \(2010\)](#) scheme.

Finally, additional analysis can be performed on the compiled dataset: the impact of aerosols on radar moments profile can be investigated by using aerosol optical depths that can be obtained from the sun photometer measurements (Ingold et al., 2001). Also, cloud regimes induced by different forcing mechanisms, i.e. clouds driven by the diabatic heating from the surface or by the long-wave radiative cooling from the top, can be identified using the skewness of the vertical velocity from wind lidar (Ebell et al., 2017). Exploiting the wind lidar observations together with co-located radar measurements allows to classify also in terms of Doppler radar moments the observed cloud regimes. Then, models, i.e. ICON-LEM, can be compared to the observations to check if they represent properly the characteristics of specific cloud regimes.

ABBREVIATIONS

AMT	Atmospheric Measurement Techniques
ARM	Atmospheric Radiation Measurement
BMBF	German Ministry for Education and Research
BT	Brightness Temperature
CCN	Cloud Condensation Nuclei
CDS	Cloud Detection System
CPR	Cloud Profiling Radar
CNRIMAA	Consiglio Nazionale delle Ricerche: Istituto di Metodologie per l'Analisi Ambientale
DWD	Deutscher Wetterdienst
DNS	Direct Numerical Simulation
DI	Drizzle Index
DSD	Drop Size Distribution
EARTHCARE	Earth Clouds, Aerosol and Radiation Explorer
EDR	Eddy dissipation rate
EG-CLIMET	European Ground-Based Observations of Essential Variables for Climate and Operational Meteorology
EC	Environment Canada
ECMWF	European Center for Medium Range Forecasts
FFT	Fast Fourier Transform
FMI	Finnish Meteorological Institute
DLR	German Aerospace Center
GCCN	Giant Cloud Condensation Nuclei
GCM	Global Climate Models
GCRM	Global Cloud-Resolving Model
HATPRO	Humidity And Temperature PROfiler
IR	InfraRed

IWV	Integrated Water Vapour
IGP	Istituto Geofisico del Peru'
ITARS	Initial Training for Atmospheric Remote Sensing
JOYCE	Jülich Observatory for Cloud Evolution
KIT	Karlsruhe Institute of Technology
LAMAR	Laboratorio de Microfísica Atmosférica y Radiación
TROPOS	Leibniz Institute for Tropospheric Research
LIDAR	Light Detection And Ranging
LWC	Liquid Water Content
LWP	Liquid Water Path
LMU	LudwigMaximilian Universität München
MPI	Max Planck Institute
MSG	Meteosat Second Generation
MRR	Micro Rain Radar
MW	MicroWave
MIRA	Microwave Radar
MWR	MicroWave Radiometers
MW	Microwave Radiometry
NASA	National Aeronautics and Space Administration
NUI	National University of Ireland
NARVAL	Next-generation Aircraft Remote sensing for Validation studies
NWP	Numerical Weather Prediction
PAMTRA	Passive and Active Microwave Transfer
PR	Precipitation Radar
PDF	Probability Density Function
POP	Probability Of Precipitation
RADARS	Radio Detection And Ranging
RTE	Radiative Transfer Equation

SGP	Southern Great Plains
SBM	Spectral Bin Microphysical schemes
SEVIRI	Spinning Enhanced Visible and Infrared instrument
STD	STandard Deviations
SCE	Stochastic Coalescence Equation
SCE	Stochastic Collection Equation
IGMK	University of Cologne
UTC	Coordinated Universal Time
VIS/IR	Visible/Infrared

SYMBOLS

a_l	Mie coefficient
b_l	Mie coefficient
B_ν	Planck function
c	speed of light
$d\Omega$	solid angle
$E_{\text{collision}}$	Collision efficiency
$E_{\text{collection}}$	Collection efficiency
$E_{\text{coalescence}}$	Coalescence efficiency
η	radar reflectivity
ϵ	eddy dissipation rate (dielectric constant in chapter 2)
ϵ'	relative permittivity
ϵ''	dielectric loss factor
Φ_{horiz}	horizontal beam width
Φ_{vert}	vertical beam width
Φ_{aut}	universal function
Γ	Gamma function
h	Planck constant
$H(q)$	Heaviside function
\mathcal{K}	Boltzmann's constant
K	dielectric factor
K_w	dielectric factor of water
k_0	wavenumber in free space
k_a	volume absorption coefficient
k_s	volume scattering coefficient
k_e	volume extinction coefficient
k_{cc}	kernel parameter
n	index of refraction
N_c	mean cloud droplet number concentration
r_c	cloud droplet radius corresponding to mean cloud droplet mass
$\omega_{d,j}$	shift in phase of scattered wave
P_a	incident power absorbed by a surface A

Q_a	absorption cross section
Q_e	extinction cross section
Q_s	scattering cross section
q_{cm}	threshold in q for activation of autoconversion
q_c	liquid water mixing ratio
\bar{q}_c	mean liquid water mixing ratio
ρ_w	water density
Re_λ	microscale Reynolds number
S	Supersaturation
S^*	Critical supersaturation
S_w	spectral width
S_k	skewness
τ_s	delay for resolving a radar echo
T_B	Brightness temperature
T_c	cosmic background brightness temperature
V_{Nyq}	Nyquist velocity
V_T	terminal velocity
V_c	mean terminal velocity
V_d	mean Doppler velocity
χ^*	separating mass between cloud droplets and drizzle
χ	size parameter
ξ_a	absorption efficiency
ξ_s	scattering efficiency
ξ_e	extinction efficiency
Z_e	equivalent radar reflectivity

BIBLIOGRAPHY

- Ahlgrimm, M. and Forbes, R. (2014). Improving the representation of low clouds and drizzle in the ECMWF model based on ARM observations from the Azores. *Monthly Weather Review*, 142(2):668–685.
- Albrecht, B. A. (1989). Aerosols, cloud microphysics, and fractional cloudiness. *Science*, 245:1227–1230.
- Atlas, D., Srivastava, R., and Sekhon, R. S. (1973). Doppler radar characteristics of precipitation at vertical incidence. *Reviews of Geophysics*, 11(1):1–35.
- Ayala, O., Rosa, B., Wang, L.-P., and Grabowski, W. W. (2008). Effects of turbulence on the geometric collision rate of sedimenting droplets. Part 1. Results from direct numerical simulation. *New Journal of Physics*, 10(7):075015.
- Babb, D., Verlinde, J., and Albrecht, B. A. (1999). Retrieval of cloud microphysical parameters from 94-GHz radar Doppler power spectra. *Journal of Atmospheric and Oceanic Technology*, 16(5):489–503.
- Baldauf, M., Seifert, A., Förstner, J., Majewski, D., Raschendorfer, M., and Reinhardt, T. (2011). Operational convective-scale numerical weather prediction with the COSMO model: description and sensitivities. *Monthly Weather Review*, 139(12):3887–3905.
- Beard, K. (1976). Terminal velocity and shape of cloud and precipitation drops aloft. *Journal of the Atmospheric Sciences*, 33(5):851–864.
- Beard, K. V. and Ochs, H. T. (1993). Warm-rain initiation: An overview of microphysical mechanisms. *Journal of Applied Meteorology*, 32(4):608–625.
- Beheng, K. D. (2013). *The Evolution of Raindrop Spectra: A Review of Microphysical Essentials*, in *Rainfall: State of the Science*, pages 29–48. American Geophysical Union.
- Berry, E. X. (1967). Cloud droplet growth by collection. *Journal of the Atmospheric Sciences*, 24(6):688–701.
- Betts, R. A., Jones, C. D., Knight, J. R., Keeling, R. F., and Kennedy, J. J. (2016). El nino and a record CO₂ rise. *Nature Climate Change*, 6(9):806–810.
- Bony, S., Colman, R., Kattsov, V. M., Allan, R. P., Bretherton, C. S., Dufresne, J.-L., Hall, A., Hallegatte, S., Holland, M. M., Ingram, W.,

- Randall, D. A., Soden, B. J., Tselioudis, G., and Webb, M. J. (2006). How well do we understand and evaluate climate change feedback processes? *Journal of Climate*, 19(15):3445–3482.
- Bony, S. and Dufresne, J.-L. (2005). Marine boundary layer clouds at the heart of tropical cloud feedback uncertainties in climate models. *Geophysical Research Letters*, 32(20).
- Borque, P., Luke, E., and Kollias, P. (2016). On the unified estimation of turbulence eddy dissipation rate using doppler cloud radars and lidars. *Journal of Geophysical Research: Atmospheres*, 121(10):5972–5989.
- Bryant, G. and Browning, K. (1975). Multi-level measurements of turbulence over the sea during the passage of a frontal zone. *Quarterly Journal of the Royal Meteorological Society*, 101(427):35–54.
- Caumont, O., Ducrocq, V., Delrieu, G., Gosset, M., Pinty, J.-P., Parent du Châtelet, J., Andrieu, H., Lemaître, Y., and Scialom, G. (2006). A radar simulator for high-resolution nonhydrostatic models. *Journal of Atmospheric and Oceanic Technology*, 23(8):1049–1067.
- Cimini, D., Frank, S., and Visconti, G. (2010a). *Integrated ground-based observing systems*. Springer.
- Cimini, D., Westwater, E. R., and Gasiewski, A. J. (2010b). Temperature and humidity profiling in the arctic using ground-based millimeter-wave radiometry and 1dvar. *IEEE Transactions on Geoscience and Remote Sensing*, 48(3):1381–1388.
- Clark, T. L. (1974). A study in cloud phase parameterization using the gamma distribution. *Journal of the Atmospheric Sciences*, 31(1):142–155.
- Clark, T. L. (1976). Use of log-normal distributions for numerical calculations of condensation and collection. *Journal of the Atmospheric Sciences*, 33(5):810–821.
- Clothiaux, E. E., Ackerman, T. P., and Babb, D. M. (1996). Ground-based remote sensing of cloud properties using millimeter-wave radar. In *Radiation and Water in the Climate System*, pages 323–366. Springer.
- Crewell, S. and Löhnert, U. (2003). Accuracy of cloud liquid water path from ground-based microwave radiometry 2. Sensor accuracy and synergy. *Radio Science*, 38(3).
- Dal Gesso, S. (2015). *Stratocumulus clouds in a changing climate*. PhD thesis, TU Delft, Delft University of Technology.

- Del Genio, A. D. and Wolf, A. B. (2000). The temperature dependence of the liquid water path of low clouds in the southern great plains. *Journal of Climate*, 13(19):3465–3486.
- Deng, M. and Mace, G. G. (2006). Cirrus microphysical properties and air motion statistics using cloud radar Doppler moments. Part I: Algorithm description. *Journal of Applied Meteorology and Climatology*, 45(12):1690–1709.
- Dong, X., Minnis, P., Ackerman, T. P., Clothiaux, E. E., Mace, G. G., Long, C. N., and Liljegren, J. C. (2000). A 25-month database of stratocumulus cloud properties generated from ground-based measurements at the Atmospheric Radiation Measurement Southern Great Plains Site. *Journal of Geophysical Research: Atmospheres*, 105(D4):4529–4537.
- Doviak, R. and Zrnic, D. (2014). *Doppler Radar & Weather Observations*. Academic press.
- Dufresne, J.-L. and Bony, S. (2008). An assessment of the primary sources of spread of global warming estimates from coupled atmosphere–ocean models. *Journal of Climate*, 21(19):5135–5144.
- Ebell, K., Löhnert, U., Päsche, E., Orlandi, E., Schween, J. H., and Crewell, S. (2017). A 1-D variational retrieval of temperature, humidity, and liquid cloud properties: Performance under idealized and real conditions. *Journal of Geophysical Research: Atmospheres*, 122(3):1746–1766.
- Ebert, E. E., Janowiak, J. E., and Kidd, C. (2007). Comparison of near-real-time precipitation estimates from satellite observations and numerical models. *Bulletin of the American Meteorological Society*, 88(1):47.
- Endo, S., Fridlind, A. M., Lin, W., Vogelmann, A. M., Toto, T., Ackerman, A. S., McFarquhar, G. M., Jackson, R. C., Jonsson, H. H., and Liu, Y. (2015). RACORO continental boundary layer cloud investigations: 2. Large-eddy simulations of cumulus clouds and evaluation with in situ and ground-based observations. *Journal of Geophysical Research: Atmospheres*, 120(12):5993–6014.
- Fang, M., Albrecht, B. A., Ghate, V. P., and Kollias, P. (2014). Turbulence in continental stratocumulus, part I: External forcings and turbulence structures. *Boundary Layer Meteorology*, 150(3):341–360.
- Feijt, A. and van Lammeren, A. (1996). Ground-based and satellite observations of cloud fields in the Netherlands. *Monthly Weather Review*, 124(9):1914.
- Feingold, G., Cotton, W. R., Kreidenweis, S. M., and Davis, J. T. (1999). The impact of giant cloud condensation nuclei on drizzle forma-

- tion in stratocumulus: Implications for cloud radiative properties. *Journal of the Atmospheric Sciences*, 56(24):4100–4117.
- Feingold, G., Stevens, B., Cotton, W., and Walko, R. (1994). An explicit cloud microphysics/LES model designed to simulate the Twomey effect. *Atmospheric Research*, 33(1):207 – 233.
- Forster, P., Ramaswamy, V., Artaxo, P., Berntsen, T., Betts, R., Fahey, D. W., Haywood, J., Lean, J., Lowe, D. C., Myhre, G., et al. (2007). Changes in atmospheric constituents and in radiative forcing. chapter 2. In *Climate Change 2007. The Physical Science Basis*. Cambridge University Press, Cambridge, United Kingdom and New York, NY, USA.
- Franklin, C. N. (2008). A warm rain microphysics parameterization that includes the effect of turbulence. *Journal of the Atmospheric Sciences*, 65(6):1795–1816.
- Franklin, C. N., Vaillancourt, P. A., Yau, M. K., and Bartello, P. (2005). Collision rates of cloud droplets in turbulent flow. *Journal of the Atmospheric Sciences*, 62(7):2451–2466.
- Frisch, A., Fairall, C., and Snider, J. (1995). Measurement of stratus cloud and drizzle parameters in ASTEX with a K-band Doppler radar and a microwave radiometer. *Journal of the Atmospheric Sciences*, 52(16):2788–2799.
- Frisch, A. S., Feingold, G., Fairall, C. W., Uttal, T., and Snider, J. B. (1998). On cloud radar and microwave radiometer measurements of stratus cloud liquid water profiles. *Journal of Geophysical Research: Atmospheres*, 103(D18):23195–23197.
- Fritsch, J. M. and Carbone, R. (2004). Improving quantitative precipitation forecasts in the warm season: A USWRP research and development strategy. *Bulletin of the American Meteorological Society*, 85(7):955–965.
- Ghosh, S., Dávila, J., Hunt, J., Srdic, A., Fernando, H., and Jonas, P. (2005). How turbulence enhances coalescence of settling particles with applications to rain in clouds. *Proceedings of the Royal Society of London A: Mathematical, Physical and Engineering Sciences*, 461(2062):3059–3088.
- Görsdorf, U., Lehmann, V., Bauer-Pfundstein, M., Peters, G., Vavriv, D., Vinogradov, V., and Volkov, V. (2015). A 35-GHz polarimetric Doppler radar for long-term observations of cloud parameters — Description of system and data processing. *Journal of Atmospheric and Oceanic Technology*, 32(4):675–690.

- Gossard, E. (1994). Measurement of cloud droplet size spectra by Doppler radar. *Journal of Atmospheric and Oceanic Technology*, 11(3):712–726.
- Grabowski, W. W. and Wang, L.-P. (2009). Diffusional and accretional growth of water drops in a rising adiabatic parcel: Effects of the turbulent collision kernel. *Atmospheric Chemistry and Physics*, 9(7):2335–2353.
- Grabowski, W. W. and Wang, L.-P. (2013). Growth of cloud droplets in a turbulent environment. *Annual Review of Fluid Mechanics*, 45:293–324.
- Gultepe, I. and Starr, D. O. (1995). Dynamical structure and turbulence in cirrus clouds: Aircraft observations during fire. *Journal of the Atmospheric Sciences*, 52(23):4159–4182.
- Han, Y., Westwater, E. R., and Ferrare, R. A. (1997). Applications of Kalman filtering to derive water vapor profiles from Raman lidar and microwave radiometers. *Journal of Atmospheric and Oceanic Technology*, 14(3):480–487.
- Hildebrand, P. H. and Sekhon, R. (1974). Objective determination of the noise level in Doppler spectra. *Journal of Applied Meteorology*, 13(7):808–811.
- Hobbs, P. V., Funk, N. T., Weiss Sr, R. R., Locatelli, J. D., and Biswas, K. R. (1985). Evaluation of a 35 GHz radar for cloud physics research. *Journal of Atmospheric and Oceanic Technology*, 2(1):35–48.
- Hogan, R. J., Mittermaier, M. P., and Illingworth, A. J. (2006). The retrieval of ice water content from radar reflectivity factor and temperature and its use in evaluating a mesoscale model. *Journal of Applied Meteorology and Climatology*, 45(2):301–317.
- Hogan, R. J. and O’connor, E. J. (1996). 2004: Facilitating cloud radar and lidar algorithms: the Cloudnet instrument synergy/target categorization product. / Cloudnet project documentation. *Journal Atmospheric Science*, pages 1649–1662.
- Hsieh, W. C., Jonsson, H., Wang, L.-P., Buzorius, G., Flagan, R. C., Seinfeld, J. H., and Nenes, A. (2009). On the representation of droplet coalescence and autoconversion: Evaluation using ambient cloud droplet size distributions. *Journal of Geophysical Research: Atmospheres*, 114(D7):2156–2202.
- Illingworth, A. J., Barker, H. W., Beljaars, A., Ceccaldi, M., Chepfer, H., Clerbaux, N., Cole, J., Delanoë, J., Domenech, C., Donovan, D. P., Fukuda, S., Hirakata, M., Hogan, R. J., Huenerbein, A., Kollias, P., Kubota, T., Nakajima, T., Nakajima, T. Y., Nishizawa, T., Ohno,

- Y., Okamoto, H., Oki, R., Sato, K., Satoh, M., Shephard, M. W., Velázquez-Blázquez, A., Wandinger, U., Wehr, T., and van Zadelhoff, G.-J. (2015). The EarthCARE Satellite: The next step forward in global measurements of clouds, aerosols, precipitation, and radiation. *Bulletin of the American Meteorological Society*, 96(8):1311–1332.
- Illingworth, A. J., Hogan, R. J., O'Connor, E. J., Bouniol, D., Delanoë, J., Pelon, J., Protat, A., Brooks, M. E., Gaussiat, N., Wilson, D. R., Donovan, D. P., Baltink, H. K., van Zadelhoff, G.-J., Eastment, J. D., Goddard, J. W. F., Wrench, C. L., Haeffelin, M., Krasnov, O. A., Russchenberg, H. W. J., Piriou, J.-M., Vinit, F., Seifert, A., Tompkins, A. M., and Willén, U. (2007). Cloudnet. *Bulletin of the American Meteorological Society*, 88(6):883–898.
- Ingold, T., Mätzler, C., Kämpfer, N., and Heimo, A. (2001). Aerosol optical depth measurements by means of a sun photometer network in Switzerland. *Journal of Geophysical Research: Atmospheres*, 106(D21):27537–27554.
- IPCC (2014). *Climate Change 2013 - The Physical Science Basis: Working Group I Contribution to the Fifth Assessment Report of the Intergovernmental Panel on Climate Change*. Cambridge University Press, New York. Available online: <http://www.climatechange2013.org/> (Accessed 22. Nov 2014).
- Jakob, C. (2003). An improved strategy for the evaluation of cloud parameterizations in GCMs. *Bulletin of the American Meteorological Society*, 84(10):1387.
- Kalesse, H., Szyrmer, W., Kneifel, S., Kollias, P., and Luke, E. (2015). Fingerprints of a riming event on cloud radar doppler spectra: observations and modeling. *Atmospheric Chemistry and Physics Discussions*, 15(20):28619–28658.
- Kessler, E. (1969). *On the distribution and continuity of water substance in atmospheric circulation*, volume 10 of *Meteorological Monographs*. American Meteorological Society.
- Khain, A. P., Beheng, K. D., Heymsfield, A., Korolev, A., Krichak, S. O., Levin, Z., Pinsky, M., Phillips, V., Prabhakaran, T., Teller, A., van den Heever, S. C., and Yano, J.-I. (2015). Representation of microphysical processes in cloud-resolving models: Spectral (bin) microphysics versus bulk parameterization. *Reviews of Geophysics*, 53(2):247–322.
- Khairoutdinov, M. and Kogan, Y. (2000). A new cloud physics parameterization in a large-eddy simulation model of marine stratocumulus. *Monthly Weather Review*, 128(1):229–243.

- Khvorostyanov, V. I. and Curry, J. A. (2002). Terminal velocities of droplets and crystals: Power laws with continuous parameters over the size spectrum. *Journal of the Atmospheric Sciences*, 59(11):1872–1884.
- Klepp, C., Ament, F., Bakan, S., Hirsch, L., and Stevens, B. (2014). *The NARVAL Campaign Report*, volume 164 of *Berichte zur Erdsystemforschung Series*. Max-Planck-Institut für Meteorologie.
- Klett, J. D. and Davis, M. H. (1973). Theoretical collision efficiencies of cloud droplets at small reynolds numbers. *Journal of the Atmospheric Sciences*, 30(1):107–117.
- Kneifel, S., Kulie, M. S., and Bennartz, R. (2011). A triple-frequency approach to retrieve microphysical snowfall parameters. *Journal of Geophysical Research: Atmospheres*, 116(D11203):1–15.
- Kollias, P. and Albrecht, B. (2000). The turbulence structure in a continental stratocumulus cloud from millimeter-wavelength radar observations. *Journal of the Atmospheric Sciences*, 57(15):2417–2434.
- Kollias, P., Albrecht, B., Lhermitte, R., and Savtchenko, A. (2001). Radar observations of updrafts, downdrafts, and turbulence in fair-weather cumuli. *Journal of the Atmospheric Sciences*, 58(13):1750–1766.
- Kollias, P., Clothiaux, E., Miller, M., Albrecht, B., Stephens, G., and Ackerman, T. (2007a). Millimeter-wavelength radars. *Bulletin of the American Meteorological Society*, 88(10):1608.
- Kollias, P., Clothiaux, E. E., Ackerman, T. P., Albrecht, B. A., Widener, K. B., Moran, K. P., Luke, E. P., Johnson, K. L., Bharadwaj, N., Mead, J. B., Miller, M. A., Verlinde, J., Marchand, R. T., and Mace, G. G. (2016). Development and applications of ARM millimeter-wavelength cloud radars. *Meteorological Monographs*, 57:17.1–17.19.
- Kollias, P., Miller, M. A., Luke, E. P., Johnson, K. L., Clothiaux, E. E., Moran, K. P., Widener, K. B., and Albrecht, B. A. (2007b). The atmospheric radiation measurement program cloud profiling radars: Second-generation sampling strategies, processing, and cloud data products. *Journal of Atmospheric and Oceanic Technology*, 24(7):1199–1214.
- Kollias, P., Rémillard, J., Luke, E., and Szyrmer, W. (2011a). Cloud radar Doppler spectra in drizzling stratiform clouds: 1. Forward modeling and remote sensing applications. *Journal of Geophysical Research: Atmospheres*, 116(D13201):1–14.
- Kollias, P., Szyrmer, W., Rémillard, J., and Luke, E. (2011b). Cloud radar doppler spectra in drizzling stratiform clouds: 2. Observations and microphysical modeling of drizzle evolution. *Journal of Geophysical Research: Atmospheres*, 116(D13203):1–14.

- Kollias, P., Tanelli, S., Battaglia, A., and Tatarevic, A. (2014). Evaluation of EarthCARE cloud profiling radar Doppler velocity measurements in particle sedimentation regimes. *Journal of Atmospheric and Oceanic Technology*, 31(2):366–386.
- Kollias, P., Tselioudis, G., and Albrecht, B. A. (2007c). Cloud climatology at the Southern Great Plains and the layer structure, drizzle, and atmospheric modes of continental stratus. *Journal of Geophysical Research: Atmospheres*, 112(D09116):1–15.
- Kolmogorov, A. N. (1991). Dissipation of energy in the locally isotropic turbulence. *Proceedings of the Royal Society of London A: Mathematical, Physical and Engineering Sciences*, 434(1890):15–17.
- Kubar, T. L., Hartmann, D. L., and Wood, R. (2009). Understanding the importance of microphysics and macrophysics for warm rain in marine low clouds. part i: Satellite observations. *Journal of the Atmospheric Sciences*, 66(10):2953–2972.
- Kummerow, C., Hong, Y., Olson, W. S., Yang, S., Adler, R. F., McColum, J., Ferraro, R., Petty, G., Shin, D.-B., and Wilhelm, T. T. (2001). The evolution of the Goddard Profiling Algorithm (GPROF) for rainfall estimation from passive microwave sensors. *Journal of Applied Meteorology*, 40(11):1801–1820.
- Kummerow, C., Simpson, J., Thiele, O., Barnes, W., Chang, A. T. C., Stocker, E., Adler, R. F., Hou, A., Kakar, R., Wentz, F., Ashcroft, P., Kozu, T., Hong, Y., Okamoto, K., Iguchi, T., Kuroiwa, H., Im, E., Haddad, Z., Huffman, G., Ferrier, B., Olson, W. S., Zipser, E., Smith, E. A., Wilhelm, T. T., North, G., Krishnamurti, T., and Nakamura, K. (2000). The status of the Tropical Rainfall Measuring Mission (TRMM) after two years in orbit. *Journal of Applied Meteorology*, 39(12):1965–1982.
- Küchler, N., Turner, D. D., Löhnert, U., and Crewell, S. (2016). Calibrating ground-based microwave radiometers: Uncertainty and drifts. *Radio Science*, 51(4):311–327.
- Lamb, D. and Verlinde, J. (2011). *Physics and chemistry of clouds*. Cambridge University Press.
- Lau, K. and Wu, H. (2003). Warm rain processes over tropical oceans and climate implications. *Geophysical Research Letters*, 30(24).
- Lebsock, M. D. and L'Ecuyer, T. S. (2011). The retrieval of warm rain from CloudSat. *Journal of Geophysical Research: Atmospheres*, 116(D20209):1–14.
- Lebsock, M. D., Stephens, G. L., and Kummerow, C. (2008). Multisensor satellite observations of aerosol effects on warm clouds. *Journal of Geophysical Research: Atmospheres*, 113(D15).

- L'Ecuyer, T. S., Berg, W., Haynes, J., Lebsock, M., and Takemura, T. (2009). Global observations of aerosol impacts on precipitation occurrence in warm maritime clouds. *Journal of Geophysical Research: Atmospheres*, 114(D9).
- Lehmann, K., Siebert, H., Wendisch, M., and Shaw, R. A. (2007). Evidence for inertial droplet clustering in weakly turbulent clouds. *Tellus B*, 59(1):57–65.
- Lhermitte, R. (1987). A 94-GHz Doppler radar for cloud observations. *Journal of Atmospheric and Oceanic Technology*, 4(1):36–48.
- Lhermitte, R. (1990). Attenuation and scattering of millimeter wavelength radiation by clouds and precipitation. *Journal of Atmospheric and Oceanic Technology*, 7(3):464–479.
- Lin, W., Liu, Y., Vogelmann, A. M., Fridlind, A., Endo, S., Song, H., Feng, S., Toto, T., Li, Z., and Zhang, M. (2015). RACORO continental boundary layer cloud investigations: 3. Separation of parameterization biases single-column model CAM5 simulations of shallow cumulus. *Journal of Geophysical Research: Atmospheres*, 120(12):6015–6033.
- Liou, K.-N. (2002). *An introduction to atmospheric radiation*, volume 84. Academic press.
- Liu, Y. and Daum, P. H. (2004). Parameterization of the autoconversion process. Part I: Analytical formulation of the Kessler-type parameterizations. *Journal of the Atmospheric Sciences*, 61(13):1539–1548.
- Lohmann, U. and Feichter, J. (2005). Global indirect aerosol effects: a review. *Atmospheric Chemistry and Physics*, 5(3):715–737.
- Lohmann, U., Lüönd, F., and Mahrt, F. (2016). *An Introduction to Clouds: From the Microscale to Climate*. Cambridge University Press.
- Löhnert, U. and Crewell, S. (2003). Accuracy of cloud liquid water path from ground-based microwave radiometry 1. Dependency on cloud model statistics. *Radio Science*, 38(3).
- Löhnert, U., Crewell, S., and Simmer, C. (2004). An integrated approach toward retrieving physically consistent profiles of temperature, humidity, and cloud liquid water. *Journal of Applied Meteorology*, 43(9):1295–1307.
- Löhnert, U., Schween, J., Acquistapace, C., Ebell, K., Maahn, M., Barrera-Verdejo, M., Hirsikko, A., Bohn, B., Knaps, A., O'connor, E., et al. (2015). JOYCE: Jülich observatory for cloud evolution. *Bulletin of the American Meteorological Society*, 96(7):1157–1174.

- Long, A. B. (1974). Solutions to the droplet collection equation for polynomial kernels. *Journal of the Atmospheric Sciences*, 31(4):1040–1052.
- Lu, M.-L., Conant, W. C., Jonsson, H. H., Varutbangkul, V., Flagan, R. C., and Seinfeld, J. H. (2007). The marine stratus/stratocumulus experiment (MASE): Aerosol-cloud relationships in marine stratocumulus. *Journal of Geophysical Research: Atmospheres*, 112(D10).
- Lu, M.-L., Sorooshian, A., Jonsson, H. H., Feingold, G., Flagan, R. C., and Seinfeld, J. H. (2009). Marine stratocumulus aerosol-cloud relationships in the MASE-II experiment: Precipitation susceptibility in eastern pacific marine stratocumulus. *Journal of Geophysical Research: Atmospheres*, 114(D24).
- Luke, E. P. and Kollias, P. (2013). Separating cloud and drizzle radar moments during precipitation onset using Doppler spectra. *Journal of Atmospheric and Oceanic Technology*, 30(8):1656–1671.
- Luke, E. P., Kollias, P., and Shupe, M. D. (2010). Detection of supercooled liquid in mixed-phase clouds using radar Doppler spectra. *Journal of Geophysical Research: Atmospheres*, 115(D19).
- Maahn, M. (2015). *Exploiting vertically pointing Doppler radar for advancing snow and ice cloud observations*. PhD thesis, Universität zu Köln.
- Maahn, M. and Löhnert, U. (2017). Potential of higher order moments of the radar Doppler spectrum for retrieving microphysical and kinematic properties of Arctic ice clouds. *Journal of Applied Meteorology and Climatology*, 56(2):263–282.
- Maahn, M., Löhnert, U., Kollias, P., Jackson, R. C., and McFarquhar, G. M. (2015). Developing and evaluating ice cloud parameterizations for forward modeling of radar moments using in situ aircraft observations. *Journal of Atmospheric and Oceanic Technology*, 32(5):880–903.
- Mann, J. A., Christine Chiu, J., Hogan, R. J., O'Connor, E. J., L'Ecuyer, T. S., Stein, T. H., and Jefferson, A. (2014). Aerosol impacts on drizzle properties in warm clouds from arm mobile facility maritime and continental deployments. *Journal of Geophysical Research: Atmospheres*, 119(7):4136–4148.
- Manton, M., Cotton, W. R., and of Atmospheric Science, C. S. U. D. (1977). *Formulation of approximate equations for modeling moist deep convection on the mesoscale*. Colorado State University, Fort Collins, Colorado.

- Maschwitz, G., Löhnert, U., Crewell, S., Rose, T., and Turner, D. (2013). Investigation of ground-based microwave radiometer calibration techniques at 530 hPa. *Atmospheric Measurement Techniques*, 6(10):2641–2658.
- Mech, M., Orlandi, E., Crewell, S., Ament, F., Hirsch, L., Hagen, M., Peters, G., and Stevens, B. (2014). HAMP-the microwave package on the high altitude and long range research aircraft HALO. *Atmospheric Measurement Techniques*, 7:4539–4553.
- Michibata, T. and Takemura, T. (2015). Evaluation of autoconversion schemes in a single model framework with satellite observations. *Journal of Geophysical Research: Atmospheres*, 120(18):9570–9590.
- Mie, G. (1908). Beiträge zur optik trüber medien, speziell kolloidaler metallösungen. *Annalen der Physik*, 330(3):377–445.
- Miles, N. L., Verlinde, J., and Clothiaux, E. E. (2000). Cloud droplet size distributions in low-level stratiform clouds. *Journal of the Atmospheric Sciences*, 57(2):295–311.
- Münkel, C., Eresmaa, N., Räsänen, J., and Karppinen, A. (2007). Retrieval of mixing height and dust concentration with lidar ceilometer. *Boundary-Layer Meteorology*, 124(1):117–128.
- O'Connor, E. J., Hogan, R. J., and Illingworth, A. J. (2005). Retrieving stratocumulus drizzle parameters using Doppler radar and lidar. *Journal of Applied Meteorology*, 44(1):14–27.
- Oue, M., Kumjian, M. R., Lu, Y., Jiang, Z., Clothiaux, E. E., Verlinde, J., and Aydin, K. (2015). X-band polarimetric and Ka-band Doppler spectral radar observations of a graupel-producing arctic mixed-phase cloud. *Journal of Applied Meteorology and Climatology*, 54(6):1335–1351.
- Petrocchi, R. and Paulsen, W. H. (1966). Meteorological significance of vertical density profiles of clouds and precipitation obtained with the An/TPQ-11 radar. In *Proc. 12th Radar Meteorology Conf, Norman, (OK)*, pages 467–474. American Meteorological Society.
- Pinsky, M. B., Khain, A. P., Grits, B., and Shapiro, M. (2006). Collisions of small drops in a turbulent flow. Part III: Relative droplet fluxes and swept volumes. *Journal of the Atmospheric Sciences*, 63(8):2123–2139.
- Posselt, R. and Lohmann, U. (2008). Influence of giant CCN on warm rain processes in the ECHAM5 GCM. *Atmospheric Chemistry and Physics*, 8(14):3769–3788.
- Prigent, C. (2010). Precipitation retrieval from space: An overview. *Comptes Rendus Geoscience*, 342(4–5):380 – 389.

- Pruppacher, H. R., Klett, J. D., and Wang, P. K. (1998). Microphysics of clouds and precipitation. *Aerosol Science and Technology*, 28(4):381–382.
- Quaas, J., Ming, Y., Menon, S., Takemura, T., Wang, M., Penner, J. E., Gettelman, A., Lohmann, U., Bellouin, N., Boucher, O., et al. (2009). Aerosol indirect effects—general circulation model intercomparison and evaluation with satellite data. *Atmospheric Chemistry and Physics*, 9(22):8697–8717.
- Randall, D., Coakley Jr, J., Lenschow, D., Fairall, C., and Kropfli, R. (1984). Outlook for research on subtropical marine stratification clouds. *Bulletin of the American Meteorological Society*, 65(12):1290–1301.
- Rauber, R. M., Ochs III, H. T., Di Girolamo, L., Göke, S., Snodgrass, E., Stevens, B., Knight, C., Jensen, J., Lenschow, D., Rilling, R., et al. (2007). Rain in shallow cumulus over the ocean: The RICO campaign. *Bulletin of the American Meteorological Society*, 88(12):1912–1928.
- Reitter, S. (2013). *Evaluating ice microphysics in NWP models with satellite observations*. PhD thesis, Universität zu Köln.
- Reverdy, M., Chepfer, H., Donovan, D., Noel, V., Cesana, G., Hoareau, C., Chiriaco, M., and Bastin, S. (2015). An EarthCARE/ATLID simulator to evaluate cloud description in climate models. *Journal of Geophysical Research: Atmospheres*, 120(21):11,090–11,113.
- Rodgers, C. D. (2000). *Inverse methods for atmospheric sounding: theory and practice*, volume 2. World scientific.
- Rogers, R. and Yau, M. K. (1996). *A short course in cloud physics*. Elsevier.
- Röhner, L. and Träumner, K. (2013). Aspects of convective boundary layer turbulence measured by a dual-doppler lidar system. *Journal of Atmospheric and Oceanic Technology*, 30(9):2132–2142.
- Rose, T., Crewell, S., Löhnert, U., and Simmer, C. (2005). A network suitable microwave radiometer for operational monitoring of the cloudy atmosphere. *Atmospheric Research*, 75(3):183–200.
- Rotstayn, L. D. and Liu, Y. (2005). A smaller global estimate of the second indirect aerosol effect. *Geophysical Research Letters*, 32(L05708):1–4.
- Schlamp, R. J., Grover, S. N., Pruppacher, H. R., and Hamielec, A. E. (1979). A numerical investigation of the effect of electric charges and vertical external electric fields on the collision efficiency of cloud drops: Part II. *Journal of the Atmospheric Sciences*, 36(2):339–349.

- Seifert, A. and Beheng, K. (2001). A double-moment parameterization for simulating autoconversion, accretion and selfcollection. *Atmospheric Research*, 59–60:265 – 281.
- Seifert, A., Nuijens, L., and Stevens, B. (2010). Turbulence effects on warm-rain autoconversion in precipitating shallow convection. *Quarterly Journal of the Royal Meteorological Society*, 136(652):1753–1762.
- Shupe, M., Brooks, I., and Canut, G. (2012). Evaluation of turbulent dissipation rate retrievals from doppler cloud radar. *Atmospheric Measurement Techniques*, 5(6):1375–1385.
- Shupe, M. D., Kollias, P., Matrosov, S. Y., and Schneider, T. L. (2004). Deriving mixed-phase cloud properties from Doppler radar spectra. *Journal of Atmospheric and Oceanic Technology*, 21(4):660–670.
- Shupe, M. D., Kollias, P., Poellot, M., and Eloranta, E. (2008). On deriving vertical air motions from cloud radar doppler spectra. *Journal of Atmospheric and Oceanic Technology*, 25(4):547–557.
- Siebert, H., Shaw, R. A., and Warhaft, Z. (2010). Statistics of small-scale velocity fluctuations and internal intermittency in marine stratocumulus clouds. *Journal of the Atmospheric Sciences*, 67(1):262–273.
- Solheim, F., Godwin, J. R., Westwater, E. R., Han, Y., Keihm, S. J., Marsh, K., and Ware, R. (1998). Radiometric profiling of temperature, water vapor and cloud liquid water using various inversion methods. *Radio Science*, 33(2):393–404.
- Sorooshian, A., Feingold, G., Lebsock, M. D., Jiang, H., and Stephens, G. L. (2009). On the precipitation susceptibility of clouds to aerosol perturbations. *Geophysical Research Letters*, 36(13).
- Stephens, G. L. and Haynes, J. M. (2007). Near global observations of the warm rain coalescence process. *Geophysical Research Letters*, 34(20):n/a–n/a. L20805.
- Stephens, G. L., L’Ecuyer, T., Forbes, R., Gettleman, A., Golaz, J.-C., Bodas-Salcedo, A., Suzuki, K., Gabriel, P., and Haynes, J. (2010). Dreary state of precipitation in global models. *Journal of Geophysical Research: Atmospheres*, 115(D24):n/a–n/a. D24211.
- Stephens, G. L., Vane, D. G., Boain, R. J., Mace, G. G., Sassen, K., Wang, Z., Illingworth, A. J., O’Connor, E. J., Rossow, W. B., Durden, S. L., Miller, S. D., Austin, R. T., Benedetti, A., Mitrescu, C., and Team, T. C. S. (2002). The CloudSat mission and the A-Train. *Bulletin of the American Meteorological Society*, 83(12):1771–1790.
- Stephens, G. L., Vane, D. G., Tanelli, S., Im, E., Durden, S., Rokey, M., Reinke, D., Partain, P., Mace, G. G., Austin, R., L’Ecuyer, T., Haynes,

- J., Lebsock, M., Suzuki, K., Waliser, D., Wu, D., Kay, J., Gettelman, A., Wang, Z., and Marchand, R. (2008). CloudSat mission: Performance and early science after the first year of operation. *Journal of Geophysical Research: Atmospheres*, 113(D00A18):1–18.
- Stevens, B., Vali, G., Comstock, K., Wood, R., Zanten, M. C. V., Austin, P. H., Bretherton, C. S., and Lenschow, D. H. (2005). Pockets of open cells and drizzle in marine stratocumulus. *Bulletin of the American Meteorological Society*, 86(1):51–57.
- Sun, Y., Solomon, S., Dai, A., and Portmann, R. W. (2006). How often does it rain? *Journal of Climate*, 19(6):916–934.
- Suzuki, K., Stephens, G. L., and Lebsock, M. D. (2013). Aerosol effect on the warm rain formation process: Satellite observations and modeling. *Journal of Geophysical Research: Atmospheres*, 118(1):170–184.
- Tennekes, H. and Lumley, J. L. (1972). *A first course in turbulence*. MIT press.
- Thies, B., Nauß, T., and Bendix, J. (2008). Precipitation process and rainfall intensity differentiation using Meteosat Second Generation Spinning Enhanced Visible and Infrared imager data. *Journal of Geophysical Research: Atmospheres*, 113(D23206):1–19.
- Tonttila, J., O'Connor, E., Hellsten, A., Hirsikko, A., O'Dowd, C., Järvinen, H., and Räisänen, P. (2015). Turbulent structure and scaling of the inertial subrange in a stratocumulus-topped boundary layer observed by a doppler lidar. *Atmospheric chemistry and physics*, 15(10):5873–5885.
- Tridon, F. and Battaglia, A. (2015). Dual-frequency radar doppler spectral retrieval of rain drop size distributions and entangled dynamics variables. *Journal of Geophysical Research: Atmospheres*, 120(11):5585–5601.
- Tridon, F., Battaglia, A., and Kollias, P. (2013). Disentangling Mie and attenuation effects in rain using a Ka-W dual-wavelength Doppler spectral ratio technique. *Geophysical Research Letters*, 40(20):5548–5552.
- Tripoli, G. J. and Cotton, W. R. (1980). A numerical investigation of several factors contributing to the observed variable intensity of deep convection over south florida. *Journal of Applied Meteorology*, 19(9):1037–1063.
- Twomey, S. (1977). The influence of pollution on the shortwave albedo of clouds. *Journal of the Atmospheric Sciences*, 34(7):1149–1152.

- Ulaby, F. T., Long, D. G., Blackwell, W. J., Elachi, C., Fung, A. K., Ruf, C., Sarabandi, K., Zebker, H. A., and Van Zyl, J. (2014). *Microwave radar and radiometric remote sensing*. University of Michigan Press Ann Arbor.
- Uttal, T. and Kropfli, R. A. (2001). The effect of radar pulse length on cloud reflectivity statistics. *Journal of Atmospheric and Oceanic Technology*, 18(6):947–961.
- Verlinde, J., Rambukkange, M. P., Clothiaux, E. E., McFarquhar, G. M., and Eloranta, E. W. (2013). Arctic multilayered, mixed-phase cloud processes revealed in millimeter-wave cloud radar doppler spectra. *Journal of Geophysical Research: Atmospheres*, 118(23).
- Vogelmann, A. M., Fridlind, A. M., Toto, T., Endo, S., Lin, W., Wang, J., Feng, S., Zhang, Y., Turner, D. D., Liu, Y., Li, Z., Xie, S., Ackerman, A. S., Zhang, M., and Khairoutdinov, M. (2015). RACORO continental boundary layer cloud investigations: 1. Case study development and ensemble large-scale forcings. *Journal of Geophysical Research: Atmospheres*, 120(12):5962–5992. 2014JD022713.
- Vogelmann, A. M., McFarquhar, G. M., Ogren, J. A., Turner, D. D., Comstock, J. M., Feingold, G., Long, C. N., Jonsson, H. H., Bucholtz, A., Collins, D. R., Diskin, G. S., Gerber, H., Lawson, R. P., Woods, R. K., Andrews, E., Yang, H.-J., Chiu, J. C., Hartsock, D., Hubbe, J. M., Lo, C., Marshak, A., Monroe, J. W., McFarlane, S. A., Schmid, B., Tomlinson, J. M., and Toto, T. (2012). RACORO extended-term aircraft observations of boundary layer clouds. *Bulletin of the American Meteorological Society*, 93(6):861–878.
- Wallace, J. M. and Hobbs, P. V. (2006). *Atmospheric science: an introductory survey*, volume 92. Academic press.
- Wang, H., Rasch, P., and Feingold, G. (2011a). Manipulating marine stratocumulus cloud amount and albedo: a process-modelling study of aerosol-cloud-precipitation interactions in response to injection of cloud condensation nuclei. *Atmospheric Chemistry and Physics*, 11(9):4237–4249.
- Wang, M., Ghan, S., Ovchinnikov, M., Liu, X., Easter, R., Kassianov, E., Qian, Y., and Morrison, H. (2011b). Aerosol indirect effects in a multi-scale aerosol-climate model PNNL-MMF. *Atmospheric Chemistry and Physics*, 11(11):5431.
- Webb, M., Senior, C., Bony, S., and Morcrette, J.-J. (2001). Combining ERBE and ISCCP data to assess clouds in the Hadley Centre, ECMWF and LMD atmospheric climate models. *Climate Dynamics*, 17(12):905–922.

- Weber, T. and Quaas, J. (2012). Incorporating the subgrid-scale variability of clouds in the autoconversion parameterization using a PDF-scheme. *Journal of Advances in Modeling Earth Systems*, 4(4).
- Westbrook, C. D., Hogan, R. J., O'Connor, E. J., and Illingworth, A. J. (2010). Estimating drizzle drop size and precipitation rate using two-colour lidar measurements. *Atmospheric Measurement Techniques*, 3(3):671–681.
- Westwater, E., Crewell, S., and C., M. (2004). A review of surface-based microwave and millimeter-wave radiometric remote sensing of the troposphere. *URSI Radio Science Bulletin*, 77(310):59–80.
- Westwater, E. R. (1978). The accuracy of water vapor and cloud liquid determination by dual-frequency ground-based microwave radiometry. *Radio Science*, 13(4):677–685.
- Westwater, E. R., Crewell, S., and Mätzler, C. (2005). Surface-based microwave and millimeter wave radiometric remote sensing of the troposphere: A tutorial. *IEEE Geoscience and Remote Sensing Society Newsletter*, 134:16–33.
- Willén, U., Crewell, S., Baltink, H. K., and Sievers, O. (2005). Assessing model predicted vertical cloud structure and cloud overlap with radar and lidar ceilometer observations for the Baltex Bridge Campaign of CLIWA-NET. *Atmospheric Research*, 75(3):227–255.
- Wood, R. (2005a). Drizzle in stratiform boundary layer clouds. Part I: Vertical and horizontal structure. *Journal of the Atmospheric Sciences*, 62(9):3011–3033.
- Wood, R. (2005b). Drizzle in stratiform boundary layer clouds. Part II: Microphysical aspects. *Journal of the Atmospheric Sciences*, 62(9):3034–3050.
- Wood, R. and Blossey, P. N. (2005). Comments on “Parameterization of the autoconversion process. part I: Analytical formulation of the Kessler-type parameterizations”. *Journal of the Atmospheric Sciences*, 62(8):3003–3006.
- Wood, R., T.L., K., and D., H. (2009). Understanding the importance of microphysics and macrophysics for warm rain in marine low clouds. Part II: Heuristic models of rain formation. *Journal of the Atmospheric Sciences*, 66(10):2973–2990.
- Xie, X. and Liu, X. (2009). Analytical three-moment autoconversion parameterization based on generalized gamma distribution. *Journal of Geophysical Research: Atmospheres*, 114(D17201):1–8.

ACKNOWLEDGMENTS

This work was founded by the Initial Training for Atmospheric Remote Sensing (ITARS; www.itars.net), European Union Seventh Framework Programme (FP7/2007–13): People, and ITN Marie Curie Actions Programme (2012–16) under Grant Agreement 289923 as well as by the research initiative High Definition Clouds and Precipitation for advancing Climate Prediction HD(CP)₂ I under grants FKZ01LK1209A and FKZ01LK1209B funded by the German Ministry for Education and Research (BMBF).

Well... from where to start....

Uli! thanks!!! I couldn't have had a better supervisor. You are great. Simply. It is amazing to work and learn for the scientist I would like to become.

Susanne. Every single time I talk, sit, work with you... I realize that... well.. you have really something special, and precious. Thanks for always being able to turn a problem in a funny and relaxing curiosity

Kerstin What to say.... sweetie you touched my heart. Thanks for giving me confidence all the way through, from Boston (mac fallen calling oklahoma and you are there catching me) passing through Bates college, Berlin and Manchester, to this thesis. You are great. You are a Friend.

Pavlos Thanks because simply without your research, I wouldn't have had a PHD to do. Thanks for teaching me. And thanks for reviewing.

Roel Thanks for accepting to review my thesis.

Montreal People thanks for making me feel at home, among the ice. I will remember Montreal forever. *Paloma and Andres* gracias por enseñarme por fin, como hacer unos mates

Infernos old and new, and non thanks for being there, always: Emiliano, Mario, Sandra, Tobi, Nils, Sara, Bernhard, Vera, Erlend, Samuel, Sebastian, Stefan, Max, Montse, Pavel, Rainer.

the ITARS: Athina, Lev, Alexander, Sophia, Mari, Iannis, Pilar, Nicolae, Umar, Stefanos, Lukas, and Doina, Christine, Susanne and Sarah for being part of the game

Karin Thanks! thanks thanks thanks

Maria gracias por bailar, siempre bailar, en cualquier lugar y lado bailar

Ed Luke thanks for showing me the magic of spectra

Steve thanks for showing me the way

and *Vincenzo* thanks for convincing me to come to Cologne, and to Germany.

It was one of the best thing I did in my life.

Harmonie, hermana mia, gracias por construir un lindo sueño, te extraño mucho.

Selin and *Victoria* for being sisters of mine, somewhere in the world

Vicky you live in me.

La mia famiglia: Paolo, Franca, Jacopo Grazie per il salvagente di amore, continuo e costante

al matematico Paolo Acquistapace, grazie per avermi aiutato a correggere la tesi.

Maura, Milla e Giulia grazie per l'amore incommensurato, trio delle meraviglie!

Thanks for the friends i found hidden in Germany *Miriam, Robert, Marcos, Bruno*

Stefan and Max: thanks for convincing me I can always be a photographer, if it goes wrong with science.

Gabriele grazie per la forza e il coraggio.

I cannoli Grazie per accogliermi.

Dario, Francesca, Nico e Corrado, che sono la mia famiglia acquisita.

Paola e Domenico che siete splendidi.

la Fra, grazie che ci sei sempre ad acchiapparmi quando cado.

and thanks to all the others, that I forgot...

ERKLÄRUNG

Ich versichere, dass ich die von mir vorgelegte Dissertation selbständig angefertigt, die benutzten Quellen und Hilfsmittel vollständig angegeben und die Stellen der Arbeit – einschließlich Tabellen, Karten und Abbildungen –, die anderen Werken im Wortlaut oder dem Sinn nach entnommen sind, in jedem Einzelfall als Entlehnung kenntlich gemacht habe; dass diese Dissertation noch keiner anderen Fakultät oder Universität zur Prüfung vorgelegen hat; dass sie – abgesehen von unten angegebenen Teilpublikationen – noch nicht veröffentlicht worden ist, sowie, dass ich eine solche Veröffentlichung vor Abschluss des Promotionsverfahrens nicht vornehmen werde. Die Bestimmungen der Promotionsordnung sind mir bekannt. Die von mir vorgelegte Dissertation ist von PD Dr. Ulrich Löhnert betreut worden.

Köln, 14. November 2016

Claudia Acquistapace

TEILPUBLIKATIONEN

Löhnert, Ulrich and Schween, JH and Acquistapace, C and Ebell, K and Maahn, M and Barrera-Verdejo, M and Hirsikko, A and Bohn, B and Knaps, A and O'connor, E and others (2015). JOYCE: Jülich observatory for cloud evolution. *Bulletin of the American Meteorological Society*. doi:[10.1175/BAMS-D-14-00105.1](https://doi.org/10.1175/BAMS-D-14-00105.1)

Acquistapace, C. and Kneifel, S. and Löhnert, U. and Kollias, P. and Maahn, M. and Bauer-Pfundstein, M. (2016). Optimizing observations of drizzle onset with millimeter-wavelength radars *Atmospheric Measurement Techniques Discussions*. doi:[10.5194/amt-2016-315](https://doi.org/10.5194/amt-2016-315)

ABOUT THE AUTHOR

PERSONAL INFORMATION

Name	Claudia Acquistapace
Date of birth	April 30 th , 1984
Place of birth	Massa, Italy
Nationality	Italian
e-mail	cacquist@meteo.uni-koeln.de

EDUCATION

since 01/2013	PhD studies in Meteorology, University of Cologne, Germany
2009 – 2012	Master degree in Physics, University of Bologna, Italy - Specialized in Atmospheric Physics and Meteorology. Thesis: <i>Satellite-based VIS/IR multispectral screening of precipitating clouds: a case study during summer at mid-latitudes.</i>
2003 – 2009	Bachelor degree in Physics, University of Pisa, Italy. Thesis: <i>Study of transport and diffusion of smoke plumes and ascending streams of hot water and applications to environmental pollution.</i>
1998–2003	High school Diploma, Liceo Scientifico F. Buonarroti, Pisa, Italy.

EXPERIENCE

Jan-Feb 2015	Visiting scientist at the McGill University, Montreal, Canada
2014	Secondment at METEK GmbH, Elmshorn, Germany

10th December 2017